AN EXPERIMENTAL INVESTIGATION OF LEAN-BURN DUAL-FUEL COMBUSTION IN A HEAVY DUTY DIESEL ENGINE

A thesis submitted for the degree of
Doctor of Philosophy

by

Ian Alexander May

Department of Mechanical, Aerospace and Civil Engineering
College of Engineering, Design and Physical Sciences
Brunel University London

May 2018

Abstract

Natural gas is currently an attractive substitute for diesel fuel in the Heavy-Duty (HD) diesel transportation sector. This is primarily attributed to its cost effectiveness, but also its ability to reduce the amount of CO_2 and harmful engine pollutants emitted into the atmosphere. Lean-burn dual-fuel engines substitute natural gas in place of diesel but typically suffer from high engine-out methane (CH_4) emissions, particularly under low load operation. In response to this issue, this work set out to improve upon the efficiency and emissions of a lean-burn dual-fuel combustion system in an HD diesel/natural gas engine.

Thermodynamic experimental engine testing was performed at various steady-state operating points in order to identify the most effective methods and technologies for improving emissions and efficiency. Low Temperature Combustion (LTC) along with several valvetrain and injection strategies were evaluated for benefits, with special attention paid to low load operating conditions.

LTC was proven to be a useful method for decreasing methane emissions while simultaneously improving engine efficiency. The benefits of LTC were a function of load with the greatest advantages experienced under medium load operation. Additionally, the low load strategies tested were determined to be effective techniques for reducing methane emissions and could possibly extend the dual-fuel operating regime to lighter load conditions.

Overall, no operating condition tested throughout the engine map resulted in a brake engine-out methane emissions level of less than 0.5 g/kWh at gas substitutions greater than approximately 75%. It is suggested that the limits of this particular lean-burn dual-fuel design were reached, and that it would likely require improvements to either the combustion system or exhaust after-treatment if Euro VI emissions levels for methane were to be achieved.

Keywords: Lean-burn dual fuel combustion; natural gas and diesel; low temperature combustion; Miller cycle; low carbon fuel; methane emissions

.

List of contents

Publications and awards related to this research

Publications:

May, I., Pedrozo, V., Zhao, H., Cairns, A., Whelan, S., Wong, H., and Bennicke, P., “Characterization and Potential of Premixed Dual-Fuel Combustion in a Heavy Duty Natural Gas/Diesel Engine,” SAE Technical Paper, 2016, doi:10.4271/2016-01-0790

May, I., Whelan, S., Wong, H.C., and Cairns, A., “Reduction of in-cylinder emissions on a dual-fuel engine,” Internationaler Motorenkongress 2016, 609–625, 2016, doi:10.1007/978-3-658-12918-7_46

May, I., Cairns, A., Zhao, H., Pedrozo, V., Wong, H.C., Whelan, S., and Bennicke, P., “Investigation of the load range of premixed micro pilot combustion in a dual-fuel natural gas / diesel engine – Part 1 of 2,” Internal Combustion Engines Conference, Institution of Mechanical Engineers, December 2015

May, I., Cairns, A., Zhao, H., Pedrozo, V., Wong, H.C., Whelan, S., and Bennicke, P., “Investigation of the load range of premixed micro pilot combustion in a dual-fuel natural gas / diesel engine – Part 2 of 2,” Internal Combustion Engines Conference, Institution of Mechanical Engineers, December 2015

May, I., Cairns, A., Zhao, H., Pedrozo, V., Wong, H.C., Whelan, S., and Bennicke, P., “Reduction of Methane Slip Using Premixed Micro Pilot Combustion in a Heavy-Duty Natural Gas-Diesel Engine,” SAE Technical Paper, 2015, doi:10.4271/2015-01-1798

Awards:

The Herbert Akroyd Stuart Award 2015 – Institution of Mechanical Engineers
Awarded to *“Investigation of the load range of premixed micro pilot combustion in a dual-fuel natural gas / diesel engine – Part 2 of 2”* for the best paper on the subject of “The Origin and Development of Heavy Oil Engines” published by the Institution during the previous year

List of illustrations

List of tables

Acknowledgements

First and foremost, I would like to thank my family for providing the love and support necessary to be able to follow my dreams abroad. I’m very grateful to my parents in particular, for providing advice as well as the means for me to pursue my degree here in the UK.

I also appreciate the support of my friends back in the US, which helped make the transition to living in the UK easier, as well as providing professional and personal advice to me along the way. A special thanks to Will for your insights and for providing me access to an opportunity like this.

Thank you to all my colleagues at Vayon Gas Technologies as well as the board of directors for providing the technical and financial means to carry out this research. Particular thanks to Paul, HC, Andrew, Rob, and Steve for their skills, thoughts, and counsel.

I am appreciative for the assistance and friendship of all the technicians at Brunel, particularly Andy, Chris, and Clive. I admire their skills and attention to detail and could not have asked for better support.

Many thanks to my friends at Brunel for providing advice in the laboratory as well as laughs in and outside of it. Particular thanks to Thompson, Mack, Yan, and Pin. Finally, I would like to acknowledge Vinicius for your friendship, as well as your considerable talents and counsel. I couldn’t have asked for a better colleague and friend, and it’s been great to work and travel with you. Thank you as well to all my non-Brunel friends in UK, which helped me to explore Europe.

I am deeply grateful to my supervisors, Professor Alasdair Cairns and Professor Hua Zhao, for their guidance and for providing the means and freedom to conduct this research. I have the utmost admiration and respect for you and cannot think of better role models. Special thanks to Alasdair, as it has really been a pleasure to work with you for the past few years.

I would like to thank the UK Knowledge Transfer Partnership program for providing the financial support for this work.

Finally, I would like to thank Alexandra for her love.

Notation

Abbreviations	**Units**
ASC: ammonia slip catalyst	-
ATDC: after top dead centre	-
BMEP: brake mean effective pressure	bar
BSFC: brake specific fuel consumption	g/kWh
BTDC: before top dead centre	-
CA: crank angle	°
CAD: computer aided design	-
CAI: controlled auto-ignition	-
CAN: controller area network	-
CARB: California Air Resources Board	-
CFD: computational fluid dynamics	-
CI: compression ignition	-
CNG: compressed natural gas	-
CO: volumetric exhaust carbon monoxide concentration	ppm
COV: coefficient of variance	%
deg: degree	°
DI: direct injection	-
DOC: diesel oxidation catalyst	-
DPF: diesel particulate filter	-
ECE: Engine Control Electronics	-
ECR: effective compression ratio	-
ECU: engine control unit	-
EER: effective expansion ratio	-
EGR: exhaust gas recirculation	%
EGT: exhaust gas temperature	°C
EIVC: early intake valve closing	-
EPA: Environmental Protection Agency	-
EQR: equivalence ratio	-
EVC: exhaust valve closing	°CA
EVO: exhaust valve opening	°CA
FID: flame ionisation detector	-

FMEP: friction mean effective pressure	bar
FSN: filter smoke number	-
GDCI: gasoline direct injection compression ignition	-
GGE: gasoline-gallon equivalent	-
GHG: greenhouse gas	-
GWP: Global Warming Potential	-
HC: unburnt hydrocarbons	ppm
HCCI: homogeneous charge compression ignition	-
HD: heavy duty	-
HD-OBD: heavy duty on-board diagnostics	-
HHR: heat release rate	J/°CA
HP: high pressure or horsepower	-
HPDI: high pressure direct injection	-
HPL: high pressure loop	-
IDI: indirect-injection	-
IEA: International Energy Agency	-
I-EGR: internal exhaust gas recirculation	-
IMEP: indicated mean effective pressure	bar
ISCH$_4$: indicated specific methane emission	g/kWh
ISCO: indicated specific carbon monoxide emission	g/kWh
ISFC: indicated specific fuel consumption	g/kWh
ISHC: indicated specific hydrocarbon emission	g/kWh
ISNO$_x$: indicated specific nitrogen oxides emission	g/kWh
ISSoot: indicated specific soot emission	g/kWh
IVC: intake valve closing	°CA
IVO: intake valve opening	°CA
LD-OBD: light duty on-board diagnostics	-
LHV: lower heating value of fuel	MJ/kg
LIVC: late intake valve closing	-
LNG: liquefied natural gas	-
LTC: low temperature combustion	-
MBDOE: million oil-equivalent barrels per day	-
MBT: minimum ignition advance for best torque	°CA
MFB: mass fraction burned	-

MK: modulated kinetics	-
MN: methane number	-
NA: naturally aspirated	-
NDIR: non-dispersive infra-red	-
NG: natural gas	-
NMHC: Non-methane hydrocarbon	ppm
NO: nitric oxide	ppm
NOx: volumetric exhaust nitrogen oxides concentration	ppm
OBD: on-board diagnostics	-
PCCI: premixed charge compression ignition	-
PDFC: premixed dual-fuel combustion	-
PFI: port fuel injection	-
PM: particle mass or particulate matter	-
PMax: maximum in-cylinder pressure	bar
PMEP: pumping mean effective pressure	bar
PN: particle number	-
PPCI: partially premixed compression ignition	-
ppm: parts per million	ppm
PRR: pressure rise rate	bar/°CA
PWM: pulse width modulation	-
RCCI: reactivity controlled compression ignition	-
RPM: revolutions per minute	rpm
SCR: selective catalytic reduction	-
SOI: start of fuel injection	°CA
TDC: top dead centre	-
THC: volumetric exhaust total unburnt hydrocarbon concentration	ppm
TJI: turbulent jet ignition	-
TWC: three-way catalyst	-
ULSD: ultra-low-sulfur diesel	-
US: United States	-
v/v: volume basis	-
VGT: variable geometry turbine	-
VVA: variable valve actuation	-
WHTC: World Harmonized Transient Cycle	-

Variables

c_p: specific heat at constant pressure	J/(kg•K)
c_v: specific heat at constant volume	J/(kg•K)
CH_4: volumetric exhaust methane concentration	ppm
CO_2: volumetric exhaust carbon dioxide concentration	ppm
$C_xH_yO_z$: oxygenated general hydrocarbon fuel	-
H_a: ambient humidity (of water vapour)	g / m^3 of air
$h_i dm_i$: mass flux in/out of control volume	kg/(s•m^2)
$IMEP_{gross}$: gross indicated mean effective pressure	bar
$IMEP_{net}$: net indicated mean effective pressure	bar
k: bulk modulus	bar
k_f: fuel specific factor	-
k_{hG}: ambient humidity correction factor	-
k_w: dry-to-wet correction factor	-
L: connecting rod length	mm
LHV_{fuel}: lower heating value of fuel	MJ/kg
LHV_{CO}: lower heating value of carbon monoxide	MJ/kg
LHV_{HC}: lower heating value of unburnt hydrocarbons	MJ/kg
m_{cr}: mass flux from piston crevice region	kg/(s•m^2)
m_{fuel}: fuel mass injected per cycle	mg/cycle
$\dot{m}_{air}$: air mass flow rate	kg/h
$\dot{m}_{dry\ air}$: dry air mass flow rate	kg/h
$\dot{m}_{fuel}$: fuel mass flow rate	kg/h
$\dot{m}_{CO}$: mass flow rate of carbon monoxide	kg/h
$\dot{m}_{HC}$: mass flow rate of unburnt hydrocarbons	kg/h
n: polytropic indices of compression/expansion	-
n: number of air moles	-
n_{TOT}: total number of moles	-
N: engine speed	rev/min
NO_2: nitrogen dioxide	ppm
O_3: ozone	ppm
p: pressure	bar
p_c: pressure rise due to combustion	bar

p_i: initial pressure	bar
p_v: pressure rise due to volume change	bar
p_a: ambient pressure	bar
P: pressure of fuel volume	bar
P_i: indicated power	kW
$\dot{q}_{exh}$: exhaust mass flow rate	kg/h
Q_{ch}: combustion energy release	J
Q_{ht}: heat transfer	J
Q_{net}: net heat release	J
R: specific gas constant	J/(g•K)
R_c: compression ratio	-
R^2: coefficient of determination	-
RH: relative humidity	%
S: stroke	mm
SP: water saturation pressure	Pa
T: temperature	°C
T_a: ambient temperature	°C
u_{CH4}: gas molar mass fraction of methane	-
u_{CO}: gas molar mass fraction of carbon monoxide	-
u_{gas}: gas molar fraction	-
u_{HC}: gas molar mass fraction of hydrocarbon	-
u_{NOx}: gas molar mass fraction of nitrogen oxides	-
U_s: gas sensible energy	J
V: volume	dm^3
V_{clr}: clearance volume	dm^3
V_d: displaced volume	dm^3
V_{ins}: instantaneous in-cylinder volume	dm^3
W: compression or expansion work	J
$W_{c,i}$: indicated work per cycle	J/cycle
W_{ALF}: hydrogen mass content in the fuel	g
W_{EPS}: oxygen mass content in the fuel	g

Greek Letters

x: normalised carbon content	-
y: hydrogen to carbon ratio	-
z: oxygen to carbon ratio	-
γ: specific heat ratio c_p/c_v	-
η_c: combustion efficiency	-
η_i: indicated efficiency	-
θ: crank angle	°
θ_i: initial crank angle	°
λ: relative air/fuel ratio (lambda)	-
λ_{cyl}: in-cylinder lambda	-
λ_{exh}: exhaust lambda	-
ρ_{ext}: exhaust gas density	kg/m^3

Chapter One

Introduction

1.1 Preface

Anthropogenic Greenhouse Gas (GHG) emissions have increased since the pre-industrial era and have resulted in the highest atmospheric concentrations of carbon dioxide (CO_2), methane and nitrous oxide in the last 800,000 years [1]. The heightened level of GHG emissions were driven by both economic activity and population growth and are extremely likely to have been the primary cause of observed global warming since the mid-20th century [1]. Global warming, also referred to as climate change, has the potential to cause severe, potentially irreversible changes to eco-systems and could result in extreme weather events such as heat waves, droughts, floods and other natural disasters [2]. Energy demand and GHG production are inherently linked, so efforts to reduce energy usage are necessary if climate change is to be avoided.

The transportation sector is a significant contributor of GHG emissions with a large amount of petroleum-based energy expended on an annual basis. In 2015, 28% of the total energy used in the United States was consumed by the transportation sector [3]. Future projections predict a 25% increase in global transportation energy demand from 2015 to 2040 [4]. Illustrated in Figure 1-1 is this trend, along with the projection that the HD sector is slated to have the largest growth by volume, while marine and aviation will increase by the largest percentages. Considering the current usage and the future growth potential of the commercial sector, attention has shifted towards improving the efficiencies of vehicles, namely HD trucks, as they comprise 4% of on-road vehicles but account for 18% of fuel consumption [5]. Raising the efficiencies of vehicles in the HD sector is challenging due to long duration, medium to high load operation which is not synergistic with passenger car technologies such as electrification [6,7]. As the direct use of electricity in commercial vehicles is in its infancy, exploration into low-carbon fuels, such as natural gas, is a potential strategy for curbing GHG emissions.

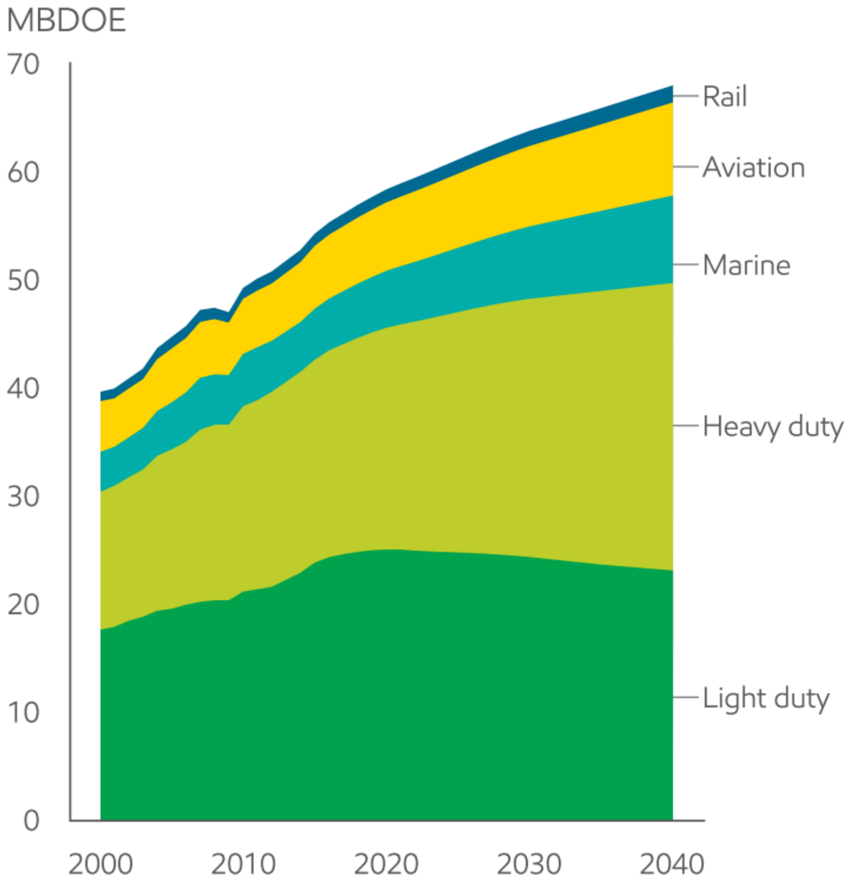

Figure 1-1: Global energy demands in million oil-equivalent barrels per day (MBDOE) from 2000 to 2040 [4]

Natural gas is an abundant and geographically diverse energy source. According to estimates from the International Energy Agency (IEA), technically recoverable natural gas resources would last for over 200 years at current demand levels [4]. Additionally, North America, Latin America, Asia, Africa, and the Middle East each hold 10% or more of the planet's remaining gas resources based on IEA estimates. This widespread availability and abundance of natural gas has made it an attractive option for reducing fuel costs for HD trucks, where diesel fuel can account for 30-40% of total fleet operating costs [8]. Adoption of natural gas has also increased due to its relatively low carbon content, being able to reduce CO_2 output by up to 10% compared with diesel fuel [7]. For these reasons, natural gas is set to play an important role in the diversification of energy for the transportation sector. Natural gas usage is projected to rise by 300% from 2014 to 2040, with global HD vehicle demand rising to 7%, up from 3% [4].

Correct implementation of natural gas is critical if the potential GHG benefits are to be captured. Studies have shown that methane, the primary constituent of natural gas, carries a Global Warming Potential (GWP) approximately 25 times higher than that of CO_2 over a 100 year timeframe [7,9]. Therefore, attention must be paid to optimise the engine design in order to best utilise natural gas without allowing either the crankcase or tailpipe emissions to negate any GHG benefits made by using the fuel in the first place.

1.2 Research Objectives

The primary purpose of this work is to improve upon the efficiency of a lean-burn dual-fuel combustion system in an HD diesel/natural gas engine while simultaneously considering the effect on exhaust emissions. Experimental engine testing is performed at various operating conditions and will strive to answer these specific objectives:

- Identify the most effective methods and technologies that can be used to achieve EURO VI methane emissions levels of <0.5 g/kWh with a natural gas/diesel combustion system
- Determine if LTC can be used to improve the efficiency and emissions of a lean-burn dual-fuel combustion system
- Define the effectiveness of Miller cycle, throttling and internal exhaust gas recirculation as ways to control engine-out emissions at light-load dual-fuel engine operating conditions

1.3 Thesis Outline

Set out in Chapter One is the context for the overall work and the scope of the research objectives. Chapter Two is a literature review of the history and evolution of diesel engine technology along with the fundamentals of diesel engine operation. Afterward, the role of natural gas as an alternative fuel is defined, followed by the potential ways in which it can be used in combination with LTC to improve dual-fuel engine combustion. Chapter Three follows, which is a definition of the research test rig used to perform the experimental test work and will describe how the data produced was analysed in both real-time and in post-processing. An engine and fuel injector validation is performed in Chapter

Four, which are used to guarantee engine health and ensure high data quality. Additionally, the combustion system of the research test rig is benchmarked against existing designs in order to confirm efficiency and emissions performance. Chapter Five is about engine hardware and combustion system optimisation which can then be used to explore advanced combustion techniques with confidence. Optimised baselines for Diesel, Conventional Dual-Fuel and Premixed Dual-Fuel Combustion (PDFC) modes are established with a focus on efficiency and emissions performance. The focus of Chapter Six is on improving light-load engine operation via more sophisticated methods, such as Miller cycle and internal exhaust gas recirculation. Finally, a summary will be included in Chapter Seven with the findings from the experimental testing, along with conclusions and recommendations for future work.

Chapter Two

Literature Review

2.1 Introduction

Fuel prices and stringent emissions standards are driving the development of increasingly efficient internal combustion engines. Diesel or Compression Ignition (CI) engines remain an efficient option due to their high compression ratio, high combustion efficiency, and un-throttled, lean operation [10]. The inherent high torque capability and thermal efficiency are the reason diesel engines remain a particularly attractive option for the HD transportation sector. Further increasing engine efficiency for the HD market is challenging due to long duration, medium to high load operation which is not synergistic with passenger car technologies such as electrification [6]. This raises the importance of increasing the efficiency of the base combustion engine as well as finding more cost-effective fuels to burn. Addressed in Section 2.2 are the history and background of the diesel engine, the evolution of technology, as well as its key operating principles. The role of natural gas as an alternative fuel is discussed in Section 2.3 before delving into the specifics of its current utilisation. Finally, Section 2.4 is about ways to improve current lean-burn dual-fuel natural gas engines via advanced combustion techniques.

2.2 The Diesel Engine

The modern diesel engine plays an important role in the transportation sector primarily due to its high brake thermal efficiency. This was not always the case as early examples of engines were cumbersome and yielded extremely low efficiencies. Discussed in Section 2.2.1 is the history of diesel engine design from its conception to modern day, while Section 2.2.2 is about the key technological advancements of the diesel engine evolution. Finally, the details of diesel engine operation are explored from an efficiency and emissions standpoint in Section 2.2.3.

2.2.1 History and Background

In thermodynamics, a heat engine is a device that operates in a thermodynamic cycle and performs net positive work as a result of heat transfer from a high-temperature body to a low-temperature body [11]. The definition is often extended to include all devices that produce mechanical work from heat transfer or combustion. Practical heat engines, such as the steam engine and internal combustion engine, have been in use for over two and a half centuries [10]. During the eighteenth and nineteenth centuries, the steam engine was the major source of power for the Industrial Revolution in Europe [12]. Fed by water and coal, these steam engines operated at an efficiency of approximately 10% [13]. The emergence and practical use of the internal combustion engine was not until the 1860s due to their temperamental nature and limited power output relative to a steam engine [14]. Early designs were developed for commercial use and burned a mixture of coal (illuminating) gas and air at atmospheric pressure. One such engine was created by Jean Joseph Etienne Lenoir (1822–1900) in 1860 and was called the Lenoir gas engine. Available from 0.5 to 3 horsepower, it required little space compared to a steam engine and didn’t require a boiler. Coal gas was burned directly inside a double-acting piston design, similar to a steam engine, at an efficiency of approximately 4% [15]. Nikolaus Otto (1832–1891) and Eugen Langen (1833–1895) later improved upon the Lenoir gas engine by creating the Otto–Langen atmospheric engine. Still operating on coal gas, it was an upright free-piston design that helped to decouple the sudden impacts on the crank drive caused by combustion. In this design, the combustion charge would accelerate a free-piston and rack assembly upward which would result in a vacuum in the cylinder after the combustion gases cooled. As the piston and rack descended from atmospheric pressure and gravity, it would perform work via a roller clutch to the output shaft [10]. The expansion ratio of this engine was higher than that of the Lenoir gas engine and enabled efficiencies of approximately 11%. Otto would later improve upon this design with the 1876 Otto Silent gas engine which achieved an overall efficiency of 14% [14]. Separating the engine’s operation into four piston motions of intake, compression before ignition, expansion, and exhaust helped to vastly reduce the weight and improve the thermal efficiency compared to the atmospheric gas engines at the time. The four-stroke Otto cycle with the compression of the fuel-air mixture prior to combustion would be the breakthrough necessary that would effectively found the internal combustion engine industry [10].

After the invention of the Otto cycle engine, rapid development took place to improve the efficiency and versatility of the internal combustion engine. The use of petroleum allowed engines to run on more accessible and easy to handle fuels and drove specialised engine designs. The desire to use low-volatility heavy fuel oils led to the emergence of low compression ratio “oil” engines. One of the most notable and popular was patented by Herbert Akroyd-Stuart (1864–1927) in 1890, as shown in Figure 2-1.

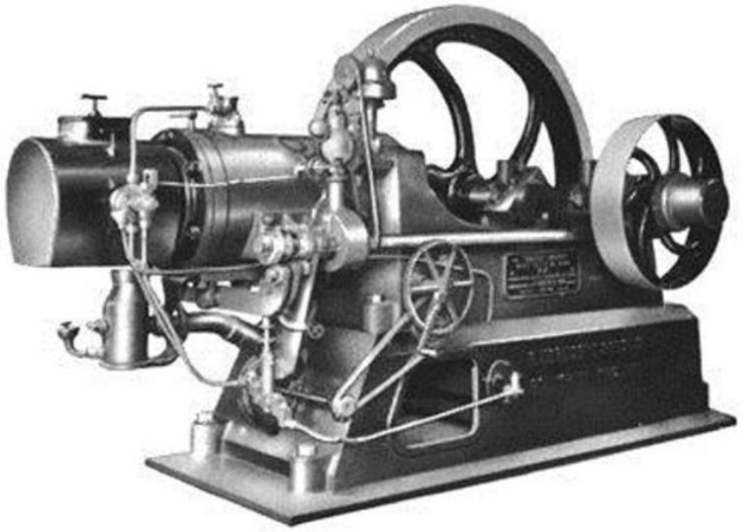

Figure 2-1: The Hornsby-Akroyd “Hot-bulb” oil engine, patented 1890 [13]

The Hornsby-Akroyd oil engine made use of a heated external fuel vaporiser where fuel would be injected and combusted with compressed air. This feature gave rise to the “hot-bulb” moniker and was mounted on the cylinder head and connected to the cylinder via a narrow passage [13], as shown in Figure 2-2.

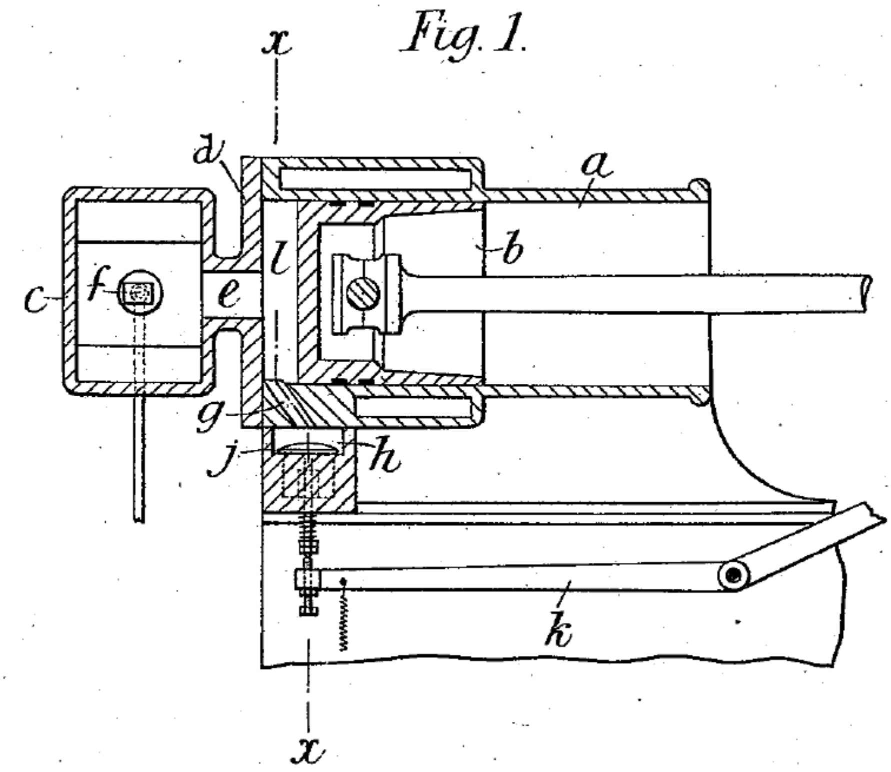

Figure 2-2: Schematic depicting hot-bulb volume (C) linked to cylinder volume (L) via passage (E) [16]

The piston would draw in fresh air during the intake stroke and compress the air into the hot-bulb to mix with the fuel that was being injected during the compression stroke. The external heat acting on the hot-bulb would ignite the fuel-air mixture and the combustion gases would pass into the cylinder through the narrow passage to perform work on the piston. This design had a limited compression ratio of approximately 3:1 in order to prevent pre-ignition of the fuel before the piston completed the compression stroke [17]. Nevertheless, the efficiency of the Hornsby-Akroyd engine was 14-18% and comparable to the gas engines at the time [10,15]. Key innovations for the Hornsby-Akroyd engine were to only induct fresh air rather than a fuel-air mixture and for the fuel to be injected into the combustion chamber [17].

For internal combustion engines, it was recognised that higher expansion ratios yielded greater fuel efficiency [10]. However, the compression and expansion ratios for the engines at the time were limited due to fuel being introduced as part of the compression stroke. Rudolf Diesel (1858–1913) recognised that a higher compression ratio and efficiency could be achieved if fuel was introduced only when it needed to be burned. In 1885, Diesel began development of his high compression ratio engine concept in Paris, France. After key publications and patents, Diesel would further develop his ideas from 1893-1897 with Maschinenfabrik-Augsburg AG (later Maschinenfabrik-Augsburg-Nürnberg or MAN) [10,13]. In 1893, the first prototype engine was built but never ran under its own power [18]. Improvements and subsequent testing on a second prototype engine culminated with the creation of a third prototype engine in 1897, as shown in Figure 2-3. This engine was a single cylinder four-stroke design and demonstrated an efficiency of 26.2% under load, which was significantly higher than any other heat engines at the time [13]. It employed air-blast injection, which utilised compressed air to introduce atomised fuel directly into the cylinder.

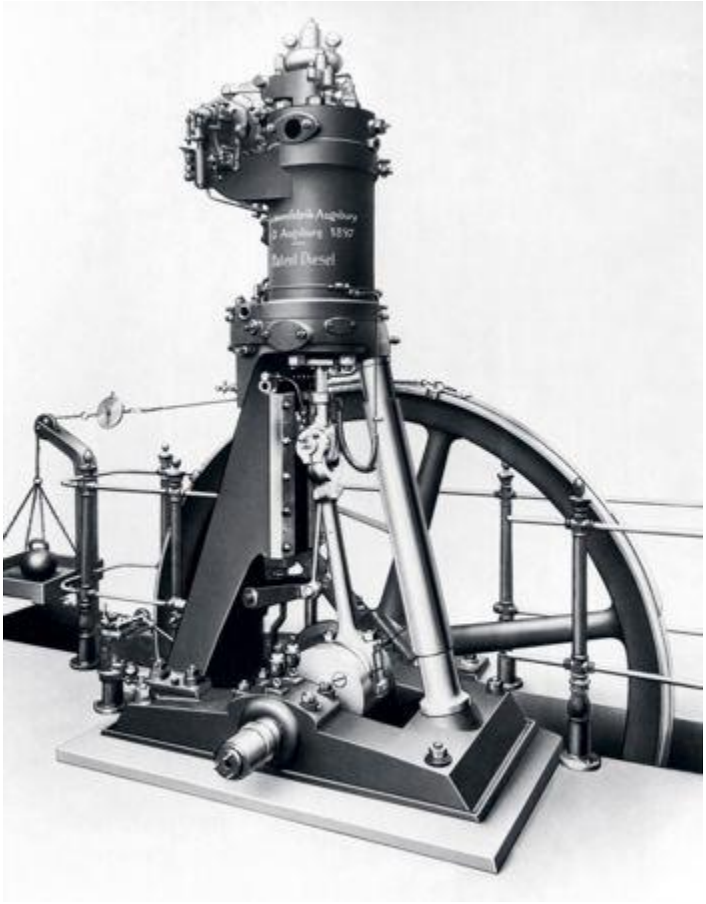

Figure 2-3: Diesel’s 1897 20 horsepower 19.6 litre test engine [13]

The technical revelation of combusting liquid fuel by directly injecting it into air that was heated by compression enabled higher geometric compression ratios without pre-ignition or knock. The greater efficiency resulting from higher expansion ratios solidified the diesel engine’s use in the commercial sector and would ultimately prove to be a viable alternative to the steam engine.

2.2.2 Evolution of Diesel Engine Technology

After the introduction of the diesel engine, further development took place to steadily widen its role in the commercial and transportation sectors. Early diesel engines were limited to low speed stationary and marine applications due to their air-blast (70 bar) injection systems, which would atomise the fuel entering the combustion chamber using a charge of compressed air. This design required a high-pressure air pump and storage vessel, which was cumbersome and consumed up to 15% of the engine’s output [17,19]. Advancements in fuel injection and atomisation needed to be made in order to develop higher speed diesel engines, which were better suited to transportation applications. In response, a liquid pump for “solid” or airless injection was devised in 1910 by James McKechnie of Vickers, which would enable injection of fuel at high pressures [17].

In parallel to fuel injection development, improvements to the combustion chamber were necessary to enable diesel powered automobiles. In 1909, the pre-combustion chamber (pre-chamber) was patented by Prosper L'Orange (1876–1939) and Benz [20]. His design comprised of a burner volume connected to the main combustion chamber via a narrow passage. During operation, fuel would be injected in to the burner volume and would ignite, forcing the fuel-air mixture into the main combustion chamber. L’Orange would improve this concept with the funnel pre-chamber, as shown in Figure 2-4, where fuel would be directly injected on to a funnel shaped insert between the pre-chamber and cylinder. This design enabled fuel to be vaporised easier which reduced carbon deposits [21]. L’Orange would also be credited with the pintle-type injection nozzle and the variable injection pump, which would allow engine power output to be controlled to the degree necessary for diesel powered automobiles.

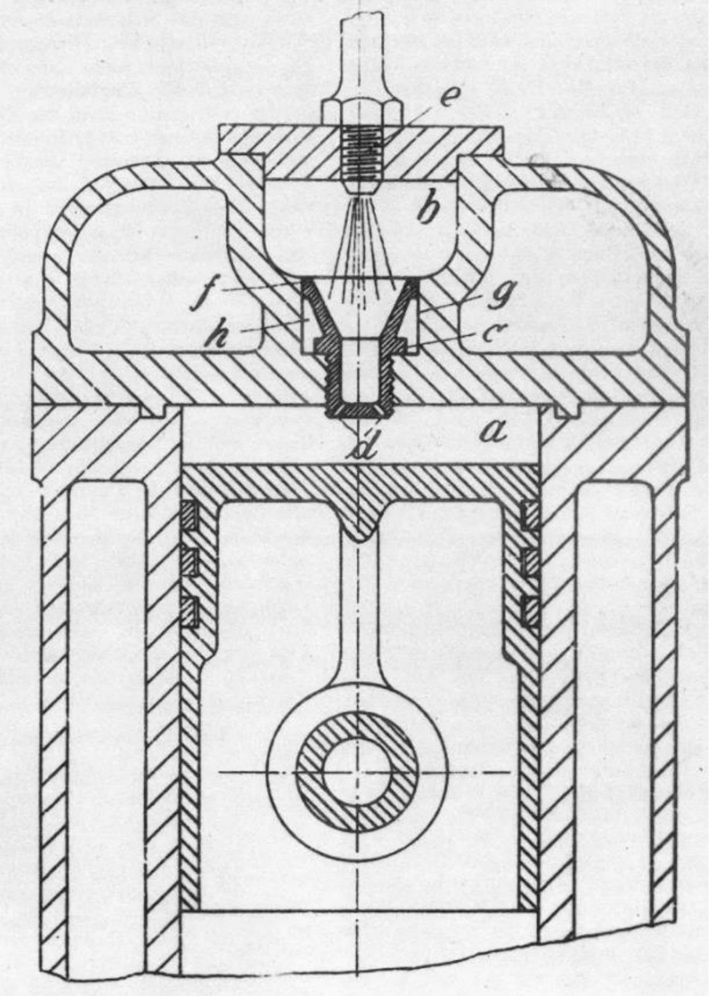

Figure 2-4: Prosper L'Orange's "funnel" pre-chamber design [22]

Further combustion chamber development took place, including the induction swirl and compression swirl chamber designs invented by Sir Harry Ricardo (1885–1974) [23]. The compression swirl chamber design, also known under the Comet Mark III moniker, was patented in 1931 and was widely used in a number of automotive applications. This combustion chamber can be seen in Figure 2-5, complete with fuel injector (top) and heater/glow plug (side).

Pre-chamber, air cell, and swirl type combustion systems are classified as indirect-injection (IDI) designs, as opposed to direct-injection (DI) where fuel is introduced directly into the main combustion chamber. IDI combustion chambers enabled smaller, lighter, and higher speed engines to be produced, which greatly expanded the diesel engine's role in transportation [17,24]. Advantages of the IDI design is that turbulence is created by the air's movement into the pre-chamber volume, which reduces the importance of very high injection pressures and fine fuel atomisation. This ultimately means that IDI fuel injection pressures can be lower (100-300 bar) compared to those of the DI design (345 bar and higher) [17]. IDI chambers also exert less stress on engine components which allowed for lighter and more compact engines to be produced.

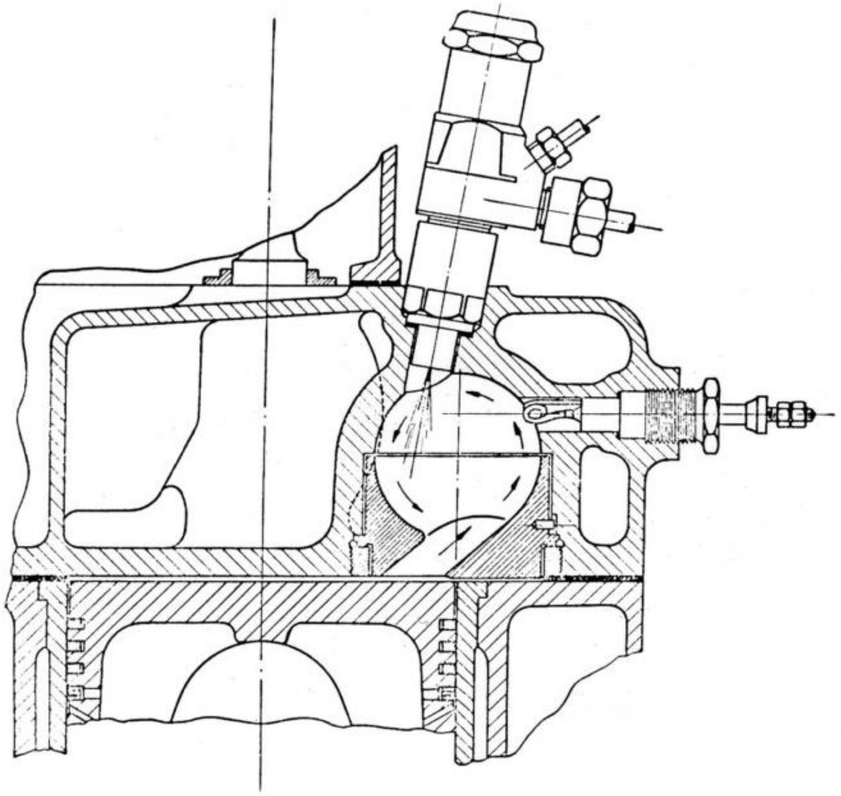

Figure 2-5: Comet Mark III compression swirl combustion chamber [23]

One of the major disadvantages of the IDI combustion chamber is a 10-15% higher fuel consumption in comparison to a DI design [17,24]. This can be attributed to the increased surface area and heat losses that result from using a pre-chamber. Furthermore, the heat and pressure exerted on the piston crown when the combustion gases exit the pre-chamber limits the IDI design from high specific power output applications due to uneven expansion and piston distortion.

Development of higher efficiency diesels took place throughout the middle of the twentieth century but automotive related air-pollution became an increasingly important issue. In 1952, A. J. Haagen-Smit demonstrated that smog was created by sunlight initiating reactions between oxides of nitrogen and hydrocarbon compounds in the air [25]. It was determined that the automobile engine was a major contributor of these air pollutants as well as the primary reason for the high carbon monoxide levels in urban areas. As a result, exhaust emissions regulations for the automobile were first introduced in California, and then nationwide in the United States in the early 1960s [10]. Regulation for HD on-road engines shortly followed in North America and Japan in the early 1970s, followed by Europe in the 1980s [26]. These regulations, along with the market demands for low fuel consumption and operating costs, were the impetus behind efficiency and emissions technology development for the following decades. Shown in Figure 2-6 is a summary of the key technologies that enabled significant reductions in NOx and particulate emissions starting in the 1980s.

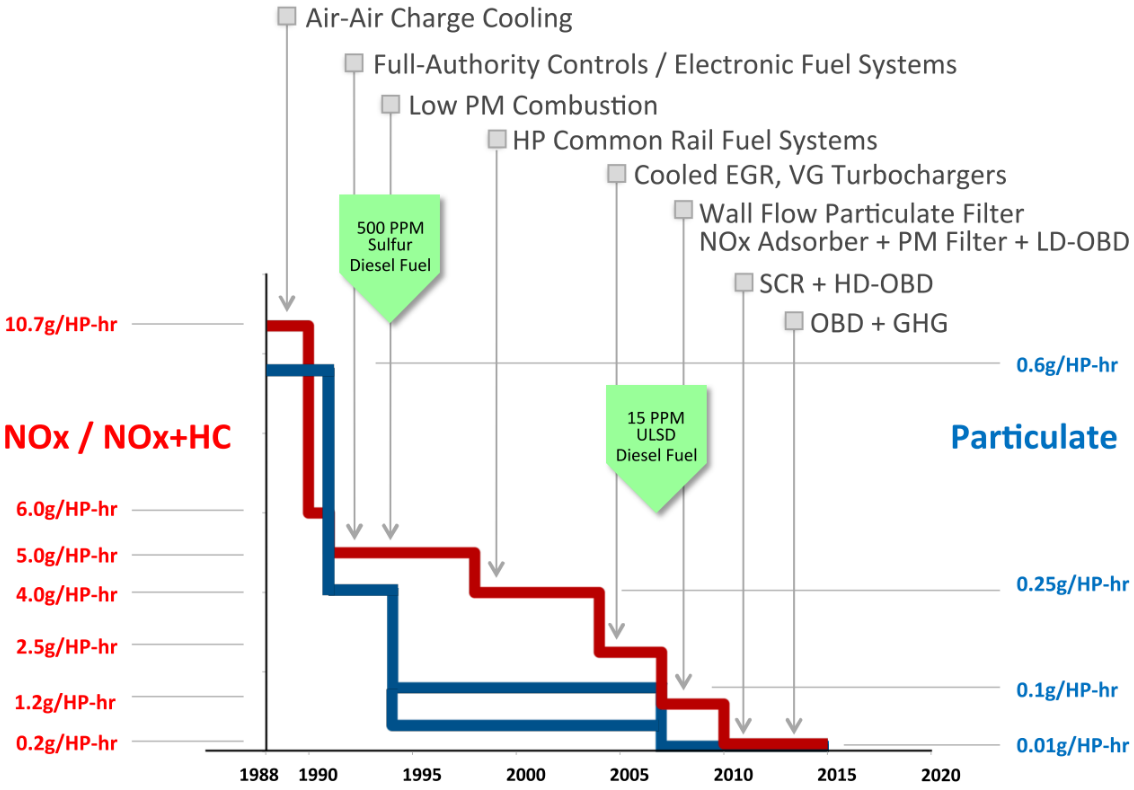

Figure 2-6: US on-highway HD diesel technology evolution with NOx and particulate emissions [27]

Initial efforts to reduce NOx emissions were made with intake manifold temperature reduction through air to air charge cooling as well as retarded injection timing. Increased fuel pressures and further combustion system development helped to offset the loss in efficiency from the retarded combustion timing. Also at this point, the high-swirl intake port coupled with DI would become more commonplace, at the expense of the IDI combustion chamber design [24].

In the late 1990s and early 2000s, cooled Exhaust Gas Recirculation (EGR) was employed with wide-spread adoption of the Variable Geometry Turbine (VGT) and the high pressure common rail fuel system [17,26]. High injection pressures were needed to offset some of the particulate emissions resulting from the implementation of cooled EGR, while the VGT would ensure sufficient exhaust manifold pressure in order to drive the requested amounts of EGR with acceptable transient response. Further emissions equipment such as NOx adsorbers and lean NOx catalysts (also known as Selective Catalytic Reduction (SCR)) were necessary in order to achieve the latest NOx emissions standards. Lowered particulate emissions were achieved via a number of engine design and fuel changes, including low sulphur diesel fuel, increased fuel injection pressure, reduced lube oil consumption and the use of Diesel Particulate Filters (DPF) [26].

In 2005, Euro IV emissions regulations for HD diesel engines were introduced in Europe with a required NOx emissions level of 3.5 g/kWh, later followed by the 2.0 g/kWh limit of Euro V in 2008 [28]. These regulations could be met with use of a urea-SCR system [29]. However, in 2013, Euro VI emissions regulations imposed a 0.4 g/kWh NOx and 0.01 g/kWh Particulate Matter (PM) limit, as well as a cap on the total number of particulates at $8.0\text{x}10^{11}$ particle/kWh [30]. These emissions levels, in combination with an ammonia limit, forced the use of cooled EGR, a DPF, and an Ammonia Slip Catalyst (ASC) in addition to the urea-SCR technology [29].

In parallel to the emissions standards for air pollutants, the first regulations for greenhouse gas and/or fuel efficiency targets became effective in the United States and Japan in the mid-2010s [26,31]. The brake thermal efficiencies of diesel engines would need to continue to improve in order to meet these requirements, including the future US Environmental Protection Agency (EPA) Phase 2 regulations [32]. The data presented in Figure 2-7 describes the steady progression of HD thermal efficiencies from the 1960s, with a brief decrease in the early 2000s due to the rapid implementation of cooled EGR. The graph also shows the future targets of the SuperTruck program funded by the US Department of Energy and select industrial partners [5]. Engine level goals were to demonstrate 50% brake thermal efficiency in the SuperTruck vehicle and to reveal the pathway to 55% in the future.

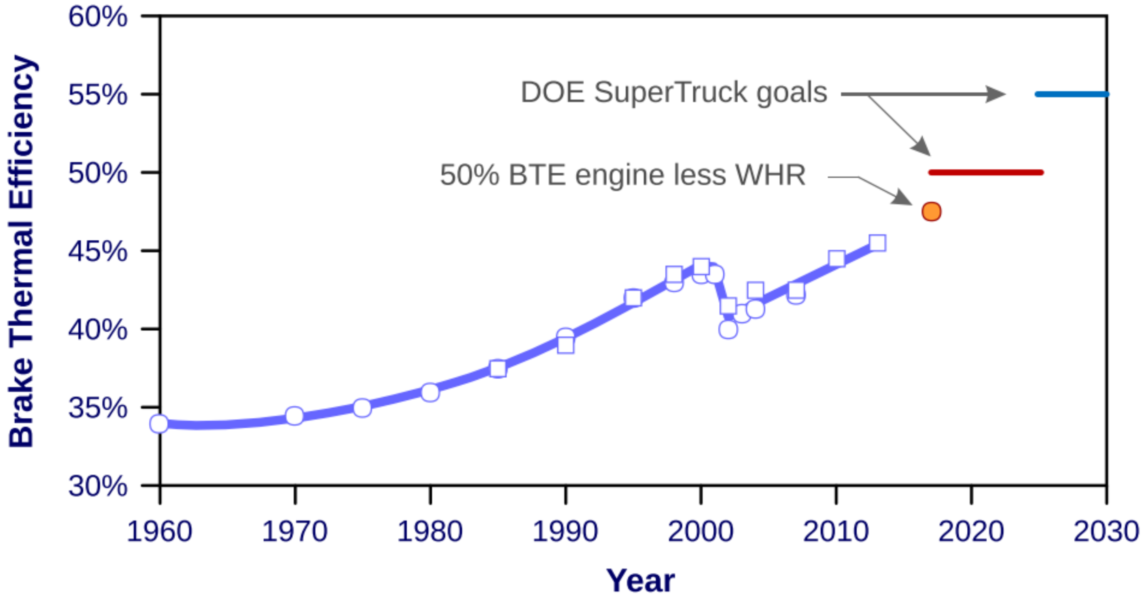

Figure 2-7: Brake thermal efficiency of US HD diesel trucks [26,27]

Alongside a systems level approach to improve vehicle fuel efficiency, many powertrain specific aspects are being explored. Future technologies involving waste heat recovery [33,34], friction and parasitic loss reduction [35–37], reduced heat transfer [35,38–40], and after-treatment optimisation [35,41] have been identified as key efficiency enablers [27]. Exploration of advanced valvetrain technology for the purposes of variable effective compression ratio and internal EGR have been introduced as well [42,43]. LTC strategies are a popular research field and will be explored later in this chapter. Finally, the role of renewable and alternative fuels including recently proposed synthetic substitutes [44,45] will play an important role in lowering fleet operating costs, as well as providing a way toward lower CO_2 emissions [7].

2.2.3 Diesel Engine Operation

The effects of engine speed and load are usually described by plotting Brake Specific Fuel Consumption (BSFC) contours on a graph of Brake Mean Effective Pressure (BMEP) versus engine speed. The contour shapes commonly reveal an “island” of minimum BSFC which designates the engine’s maximum operating efficiency. Figure 2-8 helps to visualise this trend and can be used to help understand the factors that degrade engine efficiency.

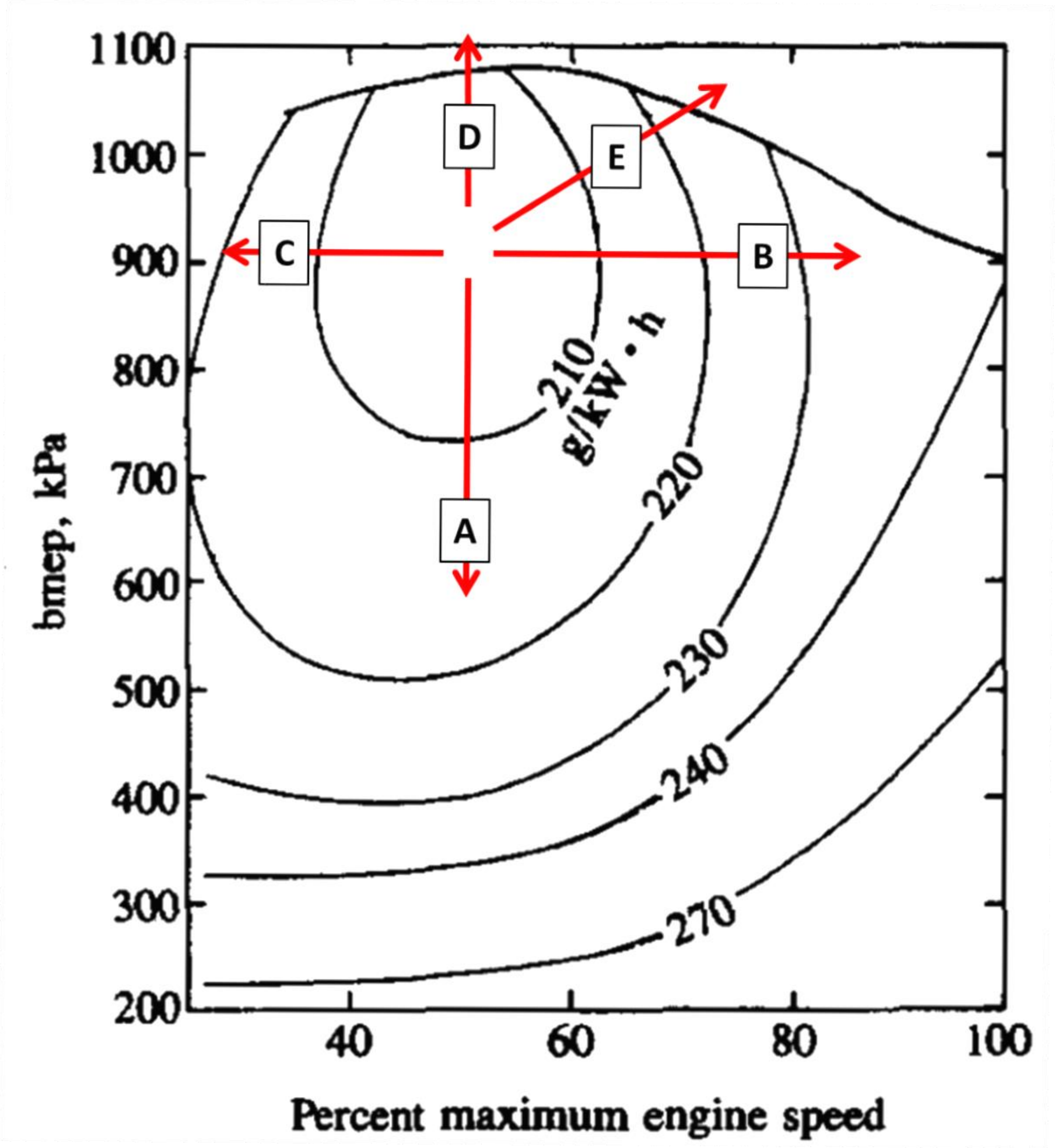

Figure 2-8: Fuel consumption map of a turbocharged 12-dm^3 six-cylinder medium-swirl HD truck DI diesel engine [10] with markings for the typical losses in a diesel engine

Letters A through E describe individual factors that degrade BSFC away from the optimum. Letter A observes increased fuel consumption with reduced load. This is mainly attributed to proportionally higher heat transfer, pumping and frictional losses [10]. The driver for higher heat transfer is a larger temperature differential between combustion gases and the interfacing surfaces of the engine, meaning more opportunity for the fuel energy to be transformed into waste heat. The pumping and frictional losses remain mostly unchanged with load at lower engine speeds, so they become a larger percentage of the fuel energy when fuelling is reduced. Slightly lowered combustion efficiency is also experienced with reduced load, but is a minor effect under diesel operation.

In the direction of letter B, engine speed increases as BSFC degrades due to larger frictional and pumping losses. Higher engine speeds translate into higher mechanical friction in the rotating and reciprocating components of the engine, leading to greater losses [10,17]. This is demonstrated by the data in Figure 2-9, which depicts a motored Friction Mean Effective Pressure (FMEP) breakdown for several DI diesel engines. Frictional losses also increase at higher combustion pressures due to greater forces acting on the engine components, including the piston and cylinder liner interface [46]. Additionally, pumping losses associated with moving gases into and out of the engine are included in Figure 2-9, and steadily increase with engine speed due to higher gas flow losses.

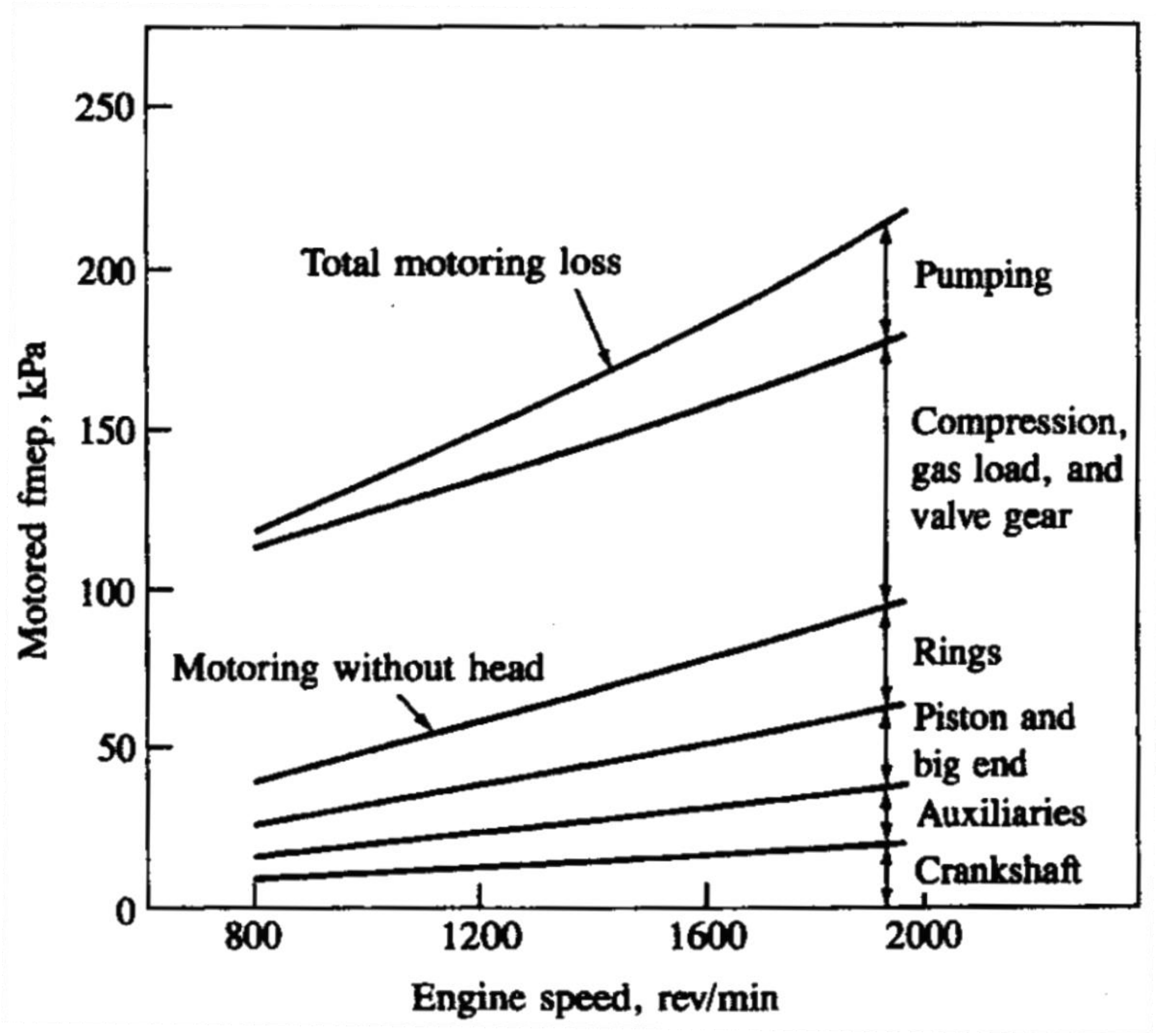

Figure 2-9: Motored FMEP versus engine speed for several four and six-cylinder DI diesel engines [10]

As engine speed is decreased towards letter C, a larger amount of heat energy is transferred from the working fluid into the interfacing engine components, such as the head, piston and bore wall. This is due to the increased amount of time that the combustion gases have in contact with the combustion chamber surfaces. The loss of heat energy from the combustion gases results in a lower amount of useful work that can be extracted by the piston during the expansion stroke. An additional effect is that small scale in-cylinder turbulence reduces with engine speed, resulting in longer combustion durations, as demonstrated in Figure 2-10. This yields a lowered value of IMEP and a loss in fuel efficiency. In recent years, efforts have been made to reduce heat losses via ‘temperature swing’ thermal barrier coatings. Presently these are mainly restricted to light-duty applications and still the subject of considerable debate [38,39].

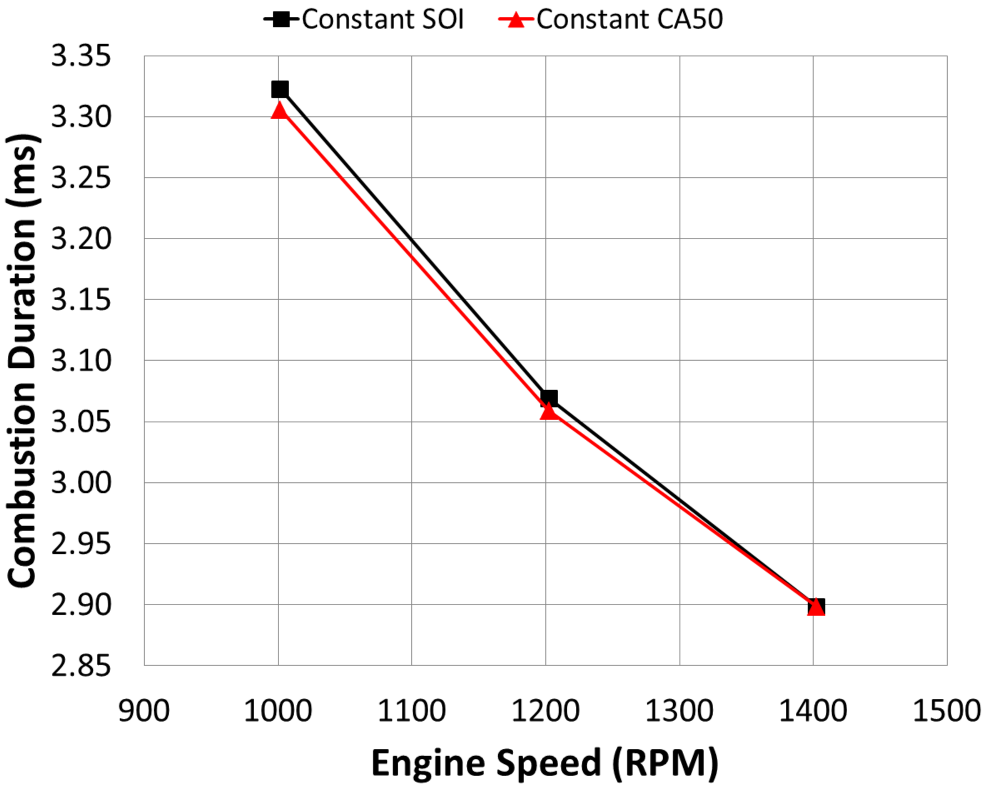

Figure 2-10: Conventional diesel combustion duration in milliseconds versus engine speed for constant Start Of Injection (SOI) and constant crank angle at 50% mass fraction burned (CA50). Data was produced on the diesel test rig used in this work.

The full load line in the direction of letters D and E are constrained by maximum cylinder pressure or the mechanical component limitations of the engine [10]. Certain precautions must be taken with the calibration, such as injection timing and boost pressure, in order to avoid running under conditions that would violate these limits. A loss in efficiency may be experienced depending on the degree of calibration concessions, such as the retarding of injection timing in order to avoid a cylinder pressure limit. Compromises are also made with respect to combustion noise and pressure rise rates, as these tend to increase with higher cylinder pressure and power output. Furthermore, depending on the degree of exhaust after-treatment, the use of retarded injection timing may be utilised as a way to control NOx and soot emissions under high load operation.

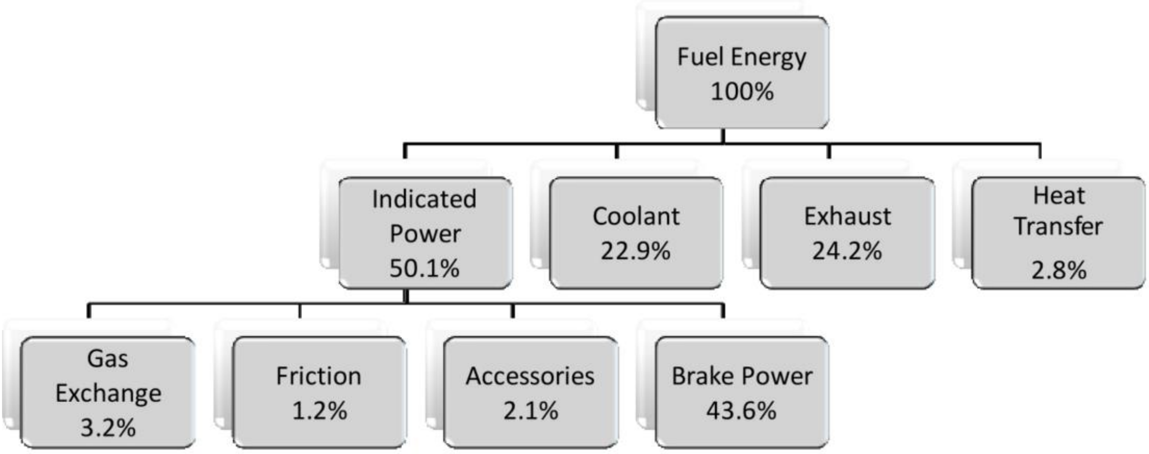

Figure 2-11: Fuel energy budget for a Cummins 15L engine in a Class 8 tractor-trailer application operating at 65 mph with zero grade [35].

Aside from the main losses outlined by letters A through E, additional losses are experienced throughout the speed and load map. Illustrated in Figure 2-11 is a fuel energy budget for a U.S. EPA 2010 compliant diesel engine which identifies the percentage of fuel energy devoted to each of the sub-categories. At this operating condition, roughly 50% of the fuel energy is transformed into heat, with 22.9% being rejected to the coolant, 24.2% to exhaust gas as sensible heat, and 2.8% to the ambient environment. Remaining is the 50.1% of indicated power, which can be converted to brake power after subtracting gas exchange, frictional, and accessory losses. The combustion efficiency was greater than 99.5% at this operating condition, so losses associated with incomplete combustion were negligible. The energy balance of Figure 2-11 can also help to identify losses due to running a non-ideal thermodynamic cycle, which would include effects such as heat transfer out of the combustion chamber and retarded combustion event timing.

In addition to performance and fuel efficiency, the diesel combustion process plays an important role in emissions formation. The reduction of emitted pollutants from engines are of particular significance as they have implications to both public health and global warming [17,25]. However, in order to understand how emissions are created, it is first necessary to understand the details of the DI diesel combustion process. The profile in Figure 2-12 helps to outline this by defining the four phases of diesel combustion: ignition delay (a→b), premixed combustion (b→c), mixing-controlled combustion (c→d), and late combustion (d→e).

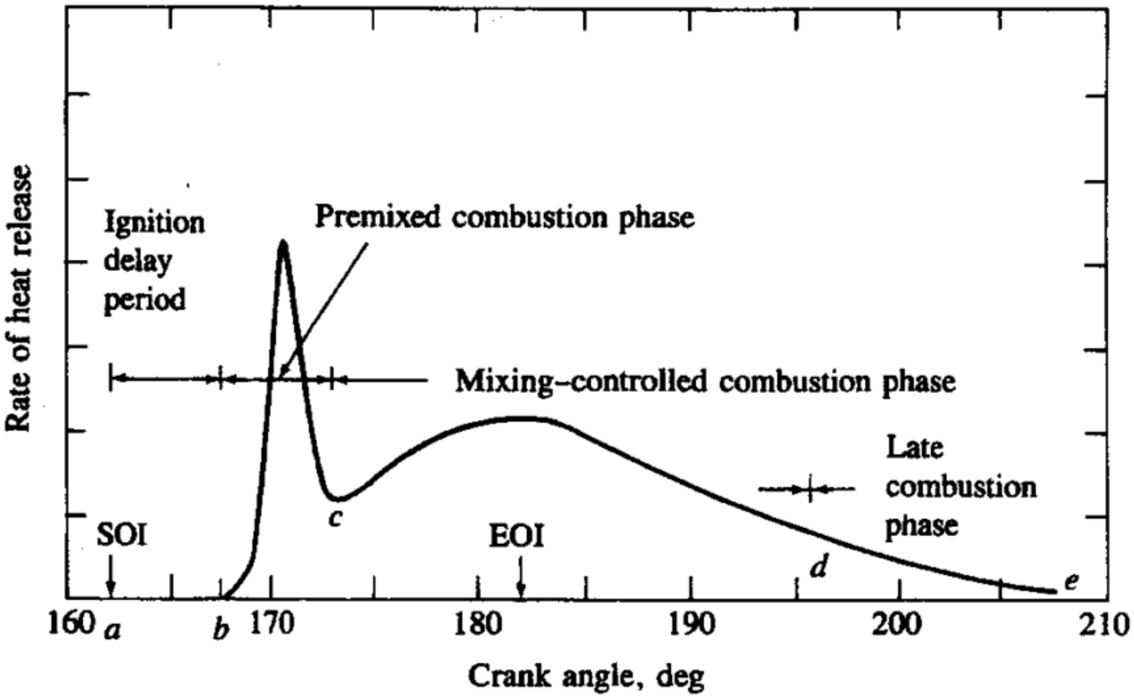

Figure 2-12: Typical DI engine heat-release-rate diagram identifying different diesel combustion phases [10]

The ignition delay period is typically defined as the time between the SOI and the start of detectable combustion, which can be determined by a change in the slope of pressure versus crank angle, heat release rate, consumption of a defined amount of fuel, or through changes in detected luminosity. The premixed (or rapid) combustion phase follows ignition delay and is characterised by high heat release and temperature. The fuel that was injected during the ignition delay period mixes with air and quickly burns once the mixture reaches auto-ignition temperature, which creates the spike in heat release shown in Figure 2-12. In the mixing-controlled combustion phase, the consumption of fuel is managed by the injection rate of the fuel and the subsequent mixing with air inside the cylinder. This phase typically has a lower heat release peak when compared to the premixed combustion phase. Finally, the remaining balance of fuel is consumed by the late combustion phase, which is characterised by a lowered rate of heat release during the expansion stroke. Combustion can carry on after the mixing-controlled phase due to the continued mixing and subsequent burning of fuel and air, or due to the oxidation of fuel-rich combustion products and soot.

The understanding of the conventional diesel combustion process described in Figure 2-12 advanced considerably during the 1990s through the use of laser-based planar imaging techniques [35,47–49]. Optical access to the combustion chamber allowed empirical measurements to validate chemical kinetic models. This led to the creation of a sequence of schematics depicting how the DI diesel combustion process evolves from SOI through to the early portion of the mixing-controlled combustion phase. The conceptual model of the diesel combustion plume during the mixing-controlled combustion phase was also generated, as shown in Figure 2-13.

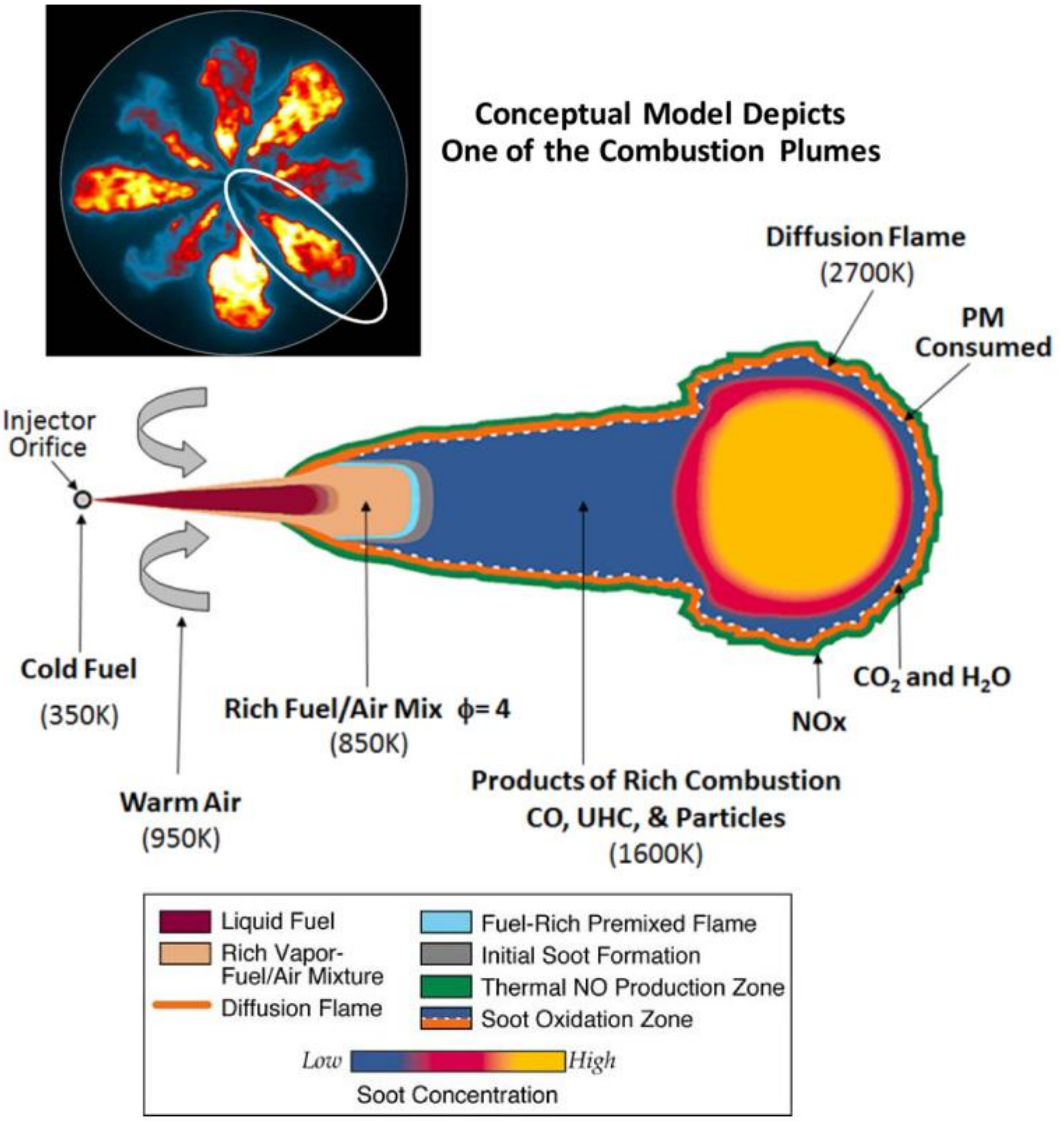

Figure 2-13: Conceptual model of a quasi-steady diesel combustion plume [35,48,49]

The model depicts that liquid fuel is injected into the combustion chamber and is entrained with a limited quantity of air, yielding a rich fuel and air mixture in the interior of the diffusion flame. Rich combustion takes place inside the plume and creates species that cause particulate formation. The particulates are subsequently consumed as they enter the high temperature diffusion flame (2700K) located toward the exterior edge of the burning plume. Soot concentrations are high on the interior of the diffusion flame, while NOx is formed on the periphery. This conceptual model is of particular importance as it provides further understanding of the emissions formation mechanism.

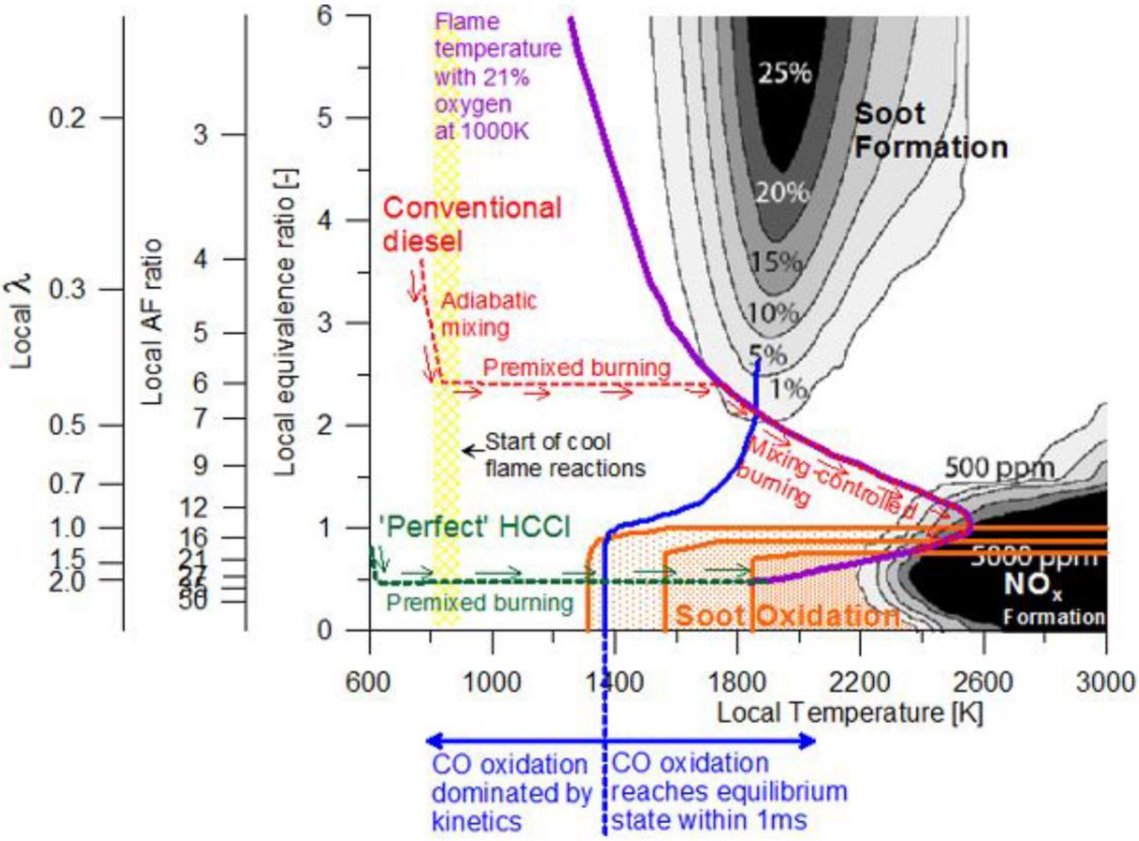

Figure 2-14: Pathway of conventional diesel combustion on a local equivalence ratio and temperature map. Emissions zones are for n-heptane fuel at 60 bar and a residence time of 2ms [47,50,51].

The diesel combustion process can also be visualised as a function of the local air-fuel ratio and flame temperature, as shown in Figure 2-14. The pathway of the combustion process as well as residency time in each of the emissions production zones is critical to the formation of NOx and particulates [50]. The dotted red line describes the typical pathway of the different diesel combustion phases previously mentioned in Figure 2-12. The borderline of fast (right) and slow (left) carbon monoxide (CO) oxidation is depicted using the blue line, while the soot oxidation zone is highlighted using orange [52]. Finally, the purple line indicates the maximum adiabatic flame temperature achieved for a fuel at 372K reacting with ambient gas at 1000K [53].

Diffusion-type combustion possesses both rich and lean high temperature areas which can result in the formation of significant PM and NOx emissions [48]. High temperatures allow the nitrogen in the intake air to combine with the available oxygen and form either nitric oxide (NO) or nitrogen dioxide (NO_2). NOx (sum of NO and NO_2) can be formed during both the premixed and mixing-controlled combustion phase and is essentially an exponential function of flame temperature [35]. PM emissions consist of any exhaust components other than water that can be collected by exhaust filters. The majority of the particles are combustion generated carbon (soot), but can also contain organic compounds which are formed from unburnt fuel or engine oil [17]. Unburnt hydrocarbon emissions are typically low for diesel engines but can arise from unburned fuel, recombined intermediate compounds or from partially decomposed fuel molecules. Combustion of lubricating oil, poor fuel atomisation, as well as poor mixture formation or quenching can also be significant sources of hydrocarbons [10]. Finally, CO emissions are typically generated as an intermediate product in the combustion of hydrocarbons and are formed in fuel-rich mixtures [17]. CO emissions are typically low for diesel combustion due to lean operation but can be formed by incomplete combustion brought about by lack of oxidants or temperature.

Exhaust after-treatment systems have been developed to significantly reduce diesel tailpipe emissions. A modern HD after-treatment system typically comprises of an SCR for NOx reduction, a Diesel Oxidation Catalyst (DOC) for CO and HC oxidation, and a DPF for particulate matter filtering [35]. These systems are effective, but generally result in an increase in fuel consumption and can also be expensive to produce, primarily due to the precious metals required for operation. Due to the disadvantages of these after-treatment systems, it is preferable to decrease engine-out emissions in-cylinder. The key variables influencing in-cylinder emissions are related to fuel, air, and EGR management. Fuel management pertains to injection rate shaping, fuel type or blending, number or timing of injections, while air and EGR management deals with swirl, tumble, and/or throttling as well as considering different boosting devices with high and low pressure loop EGR.

2.3 Role of Natural Gas

Natural gas holds promise for the transportation sector due to its potential to reduce fuel costs, lower NOx and soot emissions, as well as decrease CO_2 output by up to 10% compared with diesel fuel [7]. The strengths and weaknesses of using of natural gas as a fuel will be discussed in Section 2.3.1 while the current utilisation is explored in Section 2.3.2.

2.3.1 Natural Gas as a Fuel

The main constituent of natural gas is methane (CH_4), which comprises 87-96% of the total volume percentage. The remaining balance primarily consists of ethane (C_2H_6), inert gases of nitrogen (N_2) and carbon dioxide (CO_2), and lower amounts of propane (C_3H_8) and higher hydrocarbons. This can be quantified by Table 2-1, where the typical composition of natural gas is presented alongside the ranges for the individual components, which can vary depending on geography and season.

Table 2-1: Chemical composition of natural gas [54]

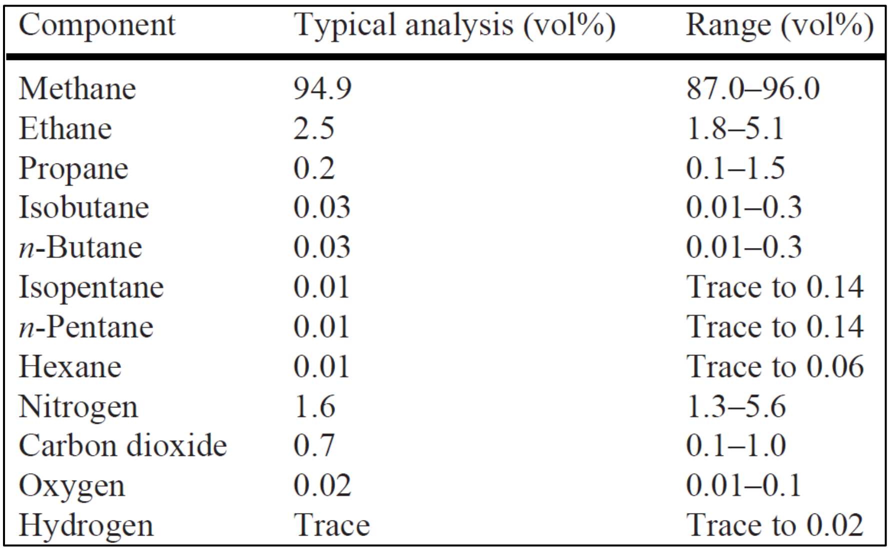

Component	Typical analysis (vol%)	Range (vol%)
Methane	94.9	87.0–96.0
Ethane	2.5	1.8–5.1
Propane	0.2	0.1–1.5
Isobutane	0.03	0.01–0.3
n-Butane	0.03	0.01–0.3
Isopentane	0.01	Trace to 0.14
n-Pentane	0.01	Trace to 0.14
Hexane	0.01	Trace to 0.06
Nitrogen	1.6	1.3–5.6
Carbon dioxide	0.7	0.1–1.0
Oxygen	0.02	0.01–0.1
Hydrogen	Trace	Trace to 0.02

Considering global energy mixes, oil will remain the world’s primary energy source through 2040, providing about one-third of the overall energy demand [4]. This projection is amplified in the transportation sector, with oil meeting approximately 95% of energy needs due to widespread availability and high energy density. However, on the global energy stage, natural gas is fast emerging and is poised to overtake coal as the world’s second-largest energy source. Natural gas is also set to play an important role in the diversification of energy for the transportation sector with a projected rise of 300% from 2014 to 2040, resulting in a global HD vehicle market share of 7%, up from 3% [4].

The use of natural gas as an alternative fuel for the HD truck sector is driven mainly by fuel costs and emissions benefits. The abundance of natural gas has historically resulted in a relatively cheap and consistent fuel price compared to other fuels, such as diesel, which are more tightly linked with oil production, as shown in Figure 2-15. The price difference between diesel and natural gas is a significant contributor for reducing operating expenses, as diesel fuel can account of 30-40% of the total fleet operating costs [8]. However, this must be carefully weighed against the investment of the natural gas hardware in place of, or in addition to, the conventional diesel fuel system, as the cost savings generated by using natural gas must result in a net benefit if is to be cost competitive.

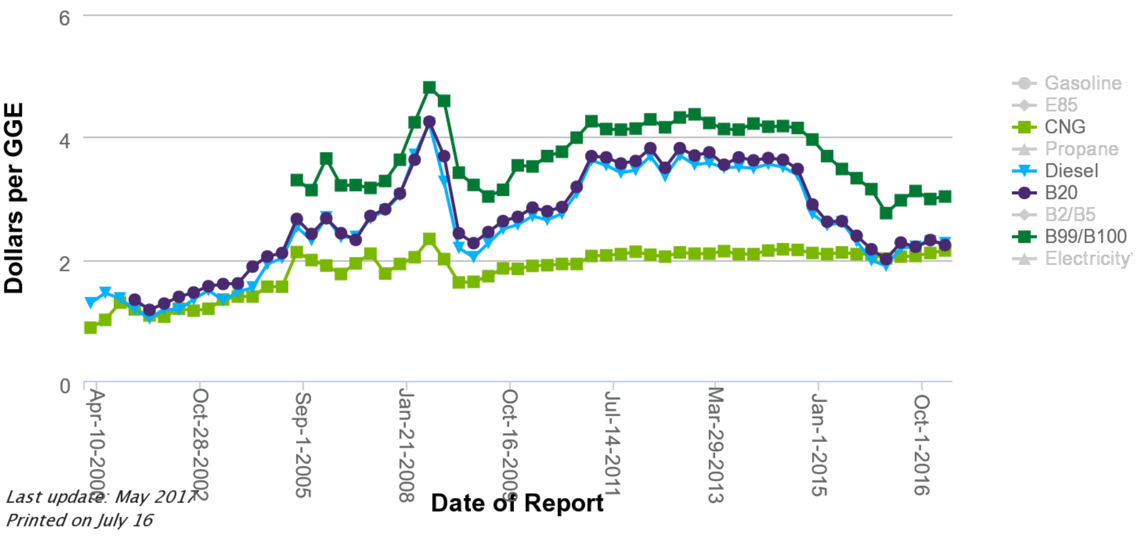

Figure 2-15: Historic average retail fuel prices in the U.S. in dollars per gasoline-gallon equivalent (GGE) [55]

The other advantage of using natural gas is that it is a low carbon content fuel, which is a benefit derived from the chemical composition of methane. As it is the simplest alkane with the highest hydrogen to carbon ratio of 4 to 1, the combustion of methane directly results in a lower output of carbon when compared to longer hydrocarbon chains, like those found in gasoline and diesel. During the combustion of natural gas, a lower amount of CO_2 molecules are generated for a given amount of energy released, which in turn helps to provide an overall GHG emissions benefit. Furthermore, natural gas can be an effective means to reduce NOx and PM emissions compared to diesel [7,56,57] due to its ability to burn cleanly. The chemical properties of methane also provide a relatively high knock resistance, which results in efficiency gains from an increased compression ratio. As a final point, efforts are also being made to make natural gas a renewable resource, particularly with the Power-to-Gas initiative. This utilises surplus electricity to create hydrogen and/or synthetic methane, but has been the subject of criticism due to the loss of energy in the overall chain from “well-to-wheel” [7].

One of the main disadvantages of using natural gas is the high GHG impact of unburnt or leaking methane, which is approximately 25 times higher than that of CO_2 over a 100-year timeframe. This has implications to the way natural gas engines are designed if they are to have a benefit for total GHG emissions, especially considering the latest EURO VI regulation where methane emissions are limited to <0.5 g/kWh. Special care must be taken during the design of the engine’s combustion system and exhaust after-treatment in order to avoid “methane-slip” where unburnt methane exits the tailpipe. Since methane is a highly stable molecule with a high activation energy, large amounts of rare earth metals such as platinum and palladium are needed in order to oxidise methane with a catalyst, which increases the cost of the after-treatment [58]. The catalyst expense would be in addition to the initial investment cost for the natural gas hardware, including storage tanks, which creates a challenging economic model when diesel prices are low.

Additional issues arise in the form of energy density, where both Compressed Natural Gas (CNG) and Liquefied Natural Gas (LNG) are less dense forms of energy when compared to petroleum-based liquid fuel, such as diesel. As a result, natural gas vehicles require larger fuel tanks to store an equivalent amount of energy. CNG is simply pressurised natural gas stored between 200 to 250 bar whereas LNG is a cryogenic liquid maintained at approximately -162°C at atmospheric pressure [59]. LNG has a higher energy density compared to CNG, so is typically selected for use in long-haul applications.

2.3.2 Current Utilisation of Natural Gas

The advantages of natural gas have resulted in the emergence of technologies that utilise the fuel in various combustion chamber orientations [57,60–66]. These designs are diverse and can range from retro-fit options to fully integrated or dedicated natural gas engines, each with their individual sets of advantages and drawbacks.

Currently, one of the most popular combustion systems is of the spark-ignited stoichiometric gas variety, as shown in Figure 2-16. In this arrangement, natural gas is introduced to the combustion chamber with Port Fuel Injection (PFI) or Direct Injection (DI) systems and uses an electronic spark plug to ignite the charge [60,67]. This combustion process is characteristic of the Otto cycle as opposed to the Diesel cycle and typically utilises a Three-Way Catalyst (TWC) for exhaust after-treatment. This design carries low-cost and complexity due to its simplified injection and after-treatment systems. However, certain drawbacks linked with high combustion temperatures ultimately limit power density, efficiency, and durability [68]. This design also suffers from decreased light-load efficiency due to throttling for stoichiometric operation [69]. Lean-burn or high dilution scenarios also create additional problems for spark-ignition engines, as they lack sufficient ignition energy for adequate flame kernel growth.

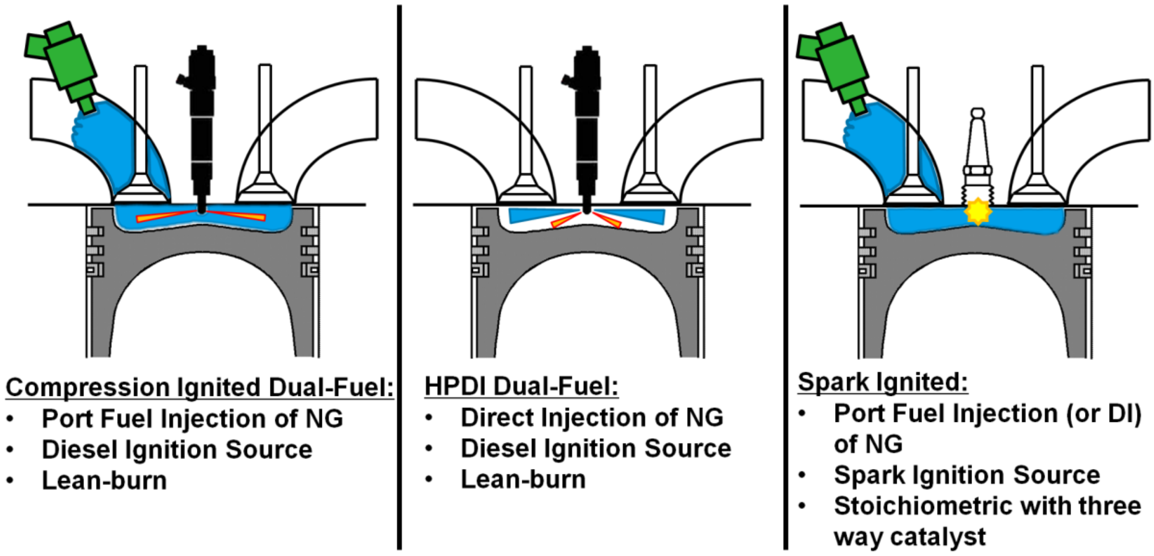

Figure 2-16: Examples of possible Natural Gas (NG) combustion system orientations (NG denoted by blue)

Lean-burn gas engines are an alternative to spark-ignited gas engines and have also been utilised in the HD sector. Lean combustion helps to reduce the in-cylinder temperatures thereby improving power density and efficiency [68]. Furthermore, elimination of pumping losses from throttling ensures superior light-load efficiency when compared to an equivalent stoichiometric design. However, these engines are typically more expensive and complex when compared to spark-ignited mainly due to the ignition and after-treatment systems [69].

A variety of different lean-burn natural gas engines currently exist and primarily revolve around a dual-fuel concept. Retro-fit designs typically use gas injectors either in the intake port or manifold which allows for the retention of the original diesel combustion system hardware, including the injectors [57,70,71]. The diesel injectors serve as the ignition source for the bulk fuel mass of natural gas being injected. Importantly for these designs, the diesel injectors allow for true dual-fuel operation in either diesel or natural gas/diesel modes. Also, more complex systems such as High Pressure Direct Injection (HPDI) have been developed and introduce natural gas directly into the cylinder with using diesel fuel as an ignition source [61]. HPDI enjoys increased volumetric efficiency and power output over PFI designs due to the gaseous fuel no longer displacing the air/EGR mixture entering the cylinder. Scavenging is also possible without having natural gas bypassing the combustion chamber, allowing for faster turbocharger response and greater low-end torque capability. However, this method of direct injection requires a relatively expensive injector in order to introduce gas and diesel in-cylinder at high pressures. Challenges are also associated with injecting fuel quickly enough for a sufficiently short combustion event, which can potentially limit maximum output and/or engine speed.

One way to save on the expense of an HPDI injector and still enable lean-burn combustion is to utilise a pre-chamber design. Turbulent Jet Ignition (TJI) combustion uses a pre-chamber with a spark plug and injector to produce jets of burning fuel and air to ignite the main combustion chamber mixture [62,63]. This enables lean operation, but does not offer any ability for diesel operation, or premixed quantities of diesel. Optical research has been performed with TJI [62] and diesel pilot ignition [70,72] and offers some direction for understanding how improvements to lean-burn engines can be made, particularly with regards to emissions.

Generally unburnt methane issues arise when natural gas is the bulk fuel mass and is homogeneously mixed with the combustion charge prior to ignition. This scenario would mainly apply to PFI natural gas designs where the combustion chamber crevice volumes (i.e. piston top land) can account for a significant portion of engine-out methane emissions. This situation is particularly problematic for lean-burn engines which lack sufficient exhaust heat in order to oxidise methane and cannot make use of a stoichiometric TWC.

2.4 Improvement of Lean Burn Dual-Fuel Natural Gas Engines

It remains a challenge for lean burn dual-fuel natural gas engines to meet tailpipe-out methane emissions, particularly considering Euro VI emissions standards capping methane to less than 0.5 g/kWh [73]. Issues with low exhaust gas temperatures during the World Harmonized Transient Cycle (WHTC) do not allow methane oxidation catalysts to reach operating temperature quickly, so significant methane slip occurs [74]. As a result, it is favourable to reduce methane emissions on an engine-out basis, which also has the benefit of decreasing after-treatment costs [75]. One potential method to reduce emissions in-cylinder is through LTC, which will be discussed in Section 2.4.1. Following this in Section 2.4.2 are some of the difficulties associated with operating lean burn natural gas engines at light load.

2.4.1 Low Temperature Combustion

Several in-cylinder emissions control strategies are in existence, but the majority of them can be consolidated into what is known as LTC. LTC strategies minimize the formation of emissions, particularly NOx and soot. These benefits are driven by reducing the local Equivalence Ratios (EQR) and by lowering peak combustion temperatures through the use of EGR. As a result, the NOx and soot formation pathways are limited, while retaining or even improving upon the efficiency of conventional diesel and gasoline engine architectures [50,76–79]. The data presented in Figure 2-17 [80] shows a typical LTC pathway compared against conventional diesel combustion on a local EQR and combustion temperature map.

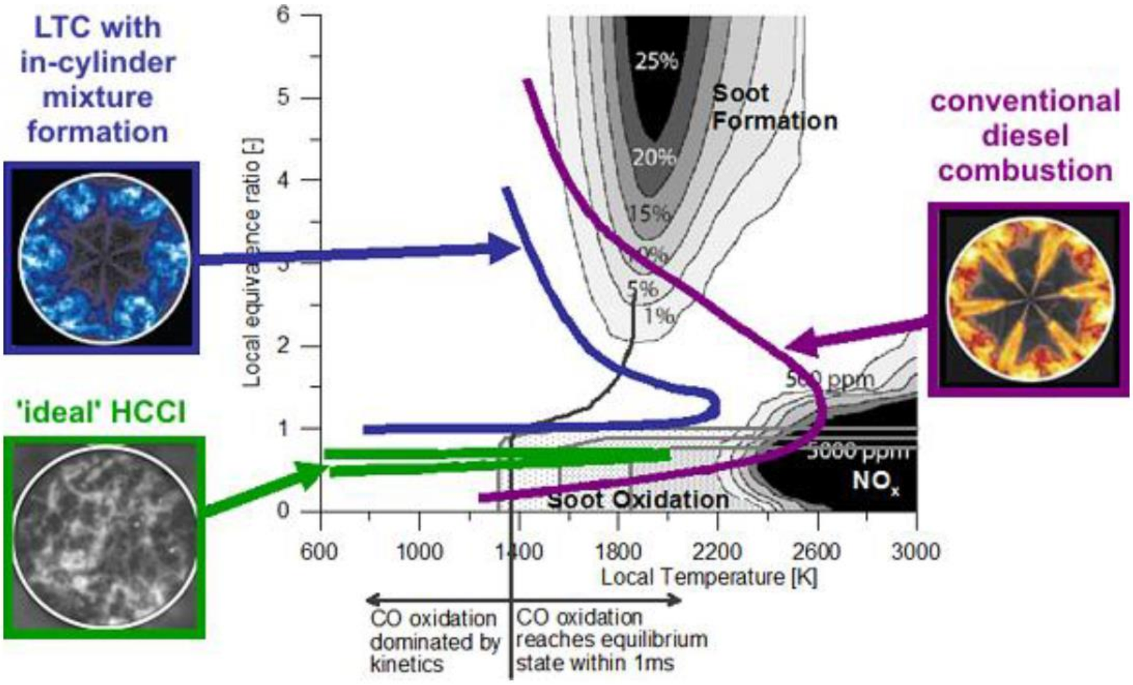

Figure 2-17: The emissions formation pathway of conventional diesel combustion compared with LTC on a local equivalence ratio and temperature map [80]

Homogeneous Charge Compression Ignition (HCCI), denoted by green in Figure 2-17, is a type of LTC that achieves low NOx and soot simultaneously with high efficiency [81–83]. HCCI is characterised by a fully premixed fuel, air and EGR mixture with no spark or injection event to initiate combustion. Instead, it relies upon the thermodynamic state and resulting chemical kinetics of the compressed charge to trigger auto-ignition. The benefits of HCCI derive from relatively lower heat transfer losses and faster combustion durations, resulting in higher thermal efficiencies under high charge dilution conditions. Homogeneous mixing of fuel and air leads to cleaner combustion, which lowers soot by avoiding local-rich areas and limits NOx production with low combustion temperatures when compared to typical spark-ignited engines. EGR also helps to decrease peak combustion temperatures due to the increased specific heat capacity of the intake charge as well as working as a diluent (less oxygen concentration). However, the main challenges with HCCI are a limited operating band and a lack of direct control of combustion phasing through injection or spark timing [84].

In comparison to HCCI or Controlled Auto-Ignition (CAI) [85], a number of less homogeneous combustion strategies have been developed. Premixed Charge Compression Ignition (PCCI) [78,86–89], Partially Premixed Compression Ignition (PPCI) [90], Modulated Kinetics (MK) [91], and Gasoline Direct Injection Compression Ignition (GDCI) [92,93] are to name a few. PCCI is characterised by a direct-injection of fuel during the compression stroke, sometimes utilising multiple injections, in order to stratify the charge. The non-uniform EQR drives differences in the local chemical kinetic reaction rates, which in turn influence the ignition delay and resulting combustion duration. In this it differs from HCCI since the fuel is less premixed, but allows for a greater degree of control for combustion phasing. Similarly, GDCI utilises premixed gasoline injections to improve combustion. Studies have also compared gasoline against diesel and occasionally both are used together simultaneously [82,83,94]. These combustion strategies offer more control over combustion phasing at low to medium loads while maintaining low soot and NOx emissions. However, these less homogeneous combustion modes tend to suffer from lower indicated efficiency when compared to HCCI along with increased unburnt hydrocarbon and CO emissions. They are also subject to a limited load range due to high EGR and boost requirements.

Reactivity Controlled Compression Ignition (RCCI) [95–100] is a dual-fuel LTC combustion strategy that uses at least two fuels of high and low reactivity to control combustion. A low reactivity fuel, such as ethanol, gasoline, or natural gas is introduced to the cylinder along with the inducted air, and EGR if applied, for a well-mixed charge. The high reactivity fuel, such as diesel, is directly injected during the compression stroke in two injections. The first injection serves as squish volume conditioning generally -80 to -50 CA deg After Top Dead Centre (ATDC) and the second serves as centre/bowl conditioning typically -45 to -30 CA deg ATDC [97,100,101]. The ratio of the low and high reactivity fuels is varied to determine mixture flammability and resulting combustion characteristics. RCCI is a distributed auto-ignition strategy with the fuel gradient controlling the speed of combustion. Similar to PCCI, RCCI operation reduces NOx and PM, but hydrocarbon and CO emissions tend to increase compared to conventional diesel combustion. This combustion strategy is also sensitive to intake air temperatures as well as EGR fractions [100].

Premixed Dual-Fuel Combustion (PDFC) is another type of LTC dual-fuel strategy and differs from Conventional Dual-Fuel and RCCI. In this instance, Conventional Dual-Fuel is defined as a gaseous fuel, such as natural gas, being introduced via PFI with having a liquid fuel, such as diesel, directly injected into the combustion chamber at around Top Dead Centre (TDC). Due to the lower auto-ignition temperature, compression ignition of the diesel fuel provides the ignition source for the homogeneously mixed natural gas. The NG typically comprises 80-98% of the total fuel energy, and the diesel that serves as the pilot is the remaining 2-20%. The combustion characteristic is a CI spray, approximately 10 CA deg Before Top Dead Centre (BTDC), that ignites the homogeneous charge giving rise to flame propagation burning of the bulk fuel mass [70,72,101], and on occasion is followed by auto-ignition of the end gas.

PDFC is primarily defined by an early injection of diesel which is partially premixed with the homogeneous charge of NG in the cylinder. The premixed fuel-air charge consists of NG as the main fuel and early injected diesel as the secondary fuel. EGR is used to prevent auto-ignition of the early injected diesel fuel and also to dilute the premixed fuel-air charge to slow the rate of heat release. PDFC differs from RCCI in that combustion is not controlled by changing fuel substitution ratios, but rather by the timing and quantity of the second diesel injection around TDC. The main difference between the RCCI and PDFC injection strategy is illustrated in Figure 2-18.

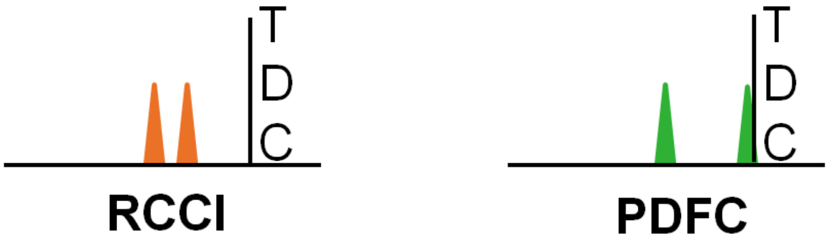

Figure 2-18: RCCI and PDFC injection events relative to TDC

2.4.2 Low Load Operation

A fundamental drawback of a lean-burn dual-fuel engine is operation under light-load conditions. Various factors surrounding mixture flammability and combustion temperature yield high hydrocarbon and CO emissions and poor efficiency [7,102]. In the specific case of PFI natural gas, combustion chamber crevice volumes have a significant effect on the unburnt methane emissions and can also contribute to a reduced operating efficiency [103–105]. The extension of the dual-fuel operating range is always desired as it helps to improve the business case of natural gas as a fuel. However, satisfactory emissions and efficiency need to be maintained under high natural gas substitution. In order to enable this, more sophisticated methods of light-load operation have been explored.

One such concept is to use the engine valvetrain and/or cylinder deactivation to improve light load performance, specifically with regard to emissions, efficiency and exhaust gas temperature. This has been tested for diesel engines [106], demonstrating that Early Intake Valve Closing (EIVC) strategies and cylinder deactivation can have positive impacts on emissions and can raise exhaust gas temperatures by greater than 50°C. Variable Valve Actuation (VVA), including Late Intake Valve Closing (LIVC) strategies, have also been used in dual-fuel engines [107–109].

Further, engine cycles in which the effective compression ratio is smaller than the effective expansion ratio are typically referred to as over-expanded cycles. Over-expanded cycles are more commonly referenced as Atkinson or Miller cycles, which bare the name of their inventors James Atkinson and Ralph Miller [110–113]. These cycles can be implemented on both spark or compression ignition engines in naturally aspirated or forced induction forms while employing either EIVC or LIVC strategies. Due to the broad range of applications, the use of the terms Atkinson or Miller cycle is not always consistent in literature and can depend on the author or scenario. Engines with LIVC strategies are sometimes referred to as Atkinson cycle engines with occasional restrictions to being naturally aspirated [114,115]. However, the original Atkinson cycle patents make no reference to actuation of the intake valve timings to achieve higher expansion ratios, but to an engine that utilizes a crankshaft mechanism to obtain a higher expansion ratio than compression ratio [110,111]. Atkinson identified the benefits of having different expansion and compression ratios, but Miller implemented over-expanded cycles with either EIVC or LIVC strategies on both naturally aspirated and forced induction engines [112,113].

Historically, the primary benefit of using an over-expanded cycle was a reduction in temperature at the end of the compression stroke which enabled the use of higher geometric compression ratios. This yielded a longer expansion ratio and an efficiency benefit though extracting more energy from the charge as well as an increase in power density [112,113]. Comparing EIVC and LIVC strategies, EIVC is typically favoured from an intake charge cooling perspective due to the additional expansion of the charge after intake valve closing. This results in a lower peak in-cylinder temperature and further efficiency benefits. However, implementation of EIVC in high speed engines may be problematic as maximum valve lift may be restricted due to piston-to-valve interference [116].

Miller cycle gained interest in the 1980s, with a number of commercial applications appearing in the 1990s where efficiency gains were realised for gasoline, diesel, and gas engines alike [19,116,117]. In diesel applications, Miller cycle has also been used to quell NOx emissions at high engine load while gasoline engines enjoy reduced pumping losses at part load to improve efficiency [19,114,115]. One other benefit of Miller cycle for diesel engines in particular is the reduction of volumetric efficiency at low load conditions. The lower volumetric efficiency reduces the in-cylinder λ (and trapped mass), which results in an increase in exhaust gas temperature [106,118]. This is especially useful for providing thermal energy to the exhaust aftertreatment systems that struggle to operate effectively under light load or warm-up conditions but comes at the expense of higher relative heat loss due to the reduced mass of the charge. For natural gas engines, these strategies can be highly effective for reducing methane emissions and can provide a way to control in-cylinder λ, providing an alternative to throttling and EGR strategies [64,109]. However, one of the shortcomings if a fixed LIVC strategy is used is that there would also be reduced volumetric efficiency at full load [118]. Additional cost would be added for either a variable valvetrain or the need to resort to two-stage (series or parallel-sequential) turbocharging to maintain power density [116].

2.5 Summary

The diesel engine has progressed from humble beginnings to become the powertrain of choice for the HD transportation sector. The history and background of this journey was touched upon in this chapter along with the key technological advancements that made it possible. Additionally, specifics of diesel engine operation were reviewed to help understand where future improvements could be made. Natural gas was identified as a relatively cheap and abundant resource that has potential synergies with HD applications. The utilisation of natural gas was also covered in conjunction with the advantages and pitfalls of various designs. Finally, the lean-burn dual-fuel natural gas engine was examined with low load operation cited as an area for improvement using LTC and advanced valvetrain technologies.

Chapter Three

Experimental Methodology

3.1 Introduction

In order to understand the complex interactions of diesel and dual-fuel combustion, a single cylinder HD research engine was utilised to produce experimental engine data. Compared to other methods, such as computer simulation, use of a physical engine was necessary because it was the only way to realistically represent all of the intricacies of combustion. Issues such as emissions formation pathways and auto-ignition cannot yet be accurately simulated for complex “real world” fuels, as the combustion chemistry and physical interactions are not yet fully understood. An overview of the experimental setup is given in Section 3.2 to provide all of the essential details of the hardware of the engine and the data acquisition methods. Included in Section 3.3 are details regarding the handling of the collected experimental data in both real-time and in post-processing.

3.2 Experimental Setup

The research engine used was a 2.0 litre single cylinder HD diesel unit, including an external boost rig, a conventional piezo DI diesel combustion system with High Pressure Loop (HPL) cooled EGR, VVA on the intake camshaft and dual-fuel diesel-natural gas capability. A schematic of the engine hardware is shown in Figure 3-1, where the air/EGR circuits are displayed along with the emissions sampling locations. Figure 3-2 is a picture of the physical engine test rig. The fresh air mass enters from the right and mixes with the cooled EGR. The charge moves towards the natural gas injection point where all three constituents of fresh air, cooled EGR, and natural gas enter the intake buffer tank. The natural gas was injected upstream of the buffer tank to ensure good mixing with air and EGR. Transient operation was not considered in this study, with all experimental test points obtained under steady-state.

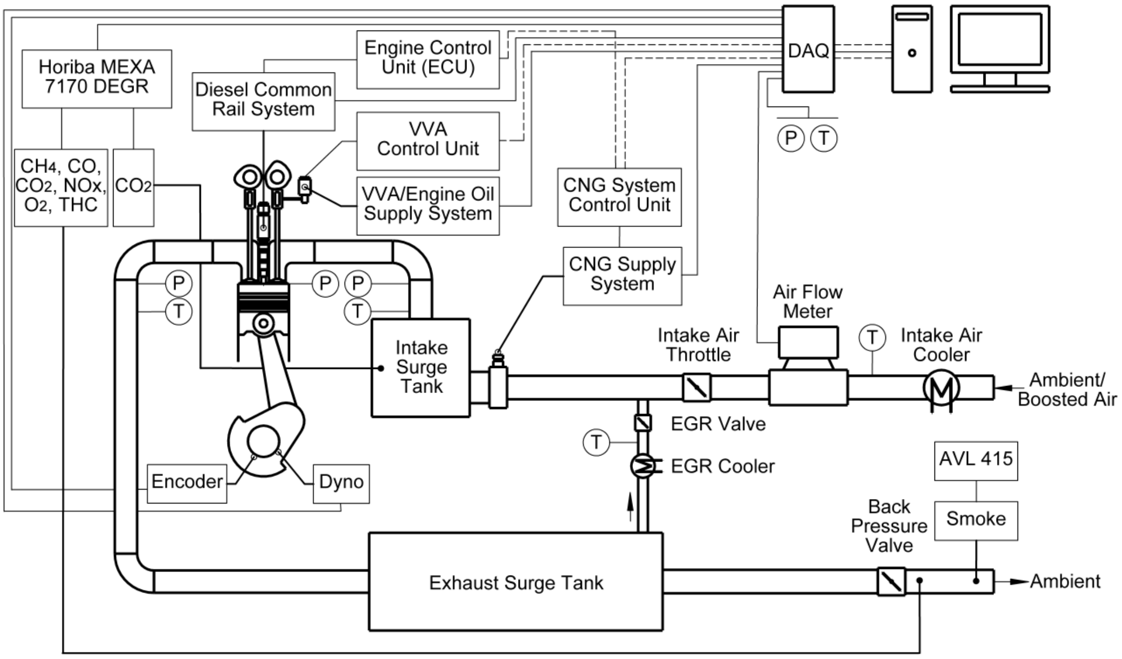

Figure 3-1: Schematic diagram of the research engine

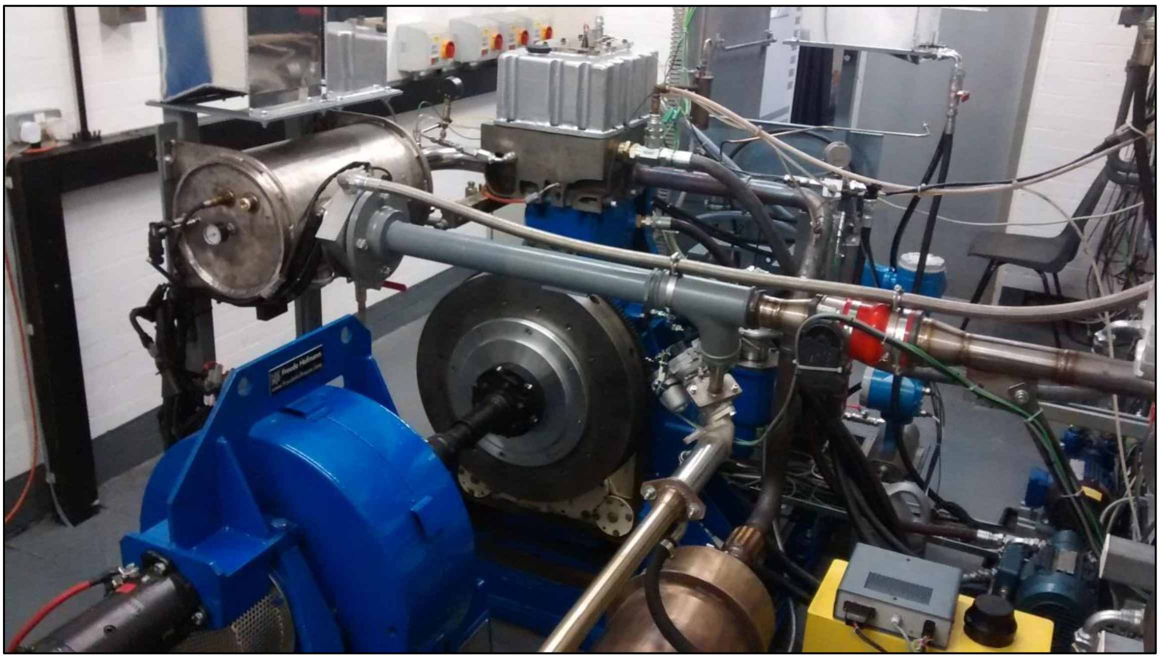

Figure 3-2: Overview of the engine test bed and experimental facilities

3.2.1 Engine Specification

Some key details of the base engine are set out in Table 3-1. The bottom end/short block was AVL-designed with two counter-rotating balance shafts to balance the single-cylinder reciprocating mass. Both the cylinder head and block were made of cast iron while the intake and exhaust piping were made using stainless steel, with the exception of the natural gas injection point (aluminium) and the intake pipe immediately before it (steel).

Table 3-1: Single cylinder engine specifications

Bore x Stroke	129 x 155 mm
Swept Volume	2026 cc
Connecting Rod Length	256 mm
Compression Ratio	16.8 (16.1 effective w/VVA)
Maximum Cylinder Pressure	180 bar
Maximum Engine Speed	1900 RPM
Piston	Re-entrant diesel bowl
Number of Valves	4
Intake/Exhaust Valve Diameter	43.9 / 40.4 mm
Intake/Exhaust Cam Duration/Lift	Int: variable, Exh: 245 CAD, 14 mm
Exhaust Cam Timing (Rel TDC_{NF})	Open: -227 CAD, Close: 18 CAD
Diesel Injector	Central DI Bosch CRIN 3.22, 8 Hole 150°, 0.176 mm hole diameter, Common Rail, 2200 bar max pressure
Natural Gas Injectors	Gaseous Port Fuel Injection (PFI) Clean Air Power SP010, upstream of intake buffer tank

The cylinder head and piston were based on a Yuchai YC-6K multi-cylinder engine and consisted of a 4-valve swirl-oriented chamber with a 93 ml volume re-entrant combustion bowl. A dimensioned piston cross section is depicted in Figure 3-3 and was installed in the engine with a 1.05 mm TDC clearance height. A CAD image of the intake and exhaust ports is provided in Figure 3-4 to indicate that the orientation of the valves induced a degree of swirl.

Observing Figure 3-1, the air path of the engine begins with the air filter inside the test cell during naturally aspirated operation, or with the external boost rig if running above atmospheric intake pressure. The external boost rig was an AVL 515 sliding vanes compressor coupled to an electric motor. The pressure supplied was closed loop controlled with a bypass valve. There was fine adjustment possible with the intake throttle, which was a pulse width modulation (PWM) controlled butterfly design of 74 mm diameter. With this combination, the total boost range can be adjusted from 0.1 to 2.2 bar gauge with an accuracy of ±0.015 bar.

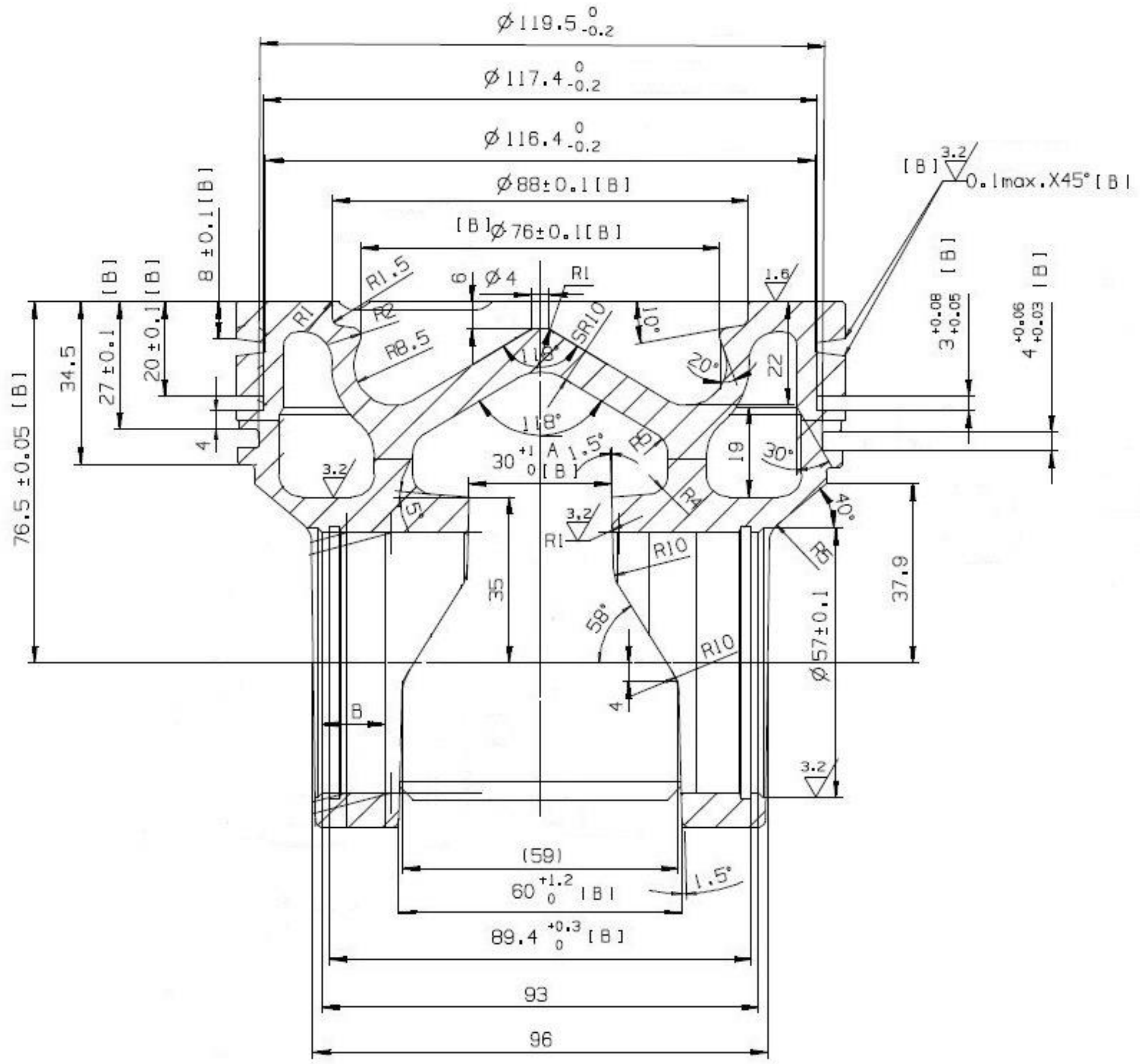

Figure 3-3: Drawing of the piston cross-section

The intake air temperature could be controlled with the boost rig or with the intake cooler, which enabled intake temperatures ranging from 15 °C above the cooling water temperature up to about 100 °C. After the intake cooler, an Endress & Hauser Proline t-mass 65F air mass flow meter was fitted, which works on the principle of thermal dispersion. During operation there are two temperature transducers introduced to the air stream, held at a differential temperature. One of the two transducers was used conventionally as a temperature sensing device, whilst the other was used as a heater. The power consumption to maintain the heated element at a constant temperature was metered so the greater the mass flow, the greater the cooling effect and power required. The measured heater power was therefore a measure of the gas mass flow rate [119].

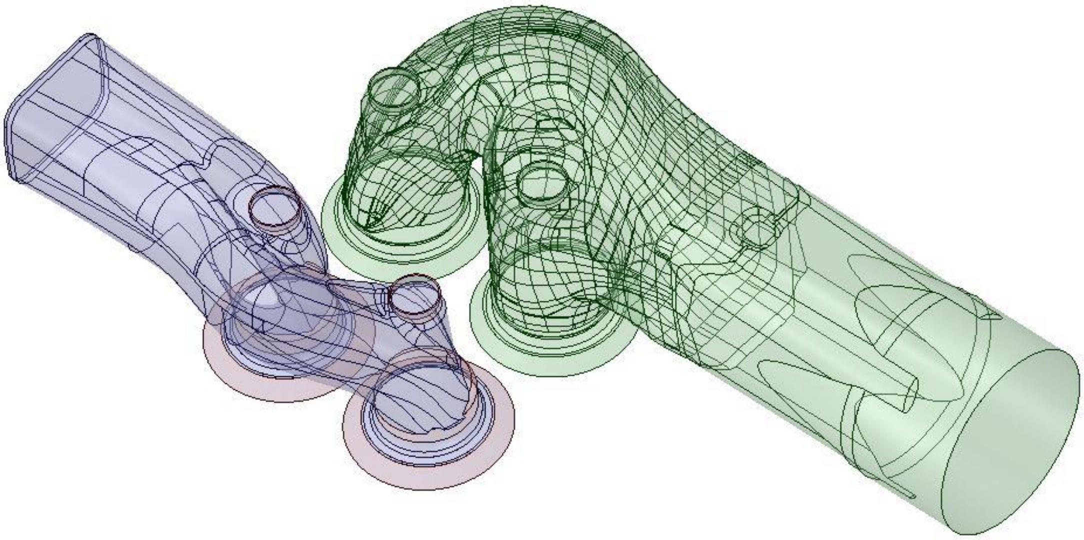

Figure 3-4: CAD model of the intake (right) and exhaust (left) ports

The quoted air mass flow meter accuracy from the manufacturer was ±1.5% of reading for 100% to 10% of full scale and ±0.15% of full scale for 10% to 1% of full scale. However, these values are for steady-state flow conditions without air pulsations from the engine, which could lead to higher readings due to air moving backwards and forwards around the transducer. In order to understand the effect of air pressure pulsations on the air flow readings, a validation test was performed. First, in order to ensure the air flow meter was reading correctly under steady conditions, a mechanical Romet rotary airflow meter verified the Proline 65F readings. After this, the engine was operated with the 65F to determine the engine speeds and loads that should be avoided, such as naturally aspirated, wide-open throttle, low speed situations that caused large intake pressure pulsations. It was found that the intake air pulsations were reduced if the engine was boosted by the external compressor, the throttle was closed (isolates flowmeter from the engine), and light loads and very low speeds were avoided. For the experiments performed in this work, the air flow accuracy was found to typically be in the range of 1-4% accuracy, and was generally used as a way to confirm the λ calculations from the emissions analyser.

After the air mass flow meter, the intake throttle was mounted just upstream of the cooled external EGR introduction point. The EGR valve was a PWM controlled poppet valve with an EGR cooler, which was cooled with dyno cell water. EGR mass flow was driven by differential pressure between the intake and exhaust, and could be articulated by changing the intake pressure via throttle or boost pressure, or increasing the exhaust backpressure via a backpressure valve. EGR temperature was monitored with a K-type thermocouple located 10 mm after the EGR valve. The thermocouples used for instrumentation were subjected to a two-point calibration using an ice-water bath and boiling water to verify accurate readings. The CNG injectors were located downstream, just before the 24 L intake surge tank. The CNG injector assembly is discussed later on. The intake surge tank was made of stainless steel and helped to dampen the intake pressure waves within the engine gas path. It also served as a way to ensure good mixing of EGR, CNG and air before the charge enters the engine, decreasing the COV of IMEP due to constituent variation.

The intake runner exited the intake surge tank with a curved 90-degree bend to direct the charge to the intake port of the engine. In the straight portion of the intake runner, intake pressure and temperature were measured. The temperature was measured 10 mm upstream of the cylinder head with a K-type thermocouple. Crank angle resolved intake pressure was measured with a water cooled Kistler 4049A10S piezoresistive absolute pressure sensor with an accuracy of ±0.5% full scale. The fast response enabled the intake pressure waves to be captured relative to crank angle, which can be useful in correlation of thermodynamic models. The average of this pressure signal was also used to compute the average intake air pressure. The same type of pressure transducer was used in the exhaust runner, and the average of that crank angle resolved signal used as the average exhaust backpressure. Also in the exhaust pipe was a K-type thermocouple mounted 10 mm downstream of the cylinder head to measure exhaust gas temperatures (EGT). The exhaust passed into a 54 L tank, from which the EGR was taken. Finally, the exhaust gas backpressure could be varied by way of an electronically controlled Froude Consine TX21 push/pull actuator, before exiting the test cell via a muffler.

The lubrication circuit uses 15W-40 oil and was driven by an independent electric motor. This oil was circulated to the crankshaft, balancer shafts, camshafts and VVA (oil driven hydraulic tappet) via an adjustable 3-4.5 bar pressure regulator. Oil was returned from the engine and cooled via a Bowman heat exchanger cooled by dyno cell water. An engine oil heater was also fitted to speed up engine warm up. Similarly, the coolant system was driven by an independent electric water pump and was circulated around the engine as well as a Bowman heat exchanger, where the dyno cell water removed engine waste heat. A heater was fitted to the engine side coolant circuit with the purpose of heating engine coolant up more quickly. Coolant temperature was measured with a K-type thermocouple before entering the cylinder head.

3.2.2 Valvetrain

A Jacobs VVA system was installed on the intake camshaft to hydraulically control the intake valve lift and duration via a high-speed solenoid assembly. The solenoid assembly, detailed in Figure 3-5, was controlled with engine oil and a calibrated TTL signal sent from the in-house MATLAB based control software. The mechanical intake camshaft was ground with the maximum possible duration and lift, with duration approaching 360 CA degrees and a lift of approximately 15.2 mm. This is the purple “Ideal Cam” depicted in Figure 3-6. The minimum valve lift is shown by the turquoise “VVA off” line and is the resulting event if oil is free to exit when the tappet is mechanically bottomed out. Lift events can be varied in duration in between these two extremes by controlling when and how much oil is free to move out of the tappet. This resulted in sinusoidal valve lift events that mimic conventional camshafts, rather than square-wave. The system also allowed for intake valve reopening for the purposes of re-breathing internal EGR (I-EGR), the lift of which is shown around 200 deg CA in Figure 3-6. LIVC was also possible and was used to adjust global in-cylinder λ and effective compression ratio.

A LORD MicroStrain S-DVRT-8 displacement sensor was used to measure intake valve lift and was installed on the valve side of the rocker arm. A validation was performed with a mechanical lift gauge to confirm the reading from the installed displacement sensor. As previously indicated in Table 3-1, the exhaust cam profile was fixed duration, timing, and lift, and followed a standard opening and closing pattern. When conventional valve events were desired, or ones that are similar to production engines, the intake valve lift duration was maintained at approximately 207 CA degrees end-of-ramp. This yielded an effective compression ratio of approximately 16.2:1 with the chosen valvetrain settings which was used for the majority of the work unless otherwise stated.

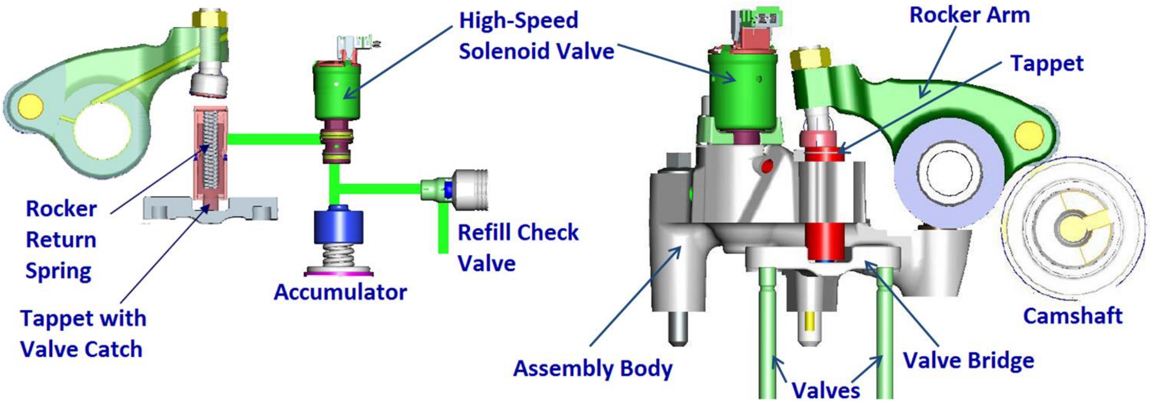

Figure 3-5: Lost-motion intake VVA system with collapsing tappet on the valve side of the rocker arm [43]

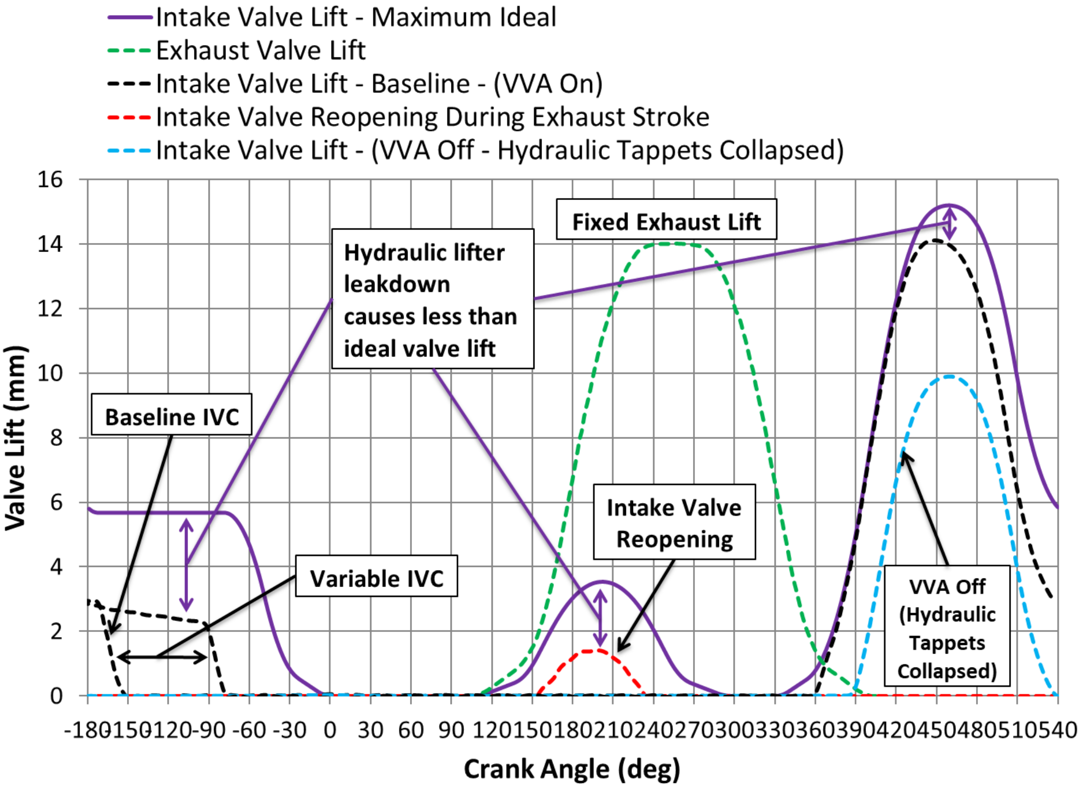

Figure 3-6: Intake valve lift with the high-speed solenoid valve held open at 600 rpm and 0°C showing failsafe lift [43]

3.2.3 Fuel Systems

Separate diesel and natural gas fuel systems were installed on the research engine, enabling dual-fuel operation under varying ratios of diesel and natural gas simultaneously. With the sizing of the diesel injector, full diesel “fall-back” mode was available as well, indicating that this engine is not a dedicated dual-fuel design, which typically has smaller flow diesel injectors and modified piston geometry. During dual-fuel operation, the bulk fuel mass of port fuel injected natural gas is ignited by a quantity of direct injected diesel. The two fuel systems will be discussed in detail, beginning with the diesel setup.

As stated in Table 3-1, diesel fuel was delivered to the cylinder using an 8-hole DI Bosch CRIN 3.22 piezo-actuated injector. The injector was coupled to a multi-cylinder Bosch common rail, with the other injector connections capped off. A Bosch CP4-S2 high pressure pump coupled to an ABB electric motor pressurized diesel from 500 to 2200 bar. An independent low-pressure system supplied diesel to the high-pressure pump via a pressure regulator and Bowman heat exchanger to moderate the fuel temperature.

For diesel mass flow measurement, a Coriolis-type mass flow meter was used, which worked on the principle of Coriolis forces. Here, a mass moving at a given velocity imposes a phase shift in the oscillating frequency of a measuring tube. The amplitude of the oscillations were analysed to determine the mass flow. Two Endress+Hauser Promass 83A Coriolis mass flow meters were used to measure the diesel flow rate by considering the total fuel supplied to and from the high-pressure pump and diesel injector return. In this instance, it was necessary to use two fuel mass flow meters due to the constraints faced for the return of the diesel injector, which specified a backflow pressure of 0 to 1.0 bar gauge. With no suction pressure allowed on the injector return line as well as a pressure limit of 1.0 bar, the fuel had to be returned along with the return from the high-pressure pump in order to be accounted for. With this setup, fuel flow deviation for diesel (and natural gas) were calculated to be <2% by $\frac{(Max-Min)}{Average}$ at all sites, average values of which were confirmed against λ measured by the emissions analyser.

The diesel was stored in external tanks and was pumped to the dyno cell via an electric scavenge pump. Details of the diesel fuel properties tested are displayed in Table 3-2. The diesel injections were controlled via a dedicated diesel ECU with the ability to support up to 3 injections per cycle. The diesel ECU was interfaced with a separate natural gas ECU to control the total amount of fuel injected. For the diesel fuel supply, temperature was controlled by using a thermocouple and Bowman heat exchanger fed with dyno cell water. The heat exchanger was placed in the flow path in-between the low and the high-pressure diesel fuel pump.

Natural gas was introduced upstream of the intake buffer tank by an injector block assembly. The assembly was billet aluminium with drillings for two Clean Air Power SP010 gas injectors as well as a temperature and pressure sensor for the natural gas passage. The gas injectors were an inward-opening ball and seat style design and were actuated with electronically controlled solenoids. The two injectors fed into a common passage from where the natural gas was introduced into the air stream. Injections were controlled with a dedicated natural gas ECU that was interfaced with the diesel ECU via a CAN bus.

The natural gas was stored in a rack of twelve interconnected 50 litre 250 bar bottles outside of the engine test cell. From here it was fed into a pair of pneumatically controlled safety valves, a high-pressure filter, and a high-pressure regulator which dropped the gas pressure to 10 bar. Water lines were fed through the pressure regulator in order to counteract the Joule–Thomson effect, which causes a reduction in temperature with large gas pressure drops. After the pressure regulator, the gas was brought inside the test cell and into a Promass 80A Coriolis mass flow meter calibrated for natural gas. A final low-pressure filter, purge/pressure regulator, and emergency shut off valve follow the mass flow meter, before a flex hose connects the gas path to the injector block.

The natural gas was stored as compressed natural gas and is comprised of 97.25% methane and 2.75% ethane by mole fraction. Fuel properties are shown in Table 3-2. Methane Number (MN) is a key parameter as it indicates the knock resistance characteristics of the NG fuel. It is analogous to octane number in that a higher numerical value indicates increased knock resistance. For this work, CARB MN estimation was used and is referenced in Table 3-2 [120].

Table 3-2: Fuel properties

Fuel Property	Gasoil Ultra Low Sulphur	Natural Gas Blend
Chemical Formula	C_8-C_{25}	CH_4 and C_2H_6
CARB Methane Number [120]	-	101.1
Mixture (Mole Fraction)	-	97.25% Methane, 2.75% Ethane
Molar Mass	~167 g/mol	16.43 g/mol
Liquid Density at STP	830 kg/m3	-
Density at STP	-	0.695 kg/m3
Cetane Number	~45	-
Octane Number	-	>120
Stoichiometric Air-Fuel Mass Ratio	14.5	17.1
Autoignition Temperature	483 K	807 K
Boiling Point/Range	443-643 K	115 K
Carbon Content	86.6%	75.3%
Hydrogen Content	13.2%	24.7%
Oxygen Content	0.2%	0%
Lower Heating Value (LHV)	42.9 MJ/kg	49.9 MJ/kg

3.2.4 Data Acquisition and Control

Engine load was added or removed by the TEXCEL V4 dynamometer controller. Fuelling was based on a speed governor principle and was controlled solely by an Engine Control Electronics (ECE) ECU-CR.8 diesel ECU. This total fuel demand was passed to the natural gas ECU to determine how much gas should be injected while it relays the quantity of diesel demand back to the diesel ECU for injection. For a given load, if the speed began to decrease, more fuel was added to raise the engine speed back to the set point. The opposite was true if the speed was above the given set point. Engine speed was measured using a Bosch inductive crankshaft sensor, which was mounted opposite a 60-tooth trigger wheel with 2 teeth omitted for reference. The camshaft sensor was a Hall-effect unit and was mounted near a camshaft gear to locate the camshaft position. Both ECUs were spliced in to read both the crankshaft and camshaft sensor signals. In diesel-only mode, the diesel ECU was responsible for controlling the rail pressure as well as the timings and quantities of the diesel injection(s). In dual-fuel mode, the timing and quantity of both the natural gas and diesel injections were determined by the natural gas ECU. However, the diesel ECU still maintained control of the rail pressure set point. Interaction with the ECUs was by way of two independent software packages. ECE developed the interface software for the diesel ECU and ATI Vision was used to communicate with the Clean Air Power natural gas ECU. Finally, injection timings were measured using real-time analysis of the injector current signals captured with a LEM PR30 current probe.

Data was gathered using a pair of National Instruments data acquisition cards which fed into a transient combustion analysis software that was developed by Zhang [121]. A USB-6210 card with a sampling rate of 250 kilo samples per second (kS/s) was used for low speed signals and a USB-6251 with a sampling rate of 1.25 Mega samples per second (MS/s) captured high speed signals. Emissions values from the emissions analyser were fed directly into the computer via Ethernet cable. A summary of the data acquisition signals is shown in Table 3-3 along with dynamic ranges and accuracies.

Table 3-3: A summary of the equipment and data acquisition cards used to measure experimental data

	Number	Measurement	Equipment	Dynamic Range	Linearity/ Accuracy	Repeatability
6210	1	Oil Pressure	GE PMP 5076 TC-A1-CA-H0-PN	0-10 bar	< ±0.2% of FS	-
	2	Diesel Rail Pressure	Bosch DS-HD-RDS4.5, 0281006117-L	0-2400 bar	±0.7 to 1.7% of FS	-
	3	Natural Gas Flow	Endress+Hauser Proline Promass 80A02	0-20 kg/h	±0.15% of reading	±0.05% of reading
	4	Intake Temp	Audon TCK-4 Thermocouple Amplifier Unit	-40 to 1200 °C	≤ ±2.5 °C or ±0.75% of readings	-
	5	Exhaust Temp				
	6	Coolant Temp				
	7	EGR Temp				
	8	Diesel Fuel Flow Meter (Return)	Endress+Hauser Proline Promass 83A01	0-100 kg/h	±0.10% of reading	±0.05% of reading
	9	Air Flow Meter	Endress+Hauser Proline T-mass 65F	0-910 kg/h	±1.5 % reading (10 to 100% FS)	±0.5 % of reading
	10	Diesel Fuel Flow Meter (Supply)	Endress+Hauser Proline Promass 83A02	0-20 kg/h	±0.10% of reading	±0.05% of reading
	11	Oil Temp	Audon TCK-4 Thermocouple Amplifier Unit	-40 to 1200 °C	≤ ±2.5 °C or ±0.75% of readings	-
	Number	**Measurement**	**Equipment**	**Dynamic Range**	**Linearity/ Accuracy**	**Repeatability**
6251	1	Intake Pressure	Kistler 4049A10S + 4049A10SP22 (@ 60 °C)	0-10 bar	≤ ±0.5% of FS within 0-80 °C	-
	2	Exhaust Pressure				
	3	In-Cylinder Pressure	Kistler 6125C11 + AVL FI Piezo (-33.53 pC/bar, 0-200 bar @ 250 °C)	0-300 bar	≤ ±0.4% of FS	-
	4	Valve Lift VVA	LORD MicroStrain S-DVRT-8 displacement sensor	0-24 mm	±1.0% of reading	±1.0 µm
	5	REF (TDC) Signal	Encoder Technology EB58	0-25000 rpm	0.25 °CA	-
	6	Diesel Injection Timing	LEM Current Probe Model PR30	0-20 A	±1% of reading	-
	7	Lambda	Bosch LSU4, Motec PLM	0.65 to ∞	±0.7 to 3% of reading	-
	8	Engine Speed (Dyno)	Texcel V4 Controller - Froude Hofmann AG150 Eddy Current Dynamometer	0-8000 rpm	±1 rpm	-
	9	Torque (Dyno)		0-500 Nm	±0.25% of FS	Within ±0.15% FS
	10	VVA TTL	VVA control	-	-	-
	11	Clock Signal	Encoder Technology EB58	0-25000 rpm	0.25 °CA	-
Ethernet from Horiba MEXA-7170-DEGR		CO	Non-Dispersive Infrared Detector	0-12 vol%	≤ ±1.0% of FS or ±2.0% of readings	Within ±0.5% FS
		CO2	Non-Dispersive Infrared Detector	0-20 vol%		
		THC	Heated Flame Ionization Detector	0-500 ppm or 0-50k ppm		
		NO/NOx	Heated Chemiluminescence Detector	0-500 ppm or 0-10k ppm		
		O2	Magnophneumatic Detector	0-25 vol%		
		CH4	Non-Methane Cutter + Heated Flame Ionization Detector	0-2.5k ppm or 0-25k ppm		
		EGR	Non-Dispersive Infrared Detector	0-20 vol%		
		HoribaLambda	Calculated	-	-	-

A screenshot of the transient combustion analyser is shown in Figure 3-7. This software visualises all of the data captured by the data acquisition and processes important engine parameters in real-time. Calculation of the IMEP, Indicated Specific Fuel Consumption (ISFC), and other critical combustion parameters are displayed, equations of which will be presented in later sections. A key set of data enabling this was the crank angle resolved in-cylinder pressure. This was measured with a Kistler 6125C11 piezoelectric pressure transducer coupled with an AVL FI Piezo charge amplifier. The pressure transducer was mounted flush to the combustion chamber surface and was capable of measuring pressures between 0 to 300 bar with an accuracy of ±0.4% full scale. The engine maximum cylinder pressure for sustained operation was 180 bar, so settings for the pressure transducer were set to a range of 0 to 200 bar (@ 250°C) with a sensitivity of -33.53 pC/bar.

Cylinder pressure transducers use a quartz crystal that produces an electrical charge proportional to the pressure that is applied to them [122]. Due to the relatively small amplitude of the charge produced, a charge amplifier is needed to boost the signal to a level that is acceptable for data acquisition hardware. The charge amplifier in this case was set to an appropriate resolution of cylinder pressure per volt output and was used with a 100 kHz upper cut-off frequency for the low-pass filter, details of which are presented in Section 4.3. The cylinder pressure transducer, leads, and charge amplifier were calibrated as a unit by using a dead-weight tester to eliminate any equipment variation. Additionally, piezoelectric pressure transducers are only able to measure relative differences in pressure and need to be “pegged” to an absolute pressure value. To account for this, all in-cylinder pressure signals were pegged to the average intake pressure measured by the aforementioned Kistler 4049A10, which also was calibrated using a dead-weight tester. Specifically, the average intake manifold pressure over a window of six crank angle degrees around the inlet bottom dead centre was used for pegging. All combustion data was analysed using an average of 300 engine cycles unless otherwise stated. The resolution of the crank angle based data was 0.25 crank angle degrees, which was the resolution of the Encoder Technology EB58 encoder mounted to the engine crankshaft.

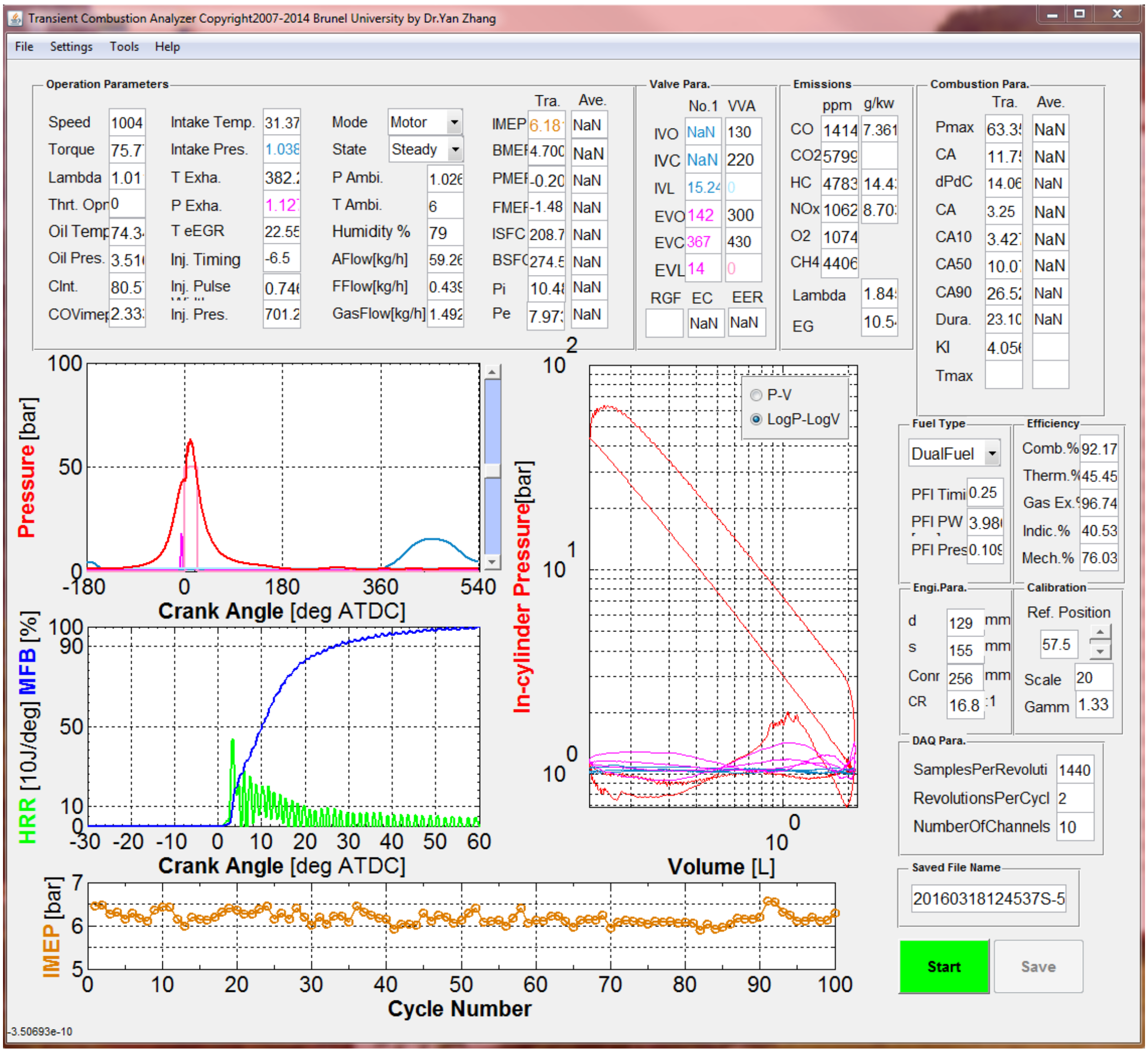
Transient Combustion Analyzer Copyright2007-2014 Brunel University by Dr.Yan Zhang

Operation Parameters

Speed 1004
Torque 75.7
Lambda 1.01
Thrt. Opr 0
Oil Temp 74.3
Oil Pres. 3.51
Clnt. 80.5
COVimep 2.33
Intake Temp. 31.37
Intake Pres. 1.038
T Exha. 382.
P Exha. 1.12
T eEGR 22.55
Inj. Timing -6.5
Inj. Pulse 0.74
Inj. Pres. 701.2
Mode Motor
State Steady
P Ambi. 1.026
T Ambi. 6
Humidity % 79
AFlow[kg/h] 59.26
FFlow[kg/h] 0.439
GasFlow[kg/h] 1.492

	Tra.	Ave.
IMEP	6.18	NaN
BMEP	4.700	NaN
PMEP	-0.20	NaN
FMEP	-1.48	NaN
ISFC	208.7	NaN
BSFC	274.5	NaN
Pi	10.48	NaN
Pe	7.97	NaN

Valve Para.

	No.1	VVA
IVO	NaN	130
IVC	NaN	220
IVL	15.24	0
EVO	142	300
EVC	367	430
EVL	14	0

RGF	EC	EER
	NaN	NaN

Emissions

	ppm	g/kw
CO	1414	7.361
CO2	5799	
HC	4783	14.4
NOx	1062	8.70
O2	1074	
CH4	4406	
Lambda		1.84
EG		10.5

Combustion Para.

	Tra.	Ave.
Pmax	63.3	NaN
CA	11.7	NaN
dPdC	14.06	NaN
CA	3.25	NaN
CA10	3.42	NaN
CA50	10.0	NaN
CA90	26.5	NaN
Dura.	23.10	NaN
KI	4.05	
Tmax		

Fuel Type

DualFuel
PFI Timi 0.25
PFI PW 3.98
PFI Pres 0.10

Efficiency

Comb.% 92.17
Therm.% 45.45
Gas Ex.% 96.74
Indic.% 40.53
Mech.% 76.03

Engi.Para.

d 129 mm
s 155 mm
Conr 256 mm
CR 16.8 :1

Calibration

Ref. Position 57.5
Scale 20
Gamm 1.33

DAQ Para.

SamplesPerRevoluti 1440
RevolutionsPerCycl 2
NumberOfChannels 10

Saved File Name

20160318124537S-5

○ P-V
● LogP-LogV

Figure 3-7: Real-time transient combustion analyser software used to view experimental data

3.2.5 Dynamometer

The engine was coupled to a Froude-Hofmann AG150 Eddy current dynamometer via a rubber-damped propshaft. Water was circulated around the rotor and stator housing to dissipate the heat energy produced by the work input. The dynamometer was rated to a maximum power of 150kW and maximum torque of 500 Nm with speeds up to 8000 RPM. Accuracies of readings were ±0.25% of full scale and ±1 RPM, which was enabled by a high mass flywheel. An electric starter was mounted to the dynamometer and was powered by a commercial truck battery. The load cell used to measure the torque is a Thames Side Sensors U4000 with a maximum load rating of 250 kg with an error of <±0.03% of full scale (confirmed prior to the start of the testing).

3.2.6 Emissions Measurement

The engine-out exhaust emissions and EGR rate were measured using a Horiba MEXA 7170-DEGR emissions analyser. The species specifically considered with this equipment were CO, CO_2, oxygen (O_2), nitrogen oxides (NO_X), methane (CH_4), and total unburnt hydrocarbons (THC). Additionally, engine-out soot emissions were determined using an AVL Smoke Meter 415SE. Exhaust gases and soot emissions were collected in the same location downstream of the exhaust backpressure valve due to the maximum pressure limitations of the emissions hardware. Good exhaust gas homogeneity was achieved in the exhaust tank before the gases passed the backpressure valve and on to the emissions sampling point. The sampling probes extended into the middle of the exhaust pipe diameter to provide the most accurate reading possible.

Various analyser principles were employed to measure the exhaust gas constituents. CO and CO_2 were measured on a dry basis (e.g. without H_2O) with a pair of AIA-722 non-dispersive infra-red (NDIR) gas analysers. This equipment works on the principle that infra-red radiation is absorbed in unique wavelengths depending on the type of gas it is passed through, so upon analysis it is possible to identify specific concentrations when comparing to a known reference cell. In practice, the exhaust gas being analysed is passed through a sample cell and is adjacent to a reference cell of known composition where a comparative reading can be made [17]. The measurement range was set to 0-120000 ppm volume by volume (v/v) for CO and 0-200000 ppm v/v for CO_2.

NOx emissions were measured on a dry basis by a CLA-720MA heated chemiluminescence detector for a range of 0-10000 ppm v/v. Exhaust gases typically contain NO and NO_2 with NOx denoting the sum of these as nitrogen oxides. Either NO or NO_2 can be measured by the detector, with the chemiluminescence technique based around the light emission of activated molecules of NO_2. Metered values of exhaust gas containing NO are combined with ozone (O_3) in a reactor to produce excited molecules of NO_2, which emit light when returning back to ground state. The light measured is directly proportional to the concentration of NO in the sample. Alternatively, in order to obtain the NOx concentration, NO_2 is first converted to NO via a catalyst before being measured. Switching between NO and NO_2–catalyst flow paths can give the value of NOx when the two independent measurements are added together.

The O_2 concentration in the exhaust was measured dry using a MPA-720 magneto-pneumatic detector with an operation range of 0-250000 ppm v/v. This analyser operates on the principle that when a test sample containing oxygen is drawn into a nonhomogeneous magnetic field and mixed with a reference gas of known oxygen concentration, it will create a differential pressure. A balancing reference gas flow is metered and thereby allows the concentration of oxygen in the sample gas to be determined. This measurement technique is possible due to the paramagnetic property of the oxygen molecule, which is able to be influenced by magnetic fields.

THC emissions were measured on a wet basis (e.g. with H_2O) using a FIA-725A heated Flame Ionization Detector (FID) with an operation range of 0-50000 ppm v/v. An FID analyser operates by burning the remaining hydrocarbons of the exhaust sample in a burner with a hydrogen-helium fuel and purified air mixture. When hydrocarbons are burned, electrons and positive ions are formed. If introduced to an electric field, the current flow is proportional to the number of carbon atoms present, so a concentration of hydrocarbons can be determined [17]. The drawback of this technique is that it cannot distinguish between different hydrocarbon species. Methane (CH_4) emissions of an exhaust gas sample can be determined using a non-methane cutter in combination with an FID. A non-methane cutter is a heated catalyst that removes any non-methane hydrocarbon from the exhaust sample before it is sent to the FID to measure the remaining methane concentration. The cutter relies on the difference in oxidation temperatures for methane compared to other larger non-methane hydrocarbons and targets a temperature to selectively combust the larger hydrocarbon chains, subsequently converting them to CO_2 and H_2O, which now pass through the FID undetected.

External EGR was also measured using the Horiba emissions analyser. An additional AIA-722 NDIR gas analyser is used to sample CO_2 concentration in the intake buffer tank of the engine. The simultaneous measurement of CO_2

concentration in the intake is compared against that in the exhaust by the following equation in order to determine volume-based EGR %:

$$EGR\ \% = \frac{CO2_{intake} - CO2_{atm}}{CO2_{exhaust} - CO2_{atm}} \tag{3.1}$$

Where $CO2_{intake}$ and $CO2_{exhaust}$ are the carbon dioxide concentrations in the inlet and exhaust manifolds respectively. $CO2_{atm}$ is the concentration in the atmospheric air.

All gaseous emissions taken from the Horiba analysers were measured with an error less than 1% of full scale or 2% of the reading, depending which is smaller. The repeatability of the sample readings were within 0.5% of full scale. Filters for the oven and analyser rack were inspected at the start of each test session for cleanliness. A heated pre-filter was used with the Horiba analyser during operation to limit the amount of soot sent to the oven, reducing the frequency of filter changes. The filter for the heated pre-filter unit was checked daily and cleaned when necessary.

Engine-out soot emissions were evaluated using an AVL Smokemeter 415SE. A known amount of exhaust gases were passed through clean filter paper, capturing soot in the process, blackening the filter paper. The blackening results in differing amounts of reflected light which is measured by a photoelectric measuring head. The output is converted to a 0-10 relative Filter Smoke Number (FSN), where 10 would be top of the scale for highest light absorption, meaning high levels of soot. Values obtained had a repeatability 1 σ ≤ ±0.005 FSN + 3 % of the measured value. The filter paper was checked for cleanliness and quantity before the start of each test session in order to ensure accuracy.

3.3 Data Analysis

Certain parameters computed by data acquisition signals, such as IMEP, ISFC, net heat release rate (HRR) and mass fraction burned (MFB), were processed in real-time by the transient combustion analyser software mentioned in Section 3.2.4. These parameters were essential for engine monitoring as well as for the subsequent data analysis; hence the equations and procedures behind attaining these values are laid out in this section. For clarity, the variables and acronyms used were defined in the notation section with the international system of units assumed unless otherwise stated.

3.3.1 Heat Release Analysis

Useful information such as the net heat release rate and mass fraction burned profiles can be derived from the in-cylinder pressure and crankshaft position measurements. A single-zone heat release model was employed where products and reactants are modelled as homogeneous. As a result, the heat added to the cylinder contents during combustion was able to be derived from the rise of in-cylinder pressure over the rise of pressure due to volume change. The combustion chamber can be modelled with Equation (3.2) representing the control volume boundary terms and is adapted from the first law of thermodynamics:

$$dQ_{ch} = dW + dU_s + dQ_{ht} + \sum h_i dm_i \tag{3.2}$$

(Q_{ch}) represents the chemical energy released by combustion, (dW) is the work done on the piston by the charge, (dU_s) is the sensible energy of the contents as a result of temperature change, and (Q_{ht}) is heat transfer to the chamber walls. The mass flux term ($h_i dm_i$) represents flow in and out of the control volume, such as fuel injection or flow from the crevice volumes of the cylinder. It should be noted that it was assumed there is uniform temperature throughout the combustion chamber and that the ideal gas constant does not vary. These assumptions allow for the formation of Equation (3.3) according to [10]:

$$dQ_{ch} = \left(\frac{c_v}{R}\right) V\, dP + \left(\frac{c_v}{R} + 1\right) p\, dV + dQ_{ht} + (h_{cr} - u + c_v T) dm_{cr} \tag{3.3}$$

Equation (3.3) can be simplified by combining the energy released term with the heat transfer and mass flux effects, resulting in the net heat release (Q_{net}). In this state, only the work performed on the piston and the sensible energy change in the gas are considered. Furthermore, dividing by the change in engine crank angle degree as well as assuming semi-perfect gas behaviour, allowing the term $\left(\frac{c_v}{R}\right)$ to be simplified to $\left(\frac{1}{\gamma-1}\right)$, Equation (3.3) becomes:

$$\frac{dQ_{net}}{d\theta} = \frac{\gamma}{\gamma-1} p \frac{dV}{d\theta} + \frac{1}{\gamma-1} V \frac{dp}{d\theta} \tag{3.4}$$

Equation (3.4) can now be used to calculate the instantaneous heat release rate by considering every 0.25 deg CA (encoder resolution) in conjunction with the measured in-cylinder pressure data. The ratio of specific heats (γ) was assumed constant at 1.33 throughout the entire engine cycle as suggested by [122], although it is known that this value changes with the mixture composition and temperature. The expected range of variation is discussed in detail in Section 4.2 and 4.3 of Chapter Four.

Mass fraction burned was estimated using the Rassweiler and Withrow method due to its simplicity and computational efficiency. In an identical manner to Equation (3.4), this process works on the assumption that a pressure rise (Δp) during a crank angle interval ($\Delta\theta$) is comprised of a pressure rise due to combustion (Δp_c) and a pressure rise due to volume change (Δp_v) as detailed in Equation (3.5):

$$\Delta p = \Delta p_c + \Delta p_v \tag{3.5}$$

As the initial crank angle (θ_i) increments to the next value (θ_{i+1}), the volume changes from V_{ins} to V_{ins+1}, and the pressure changes from p_i to p_{i+1}. This, combined with a simplifying assumption that Δp_v can be modelled by a polytropic relationship with a constant value of n, yields the following equation:

$$\Delta p_v = p_i \left[\left(\frac{V_{ins}}{V_{ins+1}}\right)^n - 1\right] \tag{3.6}$$

When combining Equations (3.5) and (3.6), Δp_c can be represented as:

$$\Delta p_c = p_{i+1} - p_i \left(\frac{V_{ins}}{V_{ins+1}}\right)^n \tag{3.7}$$

Where instantaneous in-cylinder volume (V_{ins}) can be represented by the following equation (3.8) [10]:

$$V_{ins} = V_{clr} + V_{clr} 0.5(R_c - 1)\left[\frac{2L}{S} + 1 - \cos\theta - \left(\left(\frac{2L}{S}\right)^2 - \sin^2\theta\right)^{\frac{1}{2}}\right] \tag{3.8}$$

In essence, the mass fraction burned describes the integration of Equation (3.4). A 5 point average smoothing filter was used to remove noise from the 300 cycle averaged HRR signal. As the Rassweiler and Withrow model cannot directly account for varying in-cylinder heat transfer and mass blow-by effects, the computations should only be considered in qualitative terms.

The Pressure Rise Rate (PRR) was a parameter used to help indicate how quickly the heat release process was taking place. It was expressed in bar/°CA and was calculated by correlating the instantaneous in-cylinder pressure to the crank angle position. A value of 10 bar/°CA was typically used as a production maximum (in terms of noise) with some of the experimental conditions exceeding this to determine the effect of higher PRRs. The magnitude of PRR for HD diesel engines typically range in the 10-15 bar/°CA range [99,123] and was confirmed based on internal diesel engine benchmarking against the Volvo D13 multi-cylinder engine. Excessive PRR is generally avoided due to engine durability as well as combustion noise reasons.

3.3.2 Overall Engine Parameters

In-cylinder pressure data of the engine operating cycle was plotted against volume to determine important analytical information. Integration of the pressure signal over the cylinder volume during compression and expansion cycles resulted in the indicated work per cycle ($W_{c,i}$):

$$W_{c,i} = \oint p \, dV \tag{3.9}$$

Moreover, indicated power (P_i) was expressed as the rate of work transfer from the gas within the cylinder to the piston [10]:

$$P_i = \frac{W_{c,i}N}{2} \tag{3.10}$$

In order to compare engines of different size, a useful engine performance metric is obtained by dividing Equation (3.9) by the displaced volume (V_d), resulting in Indicated Mean Effective Pressure (IMEP), as shown in Equation (3.11):

$$IMEP = \frac{W_{c,i}}{V_d} \tag{3.11}$$

It should also be noted that in a four-stroke cycle, two definitions of IMEP can arise. If work performed on the piston is considered over the compression and expansion strokes only, it is referred to as gross IMEP ($IMEP_{gross}$), as opposed to net IMEP ($IMEP_{net}$) where work is represented over the entire four-stroke cycle [10].

Insight into the combustion event cyclic variability during engine operation was achieved by comparing the standard deviation of the IMEP to its averaged value obtained over 300 cycles. This relationship can be expressed as the Coefficient Of Variation (COV) of IMEP:

$$COV_{IMEP} = \frac{IMEP_{std}}{IMEP_{average}} * 100 \tag{3.12}$$

In order to compare the relative performance of engines, it is occasionally useful to isolate the mechanical losses, particularly in single cylinder applications. As a result, indicated efficiency is a key value. Indicated efficiency is determined by calculating the ratio of the work done (or power in case of using the fuel flow rate) to the amount of energy supplied to the engine in fuel mass (or mass flow rate) multiplied by the fuel's Lower Heating Value (LHV_{fuel}), as shown in Equation (3.13).

$$\eta_i = \frac{W_{c,i}}{m_{fuel}LHV_{fuel}} = \frac{P_i}{\dot{m}_{fuel}LHV_{fuel}} \tag{3.13}$$

Finally, instantaneous in-cylinder volume was used to calculate the effective compression and expansion ratios. These related the volumes inside the cylinder at different stages during the compression and expansion process. The Effective Expansion Ratio (EER) was calculated by considering the ratio of the clearance volume to the volume at Exhaust Valve Opening (EVO) or Intake Valve Opening (IVO), whichever occurred earlier. Similarly, the Effective Compression Ratio (ECR) was calculated at Exhaust Valve Closing (EVC) or Intake Valve Closing (IVC), whichever occurred later. Both are denoted below:

$$EER = \frac{V_{ins\,EVO} + V_{clr}}{V_{clr}} \quad or \quad \frac{V_{ins\,IVO} + V_{clr}}{V_{clr}} \tag{3.14}$$

$$ECR = \frac{V_{ins\,EVC} + V_{clr}}{V_{clr}} \quad or \quad \frac{V_{ins\,IVC} + V_{clr}}{V_{clr}} \tag{3.15}$$

3.3.3 Engine-Out Emission Analysis

The emissions analyser provided emission results in the form of parts per million (ppm) to the data acquisition system. In order to relate these numbers to engine exhaust flow it was necessary to convert these values to g/kWh. This was performed in accordance with UN Regulation 49 [124]. The exhaust gases of CO and NOx were measured on a dry basis from the analyser equipment, but had to be converted to a wet basis in order to be compared. Furthermore, a humidity correction was applied to the NOx emissions to consider the dependence upon the ambient conditions. The individual exhaust gas concentrations (ppm) were multiplied by their appropriate fuel dependent molar mass fraction (u_{gas}), as presented in Table 3-4. Under dual-fuel operation, the u_{gas} values were blended based on the split of dual-fuel quantities used. Exhaust mass flow rate ($\dot{q}_{exh}$) was determined by the sum of the fuel and air mass flow rates.

$$ISCO = \frac{u_{CO}[CO]k_w\dot{q}_{exh}}{P_i} \tag{3.16}$$

$$ISNOx = \frac{u_{NOx}[NOx]k_w k_{hG}\dot{q}_{exh}}{P_i} \tag{3.17}$$

$$ISHC = \frac{u_{HC}[HC]\dot{q}_{exh}}{P_i} \tag{3.18}$$

$$ISCH4 = \frac{u_{CH4}[CH4]\dot{q}_{exh}}{P_i} \tag{3.19}$$

Table 3-4: Molar mass fractions of exhaust gases for diesel and CNG, adapted from [124]

Exhaust gas	u_{gas}	
	Diesel	CNG
CO	0.000966	0.000987
NOx	0.001586	0.001621
HC	0.000482	0.000528
CH4	0.000553	0.000565

The correction factor (k_w) was used to convert dry CO and NOx emissions to wet was dependent on the ambient conditions (recorded daily with laboratory barometer and thermometer) and the mass flow rates of fuel and air as displayed in Equation (3.20). The hydrogen (W_{ALF}) and oxygen (W_{EPS}) contents in the fuel (% mass) were also taken into account in the fuel specific factor (k_f):

$$k_w = 1.008\left(1 - \frac{1.2442H_a + 111.19W_{ALF}\left(\frac{\dot{m}_{fuel}}{\dot{m}_{dry\ air}}\right)}{773.4 + 1.2442H_a + 1000\left(\frac{\dot{m}_{fuel}}{\dot{m}_{dry\ air}}\right)k_f}\right) \tag{3.20}$$

$$k_f = 0.055594W_{ALF} + 0.0070046W_{EPS} \tag{3.21}$$

The NOx emissions required an additional correction with respect to the ambient humidity (H_a), so the factor k_{hG} was utilised:

$$k_{hG} = 0.6272 + 0.04403 H_a - 0.000862 {H_a}^2 \tag{3.22}$$

The term H_a was specified in grams of water per kilogram of dry air. As indicated in Equation (3.23), it remains a function of relative humidity (RH), water saturation pressure (SP), and ambient pressure (p_a):

$$H_a = \frac{6.211 * RH * SP}{p_a - \frac{(RH * SP)}{100}} \tag{3.23}$$

Finally, the water saturation pressure was estimated using the ambient temperature (T_a) and a polynomial regression [125] in order to avoid using a lookup-table operation:

$$\begin{aligned} SP = \ & 604.8346 + 45.9058(T_a - 273.15) + 1.2444(T_a - 273.15)^2 \\ & + 0.03522481(T_a - 273.15)^3 \\ & + 0.00009322061(T_a - 273.15)^4 \\ & + 0.000004181281(T_a - 273.15)^5 \end{aligned} \tag{3.24}$$

Soot emissions measurements could be expressed in mg/m^3 after being converted from FSN values using Equation (3.25) [126]:

$$smoke\ concentration = \frac{1}{0.405} * 5.32 * FSN * e^{0.31 * FSN} \tag{3.25}$$

Indicated specific soot emissions (ISSoot) were calculated from these values of soot in mg/m^3 as well as the fuel mass flow rate ($\dot{m}_{fuel}$), the air mass flow rate ($\dot{m}_{air}$), and the indicated power (P_i), as displayed in Equation (3.26):

$$ISSoot = \left(\frac{soot}{1000}\right)\left(\frac{\dot{m}_{fuel} + \dot{m}_{air}}{\rho_{ext} * P_i}\right) \tag{3.26}$$

Equation (3.27) depicts the density of the exhaust gas (ρ_{ext}) and was calculated in accordance with [124]. This took into account the fuel specific factor (k_f) and ambient humidity (H_a) as previously written in Equations (3.21) and (3.23), respectively.

$$\rho_{ext} = \frac{1000 + H_a + 1000\left(\frac{\dot{m}_{fuel}}{\dot{m}_{dry\ air}}\right)}{773.4 + 1.2434H_a + 1000k_f\left(\frac{\dot{m}_{fuel}}{\dot{m}_{dry\ air}}\right)} \tag{3.27}$$

The combustion efficiency was calculated by Equation (3.28). Essentially it relates the unburnt exhaust constituents to the total amount of fuel added in to the engine. The main combustible species found in the exhaust are CO and HC. The LHV value used for CO was 10.1 MJ/kg [10]. The LHV of HC in theory would contain LHVs for both diesel and CNG under dual-fuel operation, but was typically maintained at 49.9 MJ/kg. This was due to CNG being the most likely source of unburnt HC due to the way it was being introduced into the engine (MPFI) as well as the diesel fuel's nature of combustion yielding high combustion efficiency. The denominator terms were split into appropriate diesel/CNG ratios depending on if dual-fuel operation was selected.

$$\eta_c = 1 - \frac{\dot{m}_{CO}LHV_{CO} + \dot{m}_{HC}LHV_{HC}}{\dot{m}_{fuel}LHV_{fuel}} \tag{3.28}$$

The relative air/fuel ratio (λ) was calculated by the Brettschneider-Spindt algorithm, as referenced in [127]. This method solves a set of five equations to determine the coefficients for the combustion equation of a hydrocarbon fuel with air:

$$\begin{gathered} C_xH_yO_z + n(O_2 + A * N_2 + B * CO_2 + C * H_a * H_2O) \rightarrow \\ aCO_2 + bCO + cH_2 + dH_2O + eO_2 + fN_2 + gNO_X + hC_xH_yO_z \end{gathered} \tag{3.29}$$

Upon performing the carbon, hydrogen, oxygen, nitrogen, and total moles (n_{TOT}) balances in Equation (3.29), the following equations could be written with the concentrations of the exhaust emissions known prior:

$$a = [CO_2] * n_{TOT} \tag{3.30}$$

$$b = [CO] * n_{TOT} \tag{3.31}$$

$$c = \frac{y(1-h)}{2} + n * C * H_a - d \tag{3.32}$$

$$d = \frac{y(1-h) + 2n * C * H_a}{2\left(\frac{b}{a * K} + 1\right)} \tag{3.33}$$

$$e = [O_2] * n_{TOT} \tag{3.34}$$

$$f = n * A - \frac{g}{2} \tag{3.35}$$

$$g = [NO_X] \ * n_{TOT} \tag{3.36}$$

$$h = \frac{[HC] * (n_{TOT} + d)}{x} \tag{3.37}$$

$$n = \frac{2a + b + c + d + 2e + g + z(h-1)}{2 + 2B + C * H_a} \tag{3.38}$$

$$n_{TOT} = \frac{x + (B * n)}{[CO] + [CO_2] + [HC]} \tag{3.39}$$

The coefficients A, B, and C represented the nitrogen, carbon dioxide, and water vapour to oxygen ratio in the atmospheric air. The values of A, B, and C used were 3.774, 0.0014, and 0.0016 respectively, while a value of 3.5 represented the water-gas equilibrium constant (K), per [10]. The solution of equations (3.30) to (3.39) resulted in the number of air moles (n). The number air moles were divided by the number of moles required for stoichiometric air/fuel ratio combustion, which yielded the exhaust lambda shown in Equation (3.40):

$$\lambda_{exh} = \frac{n}{\left(x + \frac{y}{4} - \frac{z}{2}\right)} \tag{3.40}$$

3.4 Summary

Chapter 3 was about a comprehensive overview of the experimental test facility, the means by which data was gathered, and how the data was manipulated and used for analysis. Set out in Section 3.2 were details of all of the necessary hardware, software, and control information about the single cylinder research engine as well as the data acquisition methods. Detailed in Section 3.3 was the manipulation of the raw experimental data in both real-time and in post-processing. Overall engine parameters, heat release, as well as emissions data were summarised in this section and specified how all the data and graphs in subsequent chapters were calculated.

Chapter Four

Engine and Fuel Injector Validation

4.1 Introduction

Outlined in this chapter is a series of experiments that were performed in order to guarantee engine health and ensure collection of high quality data. First, the use of in-cylinder pressure data under motoring and firing conditions can aid in diagnosis of engine hardware throughout experimental testing and can serve as a way to confirm robust data collection. Specific attention was paid to the thermodynamic loss angle, polytropic indices (n), and in-cylinder pressure error minimization. Furthermore, benchmarking was undertaken to confirm the performance of the experimental test rig with respect to efficiency and emissions. Key variables were compared to an existing dual fuel engine in production in order to confirm the competitiveness of the combustion system used in the experiments. Finally, a diesel injector calibration was carried out in order to accurately determine how much fuel was being injected during the engine cycle. An added benefit was that injector delay could also be determined which was important to understanding exactly when fuel enters the combustion chamber.

4.2 Motored Engine Tests

In-cylinder pressure data captured under motoring conditions can be a useful tool in diagnosing engine health throughout testing. Monitoring of variables such as maximum motoring in-cylinder pressure and thermodynamic loss angle can be used to reveal issues with engine breathing, compression or even the in-cylinder pressure transducer or data acquisition system. Presented in Figure 4-1 is the recording of these two variables during engine testing while the data shown in Figure 4-2 is the expected steady degradation of motoring in-cylinder pressure with engine age. In both figures, each point represents an average of five engine cycles at approximately 850 RPM, under naturally aspirated conditions. Capturing more than five engine cycles was not possible due to the lack of motoring capability for the experimental rig, so the cycles were acquired on a transient basis using the inertia of the engine’s rotating mass to spin the engine. The maximum motoring cylinder pressure also changes with engine speed, further narrowing the useful range of data, the details of which are outlined in Appendix A – Maximum Motoring Cylinder Pressure Fluctuation with Engine Speed. The slow decline of engine speed after injection was stopped was enough time to capture semi-steady state motoring conditions.

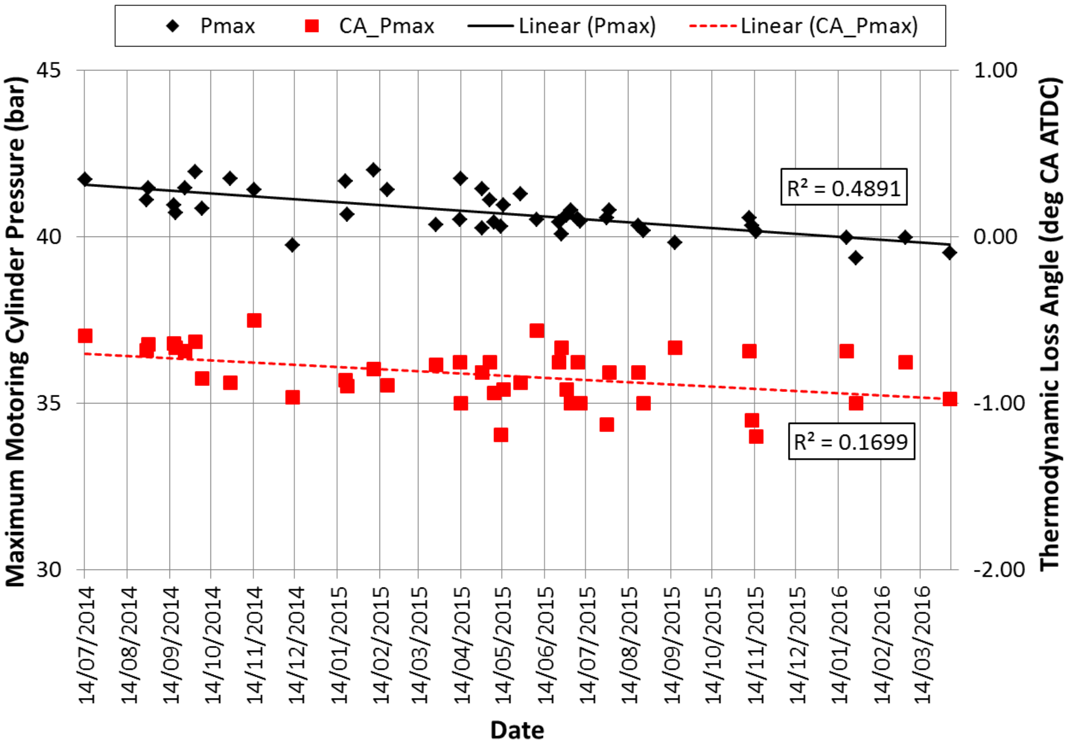

Figure 4-1: Maximum motoring in-cylinder pressure and thermodynamic loss angle logged during experimental testing at 850 RPM

As an engine accumulates running hours, a decline of maximum motoring cylinder pressure is typically observed due to decreased sealing effectiveness of the piston ring pack [128]. This is due to the piston rings wearing and not sealing as tightly against the cylinder bore, resulting in increased blow-by of the cylinder charge to the engine crankcase. A steady decline of maximum in-cylinder pressure is observed in Figure 4-1 and confirms that the engine did not have any abnormal issues with the compression or sealing of the engine. An abnormal case would likely result in a significant drop in motoring cylinder pressure rather than a slow, steady decline.

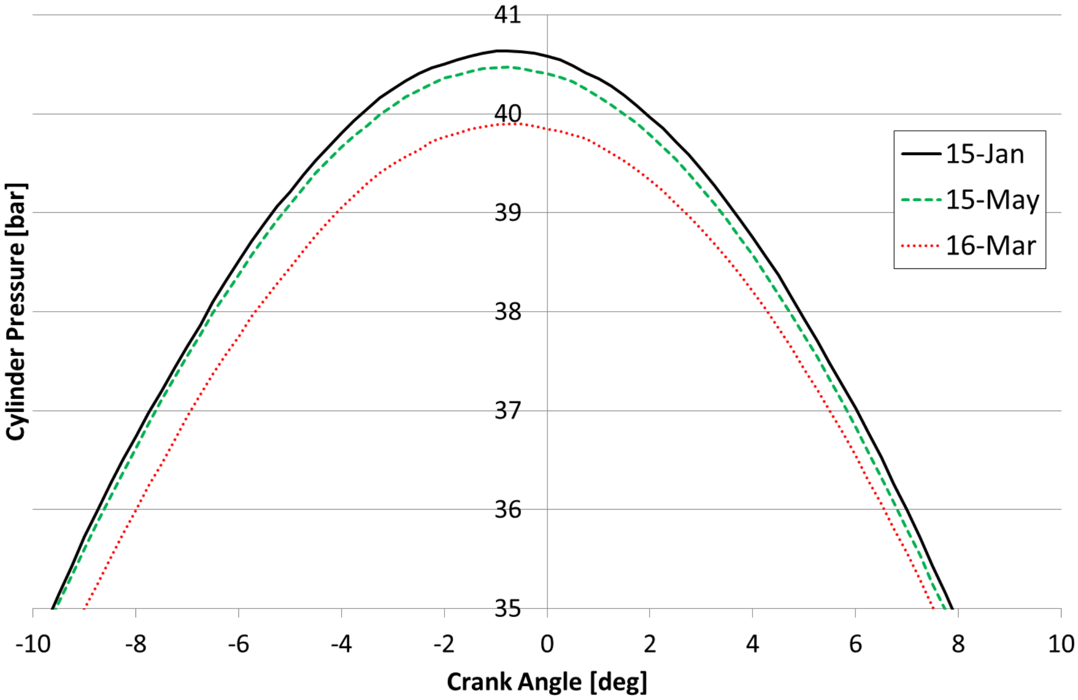

Figure 4-2: Degradation of maximum motoring in-cylinder pressure of the experimental test engine from January 2015 to March 2016

The difference in crank angle between the occurrence of geometric TDC and maximum motoring pressure is known as the thermodynamic loss angle. This value can be used to confirm the robustness of the in-cylinder pressure data. Typically, maximum motoring cylinder pressure occurs between 0.8 to 1.0 deg before TDC for large DI diesel engines and generally decreases with increasing engine speed [122]. The peak in-cylinder pressure occurs slightly before TDC because of heat loss and cylinder leakage. In the case of Figure 4-1, the values of thermodynamic loss angle occur in the expected range of approximately 0.6 to 1.0 deg before TDC, which help to ensure the phasing between the piston position and the recorded crank angle were done correctly. Initially, it is an assumption to set the thermodynamic loss angle at a specific value, as opposed to the dynamic TDC probe measurement technique where it is mechanically verified. However, if the phasing was not set correctly, it would result in incorrect motoring traces and polytropic indices, with a substantial knock-on effect for calculated parameters sensitive to this offset, such as IMEP.

The logarithmic p-V diagram can also be used for analysis of phasing and transducer performance. The relationship of pressure and volume during the compression and expansion processes of an engine can be described by the polytropic relationship pV^n = constant [122]. This relationship assumes no mass and energy transfer out of the cylinder system, so therefore it is calculated when the engine's valves are closed and no combustion is taking place. When plotting in-cylinder pressure and volume on a logarithmic scale, this would result in essentially straight lines of slope n for the compression and expansion strokes. Values of polytropic indices for diesel engines typically range from 1.3 to 1.37 [10,122]. These polytropic indices are useful to monitor because a departure from a straight line or slope values outside of the 1.3 to 1.37 window can mean potential issues with the in-cylinder pressure measurement equipment or even problems with the engine hardware. It should be noted however, that this relationship assumes minimal heat transfer and cylinder leakage. This means the value of n can vary with such things as engine speed, temperature, and charge composition [10,122].

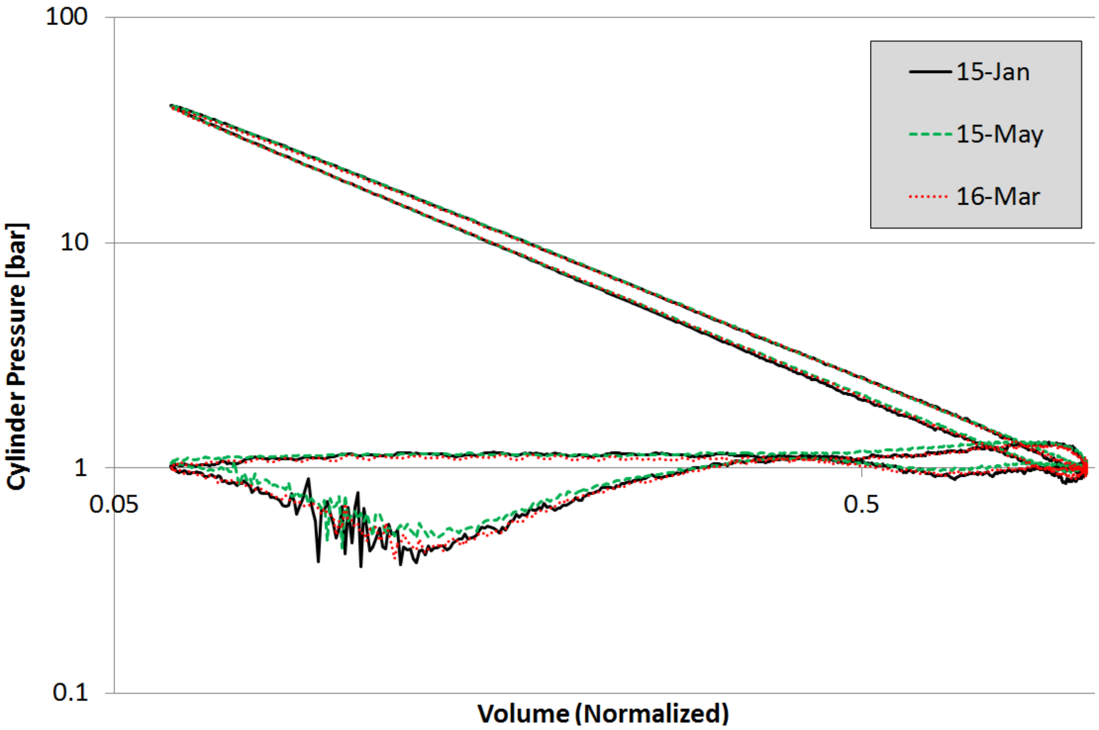

Figure 4-3: Logarithmic p-V diagram of motoring in-cylinder pressure against normalised cylinder volume at 850 RPM (Jan-2015 to March 2016)

Shown in Figure 4-3 are three motoring log p-V diagrams overlaid with one another, taken from three different periods during engine testing. Low-level noise across the entirety of the in-cylinder pressure signal was attenuated by the averaging of five engine cycles for the motoring reasons previously mentioned at the beginning of Section 4.2. The jagged saw-tooth shaped noise during the pumping loop, particularly pronounced for January 2015, is caused by the intake valve opening event. It is acceptable to ignore this noise in this specific situation since we are mainly interested in calculating the slopes of the compression and expansion process. Visual inspection of the logarithmic p-V loop reveals a satisfactory, repeatable shape of the in-cylinder pressure trace. The compression and expansion processes are close to straight lines, and there is no curvature, crossing, or looping of the signal which could point to issues with encoder phasing, transducer gains, or cylinder volume error. The values of the polytropic indices are calculated from the aforementioned p-V data and are displayed in Figure 4-4. The polytropic coefficient of compression and expansion were taken in the crank angle windows of -100 to -65 deg BTDC and 65 to 100 deg ATDC respectively. The values for compression and expansion fall within the acceptable range of 1.3 to 1.37, there by confirming the validity of engine data taken.

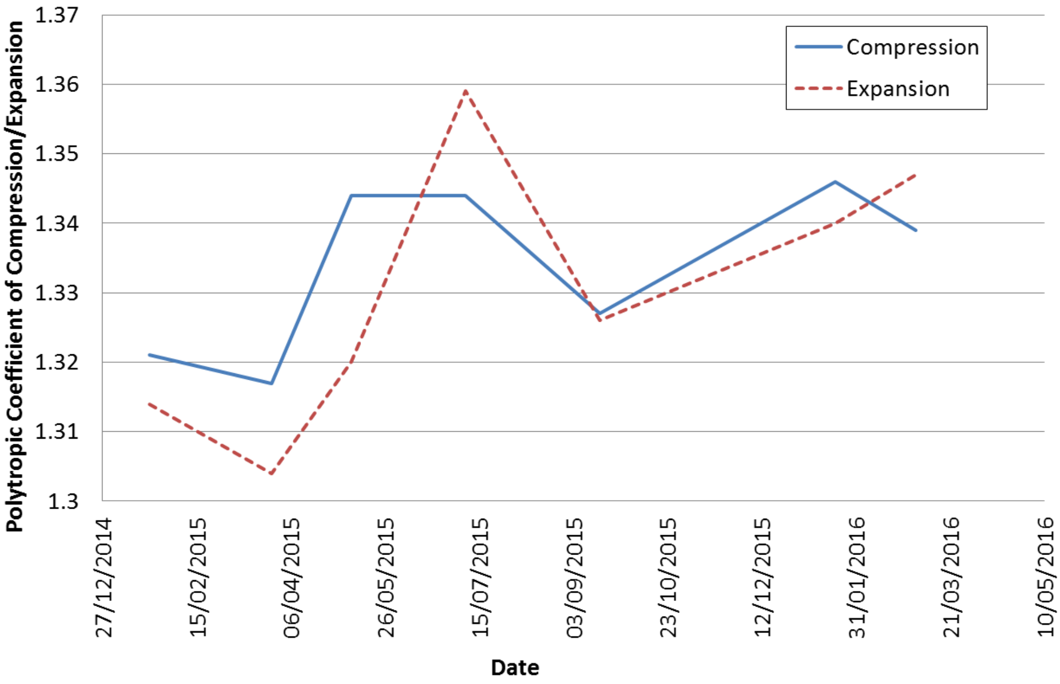

Figure 4-4: Polytropic coefficients of compression and expansion at 850 RPM

4.3 Firing Engine Tests

Engine cycles with combustion taking place can potentially introduce new sources of error compared to motoring conditions, so it is a conscientious approach to analyse these cycles to ensure quality. The data presented in Figure

4-5 are motoring and diesel-only firing in-cylinder pressure traces at 1200 RPM, 1.3 bar $IMEP_{net}$ (zero brake torque) conditions. The pressure traces are an average of 10 individual cycles in order to remove low-level noise and provide polytropic indices within ±0.5 standard deviation as shown in Appendix B – Firing Polytropic Coefficients of Compression and Expansion. The injector current signal for the firing cycles is also included in the figure to show the location of the diesel injection. The same data is depicted on a logarithmic scale in Figure 4-6.

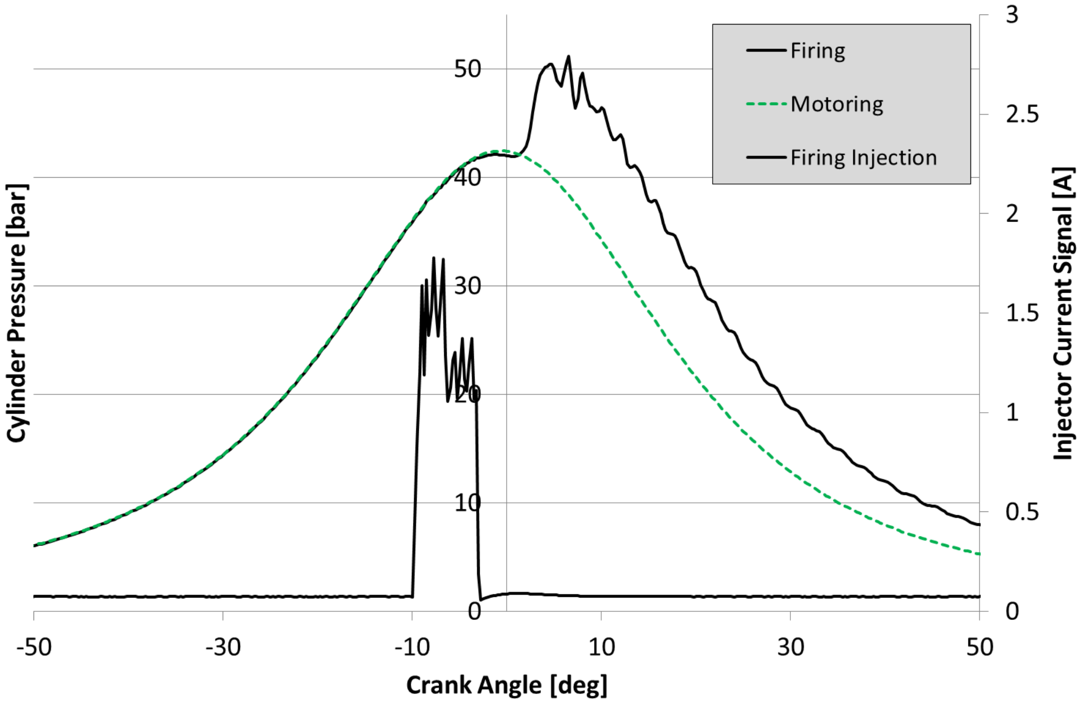

Figure 4-5: Motoring and firing in-cylinder pressure trace at 1200 RPM with diesel injector current signal imposed

It can be observed in Figure 4-5 that the firing and motoring traces are essentially identical until the injection of diesel fuel occurs at 10 deg before TDC. At this point, the in-cylinder pressure of the firing cycle slightly decreases compared to the motoring cycle due to the cooling effect of the diesel fuel injected. As expected, a sharp divergence in the in-cylinder pressure occurs between firing and motoring cycles as the fuel is combusted. The shape of this is important as this is a key assumption for the heat release and mass fraction burned calculations, as outlined in Chapter Three. Additionally, slight diesel ringing can also be observed in the firing pressure trace from 5 deg after TDC. In ringing combustion, a sudden conversion of large parts of the fresh charge excites the entire cylinder charge, causing it to oscillate at a high frequency corresponding to the local speed of sound [129]. Oscillating with a frequency of approximately 4 to 6 kHz, it can be confirmed that this is indeed diesel ringing across the bowl rather than another form of resonance or issue with the pressure measurement hardware.

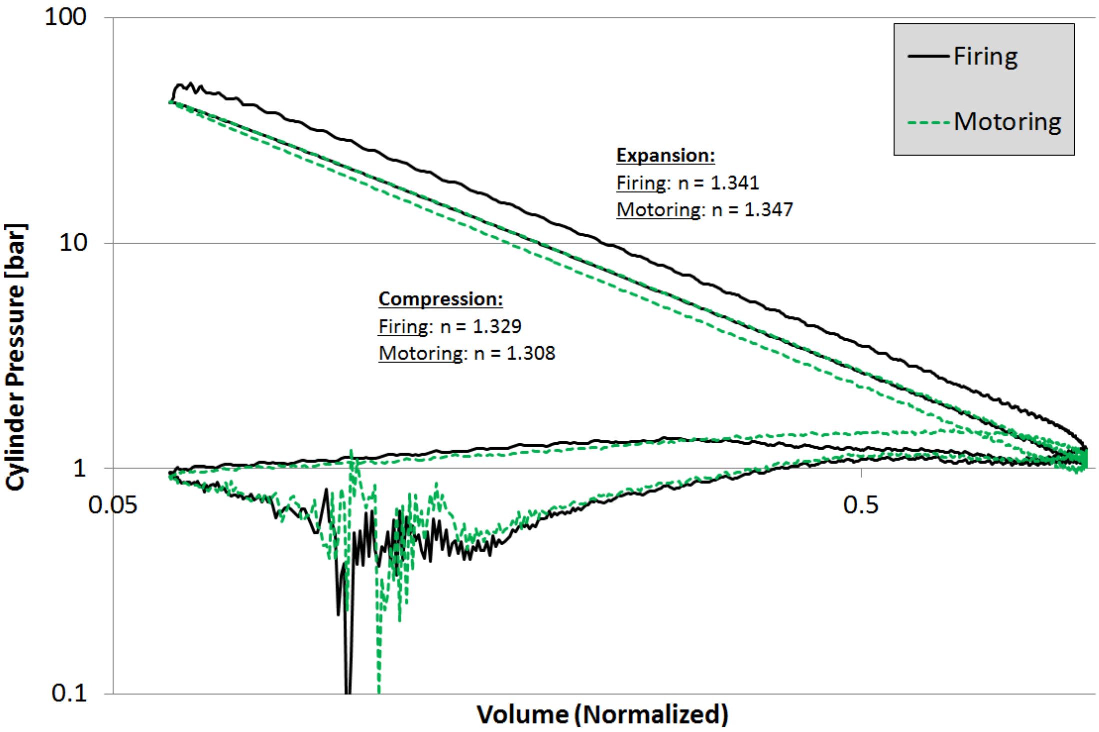

Figure 4-6: Logarithmic p-V diagram of motoring and firing in-cylinder pressure trace at 1200 RPM

The logarithmic format of Figure 4-6 allows observation of the polytropic indices of compression and expansion (calculated from the same crank angle windows as mentioned in Section 4.2). The values of the indices fall within the acceptable range of 1.3 to 1.37, but are slightly altered due to the different heat transfer conditions being imposed on the in-cylinder charge. Firing conditions yield higher polytropic values during compression because there is heat transfer to the cylinder charge from the engine metal, which is hot from the previous cycles, resulting in a higher in-cylinder pressure. For motoring, the opposite heat transfer path occurs during compression where heat is removed from the charge by the metal of the engine, which reduces the in-cylinder pressure yielding a lower polytropic value. Polytropic values for expansion would also differ from compression due to changes in charge composition and temperature.

The pumping loop is also subject to noise caused by intake valve event in both motoring and firing cases. This error, as well as other low-level noise, is minimised during experimental testing by taking 300 cycles of engine data to average out the saw-tooth noise effects [130]. Reducing noise via the in-cylinder pressure amplifier was also investigated, as it is possible to change the upper cut-off frequency of the low-pass filter. The effects of the different filter settings can be observed in Figure 4-7 and Figure 4-8. The figures include upper cut-off frequencies of 2, 10, and 100 kHz on a firing diesel case at 1200 RPM and 5 bar IMEP$_{net}$ for an average of 100 cycles, which is the largest number of cycles that could be collected for a given data acquisition window at one time. The 100 kHz filter would allow the highest amount of measured frequencies to pass, but is subject to high frequency noise. The lower filter numbers like 2 and 10 kHz attenuate this noise, caused by valve closure for example, but change the shape of the pressure signal in doing so. This could have implications on other values calculated from the in-cylinder pressure, such as IMEP and PMEP, so a value of 100 kHz was maintained.

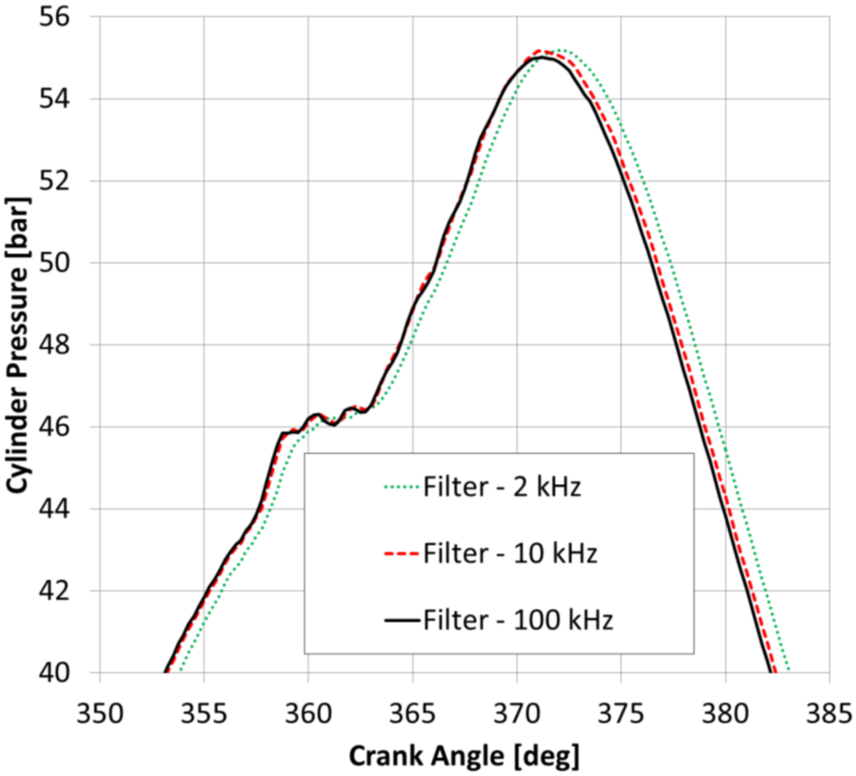

Figure 4-7: Peak in-cylinder pressure for 1200 RPM 5 bar IMEP$_{net}$ for three different cut-off frequencies of low pass filter

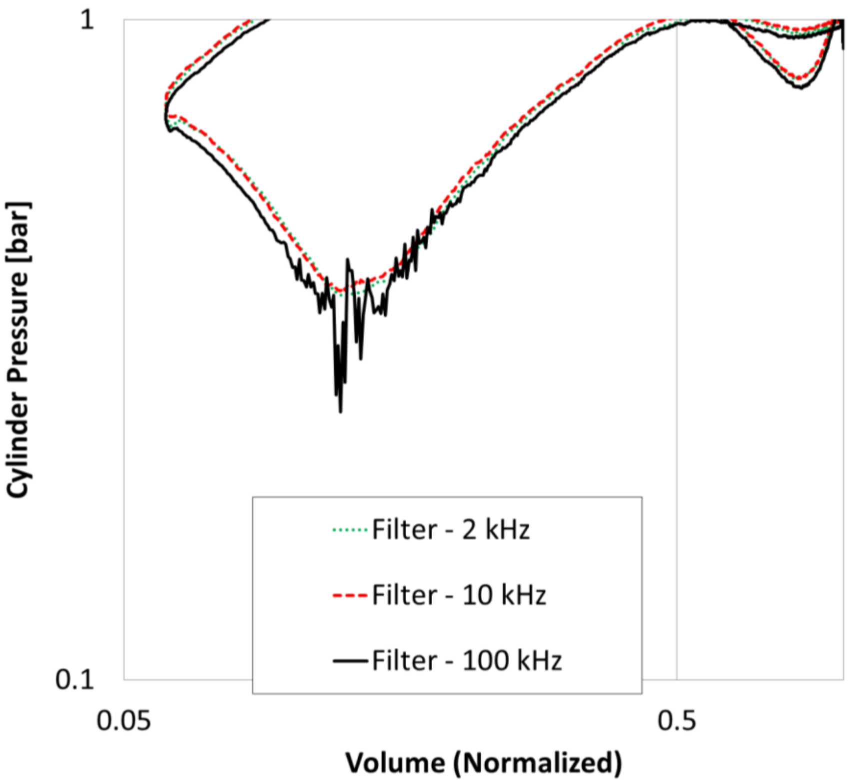

Figure 4-8: Pumping loop focused in-cylinder pressure for 1200 RPM 5 bar IMEP$_{net}$ for three different cut-off frequencies of low pass filter

Nozzle hole coking of a diesel injector is a potential issue that needs to be avoided, particularly in alternative fuel engines such as the one used in these tests. High injector tip temperatures are more likely to be experienced with alternative dual fuel engines, as there is less tip cooling available due to the reduced diesel quantity used. High temperature in the injector nozzle tip is known to accelerate nozzle coking [131]. Deposits, especially in the injector holes, significantly reduce the spray quality, leading to higher fuel consumption, deteriorated combustion, and increased exhaust emissions [132–134]. If coking was present, inconsistent fuel delivery and atomization would result, manifesting in the form of increased COV of IMEP and emissions. Therefore, in order to ensure injector health, COV of IMEP percentage values were monitored to values less than 3% in diesel operation and values of hydrocarbon and CO emissions were noted and tracked for day-to-day consistency.

4.4 Combustion System Benchmarking

The experimental rig used in this work was mainly a conventional diesel combustion system except with respect to the fuel injector and piston shape. Due to the diesel injector being slightly smaller in flow rate specification when compared to engines of similar displacement, and with the piston having a unique plume split topography, it was worthwhile to compare this experimental combustion system with a known engine. This is to understand whether the overall efficiency and emissions of the experimental engine are drastically different to that of an engine in mass production.

The engine chosen for benchmarking is an EPA10 emissions compliant Volvo D13. It is a 12.8L multi-cylinder inline-6 with a compression ratio of 16.0 and a bore/stroke of 131/158mm respectively [135]. The engine is very similar in hardware specification to the experimental test rig with the exception that the Euro V homologated D13 lacked common rail fuel injection. This D13 instead employs dual solenoid electronic unit injectors, which are mechanically driven off of the engine. In lieu of this hardware difference, the injection pressures might vary slightly between the two engines, but due to rail pressure being a secondary effect for the variables that were benchmarked, it was still deemed acceptable to compare the two combustion systems.

The key variables compared were indicated specific fuel consumption (ISFC) and indicated specific emissions of nitrogen oxides, carbon monoxide, and hydrocarbon (ISNOx, ISCO, and ISHC respectively).

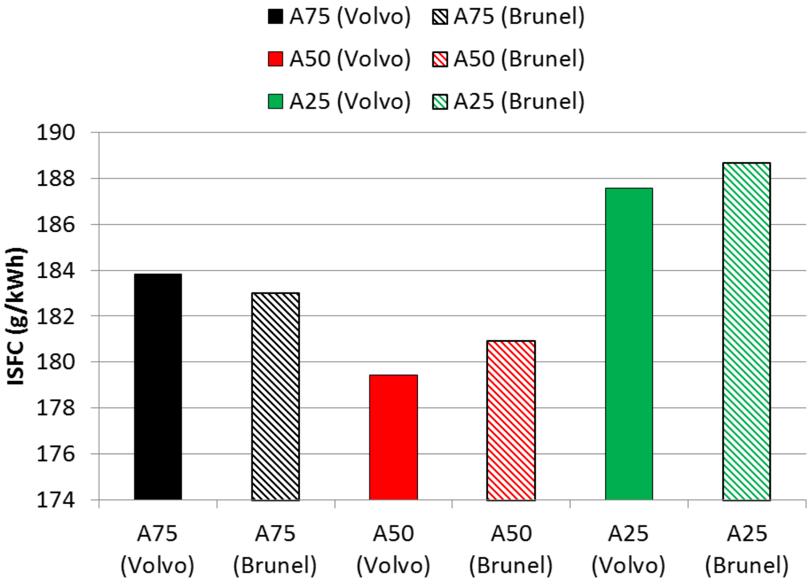

Figure 4-9: Indicated specific fuel consumption of the Volvo and Brunel engine for 6, 12, and 17 bar IMEP$_{net}$ at 1200 RPM

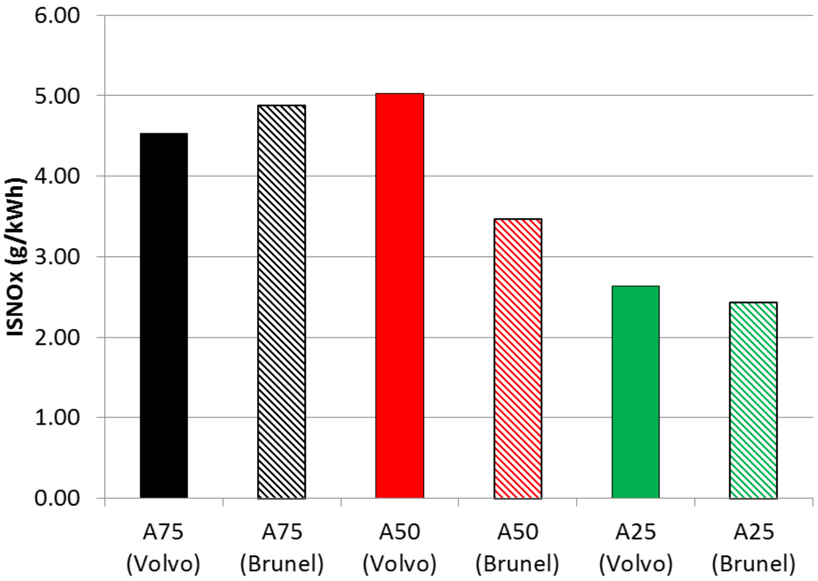

Figure 4-10: Engine-out ISNOx emissions of the Volvo and Brunel engine for 6, 12, and 17 bar IMEP$_{net}$ at 1200 RPM

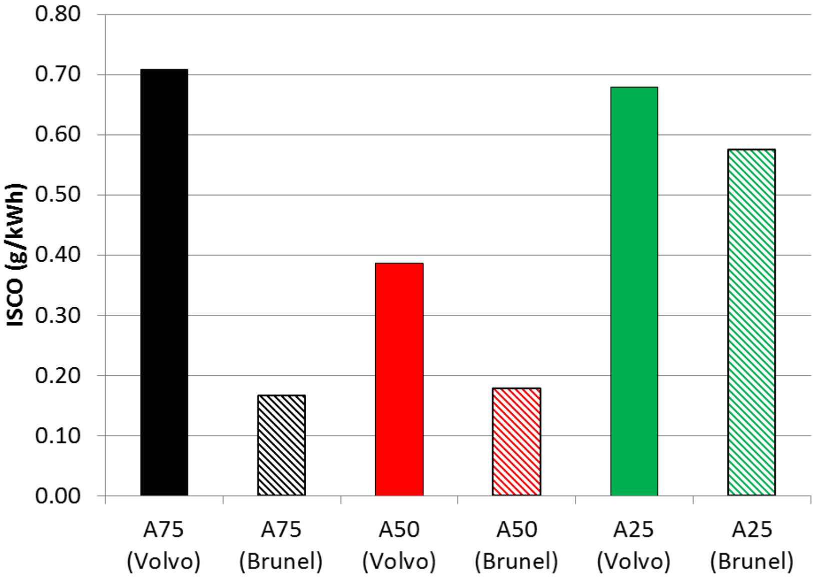

Figure 4-11: Engine-out ISCO emissions of the Volvo and Brunel engine for 6, 12, and 17 bar $IMEP_{net}$ at 1200 RPM

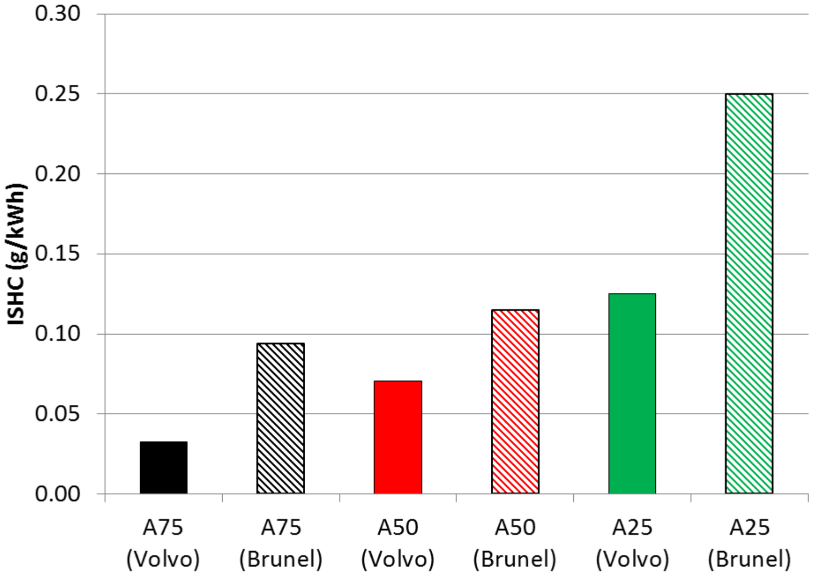

Figure 4-12: Engine-out ISHC emissions of the Volvo and Brunel engine for 6, 12, and 17 bar $IMEP_{net}$ at 1200 RPM

Three different loads of 6, 12, and 17 bar $IMEP_{net}$ were compared at 1200 RPM and are denoted as A25 (6 bar), A50 (12 bar), and A75 (17 bar). The solid bars represent Volvo D13 data and the striped the experimental test engine at Brunel. These graphs can be observed in Figure 4-9, Figure 4-10, Figure 4-11, and Figure 4-12.

ISFC values compared between the two engines are within 1% of one another for similar calibrations, so it can be concluded that the injector is functioning correctly and that the engine’s effectively converting the fuel energy into work. The trends with load are also consistent with a typical diesel efficiency map. Light load efficiency is compromised due to higher relative heat transfer and lower gas exchange efficiency for a given load, while higher load is compromised due to pressure rise rate and emissions limitations. Approximately the same engine-out ISNOx emissions levels were achieved between the two engines in Figure 4-10. Finally, engine-out ISCO and ISHC emissions were slightly different between the two engines, likely due to the hardware differences of unit and common rail diesel injection. However, macroscopically, the benchmarked emissions of the experimental engine are on approximately the same level as the Volvo D13. This helps to confirm that there is no major issue with the diesel injector or the way the diesel plume is introduced into the combustion chamber, especially involving spray impingement.

4.5 Diesel Fuel Injector Calibration

A diesel injector calibration was performed in order to quantify the amount of fuel injected for a given energizing time and rail pressure. This is important in accurately determining how much fuel is being injected per engine cycle, particularly when dealing with more than one diesel injection. Additionally, due to the experimental methodology, injector delay can also be determined which is necessary in understanding exactly when the fuel enters the combustion chamber. Finally, determining the effect of common rail pressure waves on subsequent diesel injections was important to explore, due to the variation of fuel delivered as a result of rail pressure fluctuation.

4.5.1 Experimental Setup and Methodology

The “Cup Method” and “Zeuch’s Method” were the two measurement techniques utilised for the diesel injector calibration. The goal of a calibration is to quantifying the relationship of injected fuel mass, energizing time, and rail pressure. In order to minimize hardware differences, the fuel system is identical to how it will be when the engine is performing experimental tests with the injector installed. Specifically, the same high-pressure pump, fuel rail, and fuel supply pipe to the injector was used to minimize any potential error.

The first method, named the “Cup Method,” injects diesel fuel into a semi-enclosed container for a known number of injection cycles. After a quantity of fuel is accumulated in the cup, it is weighed using a high sensitivity gravimetric scale. The total measured fuel mass is then divided by the known number of injections to determine the fuel quantity of a single injection. However, certain inaccuracies arise using this method, including error from fuel escaping or atomizing out of the small hole in the top of the container, or fuel remaining on the surface of the injector nozzle and enclosure. Moreover, a large number of injections (i.e. 1000) need to be taken for very small fuel quantities, increasing the potential for measurement error. The experimental setup of the Cup Method is shown in Figure 4-13.

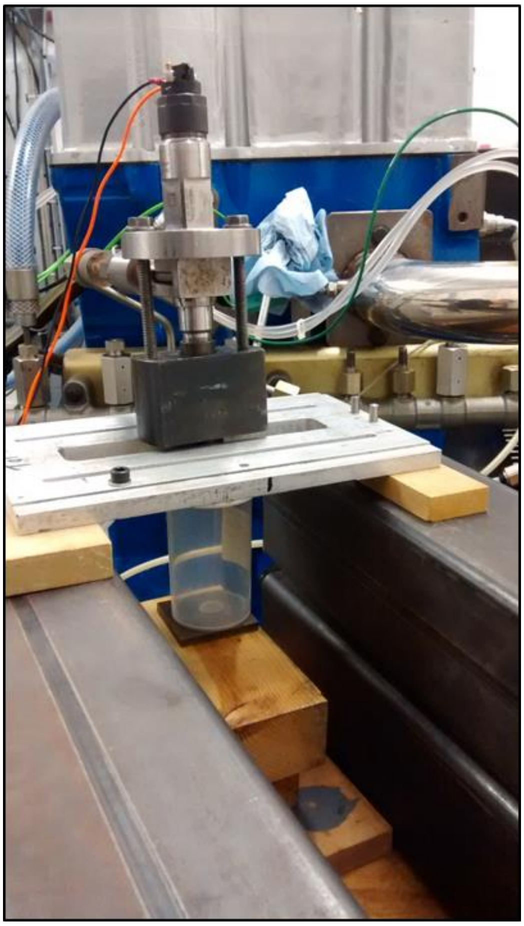

Figure 4-13: “Cup Method” experimental setup consisting of diesel fuel injector, mounting, and container

In order to address the shortcomings of the Cup Method, an alternative method was adopted. “Zeuch’s Method” is a known way of precisely measuring diesel fuel quantities based on pressure changes inside of a constant-volume chamber [136,137]. The measurement principle is based on whether fuel is injected into a constant-volume chamber filled entirely with fuel, the pressure inside the chamber would increase proportionally with the quantity of the fuel injected. Equation (4.1) describes this relationship.

$$\Delta P = k\frac{\Delta V}{V} \tag{4.1}$$

The equation describes an increase in pressure ΔP, when a fuel volume of ΔV is injected into a constant volume chamber of volume V. For these specific tests, volume V is 58 cm^3. The bulk modulus of fuel is defined as k. With this relationship, it is possible to differentiate Equation (4.1) with respect to time to obtain the fuel injection rate dV/dt as described by Equation (4.2),

.

$$\frac{dV}{dt} = \frac{V}{k}\frac{dP}{dt} \tag{4.2}$$

where t is the duration of the injection.

The bulk modulus of elasticity of the fuel needs to be taken into special consideration during the calibration because the volume of a fluid changes with the pressure that is applied to it. In order to obtain an accurate result, the bulk modulus of the laboratory diesel was tested in a compression test machine which resulted in a relationship of strain versus the applied force. From this it is possible to obtain the bulk modulus with respect to applied pressure to the fluid.

Depicted in Figure 4-14 is the experimental setup of Zeuch’s Method. Notable points are the constant volume chamber with the mounting of the diesel injector and pressure sensors. One of the pressure sensors is a piezo-resistive absolute pressure sensor (Kistler 4043A50) and is used to measure the starting backpressure of the chamber.

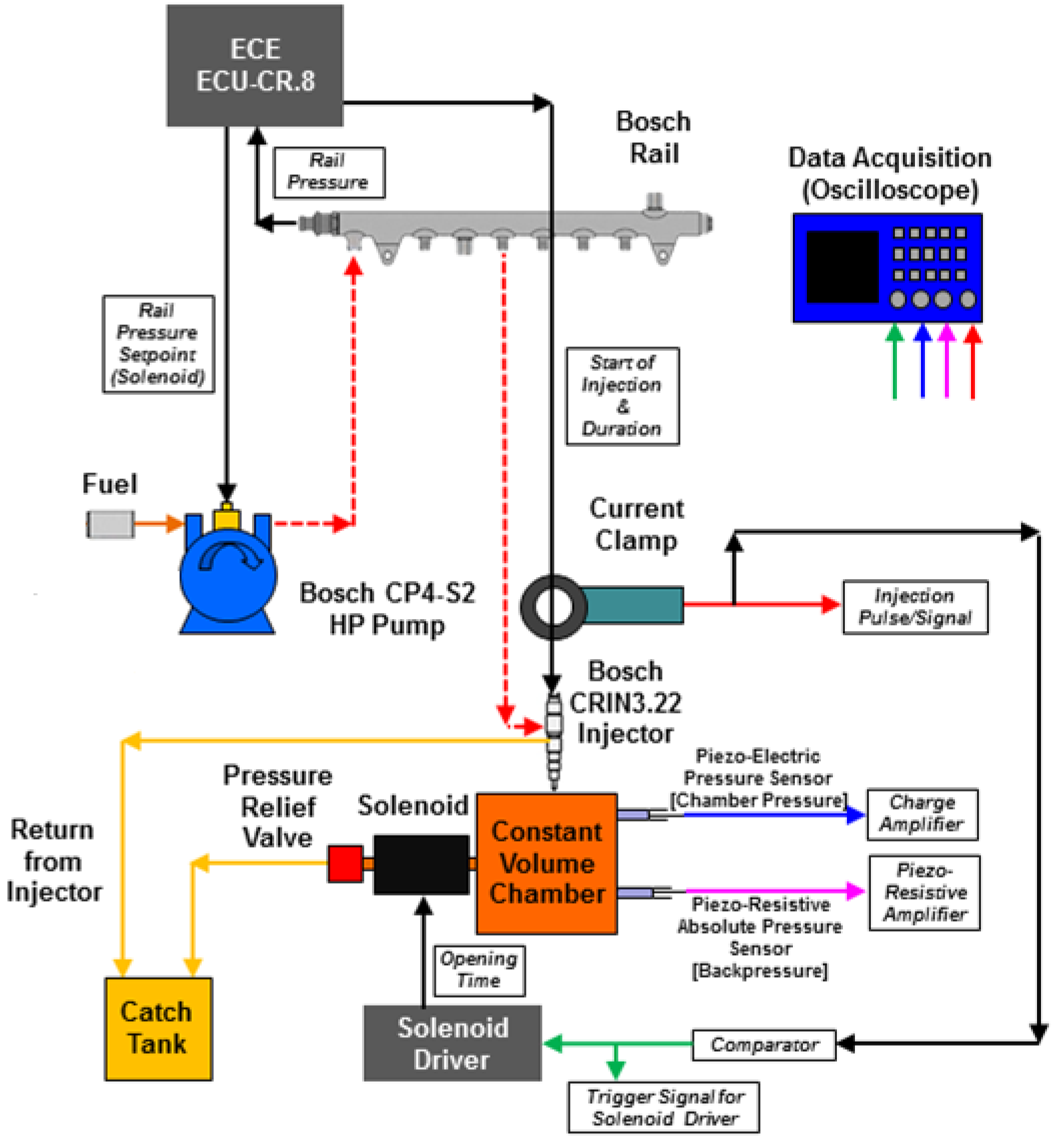

Figure 4-14: Schematic diagram of “Zeuch’s Method”

A piezo-electric pressure sensor (Kistler 701A) with a different range and more accurate measurement capability is mounted beside the piezo-resistive. It is important to have the piezo-resistive for reference as piezo-electric sensors are only able to measure differences in pressure rather than absolute values. Finally, after each injection cycle, a solenoid controlled by a comparator driven off of the diesel injection signal relieves the pressure in the chamber. An oscilloscope was used for data acquisition of all the necessary signals. Leakage tests were performed to ensure no fuel leaked out of the chamber or any of the orifices in order to guarantee accurate fuel measurement. The test plan consisted of a sweep of rail pressures performed for different injector energizing times.

4.5.2 Injector Calibration and Injector Delay

Six different fuel rail pressures were investigated using the Cup and Zeuch calibration methods. A sweep of injector energizing time yields the results shown in Figure 4-15. As expected, higher fuel rail pressures result in a larger volume of fuel injected for a given energizing time due to a greater pressure force increasing the flow rate of the fuel exiting the injector holes. The shape of the curves begin to flatten with larger values of energizing time due to the hydraulic diameter of the injector holes becoming the dominant factor dictating flow volume.

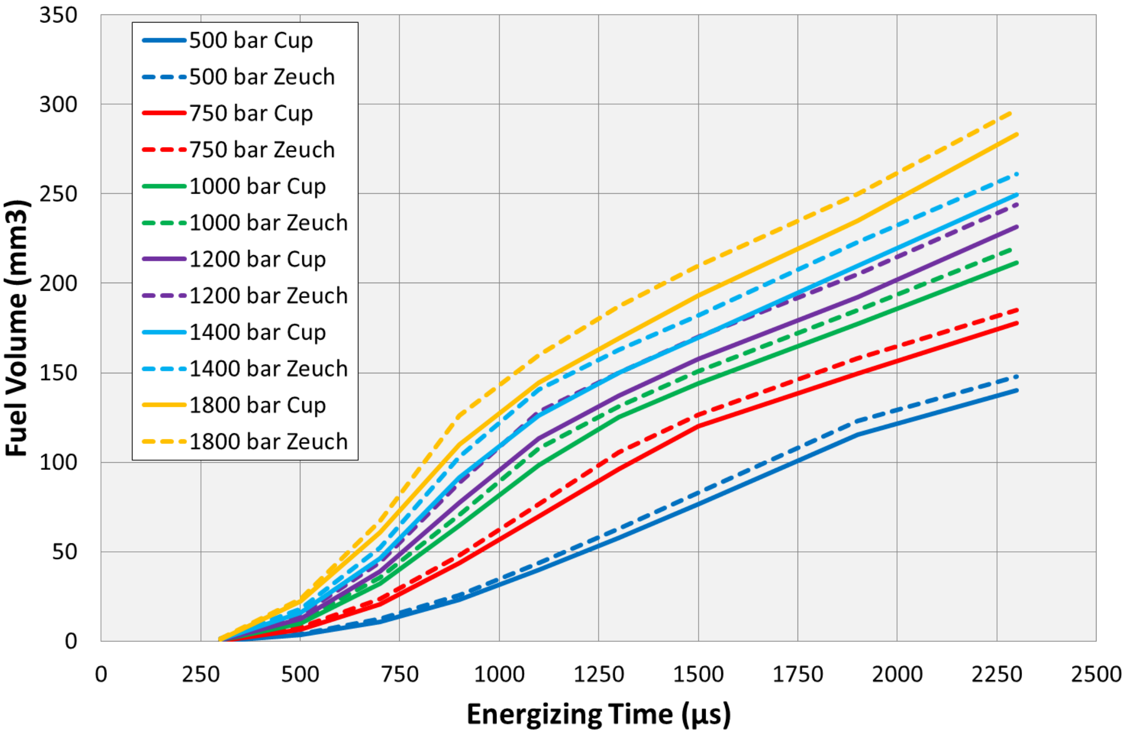

Figure 4-15: Fuel volume injected against energizing time and fuel pressure for Cup and Zeuch methods

The shortcoming of the Cup Method is clearly depicted in Figure 4-15 where Zeuch's Method consistently resulted in more fuel injected, especially when considering higher fuel rail pressures. This is likely due to fuel atomizing in the air in the container and escaping out of the small opening in the top, or fuel remaining on the surface of the injector nozzle and enclosure when the container was removed to be weighed. The final values entered into the engine ECU and used for the future experimental tests are shown in Table 4-1.

Table 4-1: Tabular results of Zeuch's Method used in the experimental engine ECU

Zeuch's Method Fuel Volume (mm3)						
	500 Bar	**750 Bar**	**1000 Bar**	**1200 Bar**	**1400 Bar**	**1800 Bar**
300 µs	0.2	0.6	0.9	1.2	1.5	1.5
500 µs	4	8	12	15	18	23
700 µs	13	23	36	44	52	67
900 µs	26	48	71	88	103	126
1100 µs	44	77	108	128	141	160
1300 µs	63	105	131	150	163	187
1500 µs	83	127	151	170	182	210
1900 µs	123	158	185	205	223	250
2300 µs	148	185	220	244	261	297

Measurement error was assessed for Zeuch's Method by performing three individual injection trials and calculating the percent error based on (Max – Min) / Mean. As expected, the smallest energizing time of 300 µs resulted in the highest percent error on average of 4.4%. This is due to the relatively small amount of fuel being injected, so it causes a very small change in chamber pressure, increasing the chances of measurement error. However, the error and repeatability of fuel volume measurement quickly improves with increasing energizing time and is very good at higher fuel flow rates. Error decreased to 2.9% for 500 µs and 1.5% for 900 µs, before settling to around 0.6% error for 1300 µs and beyond.

As previously alluded, it is possible to determine fuel injector delay using the data from Zeuch's Method. The definition of injector delay in this instance is the time it takes (in µs) for the SOI to occur after the injector solenoid receives an energizing signal from the ECU. Alternatively, it can be described as how long it takes the fuel injector needle to open to allow fuel to start flowing out of the holes of the injector. This is an important piece of information later when calculating ignition delay during experimental testing.

Shown in Figure 4-16 is an example of the data used for calculating injector delay. This particular case is for a fuel rail pressure of 1200 bar and shows a test for four different injector energizing times. The start of the injector signals were kept constant (starting at approximately 2750 µs) and the resulting rise in chamber pressure (approximately 3100 µs) would allow the injector delay to be calculated. Table 4-2 is the relationship between rail pressure and different units of measured injector delay.

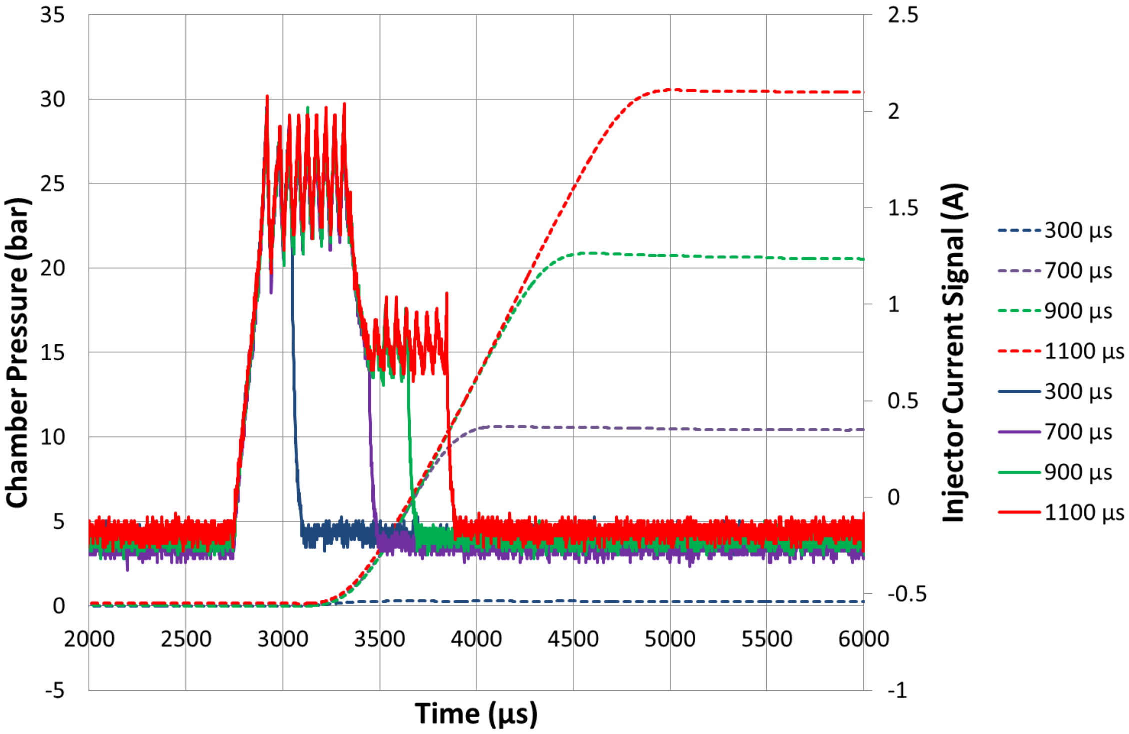

Figure 4-16: Chamber pressure (dashed) and current clamp signal (solid) against time for 1200 bar rail pressure

Table 4-2: Measured injector delay with fuel rail pressure

Rail Pressure	Measured Injector Delay		
bar	µs	ms	CA Deg @ 1200 RPM
500	406	0.406	2.923
750	364	0.364	2.621
900	358	0.358	2.578
1000	354	0.354	2.549
1100	349	0.349	2.513
1200	344	0.344	2.477
1400	344	0.344	2.477
1800	344	0.344	2.477

Energizing time has no measurable effect on injector delay, as results yielded similar values. However, the higher the fuel rail pressure tended to decrease the injector delay as the pressure of the fuel supplied to the injector plays a role in providing the mechanical force needed to move the fuel injector needle.

4.5.3 Common Rail Pressure Waves

Zeuch’s Method can also be used to observe the effect of a pilot injection on the amount of fuel delivered by the main injection. This information is useful to help understand the limits of dwell time between injections and to what extent the injector calibration can be used to determine the amount of fuel being injected. The premise is that, after a pilot injection is completed, the injector needle closes and the sudden stoppage of fuel flow results in a pressure wave sent back through the fuel supply piping and fuel rail. The pressure waves reflect and cause oscillations in the pressure of the fuel being supplied to the injector during the main injection. This is a potential problem if determining fuel quantity is reliant on the fuel injector calibration because different amounts of fuel would be injected for a constant energizing time. Sensitivity of this effect was explored by performing an experiment of four different pilot amounts for varying dwell values between the pilot and main injections. Two cases are displayed in Figure 4-17 and Figure 4-18. The test matrix and results are depicted in Table 4-3.

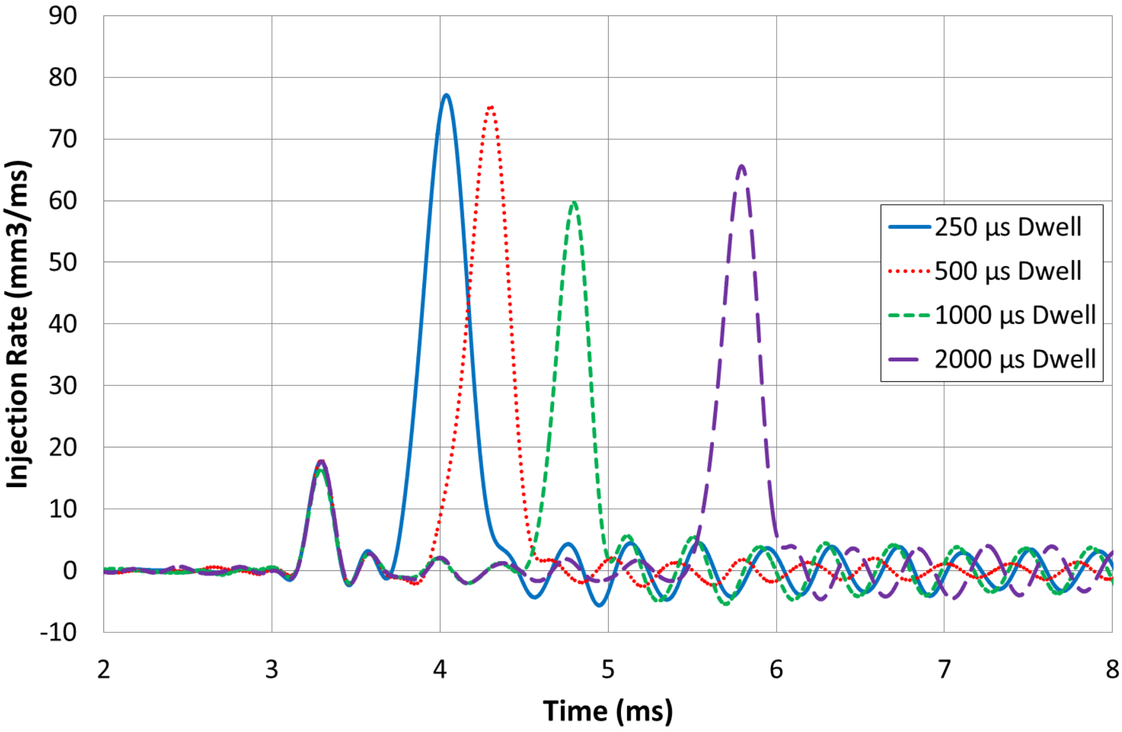

Figure 4-17: Injection rate profiles for 356/505 µs split injection case at 1200 bar rail pressure

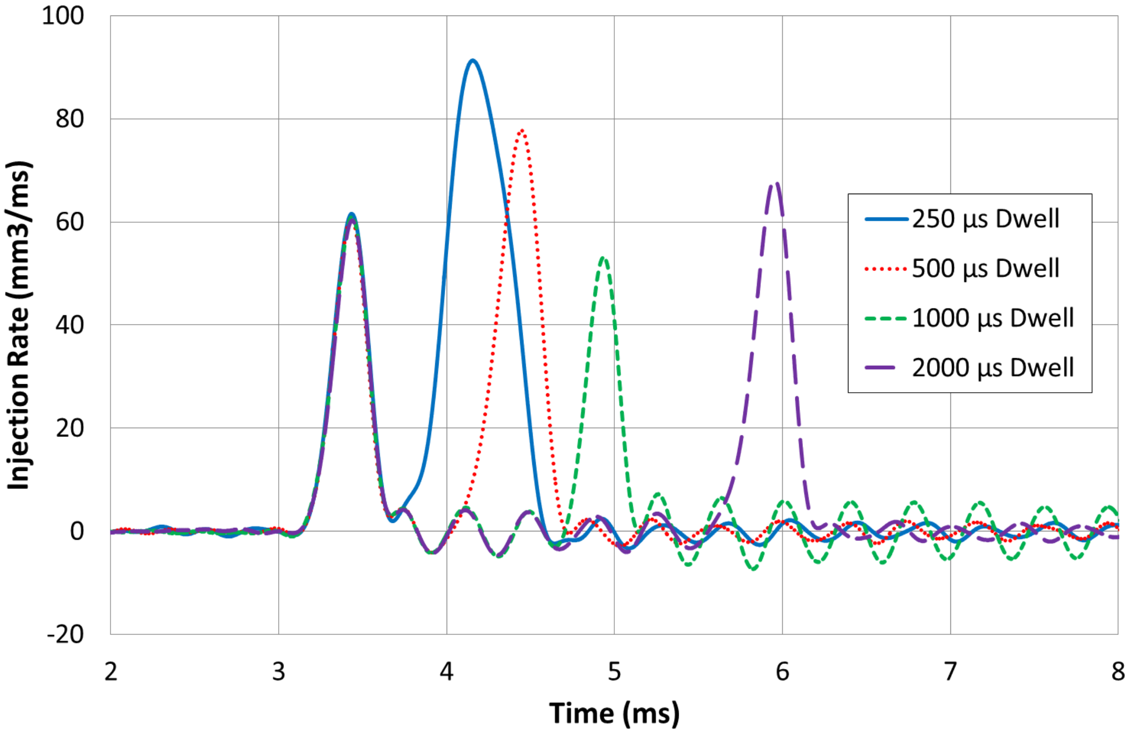

Figure 4-18: Injection rate profiles for 505/505 µs split injection case at 1200 bar rail pressure

Table 4-3: Measured fuel volume of pilot and main injections for different pilot energizing times and dwell between injections

Dwell Between Pilot & Main	Pilot Energizing Time	Measured Fuel Volume	
		Pilot	Main (constant 505 µs)
µs	µs	mm3	mm3
150	311	1.5	35.2
250	311	1.4	22.5
500	311	1.5	22.7
1000	311	1.5	16.1
250	356	2.7	24.2
500	356	2.8	22.8
1000	356	2.5	14.6
2000	356	2.7	17.6
250	430	8.3	29.6
500	430	8.5	24.3
1000	430	8.1	13.4
2000	430	8.4	18.8
250	505	15.4	40.5
500	505	15.1	23.4
1000	505	15.5	11.5
2000	505	15.3	18.3

It can be observed that for different dwell times, the pilot injection amounts are consistent in fuel injection rate, due to the quiescent state of the fuel system prior to the injection. However, there are large variations in the injection rates of the main injection and result in a wide disparity of fuel quantity delivered. The effect is non-linear and suggests that either higher or lower fuel injection quantities might result depending on the phasing of the pressure oscillations in the fuel system. The smallest values of dwell yield the highest over fuelling amounts which suggest that the magnitude of the pressure oscillations dampen with time. This theory can be confirmed in future work by installing a pressure transducer in the fuel rail pipe to directly measure the timing and magnitude of the fuel pressure waves. It can be confirmed this phenomenon is a function of pilot injection quantity, but is also likely a function of rail pressure. While not much can be done to prevent this occurrence from happening, consideration can be taken to avoid very closely coupled diesel injections for future engine tests if known fuel quantities per injection are essential.

4.6 Summary

The purpose of this chapter was to outline the approach taken in guaranteeing engine health as well as ensuring the collection of high quality data. It also helped to demonstrate that the experimental engine hardware was of suitable calibre to be a starting point of dual-fuel combustion optimisation.

In the first two sections, in-cylinder pressure data was collected and analysed under motoring and firing conditions and could be used to diagnose any potential issues with the engine as well as the cylinder pressure measurement hardware. Under motoring conditions, maximum motoring cylinder pressure was monitored throughout the duration of testing, demonstrating the sealing and compression robustness of the engine. The thermodynamic loss angle and polytropic indices were also found to be in the expected ranges, confirming that the in-cylinder pressure data under motoring and firing conditions were correctly phased and free from any anomalies.

The combustion system was also benchmarked against a Volvo D13 multi-cylinder engine. This was to understand whether the overall efficiency and emissions of the experimental engine are drastically different to that of an engine in mass production. It is confirmed that the Brunel experimental rig performs similarly to the Volvo D13 with respect to efficiency, with indicated specific fuel consumption values being within 1% of one another for similar calibrations. Similar levels of emissions were also attained, although directly comparable results were slightly convoluted by the difference of unit injectors used in the Volvo versus common rail fuel injection used at Brunel.

Finally, a diesel injector calibration was performed in order to quantify the amount of fuel injected for a given energizing time and rail pressure. Ultimately, Zeuch’s Method was used to gather the necessary calibration data needed, which resulted in the additional benefits of determining the injector delay and interaction between pilot and main injections. The injector delay was used during experimental testing to accurately calculate ignition delay. The effect of the pilot injection on the main injection quantity also provided knowledge of the physical phenomenon of pressure waves in the fuelling system and what could be done to avoid it.

With all of these preliminary experiments performed, it can be stated with a degree of confidence that the engine health and data quality were of adequate standard. Furthermore, the combustion system in the experimental test rig is of production calibre with respect to efficiency and emissions, providing a suitable starting point for further optimisation.

Chapter Five

Conventional and Premixed Dual-Fuel Combustion

5.1 Introduction

Optimisation of the engine hardware and combustion system needed to be performed in order to evaluate advanced dual-fuel combustion with accuracy. Appropriately, baselines were established for Diesel and Conventional Dual-Fuel combustion modes in order to guide development of Premixed Dual-Fuel Combustion (PDFC). Defined in Section 5.2 is each combustion mode while specifics of the test procedures are denoted in Section 5.3. These sections are followed by a diesel-only combustion baseline with elaboration on the optimisation of injection timing and rail pressure as well as exploration of the sensitivity to engine load. The second combustion mode of Conventional Dual-Fuel is discussed in Section 5.5. Optimisations of injections were discussed as well as sensitivities to engine operating conditions, including natural gas substitution percentage and engine speed. The third combustion mode of PDFC is discussed in Section 5.6, where numerous avenues were explored to minimise engine-out methane emissions. PDFC was one of the main focuses of the chapter, as it outlines the benefits from a performance and emissions standpoint when compared to all three combustion modes.

5.2 Definition of Combustion Modes

The three main combustion modes tested were defined as follows:

1. Diesel – Diffusion combustion with pilot
2. Conventional Dual-Fuel – Diffusion combustion and flame propagation
3. PDFC – Diffusion combustion and flame propagation with some premixed diesel

Figure 5-1: Proposed visual depiction of the three different combustion modes tested: Diesel (left), Conventional Dual-Fuel (middle), and PDFC (right).

Shown in Figure 5-1 is a top down view of the combustion chamber as if looking down the cylinder bore. The red triangles are meant to depict a multi-hole diesel spray. Diesel combustion (left) is typical diesel diffusion combustion with only a single direct injection of diesel. Conventional Dual-Fuel (middle) is a mix of classical diesel compression ignition and gasoline spark ignition. Diesel fuel is auto-ignited by the compression temperature, yielding multiple ignition points (grey stars surrounding diesel injections), and then flame propagation burns the natural gas charge (shown as the light blue background) [70,72]. PDFC (right) is similar to Conventional Dual-Fuel, except there is a quantity of premixed diesel involved (small red dots in the background) which in theory give rise to auto-ignition sites (smaller grey stars).

5.3 Test Procedures

Testing was performed at the engine speeds and loads depicted in Figure 5-2. The test points are denoted by red squares and span 3 different engine speeds and various loads. The loads points are 25, 30, 35, 40, 50, and 70% load of a Heavy Goods Vehicle (HGV)/HD full load torque curve. The engine speed of 1200 RPM was used most often, especially during the load comparison due to the highest number of data points. These points represent high residency areas in a typical HGV drive cycle, such as the WHTC [74].

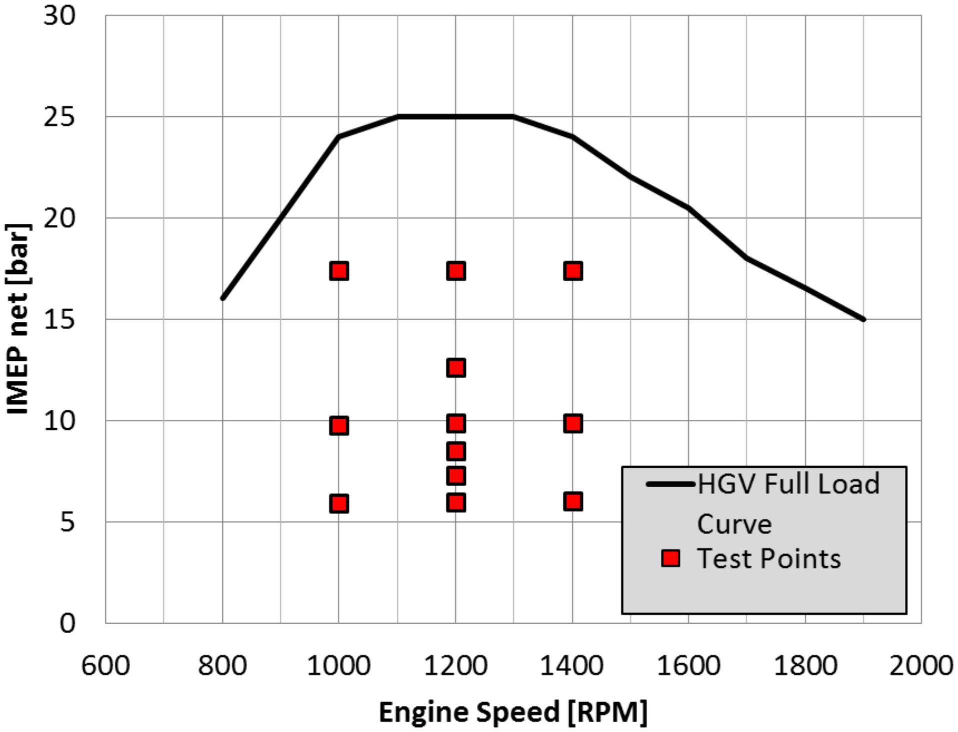

Figure 5-2: HGV full load torque curve with experimental test points highlighted in red

A maximum averaged pressure rise rate of 10 bar/deg and a cylinder pressure of 180 bar were considered as the upper bounds for calibration. Initial set points for diesel and conventional dual-fuel operation were taken from a US2010 compliant Volvo D13 multi-cylinder diesel engine (with multi-cylinder test data supplied by courtesy of Clean Air Power/Vayon). Intake boost pressure, exhaust backpressure, relative air-to-fuel ratio (λ), and EGR levels were based on the D13 in order to provide a sensible starting point, since an external boosting device was used in place of a turbocharger.

To provide a reasonable baseline to compare PDFC against, main injection timing optimisations were performed in both diesel and conventional dual-fuel combustion modes. The optimisation results were also compared against the D13 multi-cylinder engine in an attempt to validate the performance of the single cylinder combustion chamber, despite the expected differences in gas exchange and engine design. In PDFC mode, many variables were swept with the end goal of reducing methane slip while still maintaining acceptable thermal efficiency. For diesel injections, this entailed varying the timing, quantity, and pressure of the injections. Other variables pertaining to the mixture of the charge, such as EGR and λ levels, were also varied. Finally, the intake valvetrain timing was held constant for all tests and scavenging effects were minimised to ensure no methane was short-circuiting the combustion chamber via positive valve overlap. The baseline valve lift curves can be found in Figure 3-6, with intake lift depicted by the “Baseline – VVA On” case, which has a duration of approximately 207 CA degrees end-of-ramp. As a reminder, this represents an effective compression ratio of 16.2, which along with the duration, is representative of a conventional diesel engine. Specific or unique test conditions will be mentioned in each section on an as-needed basis.

5.4 Diesel Combustion Baseline

An optimisation was performed with diesel fuel only in order to provide a reference point for comparison against dual-fuel operation. The contents of this section deal with defining an optimised calibration for the diesel operating points by performing sweeps of diesel injection timing and injection pressure. Engine-out emissions and efficiency were considered when selecting an optimum and behaviour as a function of load is also discussed.

Injection timing and rail pressure are important factors in maximising engine efficiency and curbing engine-out emissions. For this reason, these parameters were swept for each engine speed/load point in order to ensure a fair comparison against other combustion modes. As previously mentioned, initial set point parameters for the sweeps were taken from a US2010 compliant Volvo D13, specifics of which are mentioned in Table 5-1 and Table 5-2 later on.

The goal of the diesel optimisation was to have the single cylinder achieve acceptably similar engine-out emissions to the Volvo D13 while minimizing ISFC. The data in Figure 5-3 to Figure 5-6 depict the sensitivity of ISNOx, ISCO, ISSoot, and pressure rise rate with respect to main injection timing. Emissions were compared on an indicated specific basis (IS), so that different exhaust flow rates would be accounted for. A selected engine speed of 1200 RPM (denoted as “A”) and sweeps from 25% to 70% load are portrayed for demonstration purposes. The selected calibrations for the different loads are denoted with a purple circle and will be compared against the other two dual-fuel combustion modes later on. Similar trends occurred for the test points not shown, so the same optimisation approach was applied across the board.

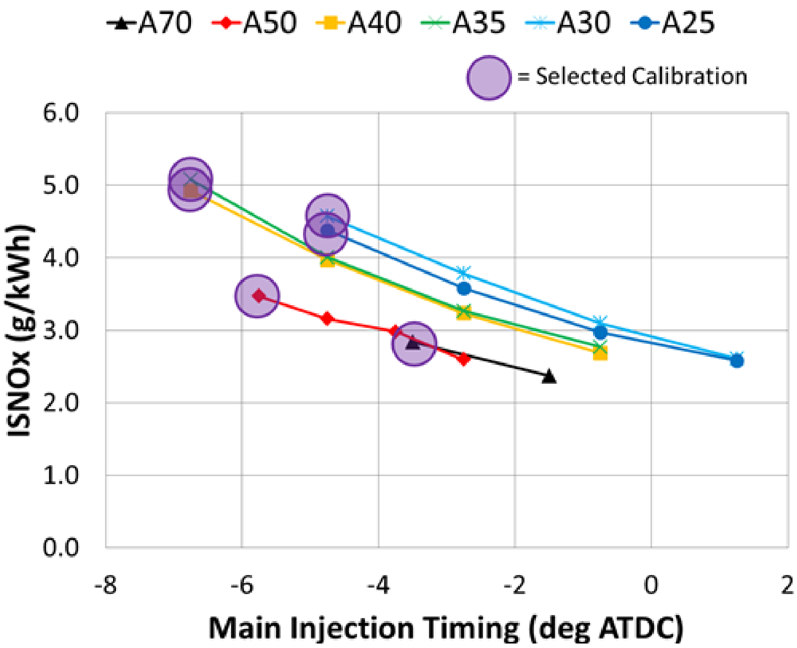

Figure 5-3: Engine-out ISNOx emissions vs main injection timing for a 1200 RPM load sweep of 25%-70% load

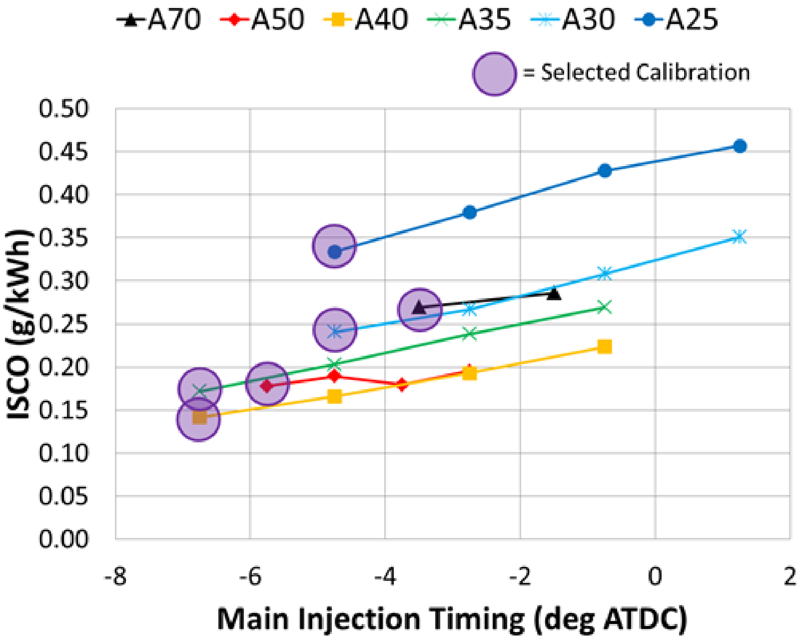

Figure 5-4: Engine-out ISCO emissions vs main injection timing for a 1200 RPM load sweep of 25%-70% load

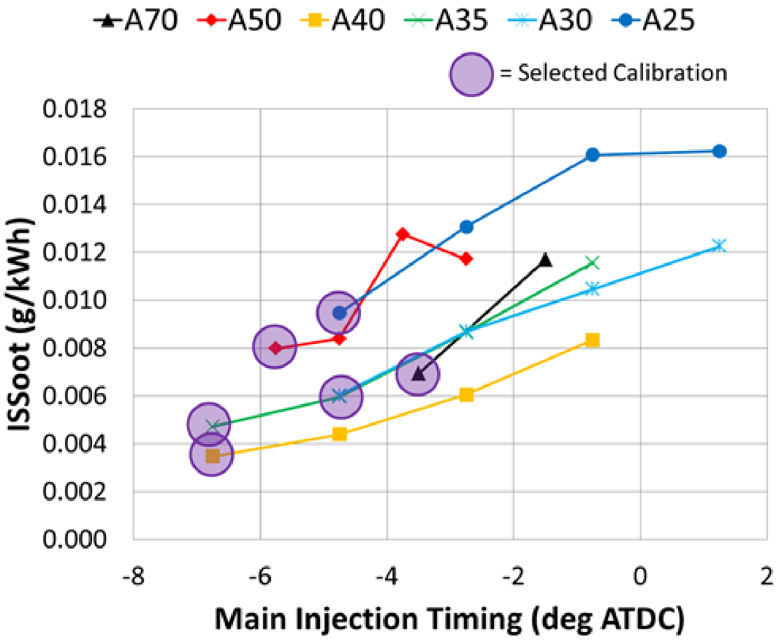

Figure 5-5: Engine-out ISSoot emissions vs main injection timing for a 1200 RPM load sweep of 25%-70% load

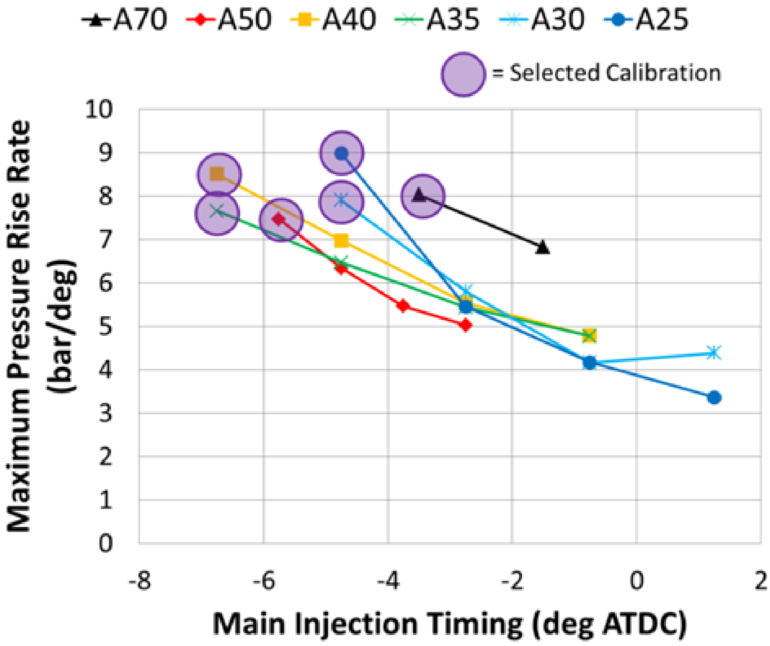

Figure 5-6: Pressure rise rate vs main injection timing for a 1200 RPM load sweep of 25%-70% load

Advancing of main injection timing results in an increase in NOx and pressure rise rate and a reduction in CO and soot for the window of main injection timings tested. CO and soot levels were relatively low in the first place due to appropriate fuel rail pressure resulting from a previously performed rail pressure sweep, which is discussed later in this section. The NOx-CO and NOx-soot trade-offs are typical for a diesel combustion system and relate directly to combustion temperature and local equivalence ratio. NOx is formed in regions of high temperature (typically fuel-lean areas of combustion) while CO and soot are formed in lower temperature, fuel-rich areas of combustion. The CA50 for the data ranges in the 4 deg to 13 deg ATDC regime which helps explain why directionally it was always more favourable to advance injection timing. Additionally, phasing of combustion relative to TDC can increase or decrease the combustion temperature, having direct implications on NOx formation.

In general, the response was similar for all loads, with the higher loads retarding CA50 due to increased pressure rise rate limits. This can be attributed to the higher temperatures and pressures associated with higher load operation. The ISFC is slightly worse for the two higher load conditions due to the compromised CA50. Details about the selected calibrations (purple circles) are shown in the following tables:

Table 5-1: Injection quantities and emissions for selected diesel calibrations

Engine Speed	Load	Load Point Name	Diesel Pilot Timing	Diesel Main Timing	Diesel Pilot/Main Quantity	NOx	CH4	THC	CO	FSN	ISCH4	ISNOx	ISFC
RPM	bar		deg CA ATDC	deg CA ATDC	mm3	ppm	ppm	ppm	ppm		g/kWh	g/kWh	g/kWh
1200	17.5	A70	-10.8	-3.5	3/232	457	40	47	65	0.14	0.1	2.8	183
1200	12.6	A50	-13.0	-5.8	3/149	508	6	52	40	0.15	0.0	3.5	181
1200	9.8	A40	-14.0	-6.8	3/117	621	7	55	28	0.06	0.0	4.9	180
1200	8.5	A35	-14.0	-6.8	3/103	606	9	59	32	0.07	0.0	5.1	181
1200	7.3	A30	-12.0	-4.8	3/87	510	9	63	42	0.09	0.0	4.6	184
1200	6.0	A25	-12.0	-4.8	3/73	462	10	72	54	0.13	0.0	4.4	187

Table 5-2: Test conditions and cylinder pressure specifics for selected diesel calibrations

Engine Speed	Load	Load Point Name	Pmax	PRR	CA50	Combustion Duration	Combustion Efficiency	Lambda	EGR %	Intake Pressure	Rail Pressure	Exhaust Gas Temp
RPM	bar		bar	bar/deg	deg CA	deg CA	%		%	bar	bar	degC
1200	17.5	A70	144.8	8.0	11.6	26.2	99.91%	1.38	20.1	2.2	1700	488
1200	12.6	A50	132.9	7.5	8.6	25.0	99.90%	1.67	21.1	2.0	1307	396
1200	9.8	A40	127.5	8.5	5.6	21.9	99.89%	1.96	21.2	1.9	1306	338
1200	8.5	A35	117.3	7.7	5.3	22.0	99.88%	2.07	21.1	1.7	1211	322
1200	7.3	A30	98.4	7.9	6.8	20.9	99.85%	2.18	20.3	1.5	1211	309
1200	6.0	A25	85.2	9.0	6.6	21.1	99.82%	2.27	19.8	1.3	1109	299

Ultimately, the selected calibrations were limited by pressure rise rate and were selected for having similar NOx values when compared against the production

Volvo D13. ISFC was considered, as the main injection timing was varied in a range where advancing it would result in a decrease in ISFC. Over advancing the injection timing was avoided as it would result in an increase in fuel consumption due to work being done on the piston as it is still moving toward TDC.

The selected calibrations and rail pressure shown in Table 5-2 were the result of a prior fuel rail pressure optimisation. Each load condition was ran with different rail pressures until the point with the best set of trade-offs was selected. To illustrate the compromises, three different load conditions for key parameters are depicted in Figure 5-7 to Figure 5-10. Low, medium, and high load operation are represented by A25, A50, and A70 respectively, with different rail pressures portrayed by line colour and marker shape.

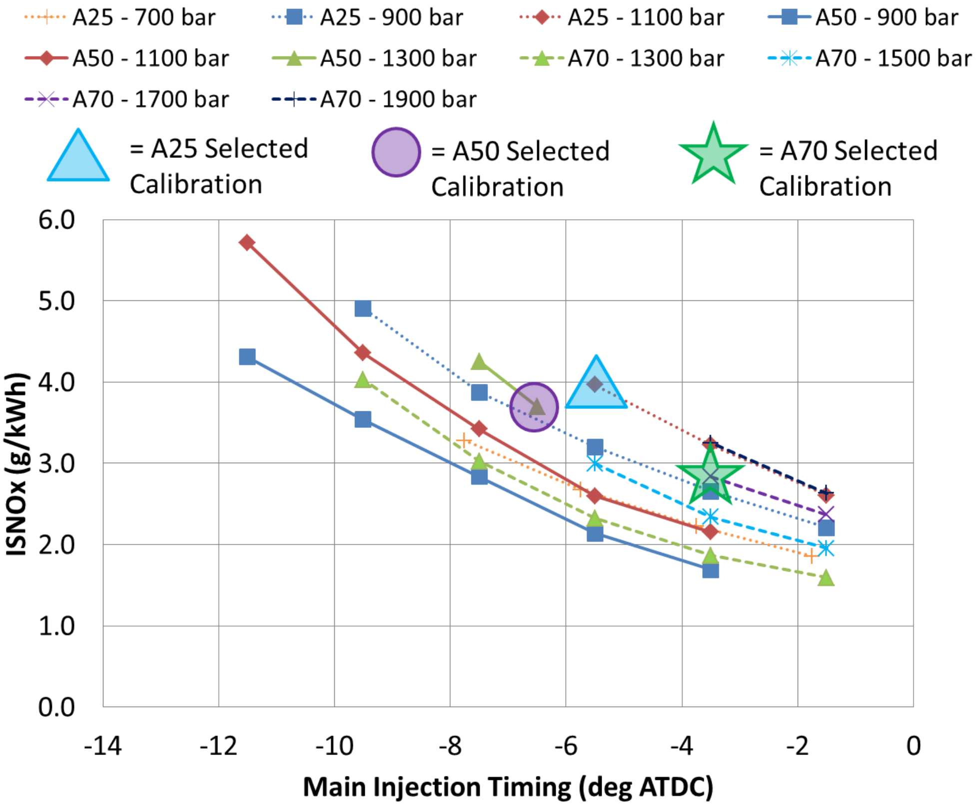

Figure 5-7: Engine-out ISNOx emissions vs main injection timing for varying rail pressure and load

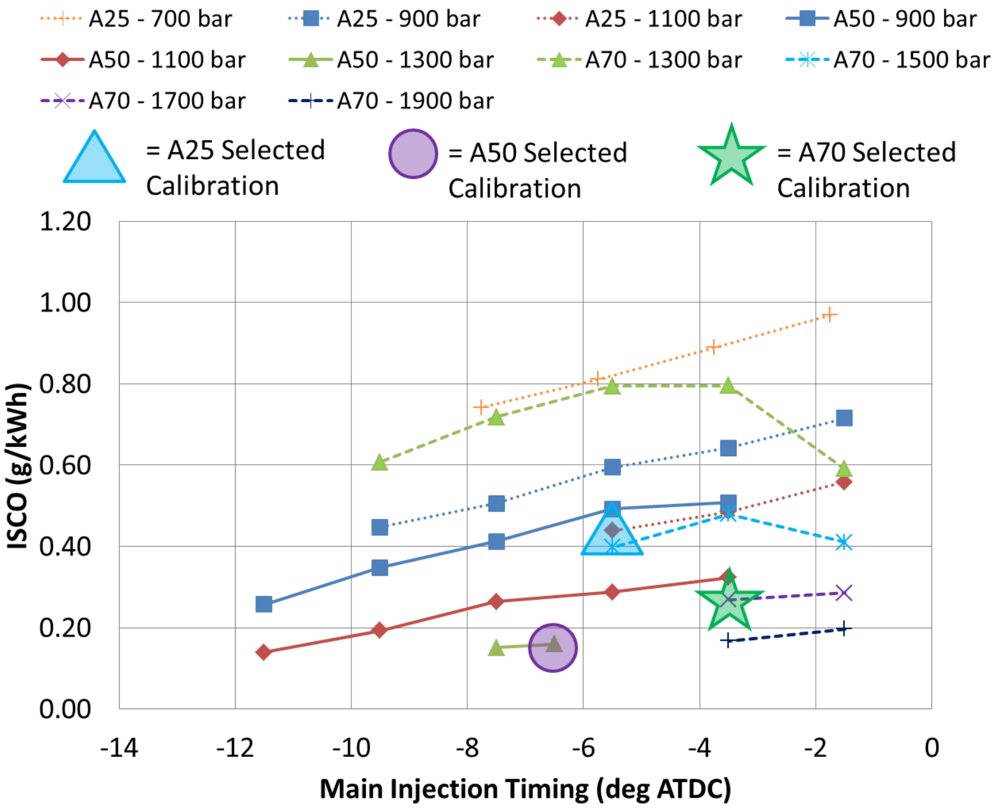

Figure 5-8: Engine-out ISCO emissions vs main injection timing for varying rail pressure and load

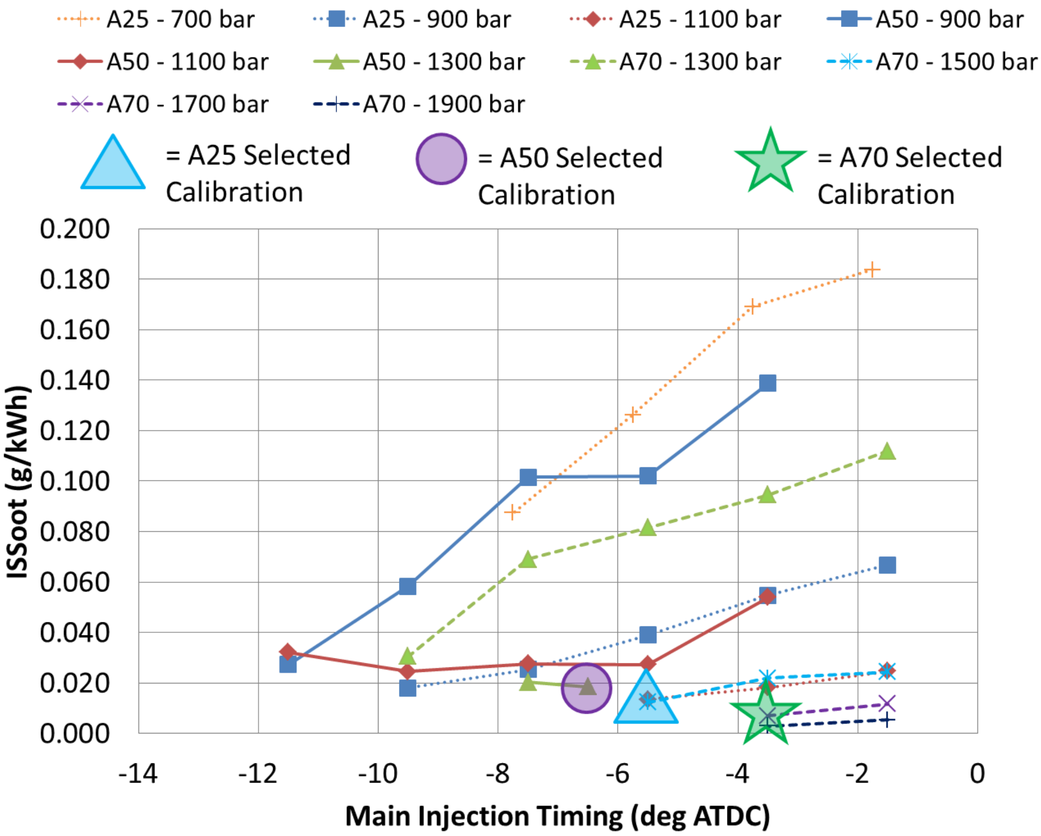

Figure 5-9: Engine-out ISSoot emissions vs main injection timing for varying rail pressure and load

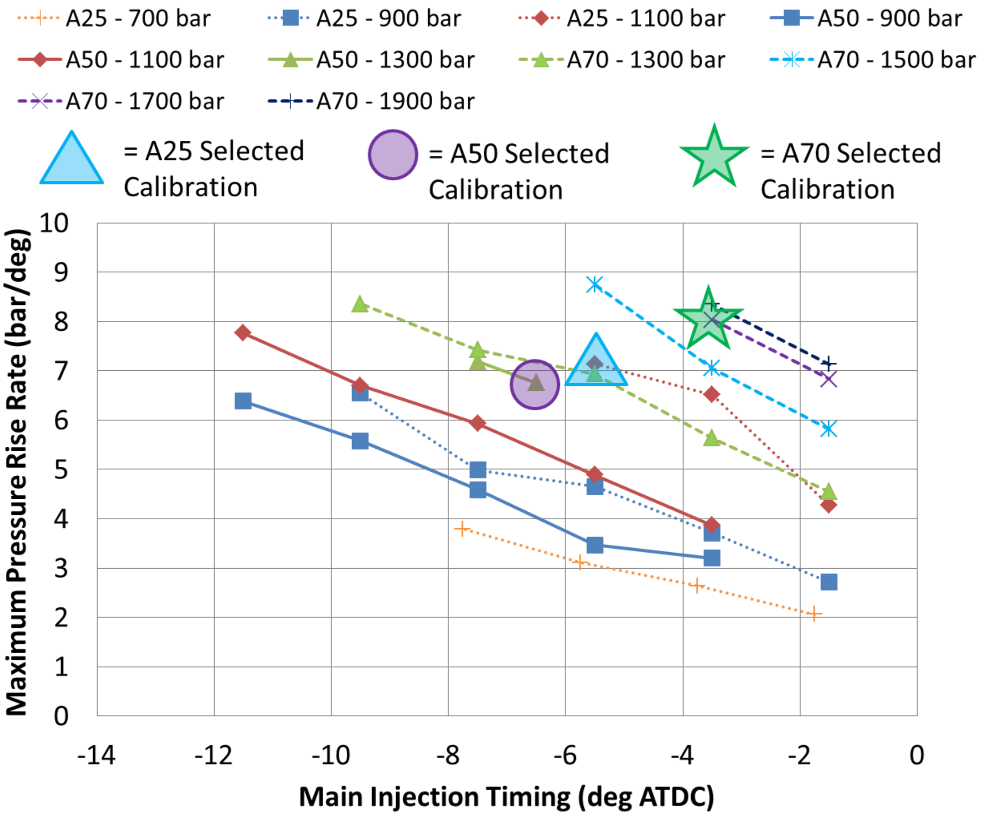

Figure 5-10: Maximum pressure rise rate vs main injection timing for varying rail pressure and load

A main injection sweep was performed for each rail pressure, with similar rail pressures represented by alike colours and markers. The line patterns are based on each individual load, with the shapes (triangle, circle, and star) depicting the selected rail pressure calibration. Similar trends occur with the advancing of main injection timing as NOx and PRR increase and CO and soot decrease. These trends hold true for essentially all of the rail pressures tested, but sometimes with varying rates of change. This is best illustrated by soot emissions in Figure 5-9, with diminishing benefits to soot with advancing of injection timing for higher rail pressures.

Generally, an increase in rail pressure resulted in an increase in NOx and pressure rise rate and a reduction in CO and soot. The increased rail pressure mainly helps with fuel atomization and promotes lower local equivalence ratios, which is particularly beneficial for CO and soot emissions. If the rail pressure is set too high it results in elevated pressure rise rates and NOx emissions for a given amount of EGR. It also has a diminishing return for decreasing soot and CO emissions. Only two points were taken for the A70 case, due to these limitations. If the main injection timing was advanced, a pressure rise rate limit would be reached, with high NOx emissions. If main injection timing was retarded further, this would result in degradation of ISFC. Higher rail pressures also led to slightly higher combustion efficiency due to the increased atomisation of the fuel.

Certain parameters also carry a higher sensitivity to load than others. NOx and PRR are fairly predictable with load and rail pressure, producing a measured response. However, soot has a heightened sensitivity to rail pressure at low loads, but a relatively benign response at high loads for the injection timings tested. Too low of a rail pressure at low load results in very high soot emissions as the fuel is not being properly atomised and mixed with the air in the cylinder before combustion is initiated. Higher initial rail pressures at higher loads (along with increased mixing and in-cylinder temperature) can help calm these effects, resulting in a relatively minor response in soot to rail pressure. Further, if comparing similar injection pressures for different loads, the higher temperatures associated with increased load cause the diesel fuel to ignite more readily. This allows less opportunity for the fuel to mix with air first, leading to increased CO and soot emissions for a given rail pressure.

Similar to the main injection optimisation, preference was given to matching the engine-out NOx emissions and pressure rise rates from the Volvo D13 multi-cylinder. There exists a slight amount of scatter in the optimums as a result of this, as well as some testing variability, but the same physics apply to all data points. Sensitivities to pilot quantity and timing were also performed. A pilot injection of approximately 3 mm^3 and 7 crank angle degrees before the main injection timing was used to decrease pressure rise rates.

5.5 Conventional Dual-Fuel Combustion

As with diesel combustion, a similar process was taken to ensure conventional dual-fuel was optimised before ultimately being compared to PDFC. This section consists of three individual parts. The first section is an outline of the optimisation of injection timing and rail pressure with consideration to emissions and efficiency. Included in the subsequent sections are details of the role of natural gas substitution and engine speed and how that factored into the process of calibration selection.

5.5.1 Injection Timing and Rail Pressure Optimisation with Engine Load

In order to obtain a level comparison between diesel and PDFC combustion modes, an optimisation was first performed to determine the timing and rail pressure of the diesel injection (ignition source) in conventional dual-fuel. After these tests are discussed, a sensitivity to engine load will follow. For these tests, the gas for diesel substitution was calculated by energy, and was approximately 83% ± 2% substitution of natural gas in place of diesel. This substitution amount was selected to provide a high percentage of natural gas usage, as is required for a compelling business case (natural gas is typically less expensive compared to diesel). Additionally, the upper bound was limited to allow for a sufficient quantity of diesel fuel to premix in the PDFC tests later on. This is necessary in order to compare PDFC and conventional dual-fuel at the same gas substitution percentage. No diesel pilot injection was used ahead of the main diesel injection.

An example of a rail pressure optimisation versus key parameters is depicted in Figure 5-11 to Figure 5-13. These figures include details of the results of rail pressure sweeps for the A50 load condition, with A70 as a relative comparison. A50 and A70 were chosen as an example as these sites incurred the highest number of data points that were ran on the same day (selected to reduce day-to-day variation). As in the previously mentioned diesel optimisation, the purple circles are the selected calibration for A50, and the green stars are the selected calibration for A70. Rail pressure optimisations were carried out for the additional speeds/loads (not shown), the results of which were published in Table 5-4 and Table 5-5 at the end of the chapter.

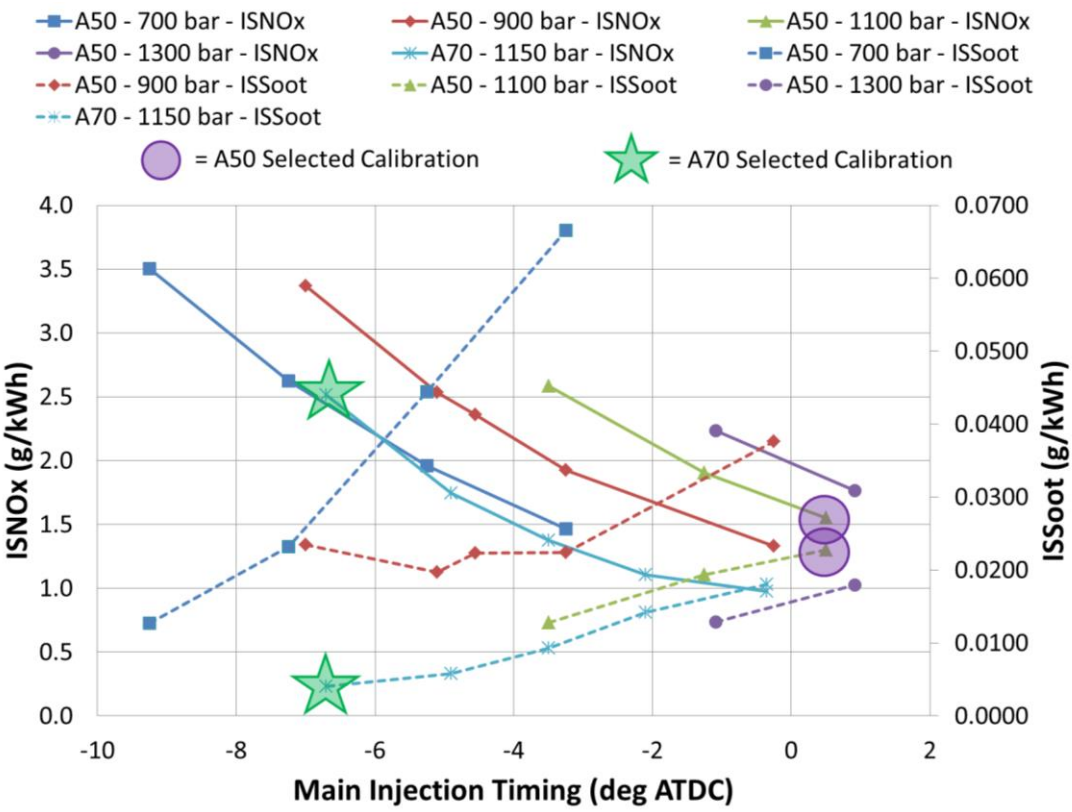

Figure 5-11: Engine-out ISNOx and ISSoot emissions vs main injection timing for A50 and A70

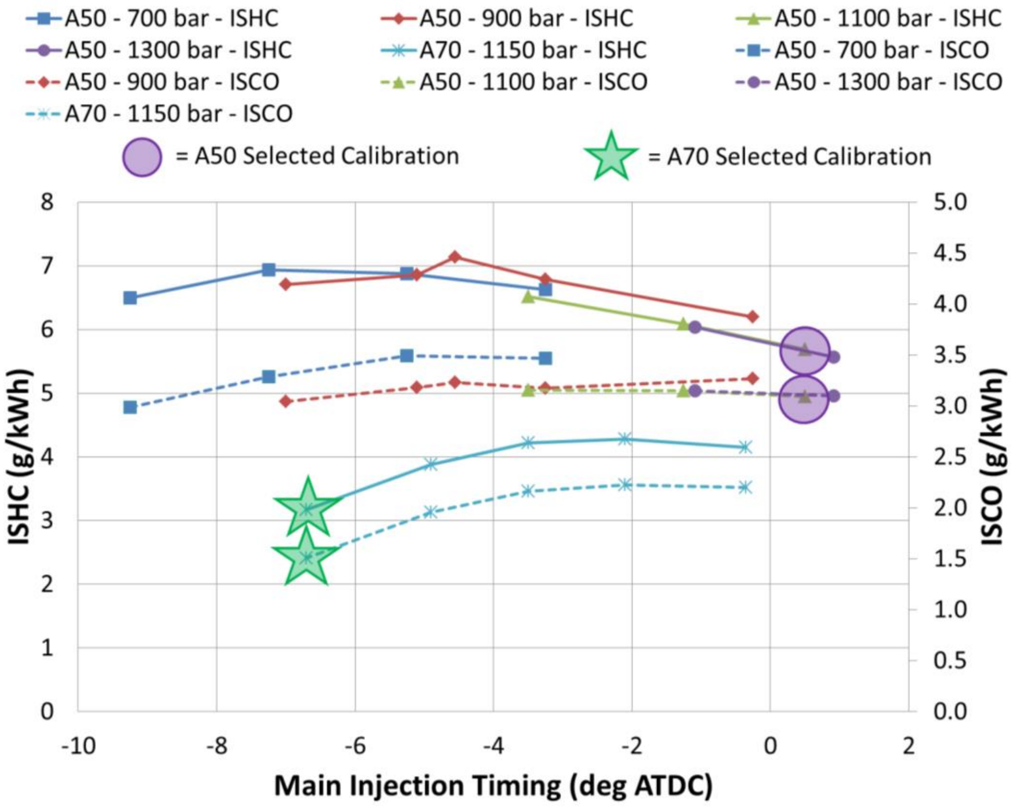

Figure 5-12: Engine-out ISHC and ISCO emissions vs main injection timing for A50 and A70

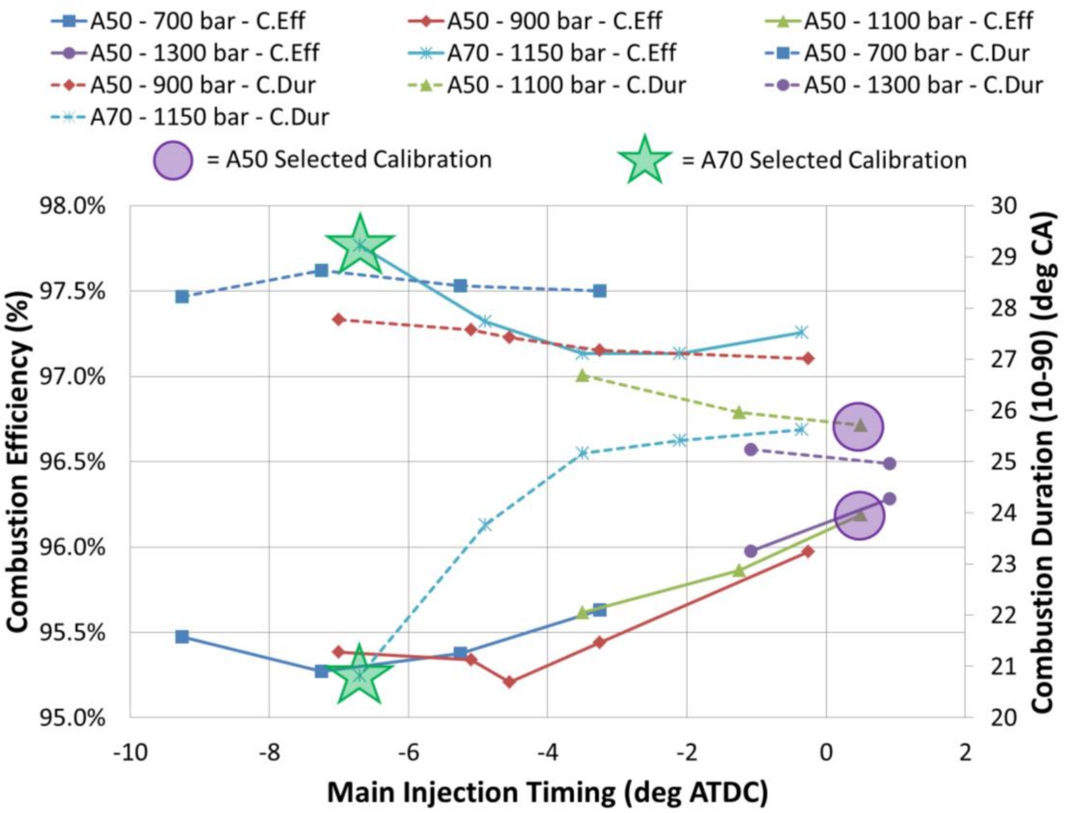

Figure 5-13: Combustion efficiency and duration vs main injection timing for A50 and A70

In many respects, the results of these tests yielded similar trade-offs to the diesel baseline, since combustion temperature and local equivalence ratio still drive emissions formation. Depicted in Figure 5-11 is the standard ISNOx and ISSoot relationship with main injection timing and rail pressure. A consistent trend occurred where ISNOx increased and ISSoot decreased with the advancing of injection timing. The higher the injection pressure, the more retarded the injection timing had to occur in order to output the same level of NOx. In general, this relationship was very repeatable, with approximately a 200 bar rise in injection pressure resulting in a 2 deg CA retarding of injection timing for equivalent NOx production at A50. ISSoot decreased with higher injection pressure, as the diesel spray was more finely atomised. It should be observed that the levels of soot production in conventional dual-fuel were less than that of diesel combustion, due to the smaller amount of diesel fuel being used. All of these observations were true for both load conditions.

ISHC and ISCO emissions are both displayed in Figure 5-12. Compared to diesel combustion, the levels of total hydrocarbon (THC) and CO emissions are significantly higher due to the majority of the combustion mode changing from diffusion burning to flame propagation. Flame propagation, and the subsequent quenching, yields a portion of the fuel not being consumed during the combustion event. Generally, increased rail pressure helps to reduce THC and CO emissions, but is more dependent on main injection timing. The data in Figure 5-13 supports this by showing a decrease in combustion duration with increased rail pressure accompanied by an increase in combustion efficiency for retarded injection timings. A70 has a different behaviour, with THC emissions decreasing with injection timing advance, and will be discussed in the load portion of this section.

Overall, the selected calibrations for A50 and A70 were made based on balancing constraints for NOx, pressure rise rate, and maximum cylinder pressure (for higher loads), while trying to achieve the lowest level of THC emissions. THC emissions weighed heavily due to the bulk of it being made of up CH_4, which is a potent greenhouse gas and difficult for the exhaust after-treatment to oxidise. Seeking out the highest combustion efficiency went hand-in-hand with searching for the lowest THC emissions, as it meant the highest amount of fuel was being utilised in-cylinder. Soot emissions were reduced with rail pressure and the inherent clean burning fuel properties of natural gas and dual-fuel combustion. Finally, not shown, advancing main injection timing also results in an improvement in ISFC for this particular window. Similar approaches were taken when selecting suitable injection pressures for the remaining speed and load conditions.

Fair comparisons for engine load can now be made with the predetermined injection pressures. The data presented in Figure 5-14 to Figure 5-16 detail the results of injection timing sweeps for 1200 RPM (A) and 30, 40, 50, and 70% (30-70) load conditions. Selected calibrations are highlighted with the appropriate shape marker corresponding to the given load. A detailed summary of the calibrations is shown in Table 5-4 and Table 5-5.

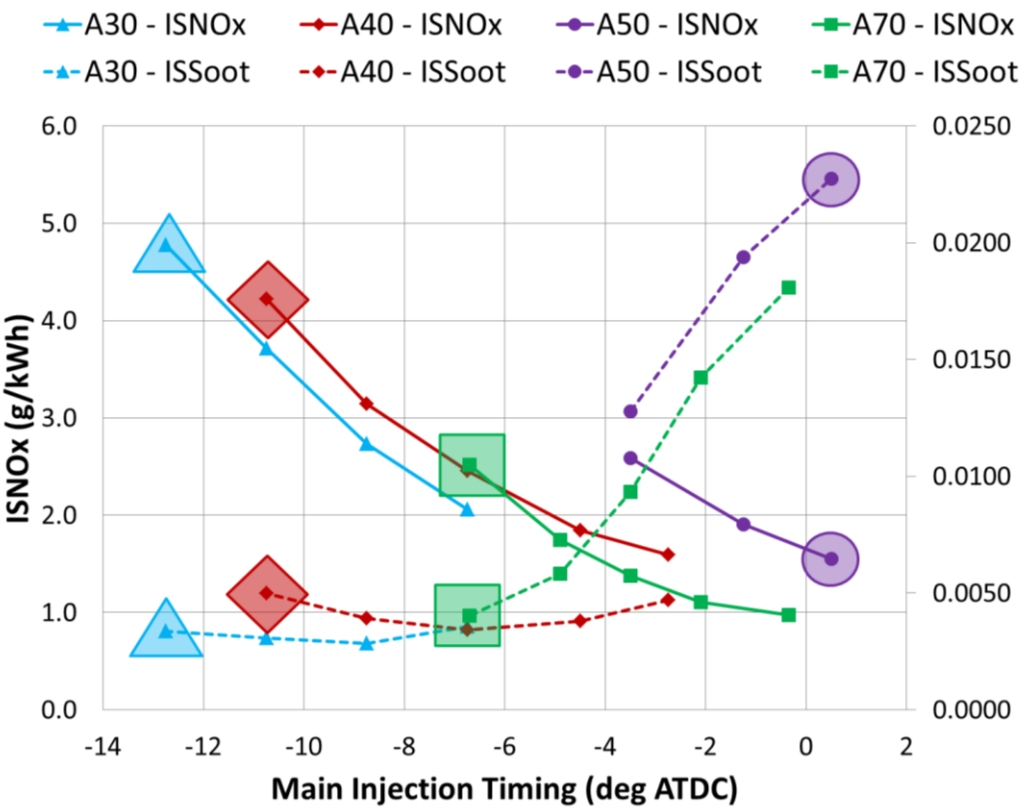

Figure 5-14: Engine-out ISNOx and ISSoot emissions vs main injection timing for four engine loads

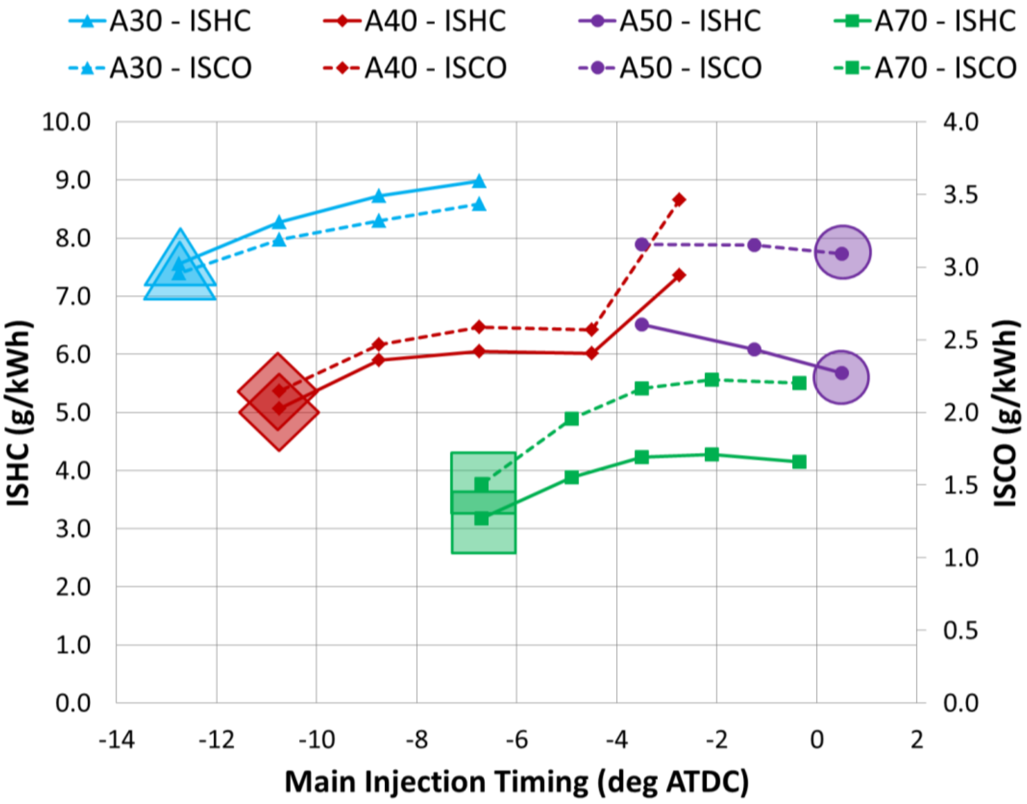

Figure 5-15: Engine-out ISHC and ISCO emissions vs main injection timing for four engine loads

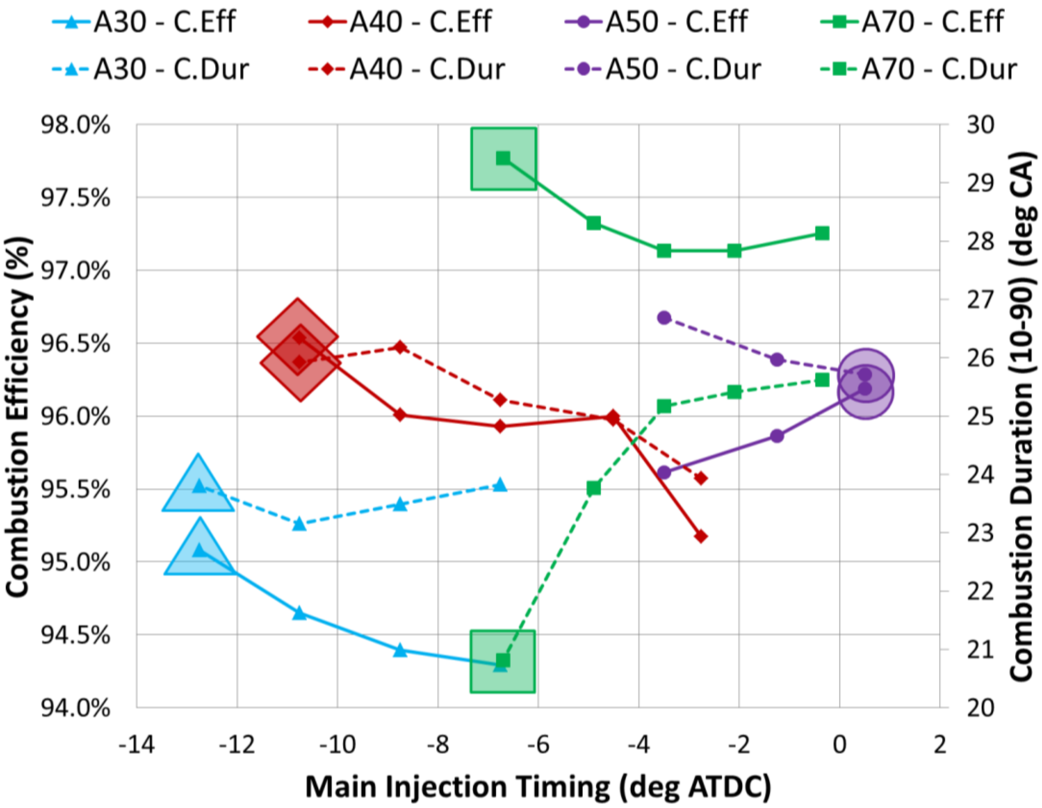

Figure 5-16: Combustion efficiency and duration vs main injection timing for four engine loads

Once again, the results of these tests yielded similar trade-offs to prior results, but some interesting load based observations can be made. These mainly involve the effect of diesel injection timing on CO and THC emissions, depicted in Figure 5-15. THC/CH_4 decreases with retarding of the injection timing for A50 at this particular rail pressure (1100 bar). As shown in Figure 5-12, lower rail pressures, such as 700 or 900 bar, allowed more advanced combustion phasing and a different shaped trade-off, but increased soot and THC. However, for 1100 bar, later injection timing yielding higher exhaust gas temperatures which increased oxidation of late cycle THC. Also, more time is available for better mixing between the diesel injection and the inducted charge before ignition. Lower peak in-cylinder pressure can also help to introduce a less dense fuel and air/EGR charge into the piston ring packs, which are a well-known major source for unburnt hydrocarbons [96,103,104].

Conversely, for A70, CO and THC decreased at a faster rate when the injection timing was advanced. This phenomenon is accompanied by a decrease in combustion duration as shown in Figure 5-16. Combustion durations remained fairly consistent for A50, A40, and A30, but decreased significantly for A70 when the injection timing was advanced. In-cylinder temperatures and pressures were likely not high enough for a reduction in combustion duration to occur for A50, but when load is increased, bulk ignition of the end gases usually contributes to the burning of THC and CO. This is the reason behind a different behaviour with A70 when compared to A50. In terms of non-methane hydrocarbon (NMHC) emissions, higher rail pressures can help reduce NMHCs by aiding with the atomisation of the diesel fuel used for ignition. The CH_4/THC ratio generally increases with decreasing load, mainly due to the larger amount of CH_4 remaining unburnt. The selected calibrations were chosen mainly by minimising THC emissions as well as maximising combustion efficiency while remaining within the limitations of NOx, pressure rise rate, and maximum cylinder pressure.

5.5.2 Natural Gas Substitution

Engine emissions, efficiency, and calibration are a function of the substitution of natural gas for diesel, so it is important to understand the trade-offs in the intended operating regime. Typically, the highest possible substitution percentages are targeted due to the cost and emissions benefits of using natural gas in place of diesel fuel. The highest substitution percentages are dependent on operating conditions and how much diesel is necessary to provide a reliable ignition source. To help understand substitution effects in conventional dual-fuel, a DOE was performed at 6 and 12 bar $IMEP_{net}$ at 1200 RPM at three different substitution percentages:

6 Bar $IMEP_{net}$ (A25 - 25% Engine Load):
81%, 86%, 90% CNG Substitution
20% EGR, 18.8% Intake O2, 900 bar diesel rail pressure, λ_{cyl} = 2.0

12 Bar $IMEP_{net}$ (A50 - 50% Engine Load):
82%, 87%, 93% CNG Substitution
20% EGR, 18.2% Intake O2, 1100 bar rail pressure, λ_{cyl} = 1.68

The engine load and speed were chosen because they represent high residency areas in a typical HGV drive cycle, such as the WHTC [74]. The highest percentage tested was a result of attempting to achieve the maximum CNG substitution at the given load condition (misfire and emissions limited), with a 5% spacing separating the substitution amounts. Control issues with small diesel injections led the 6 bar IMEP$_{net}$ point to be a 4% difference between 86% and 90% rather than 5%. Three substitution levels were tested to provide enough data to extract a trend, while 5% separation between the substitutions would cover the desired operating regime of approximately 80-93%, based off of the aforementioned Volvo D13 multi-cylinder dual-fuel reference data.

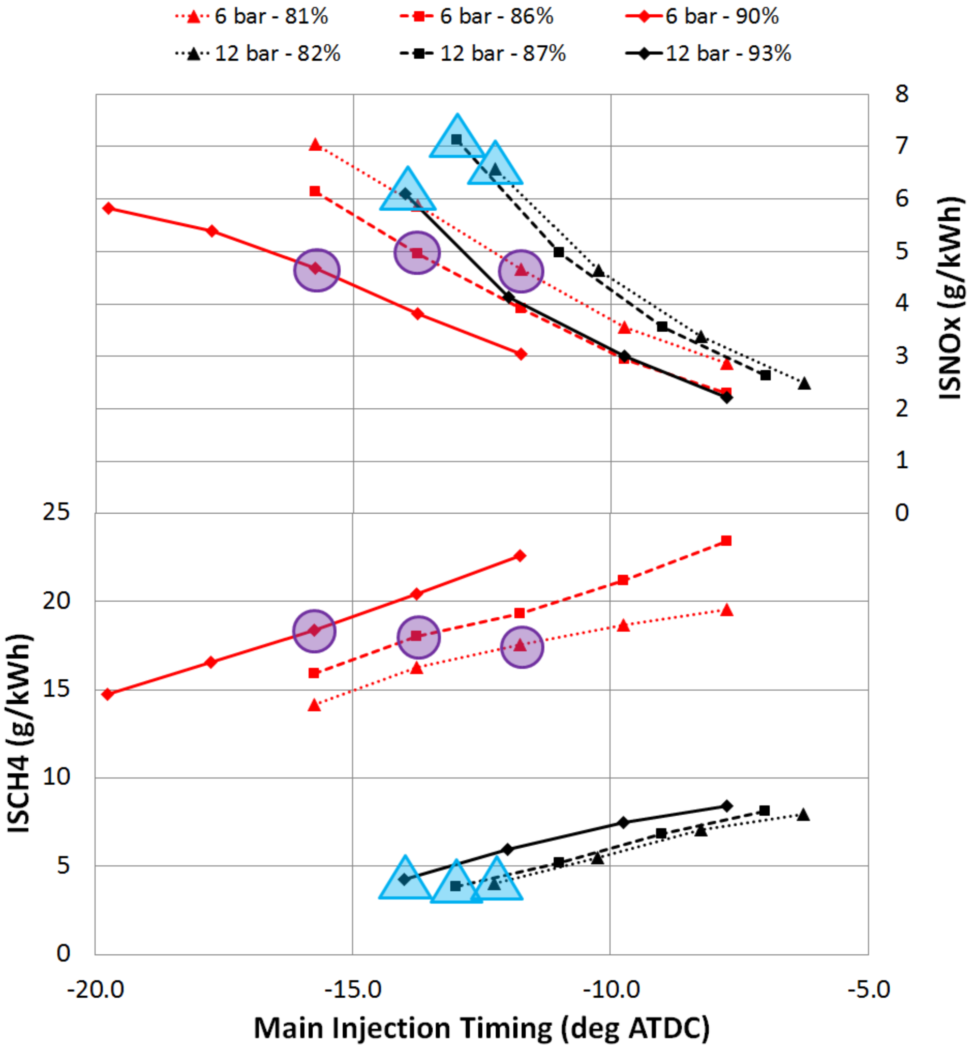

Figure 5-17: Engine-out ISNOx and ISCH$_4$ emissions vs main injection timing for three substitution percentages at 6 and 12 bar IMEP$_{net}$

A main injection timing sweep was performed for each substitution percentage. Once again, a single diesel injection was used to ignite the natural gas mixture with no diesel pilot injection used prior to the main diesel injection. The selected calibrations for comparison are denoted by a purple circle for 6 bar and a blue triangle for 12 bar operation. These signify points with approximately the same CA50 of around 4 deg ATDC. A constant CA50 was chosen for a comparison method, as it would best represent realistic changes made to an engine calibration in order to compensate for an adjustment to natural gas substitution. Engine emissions and efficiency metrics are discussed initially, followed by a crank angle based heat release comparison.

Set out in Figure 5-17 and Figure 5-18 are key emission metrics for the two engine loads and varying substitution percentages. Red lines and purple circles denote 6 bar and black lines with blue triangles depict 12 bar. Generally, it can be observed that equivalent emissions can be achieved if an adjustment to main injection timing is made. Increasing natural gas substitution forces an advancing of main injection timing in order to maintain emissions and combustion phasing. This is likely due to less ignition energy (diesel fuel) being available at the start of the ignition process. 6 bar has a higher sensitivity to CO and soot emissions than 12 bar, possibly due to the in-cylinder conditions as well as the spray formation and rail pressure.

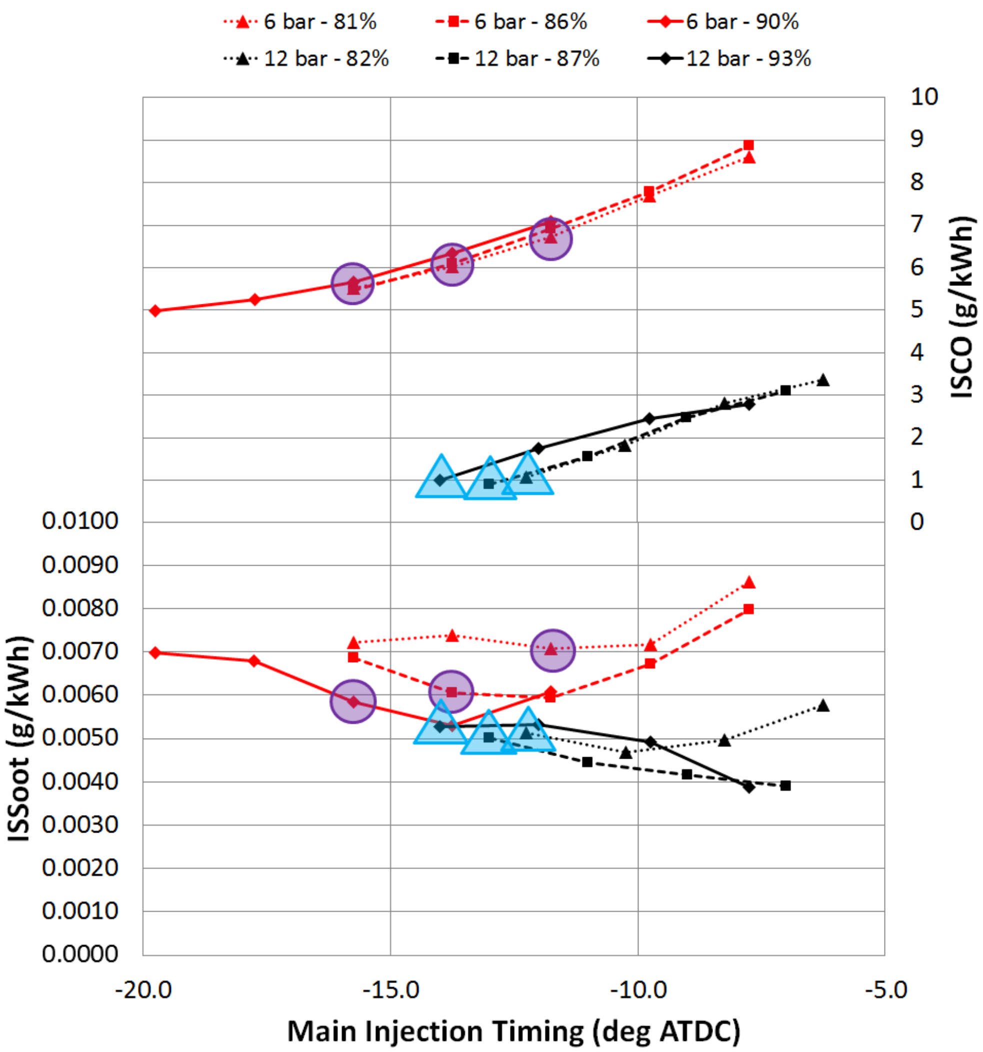

Figure 5-18: Engine-out ISCO and ISSoot emissions vs main injection timing for three substitution percentages at 6 and 12 bar $IMEP_{net}$

The data graphed in Figure 5-19 and Figure 5-20 demonstrates that the indicated specific fuel consumption as well as the combustion efficiency can be maintained with the advancing of injection timing. The phasing of the diesel injection timing earlier in the combustion process likely compensates for the reduced amount of ignition energy provided by the smaller diesel injections. The targeting of approximately the same CA50 values can help with maintaining ISFC and combustion efficiency, as the majority of the combustion process is occurring at a similar crank angle. Pressure rise rate is decreased with increased substitution due to smaller diesel injection quantities. However, this lack of initial ignition energy has a trade-off in that with increased substitution, 10-90% combustion duration generally tends to increase, especially at constant injection timing.

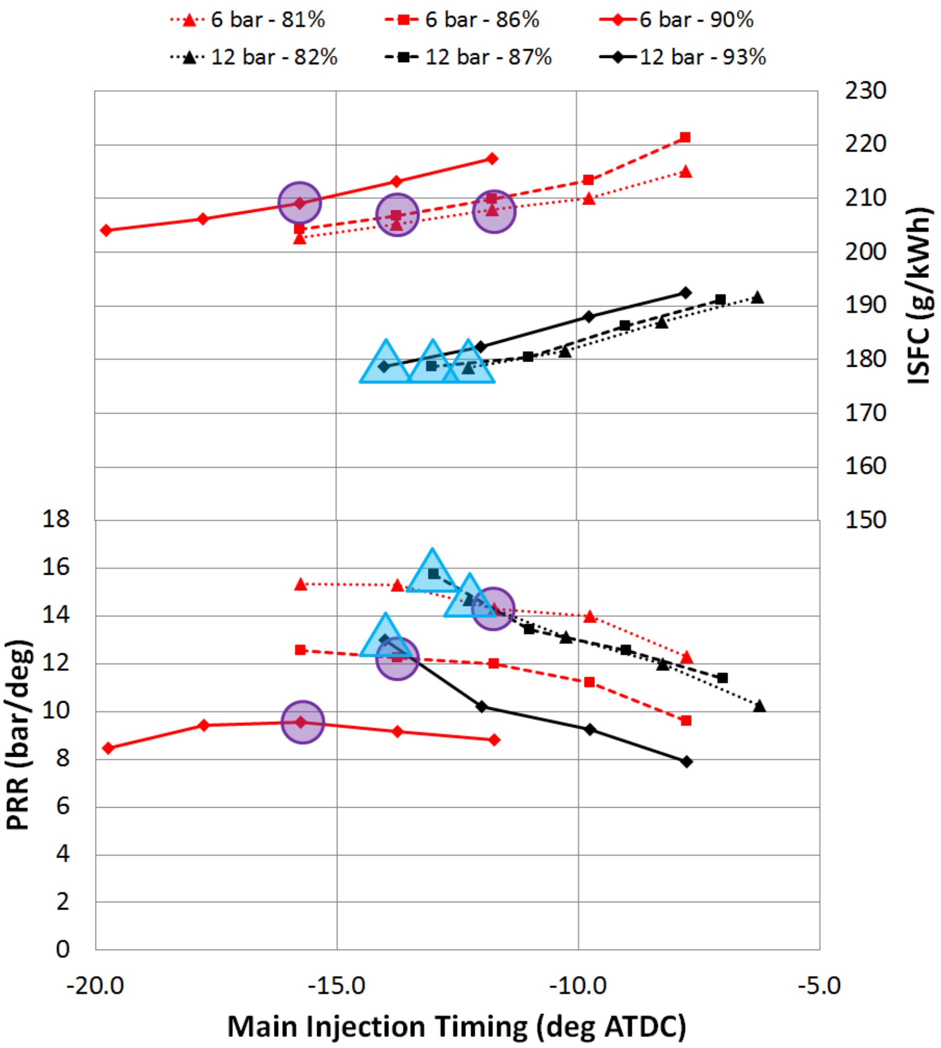

Figure 5-19: ISFC and maximum pressure rise rate vs main injection timing for three substitution percentages at 6 and 12 bar IMEP$_{net}$

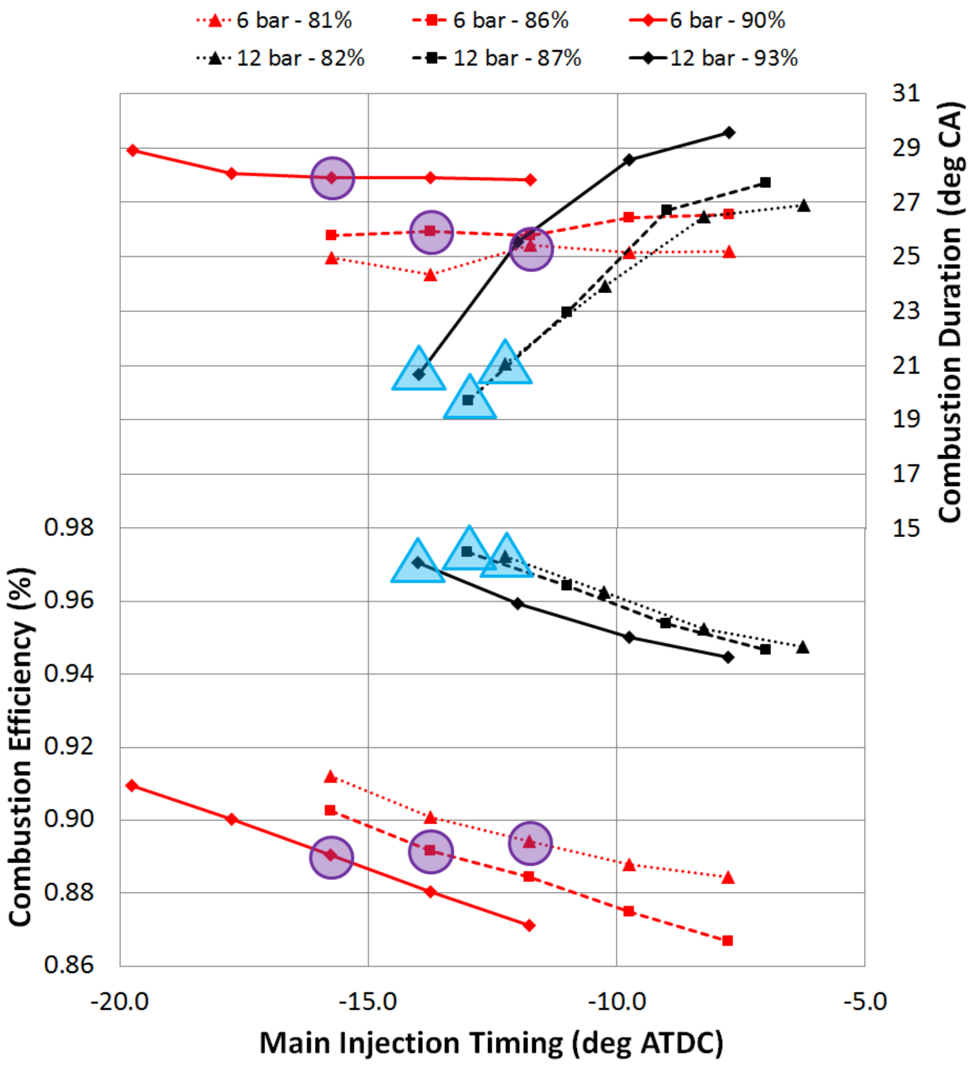

Figure 5-20: Combustion Duration (10-90%) and combustion efficiency vs main injection timing for three substitution percentages at 6 and 12 bar IMEP$_{net}$

The data in Figure 5-21 and Figure 5-22 further illustrate this combustion duration phenomenon by displaying the crank angle based apparent net heat release for 6 and 12 bar. The three solid lines depict the constant CA50 cases, while the dotted lines show the effect on HRR when start of injection (i.e. diesel injection) is held constant. A lower initial bump is observed for the higher gas substitution (90%) due to less diesel being available to burn. It is also likely due to less diesel spray penetration resulting in a decreased ignition source for natural gas flame propagation. In general, a longer heat release is observed for the higher gas substitution.

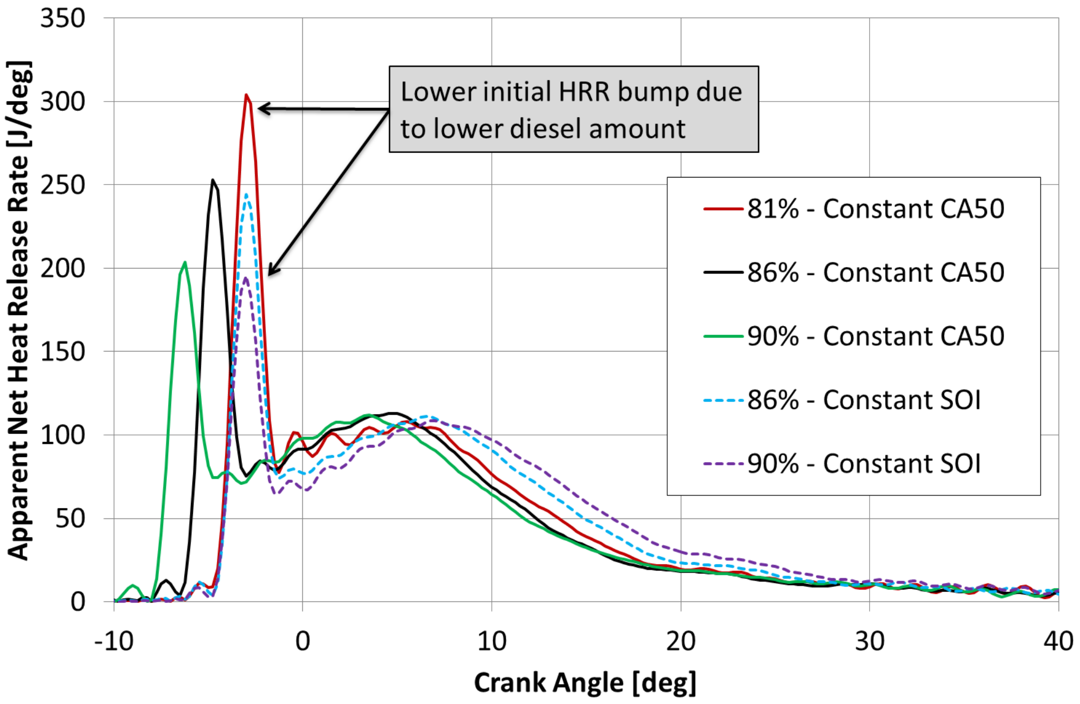

Figure 5-21: Apparent net heat release rate for three different substitution percentages at 6 bar IMEP$_{net}$

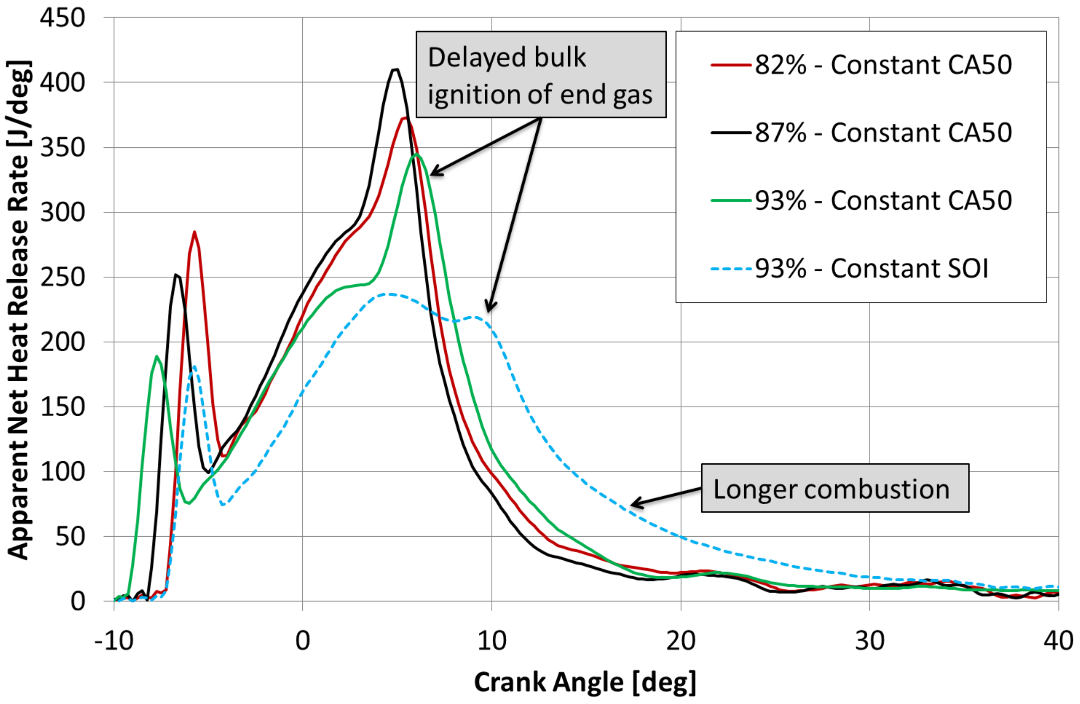

Figure 5-22: Apparent net heat release rate for three different substitution percentages at 12 bar IMEP$_{net}$

The data in Figure 5-22 shows additional insight in to the dual-fuel combustion process when compared to that of Figure 5-21. Temperatures are elevated at higher load conditions to the point where bulk ignition of the end gas is a regular occurrence. This results in a different heat release rate shape, as there is a sudden rise in heat release in the 5-10 deg crank angle regime. This allows for faster burn durations when compared to 6 bar, as well as a more efficient combustion process resulting in more burnt fuel and less emissions. However, at very high load conditions, this bulk auto-ignition will result in high cylinder pressures and knock, which would limit natural gas substitution. Conversely, for very light load conditions, it is sometimes necessary to decrease the natural gas substitution due to very high air-fuel λ, where the flammability limits of the natural gas are encroached. This results in poor combustion efficiency and emissions, with considerable CH_4 remaining unburnt. Finally, the cases of constant SOI support the need to adjust main injection timing when varying natural gas substitution. If left unaltered, the lengthened combustion durations will have adverse effects on engine efficiency and emissions.

5.5.3 Engine Speed Sensitivity

The effect of engine speed is an important variable to understand as it could have implications on breathing, in-cylinder turbulence, heat transfer, emissions and efficiency. As typical HD dual-fuel engines operate on a transient basis, engine speed is constantly in flux, with significant time being spent in the 1000 to 1400 RPM regime. Three steady-state engine speeds of 1000, 1200, and 1400 RPM were run to determine the effect of engine speed on combustion. Conventional dual-fuel operation with 80 and 90% NG substitution percentages were ran at 6 Bar $IMEP_{net}$. An external EGR rate of 20% (18.2% Intake O_2) was used with 700 bar diesel rail pressure. No diesel pilot injection was used. The relative AFR (λ_{cyl}) ranged from 1.52-1.57, with combustion phasing adjusted to maintain approximately a CA50 of 10 deg ATDC. Engine emissions and efficiency metrics are discussed initially, followed by a crank angle based heat release comparison.

The data plotted in Figure 5-23 and Figure 5-24 illustrates the relatively low sensitivity of emissions to engine speed. The solid lines correspond to the left y-axis and dotted to the right y-axis. A gas substitution of 80% is shown with black diamonds with 90% denoted by red squares. A small increase in NOx emissions can be seen at 1200 RPM, but the scale is relatively small, as this represents a difference of about 20 ppm. NOx is extremely sensitive to engine calibration variables, so it is likely caused by a slight variation in engine operating conditions, such as in-cylinder λ. Similarly, CH_4 increased with engine speed, but was more likely due to the slight variation in engine calibration, which drove a retarding of CA50 from 9.6 to 9.9 to 10.3 deg ATDC for 1000, 1200, and 1400 RPM respectively.

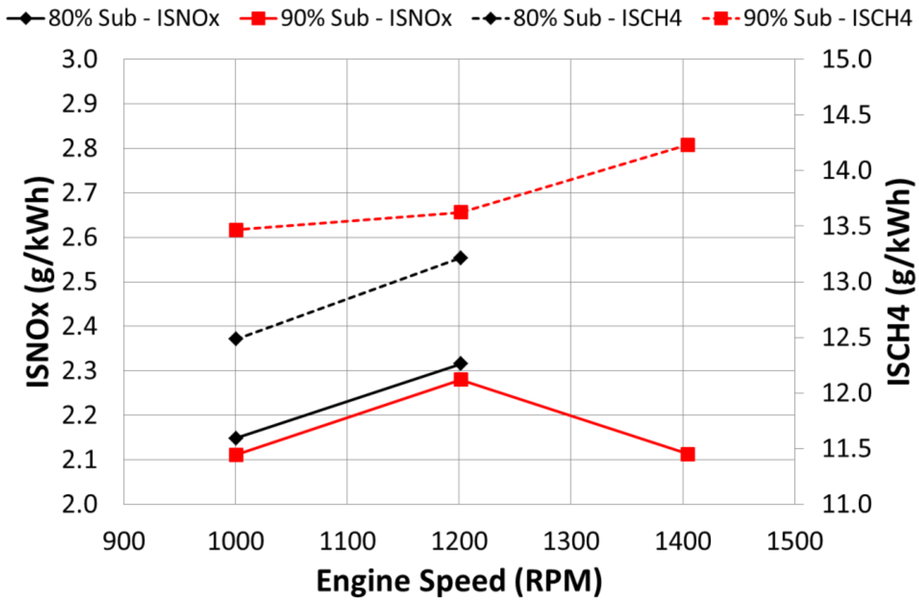

Figure 5-23: Engine-out ISNOx and $ISCH_4$ emissions vs engine speed for 80 and 90% gas substitution

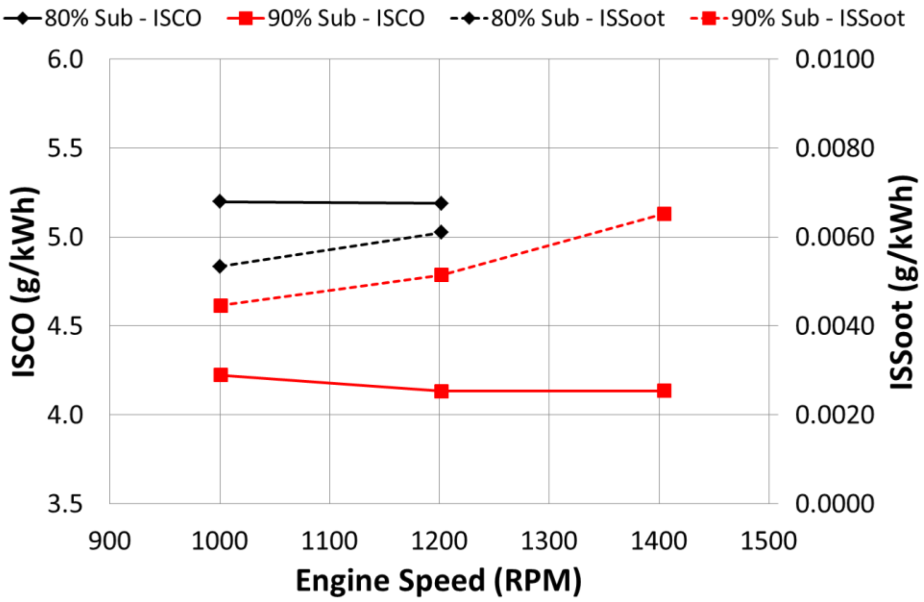

Figure 5-24: Engine-out ISCO and ISSoot emissions vs engine speed for 80 and 90% gas substitution

CO and soot emissions remained more or less steady, with soot increasing slightly with engine speed. Overall, the soot levels are low, but the small increase with speed may be a result of the constant rail pressure used for comparison, which have implications for the diesel plume formation. The selection of this particular rail pressure of 700 bar might result in trends that are more discernible than if a higher rail pressure was chosen. A change of natural gas substitution resulted in an offset in emissions, particularly for CH_4 and CO. This was associated with the change in the quantity of the diesel injected, which resulted in a different injection plume and emissions formation pathway.

Shown in Figure 5-25 are the air and fuel mass flow rates for 80 and 90% substitution. With higher engine speed, air flow rate increases proportionally with fuel flow rate to maintain an in-cylinder λ of approximately 1.54 on average. It is also shown the amount of diesel and natural gas adjusts appropriately with substitution percentage.

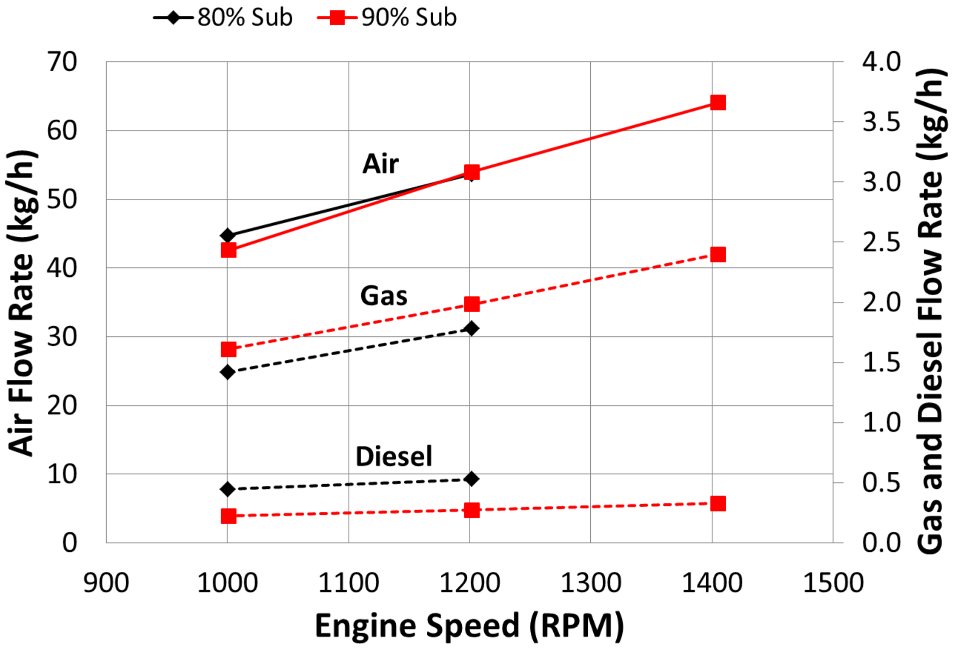

Figure 5-25: Air, natural gas, and diesel mass flow rate vs engine speed for 80 and 90% gas substitution

The data presented in Figure 5-26 confirms the calibration details of the test. CA50 was held in a range of 9.6 to 10.3 deg ATDC with an advancing of SOI to help compensate for the higher engine speed. In-cylinder λ was held between 1.52 and 1.57. The data plotted in Figure 5-27 shows that crank angle based combustion duration lengthens by approximately 1 CAD with every 200 RPM increase. The time it takes for a crank angle to occur decreases with higher engine speed, so combustion duration plotted on a timescale basis is also included. Now considering combustion duration with respect to time, it can be seen that it decreases with higher engine speed as there is greater overall in-cylinder turbulence during the gas exchange process. The higher small scale turbulence increases flame propagation speed, an effect which is well known from SI engines [10]. Furthermore, combustion efficiency decreased with higher engine speed due to the longer combustion duration as well as the diesel rail pressure remaining constant.

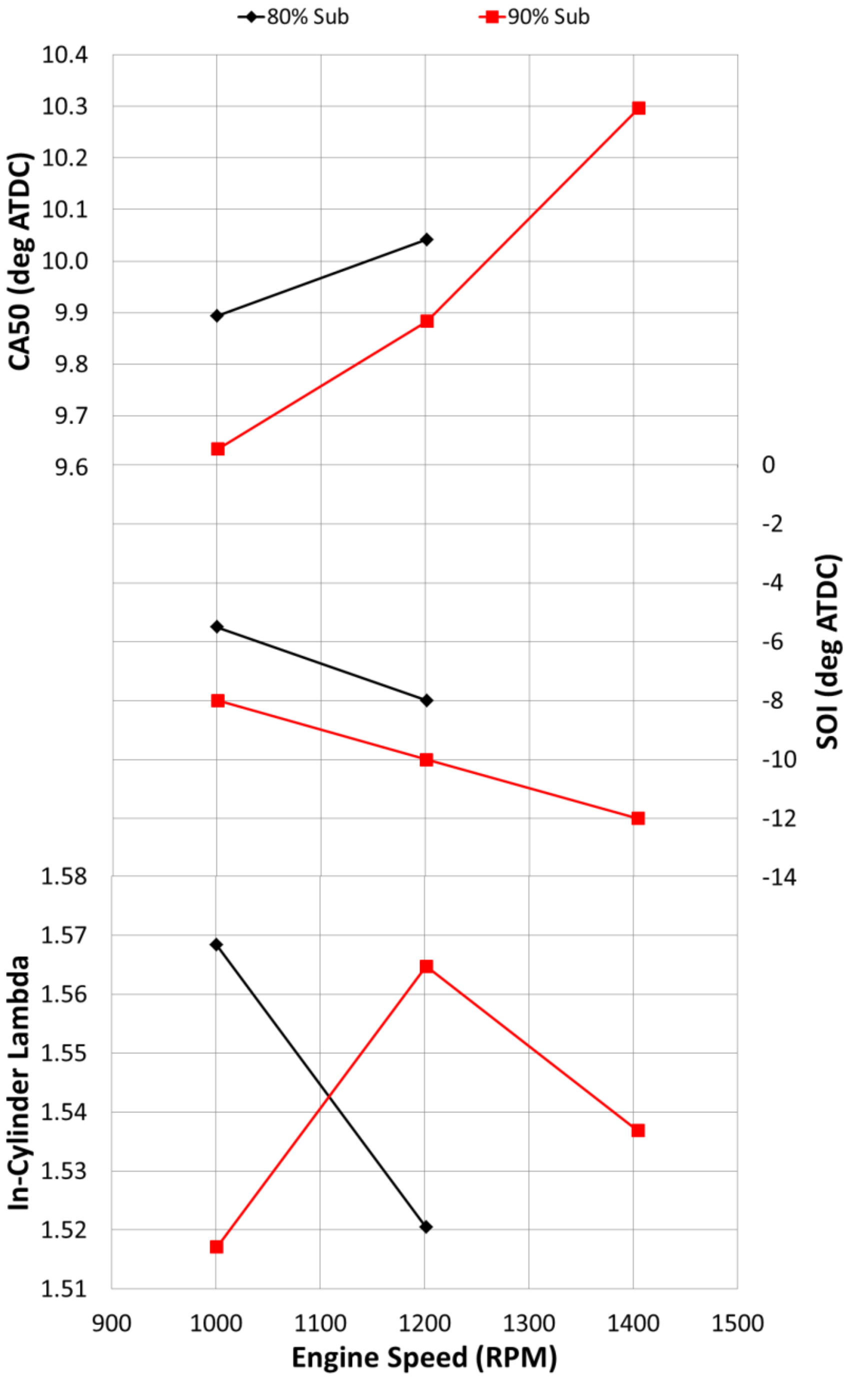

Figure 5-26: CA50, start of injection, and in-cylinder λ vs engine speed for 80 and 90% gas substitution

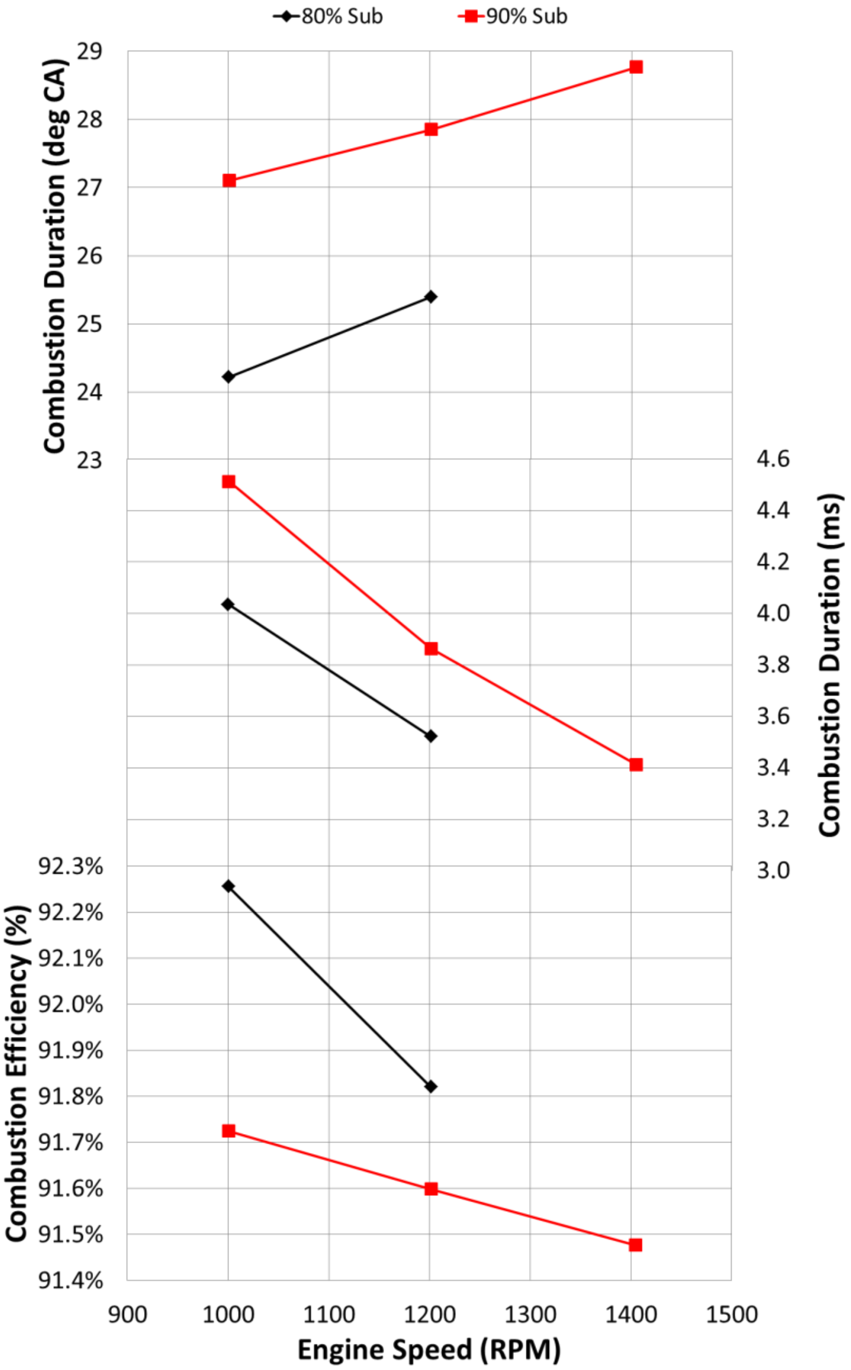

Figure 5-27: Combustion duration (10-90%) and efficiency vs engine speed for 80 and 90% gas substitution

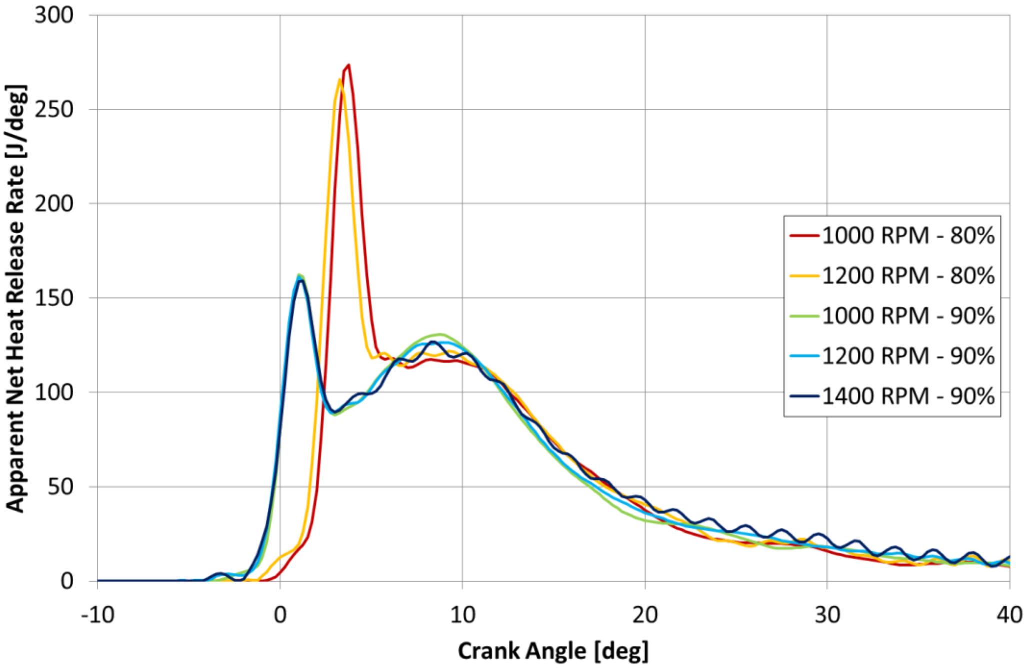

Figure 5-28: Apparent net heat release rate vs crank angle for three different engine speeds and two substitution percentages

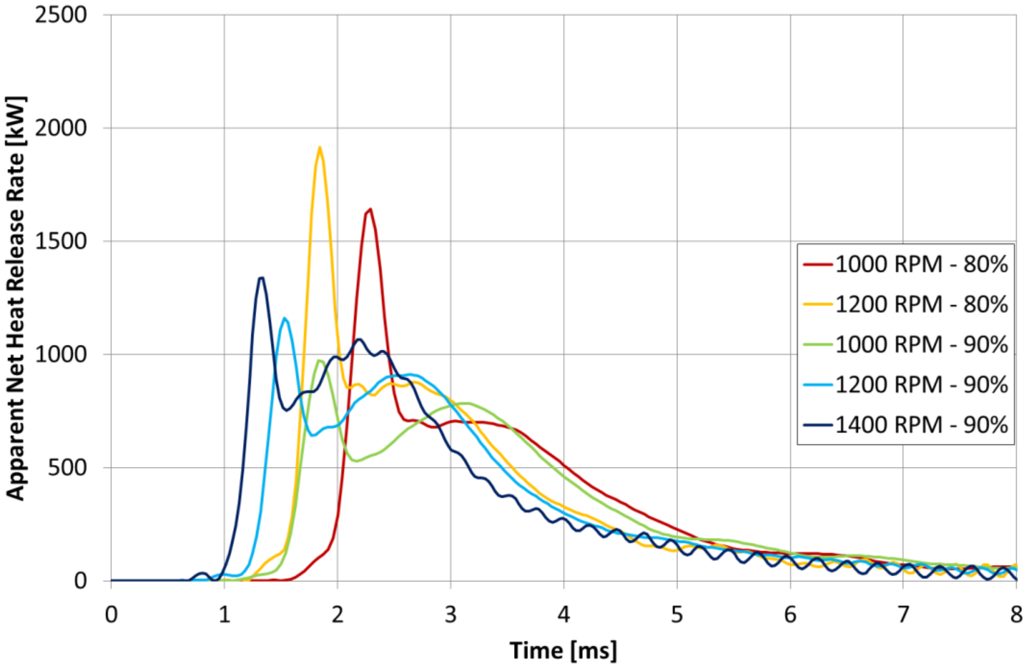

Figure 5-29: Apparent net heat release rate vs time (ms) for three different engine speeds and two substitution percentages

Depicted in Figure 5-28 is the crank angle based heat release for different engine speeds and substitution percentages. From a macroscopic view, it would appear that different engine speeds result in similar very similar HRR profiles when compared on a crank angle degree basis. The data in Figure 5-27 indicates a slight lengthening of 10-90% combustion duration with engine speed. This would be longer if it was not offset by the increased speed in which combustion takes place, as suggested by the data in Figure 5-29. This illustrates the same HRR profiles plotted on a timescale basis and shows the profiles shift to the left (faster) with higher engine speed. This is accompanied by the first combustion peak of the diesel and natural gas fuel being higher, possibly due to better mixing of diesel/air/NG due to increased mixture motion.

Additional observations include that the larger difference in HRR shapes resulted from different gas substitution percentages. A lower initial bump is observed for the higher gas substitution (90%). This is likely to be due to less diesel being available to burn, less diesel spray penetration, and less “ignition area” for NG flame propagation. The larger diesel injection of the 80% case results in a higher initial heat release bump that slightly masks the second bump, which is characteristic of the natural gas portion of the heat release. In the 90% case, the second bump appears to be more pronounced due to the peaks having more separation due to time. However, approximately the same magnitude of heat release is achieved for the second bump in J/deg and kW for both 80% and 90% gas substitution scenarios.

Figure 5-30 includes data for HRR on a timescale basis for diesel-only combustion at 10 bar $IMEP_{net}$. This supports the observation that increased in-cylinder turbulence results in faster combustion in combustion modes other than SI or conventional dual-fuel.

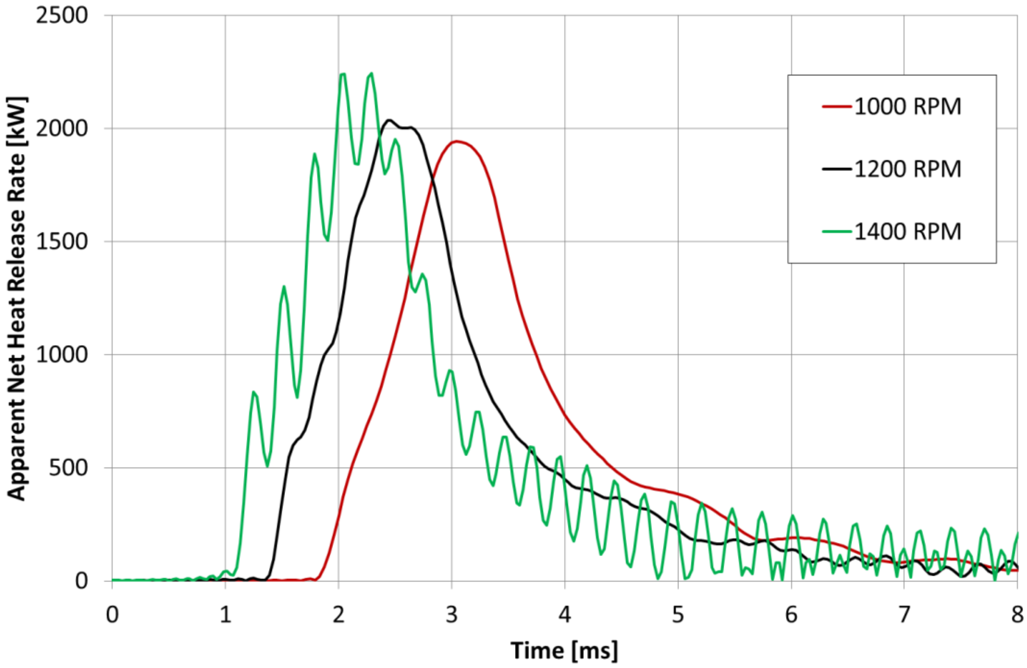

Figure 5-30: Diesel apparent net heat release rate vs time (ms) for three different engine speeds

5.6 Premixed Dual-Fuel Combustion

The goal of the PDFC combustion mode was to achieve lower engine-out emissions and higher thermal efficiency than the diesel and conventional dual-fuel combustion modes outlined in Section 5.4 and 5.5. Once the appropriate baselines for comparison were established, numerous avenues were explored to tackle the emissions and efficiency issues, with special consideration for minimising engine-out methane emissions. For diesel injections, this entailed varying the timing, quantity, and pressure of the injections. Other variables pertaining to the mixture of the charge, such as EGR and λ levels, were also varied. Outlined in Section 5.6.1 are the different trade-offs encountered with engine load along with the most effective way to implement premixed diesel injections. Set out in Section 5.6.2 is a comparison between conventional and PDFC dual-fuel combustion modes with contour plots used to display the emissions and efficiency metrics.

5.6.1 Low, Medium, and High Load Operation

In this section, low (A25), medium (A50), and higher (A70) load conditions are discussed in detail. As in previous sections, the “A” moniker corresponds to an engine speed of 1200 RPM, while 25, 50, and 70 represent loads of 6.0, 12.6 and 17.5 bar $\mathrm{IMEP}_{\mathrm{net}}$, respectively. Scatter plot comparisons of the benefit of PDFC over conventional dual-fuel are shown for A50 and A70, followed by crank angle resolved data for A25, A50, and A70 conditions. Natural gas substitution was calculated by energy, and was approximately 83% ± 2% substitution of natural gas in place of diesel. The reasoning behind this percentage of gas substitution was for a level comparison between PDFC and conventional dual-fuel combustion.

Scatter plots of A50 and A70 were chosen for comparison due to a large and varied data set being available. This allowed for production of a “cloud” of points due to the variety of different sweeps performed. The sweeps performed included changing timing and quantities of the first and second diesel injections, as well as varying injection pressure. Introduction of a third injection for a split pilot injection as well as a post injection were added as well. Finally, experiments adjusting global lambda through fresh air as well as diluent (EGR) were performed. All of the data points from these tests were plotted simultaneously as points on the scatter plots and share the characteristic of using premixed diesel to promote charge flammability. The end goal was to explore the effects of diesel injections as well as overall mixture composition on emissions, specifically that of CH_4.

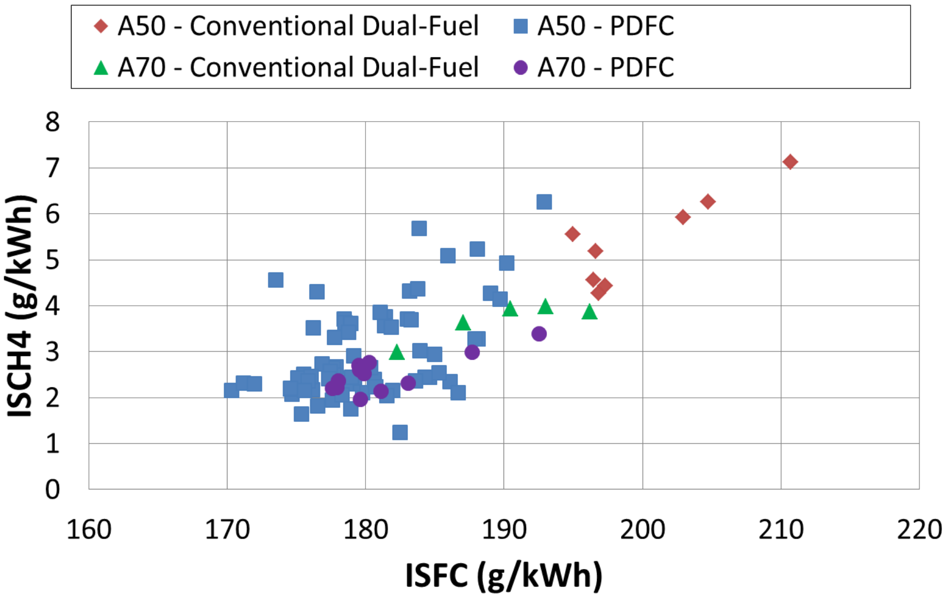

Figure 5-31: $ISCH_4$ vs ISFC for engine operation under PDFC and conventional dual-fuel

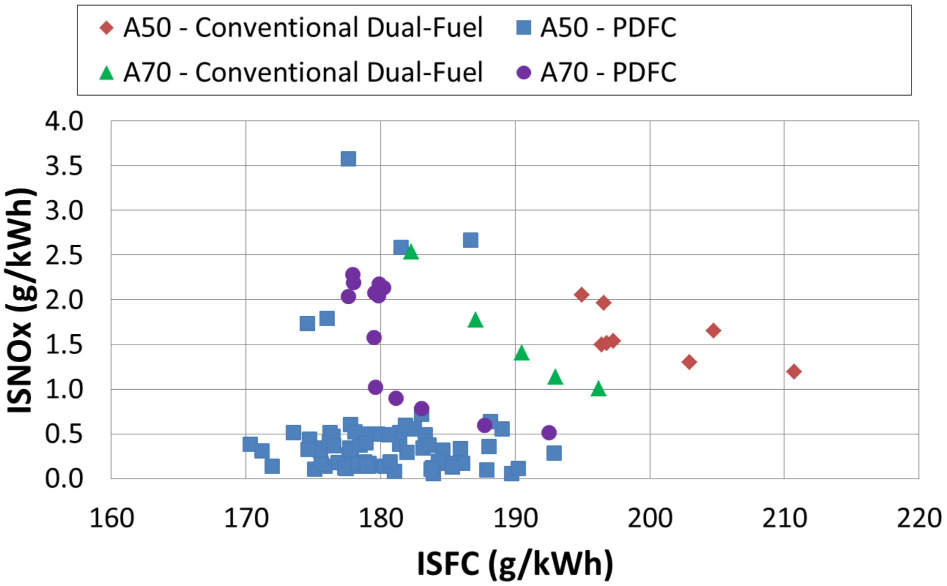

Figure 5-32: ISNOx vs ISFC for engine operation under PDFC and conventional dual-fuel

In Figure 5-31 and Figure 5-32, conventional dual-fuel is depicted by the red diamonds and green triangles for A50 and A70 and the PDFC data is illustrated as blue squares and purple circles, respectively. The premixed diesel injections of PDFC lowers NOx, CO (not shown), ISFC, and CH_4 simultaneously for both A50 and A70 test points. The ISFC values are properly corrected to diesel to account for the differing lower heating values of the fuels. A70 benefits less than A50 due to limitations of maximum cylinder pressure, which is discussed later. The higher values of NOx under PDFC operation in Figure 5-32 are caused by decreasing the EGR amount from approximately 36% to 26%, so the EGR-NOx trade-off remains. The overall shift of improved ISFC for PDFC is driven by increased combustion efficiency and greater thermodynamic efficiency as a result of shorter combustion duration. These traits are associated with PDFC and will be discussed later.

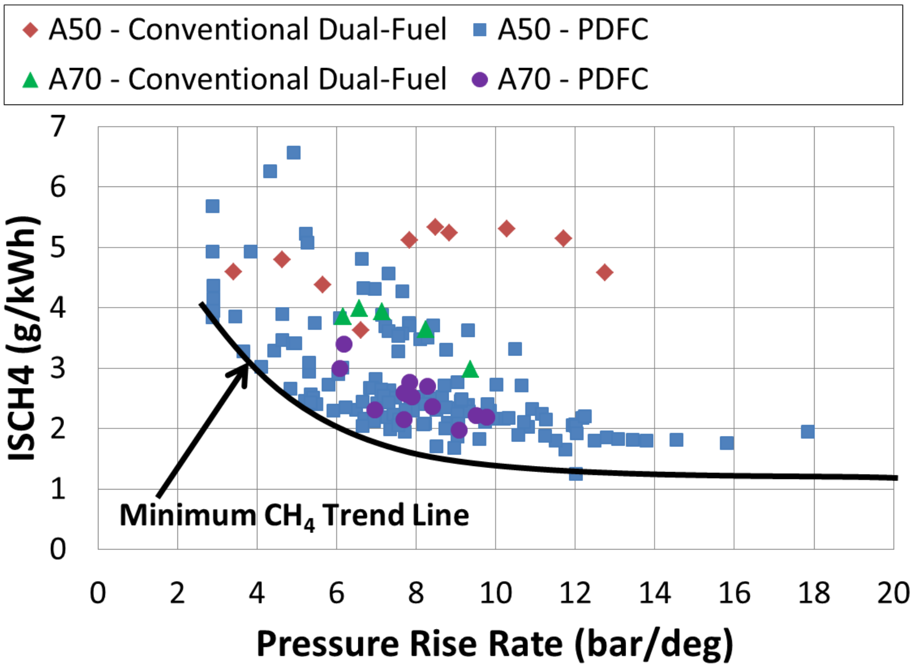

Figure 5-33: $ISCH_4$ vs pressure rise rate for engine operation under PDFC and conventional dual-fuel

A slightly larger data set was considered for Figure 5-33, where methane emissions (CH_4) are plotted against pressure rise rate. Although this includes data from a variety of a different injection, λ, and EGR sweeps, the figure illustrates an interesting trend. PDFC carries a correlation between pressure rise rate and engine-out methane emissions. Points from each of the sweeps appear to reach a minimum CH_4 value which remains steady despite increasing pressure rise rates beyond 10 bar/deg. The exception to this general trend is where very early pilot injections ranging from -160 to -100 deg ATDC as well as split injections (i.e. totalling 3 diesel injections including main) can be made to have a negative effect on CH_4 emissions while maintaining pressure rise rates.

A more in-depth view is shown in Figure 5-34 where $ISCH_4$ is plotted against ISNOx for different case studies. The “X’s” denote very early pilot injections as well as split pilot injections, which resulted in higher CH_4 emissions while maintaining NOx production. Timings and quantities of the diesel injections were swept with the goal of entraining diesel fuel gradually into the mixture, but ultimately this did not prove as effective as a well-timed single pilot injection strategy. This approach might have yielded better results at lower substitution amounts (i.e. 50/50 diesel and natural gas) as it would allow for more diesel fuel to be pre-injected, but the amount of diesel available was limited for higher substitution percentages. Similarly, post injection timings were investigated with the thought that late injections would help burn any remaining CH_4 in the combustion chamber, but this did not have any beneficial effects. Diesel pilot and main injection strategies are shown as effective methods of achieving low NOx and CH_4, but are highly dependent on timing and quantity, which will be discussed later in the chapter. Pushing to higher pressure rise rates (>20 bar/deg) was also tested, but only resulted in slightly lower CH_4 emissions, sometimes at the expense of high NOx. Rail pressure was considered, but was predominately a secondary effect, especially when compared against injection timing and amount.

The influence of EGR and in-cylinder λ on emissions was also addressed. General trends show that for PDFC, there remains a NOx – EGR trade off, where a sufficient amount of EGR is needed to suppress NOx. This typically ranged between 15 to 25% depending on operating conditions. However, CH_4 emissions seem to be independent from this phenomenon once reaching a combustion chamber limited minimum. One exception is at points of very high EGR amounts (>45%), where combustion efficiency rapidly deteriorates due to too much diluent impeding flame propagation. It is known from literature that the presence of burned gas either from EGR or internal residual causes a substantial reduction in the burning velocity and acts as a diluent [10,138]. As burned gas is introduced to the unburnt mixture, it reduces the heating value per unit mass of mixture and results in a lower adiabatic flame temperature. Further, the reduction of burning velocity consequently increases flame stretch [138,139], which can lead to local quenching of fuel and increased CH_4 emissions. When this occurs, emissions quickly deteriorate to conventional dual-fuel levels of CH_4 emissions. In-cylinder λ is also an important factor for natural gas flammability, and generally lower (towards $\lambda = \sim 0.95$) is more favourable [10,138,140,141]. However, along with lower λ typically comes increased NOx production, which can be seen by the blue diamonds off to the right-hand portion of the graph.

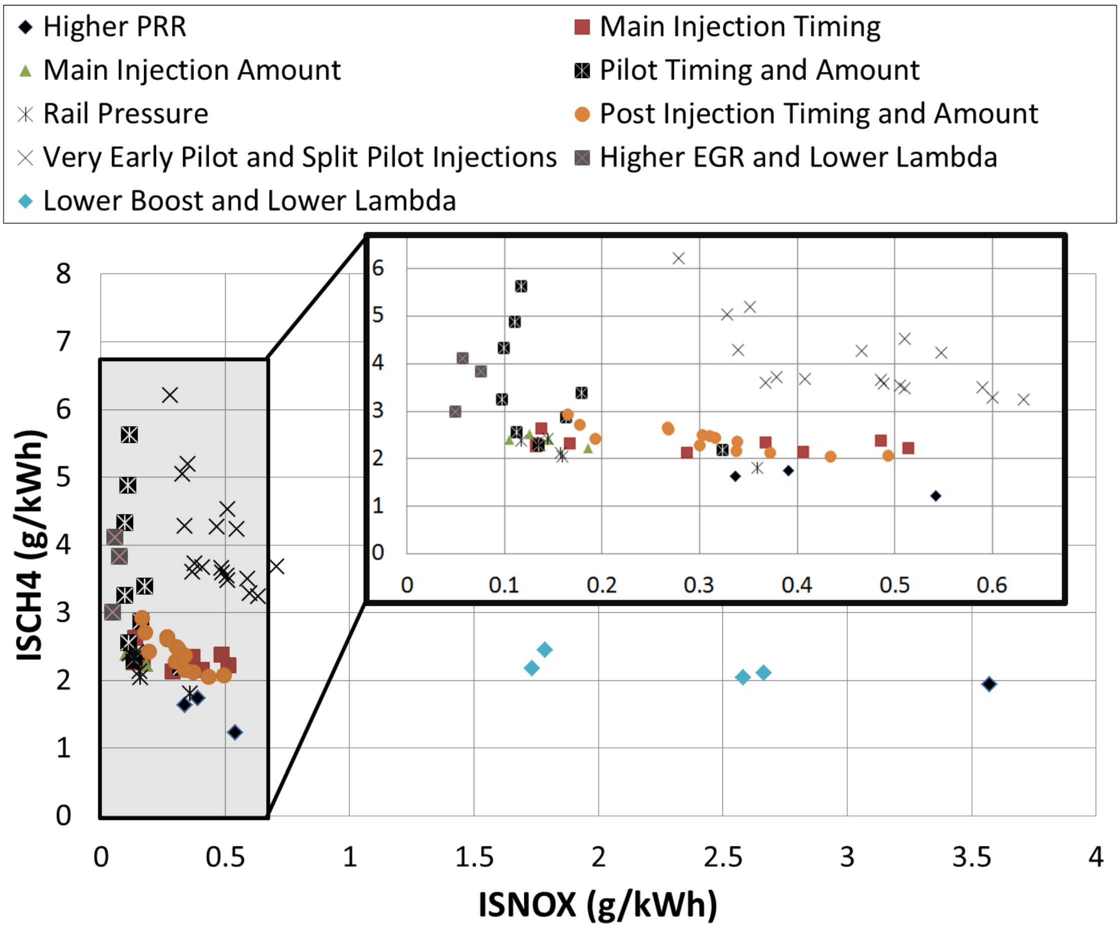

Figure 5-34: $ISCH_4$ emissions vs ISNOx for various sweeps in PDFC

The minimum value of CH_4 emissions are likely caused by limitations of the combustion chamber geometry. Characteristics of conventional diesel combustion chambers include large crevice and squish volumes and piston top lands, which now become relevant if fuel is being included in the premixed charge. Fuel escapes into these crevices and volumes avoiding the combustion flame, ultimately re-emerging and exiting out the tail pipe. These emissions remain, regardless of what can be done in the combustion chamber which serves as an explanation for the levelling out of CH_4 emissions with higher pressure rise rates.

The contribution of the crevice volume on methane emissions can be understood by performing basic hand calculations in conjunction with a few simplifying assumptions. First would be to assume that a homogeneous charge of natural gas, air, and EGR would be introduced into the cylinder, which is reasonable for a gaseous PFI design. The next would be to assume that if 1% of the charge is trapped in crevices, then 1% of the methane injected is not being burned. In an example of PDFC at A50, 3.2 kg/h of natural gas is injected in to the engine, which yields 0.0316 kg/h of methane with an assumed combustion efficiency of 98.6%. Assuming no oxidation or conversion of methane by the exhaust after-treatment, the CH_4 emissions would be roughly equivalent to 600 ppm. Converting 600 ppm to a brake specific CH_4 basis would yield a value of about 1.4 g/kWh, which would be nearly three times the Euro VI limitation of 0.5 g/kWh. A combustion efficiency of at least 99.6% would be needed to achieve 0.5 g/kWh methane emissions on a brake specific basis, something that is likely beyond the limits of a conventional diesel combustion system, as supported by other works [103,104].

Compared in Figure 5-35 to Figure 5-37 are the cylinder pressure traces between diesel, conventional dual-fuel, and PDFC for A25, A50, and A70. The corresponding diesel injection signals are also plotted relative to crank angle. A pilot injection was utilised for the diesel combustion mode.

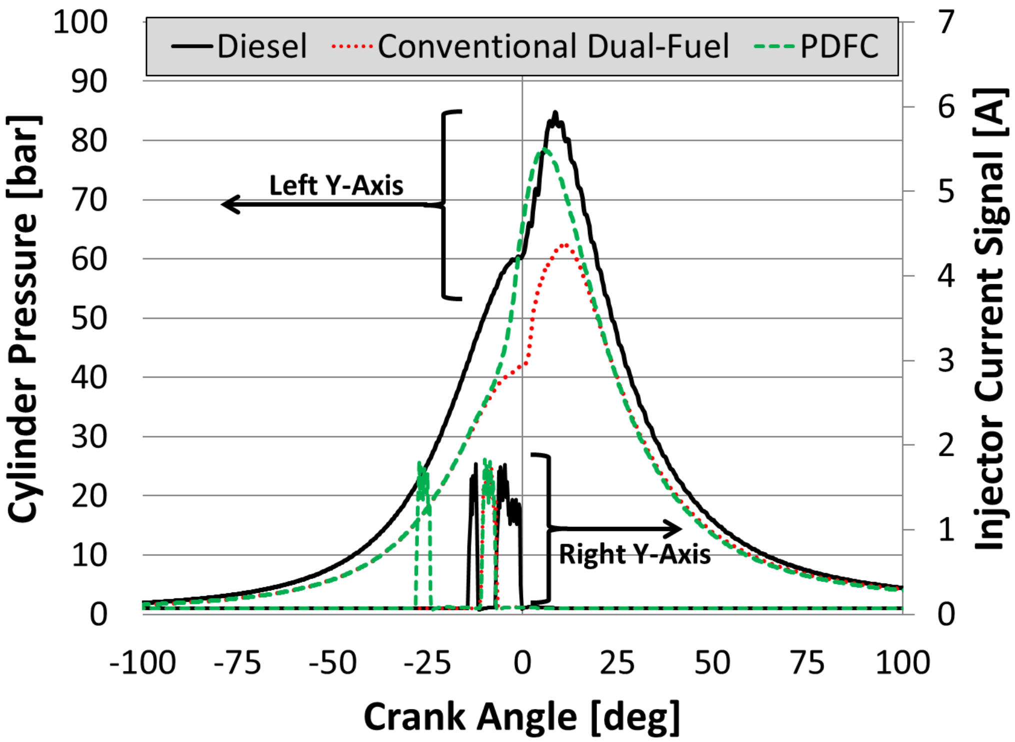

Figure 5-35: Cylinder pressure traces and injection signals vs crank angle for the three combustion modes for A25 (1200 RPM, 25% load)

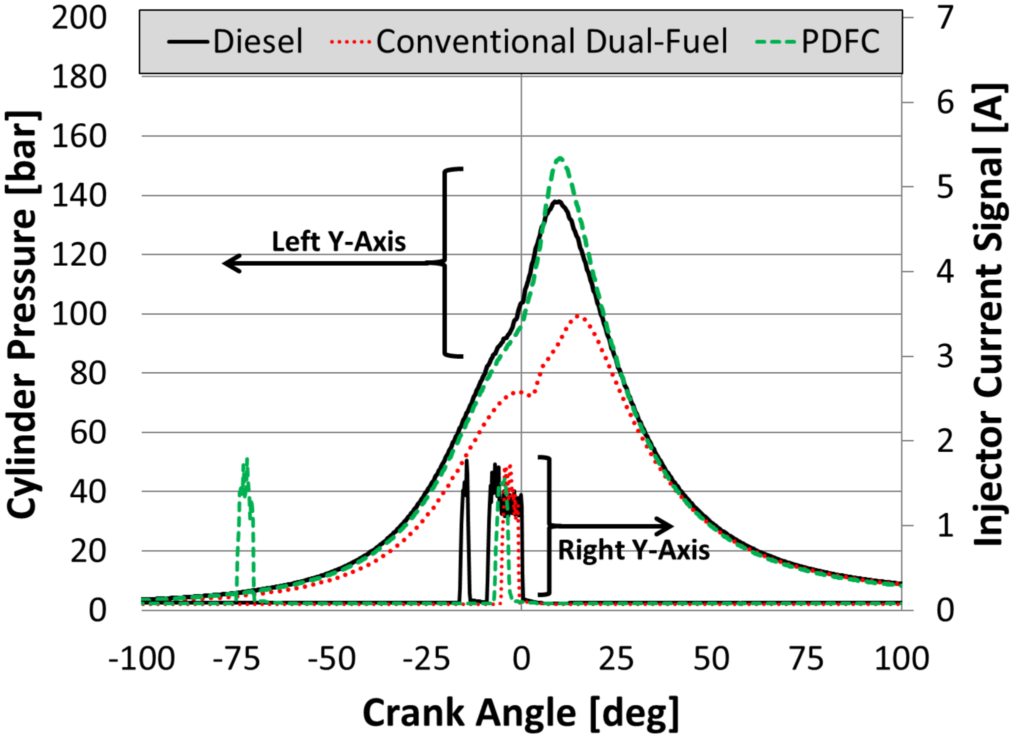

Figure 5-36: Cylinder pressure traces and injection signals vs crank angle for the three combustion modes for A50 (1200 RPM, 50% load)

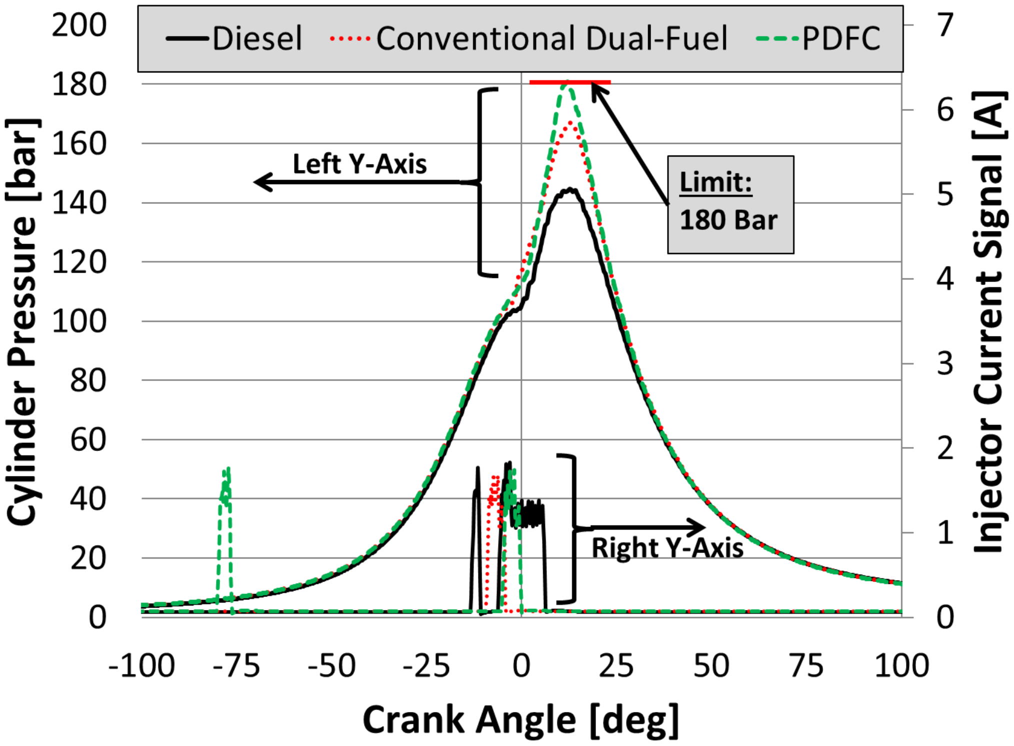

Figure 5-37: Cylinder pressure traces and injection signals vs crank angle for the three combustion modes for A70 (1200 RPM, 70% load)

For Figure 5-35, A25 diesel was matching D13 multi-cylinder conditions of λ = 2.3 with intake boost pressure of 1.3 bar absolute. This is the reason for the higher motoring cylinder pressure relative to dual-fuel as well as higher maximum cylinder pressure. Both conventional dual-fuel and PDFC were run with λ = 1.4, so the cylinder pressures overlay one another until start of combustion. PDFC results in higher maximum cylinder pressure when compared to conventional dual-fuel. A premixed injection (green) is introduced at approximately 26 degrees before TDC, while the second diesel injection is held at roughly 8.6 degrees before TDC.

In Figure 5-36 and Figure 5-37, early injection of diesel can be seen at 72.5 degrees before TDC for A50 and 77.5 degrees before TDC for A70. For A50, there is a large difference between the peak cylinder pressures for conventional and PDFC dual-fuel modes for two reasons. One is the inherent benefit of PDFC adding a premixed diesel injection to promote flammability, and the second is due to the slightly retarded optimisation timing of A50 to minimize THCs. Also for A50, the motoring cylinder pressure trace is slightly lower for conventional dual-fuel because it required less boost pressure due to lower EGR percentage and λ requirements. For Figure 5-37, PDFC is limited at A70 due to the maximum cylinder pressure of 180 bar. A further analysis for these three loads will be discussed at the end of this sub-section.

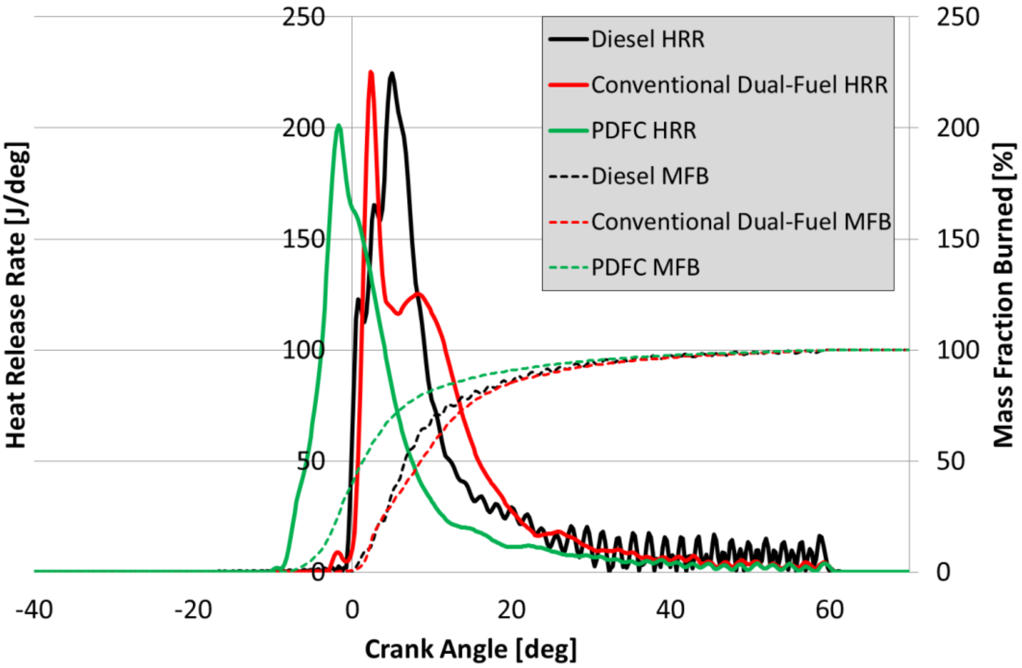

Figure 5-38: Apparent net heat release rate and mass fraction burned for the three different combustion modes for A25

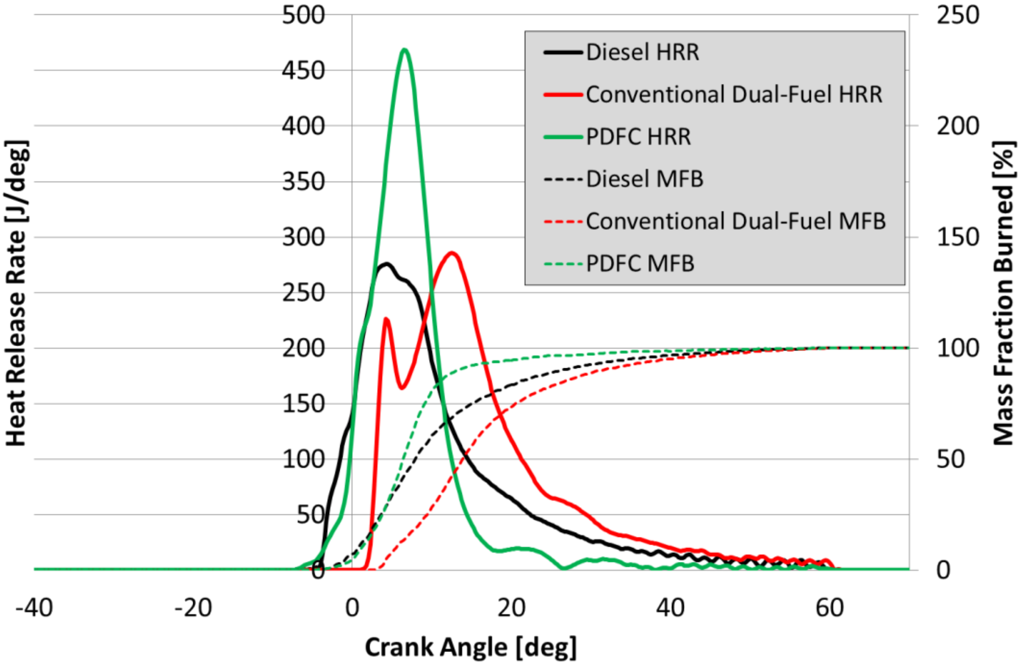

Figure 5-39: Apparent net heat release rate and mass fraction burned for the three different combustion modes for A50

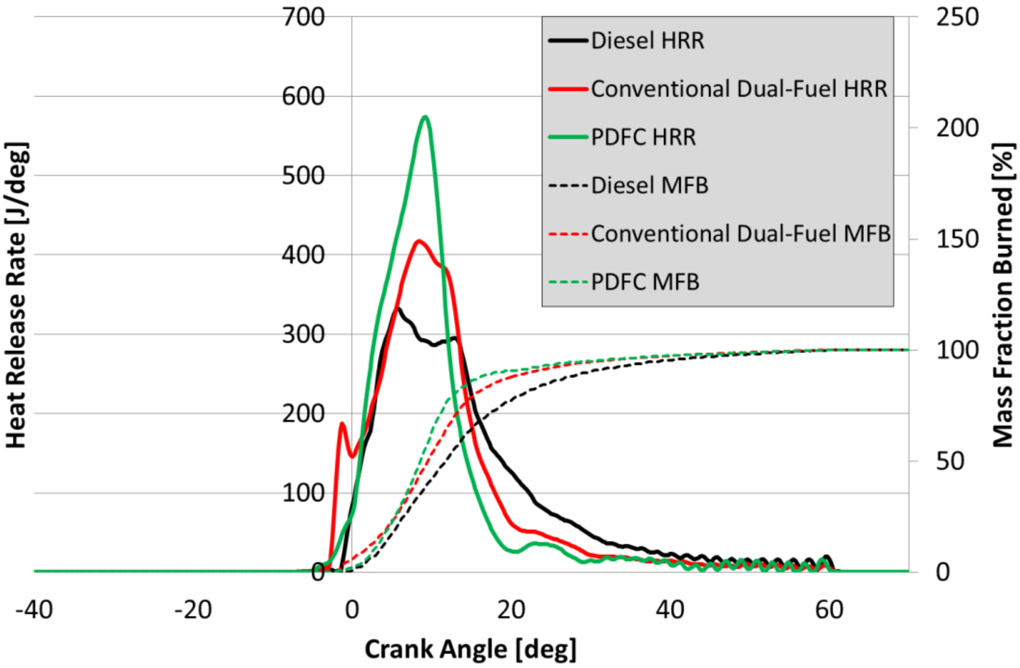

Figure 5-40: Apparent net heat release rate and mass fraction burned for the three different combustion modes for A70

Shown in Figure 5-38 to Figure 5-40 are the apparent net heat release rate and mass fraction burned for the different combustion modes and loads. Comparing the red heat release traces for conventional dual-fuel, there is a distinct “double-humped” nature, where an initial heat release from the diesel injection occurs followed by the ignition and burning of the bulk fuel mass of natural gas. The effect of load can be seen on the rates of heat release, as the shape of the double-hump changes. At low load (A25), the diesel heat release spikes, followed by a slow burning and low levels of heat release of the natural gas charge. For A50, the second hump is larger in magnitude, helped by a slightly lower lambda and higher in-cylinder temperatures. Finally, there is A70 which has a highest level of heat release in the second hump, aided by bulk ignition of the end gas as mentioned in the conventional dual-fuel baseline section.

For A50 and A70, PDFC (green) is characterised by high heat release rate, short combustion duration, and high cylinder pressure when compared against diesel and conventional dual-fuel. The early injection of diesel alters the flammability of the natural gas/EGR/fresh air charge, so when the main diesel injection occurs, there are multiple sites for ignition and potential flame propagation due to favourable chemical kinetics. This differs from the double-hump nature of conventional dual-fuel as there are no longer two distinct humps. For A25, the peak heat release is slightly lower but the shape of the HRR line is closer to a single peak, resulting in shorter combustion duration. The optimum heat release is also phased slightly before TDC in this particular case, but could be retarded by altering the split ratio between the two diesel injections. Finally, Figure 5-41 includes the PDFC heat release and mass fraction burned traces overlaid for the three different loads, demonstrating the similar shapes between them.

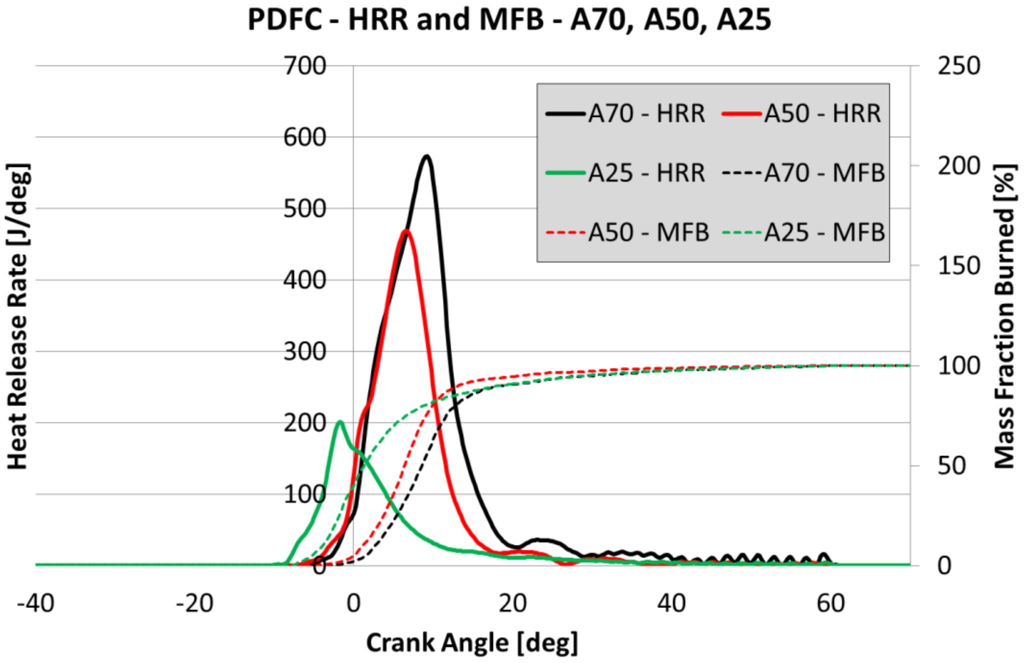

Figure 5-41: Apparent net heat release rate and mass fraction burned for A25, A50, and A70 operating under PDFC

The quantities and timings of the diesel injections are critical in determining combustion behaviour. The diagram in Figure 5-42 shows the sensitivity tests performed to the first and second diesel injections. The results of the timing and quantity sweeps are summarised in the bullet points below.

- First (Premixed) Injection Timing ([A] and [C]):
  Advancing timing results in lower heat release rates, PMax, pressure rise rates, longer combustion but worse emissions (except NOx). The opposite is true for retarding timing [C].

- First (Premixed) Injection Quantity [B]:

  Increasing quantity yields similar effects to retarding first injection timing and decreasing quantity yields similar effects to advancing first injection timings.

- Second (Ignition) Injection Timing ([D] and [F]):

  Advancing timing (to optimum/MBT) results in higher heat release rates, PMax, pressure rise rates, and shorter combustion. The opposite is true for retarding timing [F].

- Second (Ignition) Injection Quantity [E]:

  Increasing/decreasing quantity yields similar effects to advancing/retarding second injection timing respectively.

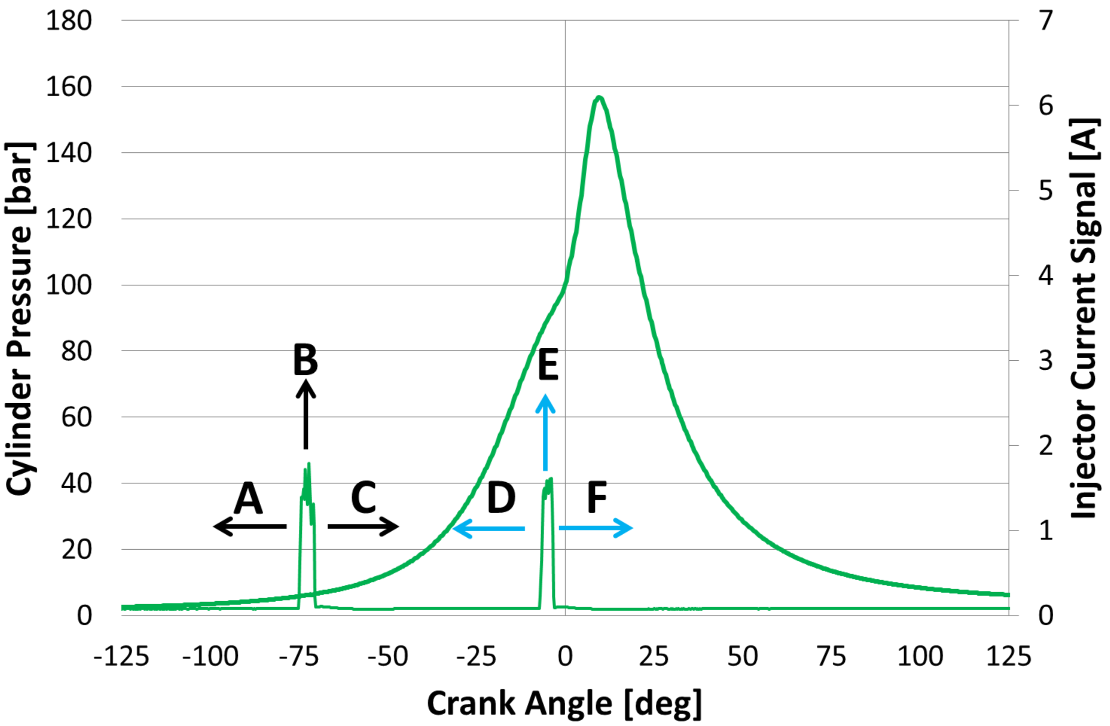

Figure 5-42: PDFC cylinder pressure trace with pilot and main injection signals

These observations are true for all speed-load conditions that were tested for PDFC, as opposed to RCCI or HCCI combustion modes. Additionally, this would cover injection timings from approximately -160 to -25 deg ATDC for the first injection, and -20 to 25 deg ATDC for the second injection.

The first diesel injection adjusts the degree of premixing that takes place. There are two ways to adjust mixture flammability using this injection, either by timing or quantity. Non-uniform EQR drives differences in the local chemical kinetic reaction rates, which in turn influence the ignition delay and resulting combustion duration. The later the diesel is injected, the higher the non-uniformity is in the cylinder charge before it reaches ignition temperature and pressure. Since diesel is a highly reactive fuel it will be more likely to ignite with the pressure and temperature of compression than if mixed with diluent and less reactive CH_4. However, introducing diesel fuel too late will reduce the chance for premixing and uniform adjustment of mixture flammability resulting in increased emissions. Finally, the quantity of diesel fuel injected can also adjust the mixture flammability by entraining larger or smaller amounts of high reactivity fuel.

The second injection timing of diesel is analogous to spark timing effects in gasoline engines. Advancing injection timing phases the start of combustion closer to TDC, resulting in higher cylinder pressures and pressure rise rate. It also has an effect on the premixed charge since the rise in pressure and temperature will adjust the timing of auto-ignition of the entrained diesel fuel. Increasing or decreasing the quantity of the second injection adjusts the local equivalence ratio of the diesel, shifting the ignition delay to earlier or later, respectively. It should also be noted that the sensitivity to the second injection timing and quantity is decreased when combustion is closer to auto-ignition, which is primarily controlled with the first injection. The effect of the second injection is also affected by the charge composition or temperature, with the timing and quantity having less of an influence on combustion timing with increased amounts of EGR.

As load is decreased, less diesel fuel is available for the two injections simply because of the lower total fuelling amount, assuming a constant substitution ratio of natural gas. This is an issue for light load conditions, as more diesel fuel would need to be premixed in order to promote mixture flammability at leaner and lower temperature/pressure situations. Additionally, the second injection would still be required to provide adequate ignition energy for an increasingly inert mixture. To address these issues, it is necessary to move the premixed injection closer to

TDC in order to introduce stratification and non-uniform EQRs. However, reducing the amount of diesel injected in combination with retarding the first injection will result in an increasingly stratified mixture, yielding a smaller number of ignition sites when auto-ignition of the bulk end-gas occurs. There is still a benefit to CH_4 and CO emissions, but increasingly at the expense of NOx.

At higher loads, the first diesel injection can be moved further away from TDC, increasing the uniformity of the entrained diesel. This in theory is beneficial due to the larger number of ignition sites when auto-ignition occurs. However, the first diesel injection of the A70 case is limited in quantity due to the cylinder pressure limitation of 180 bar. It should also be stated that injecting too far advanced with a premixed injection with too large of a quantity of diesel results in high CO and HC emissions, most likely due to the diesel spray impinging on the cylinder bore.

Finally, a combustion mode comparison in terms of a frequency spectrum is shown in Figure 5-43. All three combustion modes have high amplitudes of frequency around 4-5 kHz suggesting a first circumferential mode of resonance, as expected for this diesel bowl combustion chamber layout [122,142].

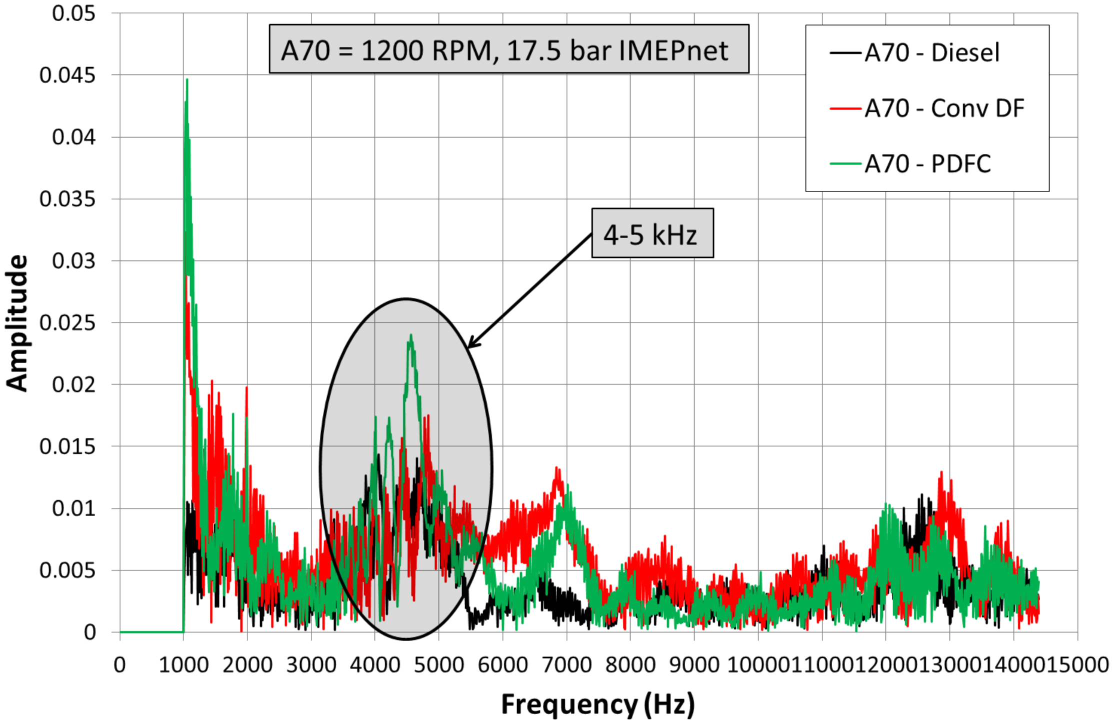

Figure 5-43: Frequency spectrum for three combustion modes at A70

PDFC has the highest normalised amplitude in the 4-5 kHz region when compared against diesel and conventional dual-fuel modes, which might suggest higher levels of auto-ignition.

5.6.2 Conventional Dual-Fuel and Premixed Dual-Fuel Combustion

This section includes a comparison of conventional dual-fuel and PDFC combustion modes with respect to emissions and efficiency. Percent reductions and improvements are calculated by subtracting the PDFC value from conventional and dividing the difference by the original conventional value.

Shown in Table 5-3 is the percent reduction in key emissions as well as improvements in efficiency when utilizing PDFC over conventional dual-fuel. This is for the selected test points and shows the benefit sensitivity to speed and load. The values are colour-scaled in that green shows a positive improvement to emissions or efficiency while red depicts degradation. A positive % benefit of ISFC indicates improved (lower) ISFC. The details of these calibrations can be found in Table 5-4 and Table 5-5, including soot values which remain comparable between the two dual-fuel modes.

Figure 5-44 to Figure 5-50 include speed/load contour plots that were generated with a larger dataset. Intention was to better visualize the significant improvements brought about by the premixed diesel injections of PDFC and the limitations it faces with load.

Table 5-3: Percent reduction in key emissions and improvements in efficiency comparing PDFC to conventional dual-fuel for selected test points

	Engine Speed	**Load**	**NOx**	**CH4**	**THC**	**CO**	**ISFC**	**Combustion Efficiency**	**Combustion Duration**
	RPM	**bar**	**%**	**%**	**%**	**%**	**%**	**%**	**%**
A70	1200	17.5	9	25	26	26	2.4	-0.6	22
A50	1200	12.6	58	61	54	48	6.9	-1.7	55
Z40	1000	9.8	-54	66	63	62	5.9	-3.5	53
A40	1200	9.8	-30	64	61	57	5.2	-3.6	51
A35	1200	8.5	-10	73	69	61	7.4	-4.8	53
A30	1200	7.3	52	43	35	22	3.7	-1.7	20
Z25	1000	6.0	45	27	24	25	3.4	-1.6	22
A25	1200	6.0	-75	15	16	14	2.1	-1.2	4

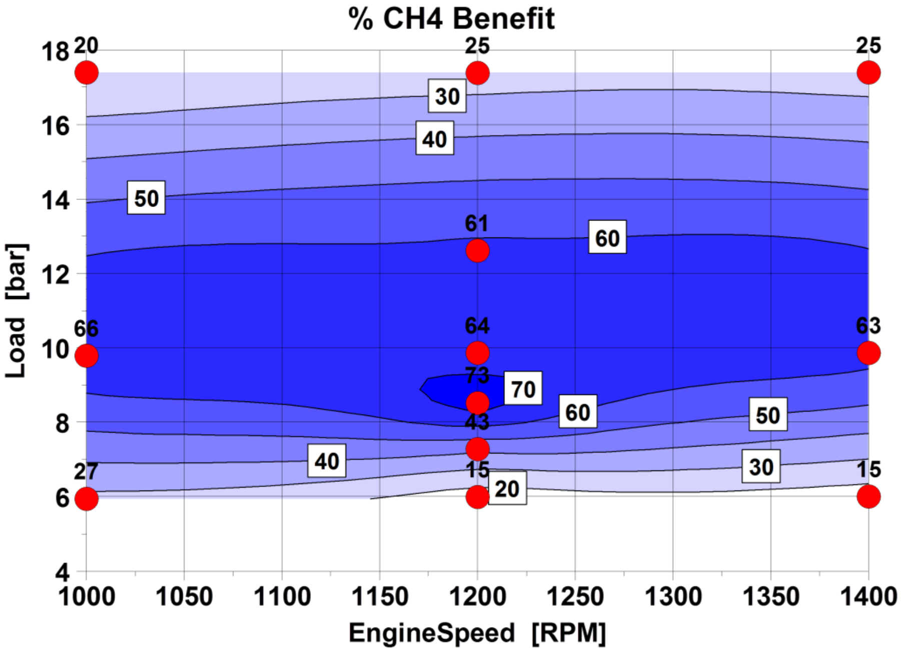

Figure 5-44: Speed/load contour plot depicting the percent reduction in engine-out CH_4 emissions operating under PDFC over conventional dual-fuel

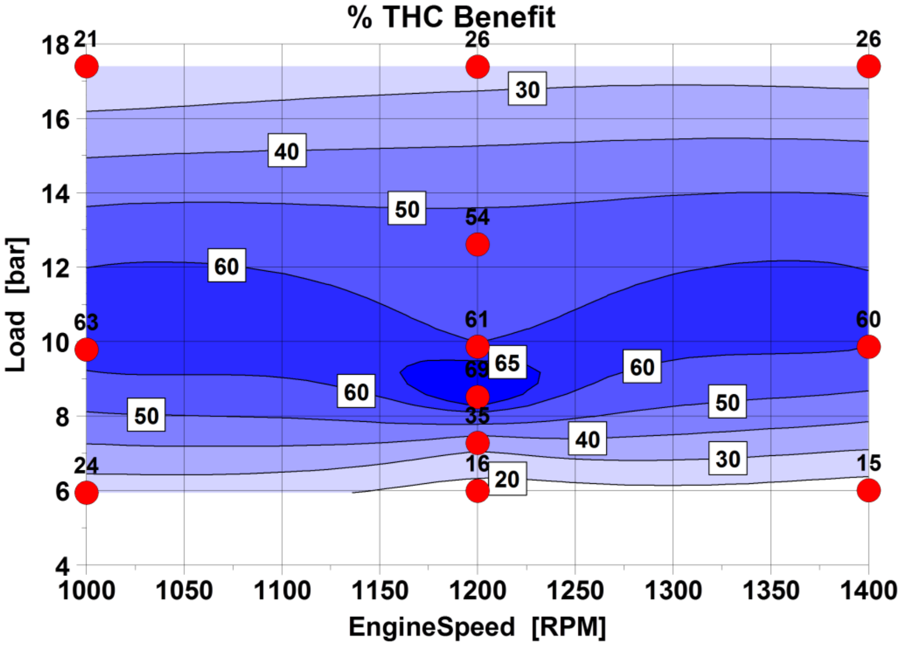

Figure 5-45: Speed/load contour plot depicting the percent reduction in engine-out THC emissions operating under PDFC over conventional dual-fuel

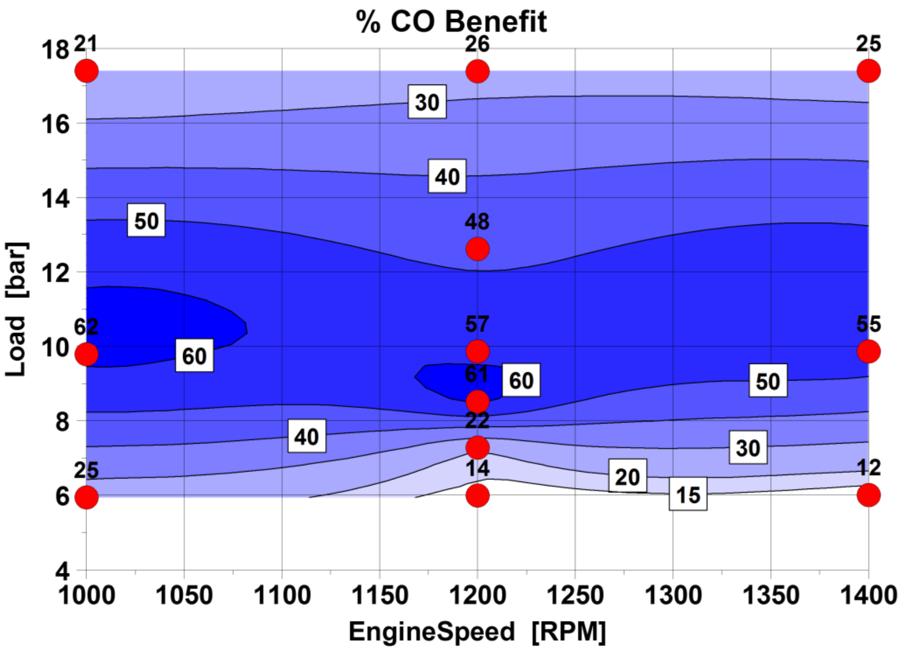

Figure 5-46: Speed/load contour plot depicting the percent reduction in engine-out CO emissions operating under PDFC over conventional dual-fuel

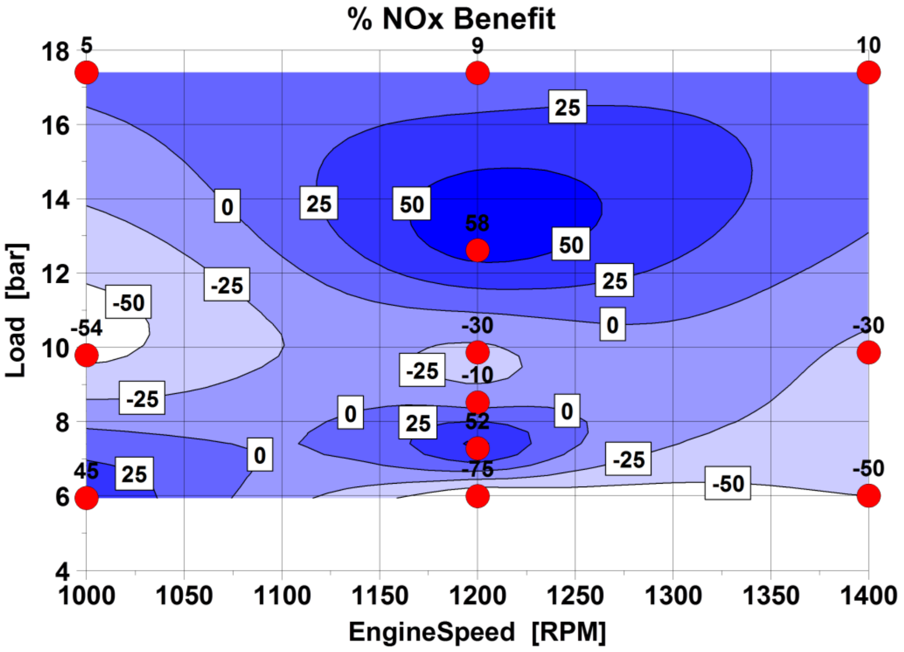

Figure 5-47: Speed/load contour plot depicting the percent reduction in engine-out NOx emissions operating under PDFC over conventional dual-fuel

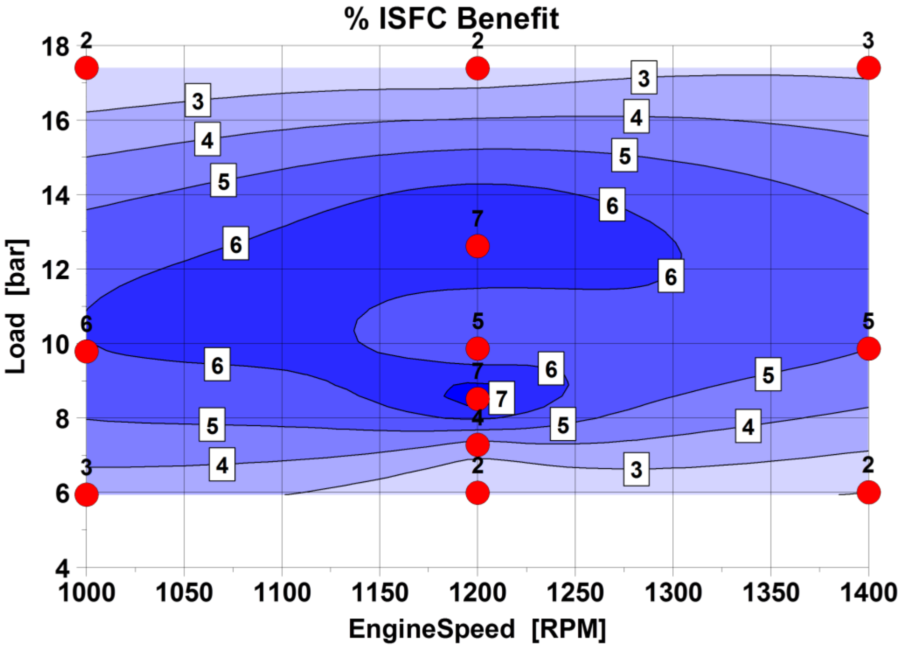

Figure 5-48: Speed/load contour plot depicting the percent improvement in ISFC operating under PDFC over conventional dual-fuel

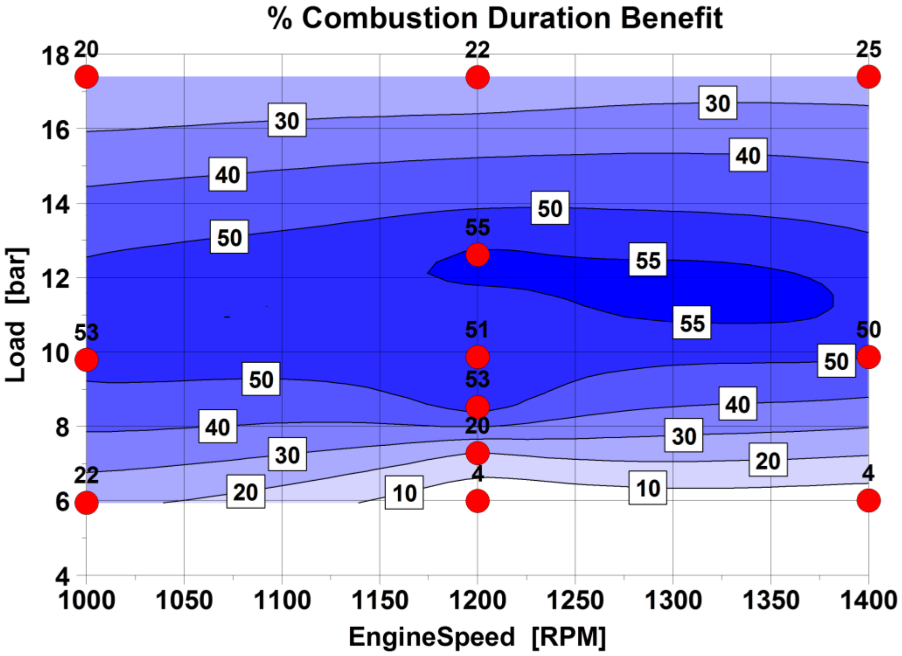

Figure 5-49: Speed/load contour plot depicting the percent reduction in combustion duration (10-90%) operating under PDFC over conventional dual-fuel

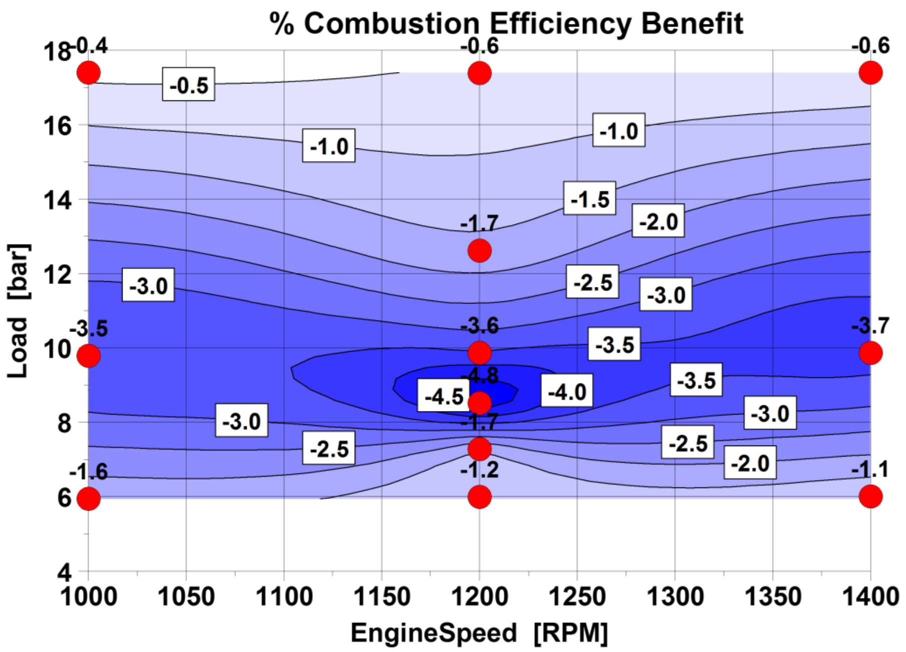

Figure 5-50: Speed/load contour plot depicting the percent benefit in combustion efficiency operating under PDFC over conventional dual-fuel

PDFC demonstrates its ability to reduce emissions (Figure 5-44 to Figure 5-47) as well as improving fuel efficiency (Figure 5-48) over conventional dual-fuel. From the previous section, it is shown that premixing a quantity of diesel adjusts the mixture flammability and presumably allows for multiple ignition sites to occur. The more complete combustion reduces flame quenching, resulting in reduced combustion duration and increased combustion efficiency, as shown in Figure 5-49 and Figure 5-50. The combination of burning more of the fuel supplied to the cylinder, along with the increased thermodynamic efficiency resulting from shorter combustion duration are the reasons for the reduction in emissions as well as improvement in efficiency.

These benefits to emissions and efficiency are best observed in the medium load regime, where the engine is not yet cylinder pressure limited, but there are favourable in-cylinder conditions for combustion (temperature, pressure, and lower λ). Net indicated thermal efficiency increased from 44.5% in conventional dual-fuel to 47.7% in PDFC for 1200 RPM 50% load. The diesel injection strategy for A50 PDFC operation was approximately a 55/45 split of diesel between the first and second injections. For this particular speed load condition, a 15 mm^3 first injection was used with a 13 mm^3 second injection.

Higher loads, such as A70, have a reduced benefit due to the hard limitation of maximum cylinder pressure. The reduced amount of premixed diesel resulted in a 42/58 split between injections, amounting to a 16 mm^3 first and a 22 mm^3 second injection. Furthermore, NOx emissions could have been improved with adding more EGR, but CO emissions and ISFC would begin to degrade. If more boost was applied to maintain λ, then even less diesel could be premixed, as the cylinder pressure limitation of 180 bar would be reached sooner due to the additional in-cylinder mass.

For light load conditions, there is still a benefit to PDFC, but there are concerns regarding λ, as well as having enough temperature and pressure to auto-ignite the ever-decreasing quantity of diesel available, if reducing load. This is the reason for the degradation of benefits as load is decreased. Several strategies exist that could change the effectiveness of dual-fuel combustion at light load. Some of these include throttling to decrease in-cylinder λ, Miller cycle operation to raise exhaust gas temperatures for after-treatment and decrease in-cylinder λ, use of internal EGR to raise in-cylinder temperature, or simply decreasing the substitution ratio of natural gas. These improvements will generally come at the expense of NOx emissions however. These strategies, among others, will be discussed in Chapter Six.

The NOx trade-off is something that can be observed in Table 5-3. NOx is extremely sensitive to combustion temperature, effectively translating into ignition timing, quantities of diesel premixed, and EGR for the purposes of this work. There exists some “noise” or experimental variability in the calibrations chosen for comparison, which is the reason for the inconsistent production of NOx observed in Figure 5-47. If a more consistent level of NOx production is desired, then it can be traded off with all other emissions and efficiency, as shown between the comparisons of A30 and A35. The importance of reducing CH_4 at the expense of NOx is something that must be considered as well.

The improvement in emissions and fuel efficiency are typical of LTC. NOx emissions are reduced by decreasing peak combustion temperatures with EGR. The EGR decreases the combustion temperature due to the increased specific heat capacity of the intake charge as well as working as a diluent (less oxygen concentration). As alluded to in Section 5.6.1, a sufficient amount of EGR was necessary to achieve this form of combustion with acceptable NOx, indicating at approximately 21%. Removing EGR did not have a large effect on CH_4 emissions but had a large impact on NOx emissions, which quickly increased. Once again, adding EGR amounts greater than 45% while maintaining boost pressure resulted in poor combustion efficiency, longer combustion durations, and high CO and THC emissions. This was likely due to the diluent impeding adequate flame propagation and curbing combustion temperature. Furthermore, high amounts of EGR are not favourable or production feasible. High EGR percentages place greater demands on the boosting systems of the engine in order to supply enough fresh air for lean operation and it increases the maximum cylinder pressure of the engine, which will limit the upper load range of LTC operation.

Finally, the combustion efficiency of conventional dual-fuel is less than that of diesel due to the flame propagation type combustion as well as fuel likely being trapped in piston crevices with the stock diesel piston. PDFC improves combustion efficiency to 98.3% for the best cases, but is likely limited by the crevice volumes of the stock diesel piston. Modifications can be made to the standard diesel piston to improve combustion efficiency and reduce emissions in dual-fuel operation [96,103,104]. These can include machining a chamfer on the piston top land to assist out-gassing and flame penetration. Surface area of the diesel piston bowl can also be optimised to reduce heat losses during combustion.

The calibrations found in the Table 5-4 and Table 5-5 support that PDFC can attain near diesel levels of ISFC with similar or lower levels of NOx and PM emissions at medium to higher loads. Dual-fuel encounters challenges relative to diesel operation at lighter loads, where low combustion efficiency (94%) compared to diesel (99.9%) inhibits efficient fuel conversion. THC, CH_4, and CO emissions for diesel remain low, but utilization of natural gas would prove to be more cost effective.

Table 5-4: Injection quantities and emissions summary of selected test points

Engine Speed	Load	Combustion Mode	Diesel Pilot Timing	Diesel Main Timing	Diesel Pilot/Main Quantity	NOx	CH4	THC	CO	FSN	ISCH4	ISNOx	ISFC
RPM	bar		deg CA ATDC	deg CA ATDC	mm3	ppm	ppm	ppm	ppm		g/kWh	g/kWh	g/kWh
1200	17.5	Diesel	-10.8	-3.5	3/232	457	40	47	65	0.14	0.1	2.8	183
1200	12.6	Diesel	-13.0	-5.8	3/149	508	6	52	40	0.15	0.0	3.5	181
1000	9.8	Diesel	-10.8	-4.8	3/117	728	9	55	24	0.05	0.0	5.8	180
1200	9.8	Diesel	-14.0	-6.8	3/117	621	7	55	28	0.06	0.0	4.9	180
1200	8.5	Diesel	-14.0	-6.8	3/103	606	9	59	32	0.07	0.0	5.1	181
1200	7.3	Diesel	-12.0	-4.8	3/87	510	9	63	42	0.09	0.0	4.6	184
1200	6.0	Diesel	-12.0	-4.8	3/73	462	10	72	54	0.13	0.0	4.4	187
1200	17.5	Conv DF	None	-6.7	32	477	1478	1715	430	0.10	3.0	2.5	182
1200	12.6	Conv DF	None	-3.1	23	248	2101	2655	645	0.19	4.2	1.4	190
1000	9.8	Conv DF	None	-6.3	21	369	3876	4028	875	0.10	8.8	2.2	195
1200	9.8	Conv DF	None	-10.8	19	812	2439	2665	597	0.12	5.0	4.2	186
1200	8.5	Conv DF	None	-9.0	17	435	4610	4827	947	0.07	10.8	2.7	197
1200	7.3	Conv DF	None	-12.8	16	797	3436	3641	753	0.07	7.7	4.8	194
1000	6.0	Conv DF	None	-15.8	11	758	4755	4919	871	0.05	11.6	4.9	199
1200	6.0	Conv DF	None	-8.7	13	391	5122	5475	1036	0.22	12.4	2.5	199
1200	17.5	PMPC DF	-77.5	-2.5	16/22	434	1108	1274	317	0.10	2.2	2.3	178
1200	12.6	PMPC DF	-72.5	-4.3	15/13	104	812	1214	336	0.10	1.7	0.6	177
1000	9.8	PMPC DF	-60.8	-8.3	12/10	568	1310	1484	336	0.14	3.0	3.5	184
1200	9.8	PMPC DF	-65.5	-8.5	12/10	1055	878	1039	257	0.11	1.8	5.5	177
1200	8.5	PMPC DF	-55.8	-9.0	11/10	477	1232	1479	369	0.12	2.9	2.9	182
1200	7.3	PMPC DF	-55.8	-11.0	10/8	379	1973	2379	585	0.05	4.4	2.3	187
1000	6.0	PMPC DF	-34.0	-11.5	7/4	416	3450	3751	656	0.08	8.4	2.6	192
1200	6.0	PMPC DF	-25.8	-8.6	9/8	684	4329	4588	891	0.28	10.5	4.4	195

Table 5-5: Test conditions and combustion parameters of selected test points

Engine Speed	Load	Combustion Mode	Pmax	PRR	CA50	Combustion Duration	Combustion Efficiency	Lambda	EGR %	Intake Pressure	Rail Pressure	Exhaust Gas Temp
RPM	bar		bar	bar/deg	deg CA	deg CA	%		%	bar	bar	degC
1200	17.5	Diesel	144.8	8.0	11.6	26.2	99.91%	1.38	20.1	2.2	1700	488
1200	12.6	Diesel	132.9	7.5	8.6	25.0	99.90%	1.67	21.1	2.0	1307	396
1000	9.8	Diesel	128.0	10.4	5.8	20.0	99.89%	1.97	20.3	1.9	1209	330
1200	9.8	Diesel	127.5	8.5	5.6	21.9	99.89%	1.96	21.2	1.9	1306	338
1200	8.5	Diesel	117.3	7.7	5.3	22.0	99.88%	2.07	21.1	1.7	1211	322
1200	7.3	Diesel	98.4	7.9	6.8	20.9	99.85%	2.18	20.3	1.5	1211	309
1200	6.0	Diesel	85.2	9.0	6.6	21.1	99.82%	2.27	19.8	1.3	1109	299
1200	17.5	Conv DF	166.9	9.4	9.3	20.8	97.77%	1.27	23.6	2.4	1153	488
1200	12.6	Conv DF	99.4	6.0	13.7	26.0	96.70%	1.22	21.9	1.7	1067	528
1000	9.8	Conv DF	99.3	9.7	9.1	26.4	94.54%	1.34	21.9	1.5	896	428
1200	9.8	Conv DF	105.4	9.1	5.1	25.9	94.90%	1.29	20.6	1.3	997	434
1200	8.5	Conv DF	89.5	9.5	7.9	26.7	93.33%	1.38	21.8	1.3	989	408
1200	7.3	Conv DF	87.6	9.8	3.3	23.8	95.08%	1.34	21.3	1.1	997	404
1000	6.0	Conv DF	75.7	6.4	2.1	29.1	92.99%	1.44	21.5	1.0	803	359
1200	6.0	Conv DF	62.6	6.6	8.6	23.1	92.28%	1.41	21.2	1.0	1001	393
1200	17.5	PMPC DF	181.0	9.5	8.6	16.2	98.32%	1.29	23.6	2.4	1145	475
1200	12.6	PMPC DF	152.5	8.5	6.6	11.6	98.33%	1.34	33.9	2.0	1069	390
1000	9.8	PMPC DF	124.9	9.5	4.5	12.5	97.83%	1.46	21.3	1.5	897	387
1200	9.8	PMPC DF	108.9	7.6	6.5	12.7	98.30%	1.31	20.8	1.3	994	421
1200	8.5	PMPC DF	107.5	9.5	4.9	12.6	97.78%	1.48	21.9	1.3	992	377
1200	7.3	PMPC DF	75.6	4.4	8.2	19.2	96.65%	1.39	21.4	1.1	996	401
1000	6.0	PMPC DF	77.9	4.7	2.7	22.6	94.51%	1.48	21.6	1.0	802	355
1200	6.0	PMPC DF	78.6	6.0	1.3	22.0	93.38%	1.44	21.2	1.0	998	375

5.7 Summary

Various steady-state operating points spanning different speeds and loads were tested, comparing three different combustion modes. Diesel combustion, conventional dual-fuel, and PDFC were compared against one another in terms of emissions and overall operating efficiency. The intent was to characterize the potential and limitations of PDFC relative to conventional dual-fuel operation as well a diesel baseline.

During the baselining, typical NOx-CO and NOx-soot trade-offs were present for diesel and conventional dual-fuel combustion modes and the majority of the injection timings optimised up against the pressure rise rate limit of 10 bar/deg. In conventional dual-fuel, bulk auto-ignition of the end-gas occurred at A70 and resulted in decreased CO and THC/CH_4 emissions as injection timing was advanced. This behaviour differed from other speed load points, where in-cylinder temperature and pressure were not high enough to initiate auto-ignition.

In conventional dual-fuel, sensitivities to natural gas substitution percentage as well as engine speed were investigated. For most engine loads, emissions and efficiency were found to have low sensitivity to natural gas substitution for the 80 to 90% regime tested. Exceptions to this would be very high or low load conditions. Engine speed also demonstrated low sensitivity towards emissions and efficiency in the 1000 to 1400 RPM envelope.

PDFC showed significant reductions in methane slip as well as CO emissions when compared to conventional dual-fuel combustion. ISFC was decreased and thermal efficiency was increased, and approached diesel levels of combustion efficiency. For most loads, PDFC lowered emissions simultaneously, but there were some cases where NOx production was increased. This NOx production could be curtailed if some benefits to the other emissions and efficiency were sacrificed. Low soot production was maintained by operating lean enough to avoid local-rich combustion. Improvements in ISFC were realised by lowered heat transfer losses and faster combustion duration, which resulted in higher thermal efficiencies. Higher combustion efficiency also contributed by simply burning more of the fuel injected.

It was also determined there are load based limitations of PDFC. Higher loads are limited by the maximum cylinder pressure of the engine. This was attributed to short duration combustion phased relatively close to TDC, a characteristic of auto-ignition. This could be managed by altering the amount or timing of the premixed diesel injections, but would ultimately require raising the maximum cylinder pressure of the engine in order to realize larger benefits. Medium load conditions did not have this limitation, so were able to benefit the most from PDFC. Light load conditions suffered due to the flammability issues of natural gas in lean, low temperature and pressure conditions.

The CH_4 reduction mechanism was due to the premixed diesel injection introducing stratification into the combustion charge. This adjusts the mixture's flammability by introducing a high reactivity fuel into a low reactivity fuel-air mixture. Non-uniform mixture strength drives differences in the local chemical kinetic reaction rates, which in turn influenced the ignition delay and resulting combustion duration. In theory, the pockets of highly reactive fuel also resulted in many different ignition sources once temperature and pressure were high enough for bulk ignition of the fuel mass to occur.

PDFC could potentially minimize the need for exhaust after-treatment of methane. However, Euro VI emissions standards for CH_4 still present a challenge. The best case PDFC scenario yielded CH_4 engine-out emissions of approximately 1.9 g/kWh ($BSCH_4$) which remains almost four times the Euro VI level of 0.5 g/kWh, assuming no conversion from the after-treatment system.

Chapter Six

Advanced Conventional and Premixed Dual-Fuel Operation

6.1 Introduction

One fundamental drawback of a lean-burn dual-fuel engine is operation under light-load conditions. As outlined in Chapter Five, various factors surrounding mixture flammability and combustion temperature lead to poor emissions and efficiency at light-load when traditional combustion methods are utilised. Further extension of the dual-fuel operating range is always desired, as it helps to improve the business case of natural gas as a fuel. However, satisfactory emissions and efficiency need to be maintained under high natural gas substitution. In order to enable this, more sophisticated methods of light-load operation are explored in this section.

6.2 Methodology

In the following sections, different experimental approaches were systematically evaluated with the end-goal to improve light-load engine operation. The engine speed-load condition of 1000 RPM and 6 bar $\mathrm{IMEP}_{\mathrm{net}}$ was maintained for all experiments with the objective to determine which method was the most effective for reducing emissions and increasing efficiency. In Section 6.3, Miller cycle and throttling were utilised to lower in-cylinder λ. The premise was that this could potentially help create conditions more conducive to the burning of the pre-mixed natural gas. Included in Section 6.4 is the role internal-EGR could have in increasing the temperature of the in-cylinder mixture while Section 6.5 is about the auto-ignition focused injection strategy of RCCI. Evaluated in Section 6.6 are the performance of each of these methodologies and the suggested advantages and drawbacks of each. The specific test conditions were detailed under the “Test Procedure” sub-section for the individual strategies.

6.3 Miller Cycle and Throttling

The engine valvetrain and throttle are two avenues by which to control the in-cylinder λ of the engine during light load operation. Reduction of the inhaled air can help to increase the burning velocity of natural gas [141], thereby reducing quenching and decreasing methane emissions. Throttling limits the mass flow of fresh air into the engine via a butterfly valve which results in increased pumping losses. One potentially more efficient method would be to utilise a LIVC Miller cycle strategy as it generally has lower pumping losses due to the piston not working against the depression caused by the throttle. Both of these λ control mechanisms were explored in Section 6.3.3, with specifics of the test procedures and effective compression ratio calculations discussed in Sections 6.3.1 and 6.3.2, respectively. An additional Miller cycle study at constant λ was presented in Section 6.3.4 with the goal of reducing NOx emissions.

6.3.1 Test Procedures

For Section 6.3.3, the experimental testing was structured to sweep in-cylinder λ by throttling the engine with a butterfly valve and subsequently with the engine valvetrain via LIVC. All testing took place at 1000 RPM and 6 bar $IMEP_{net}$ under naturally aspirated conditions (boosting is not favourable as in-cylinder λ was trying to be reduced). Conventional dual-fuel was run with a single diesel injection around TDC with no pilot injection used. Rail pressure was set at a constant 700 bar in an attempt to match the approximate NOx and soot emissions levels of the Z25 points in Table 5-4 on the day of testing. Miller cycle tests with 21% EGR were ran separately with 800 bar as well (to match optimums for Z25 in Table 5-5), the key graphs of which are shown in Appendix C – Miller Cycle with 800 bar Rail Pressure. Overall, the difference between 700 and 800 bar fuel pressure is low with the main emissions of concern being more a function of global in-cylinder λ. Gas substitution was approximately 85% (80% targeted but controls issues caused deviation) with diesel fuel comprising the 15% balance. The role of cooled external EGR was tested with both the throttling and Miller cycle strategies, with 0 and 21% EGR rates tested. The rate of 21% EGR was targeted in order to compare against previously ran data, which originally had an EGR percentage derived from the Volvo D13 multi-cylinder data. Injection timing was adjusted to hold a constant CA50 of approximately 9 deg ATDC for throttled cases and 8 deg ATDC for Miller cycle. Intake valve closure was delayed to achieve the desired in-cylinder λ along with the resulting drop of effective compression ratio. This is detailed in Figure 6-1, as well as Section 6.3.2.

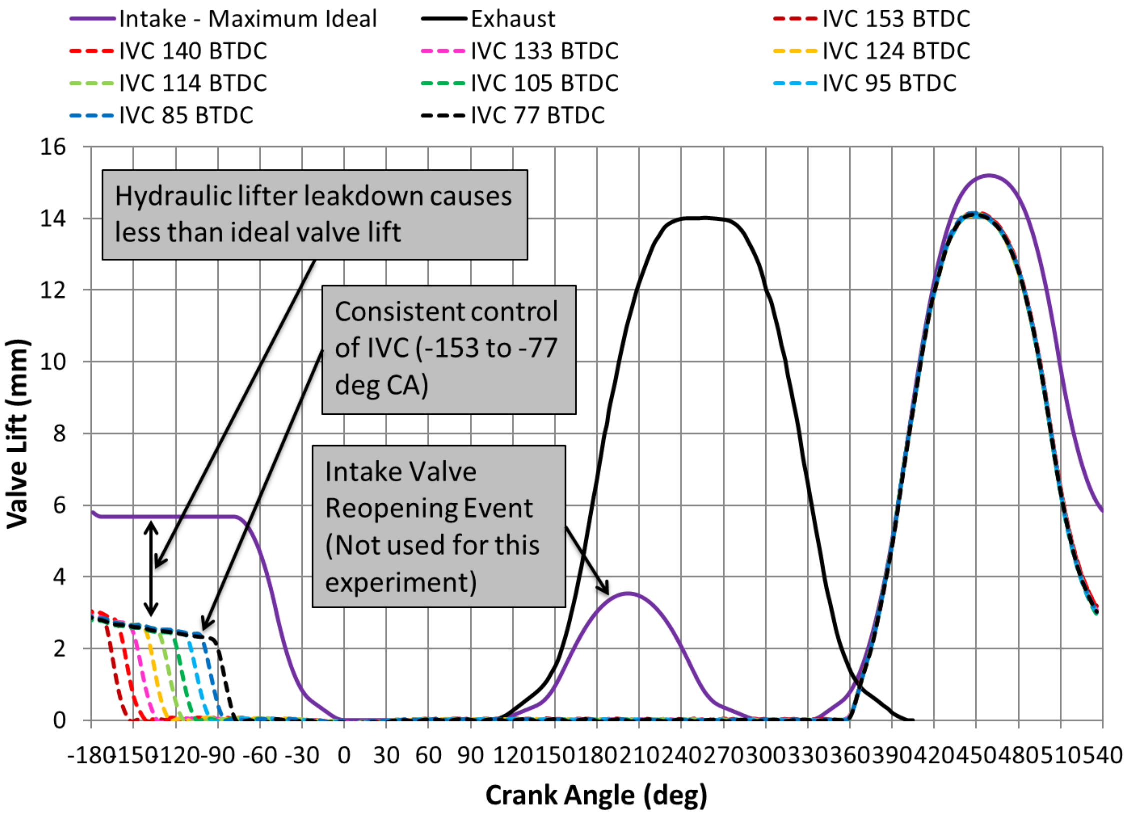

Figure 6-1: Engine valve lift curves depicting the LIVC strategy used to adjust λ

Included in Section 6.3.4 is a Miller strategy that maintains in-cylinder λ at approximately 1.83. This differs from the previous section because the goal with this approach is to provide a possible means of NOx reduction. The premise is that NOx emissions would be lowered via longer ignition delay/better mixing of the diesel pilot before ignition. This would be due to lower compression temperatures due to the compression work being done outside of the cylinder by the boosting device. ECR was varied from 16.8 to 12.1 with fresh air boost increased with later IVC in order to maintain in-cylinder λ. Intake air temperature was held at approximately 32 °C (lowest temperature possible on external boost rig and was representative of charge air cooler temperatures from Volvo D13 multi-cylinder data), with gas substitution at approximately 80%, and diesel rail pressure at 700 bar. A gas substitution of 80% was selected as it would represent the lower gas substitution range of a Volvo D13 multi-cylinder and would provide a relatively large diesel injection quantity, which would be necessary to provide accurate and large enough injections if the diesel injection were to be split (used in later sections). No cooled external EGR was used. Once more the SOI was adjusted to maintain a CA50 of approximately 10 deg ATDC.

6.3.2 Effective Compression Ratio Calculation

The ECR is a useful parameter for qualifying the effect LIVC has on the thermodynamic state of the in-cylinder charge. However, ECR can have more than one definition depending on calculation. Traditionally, geometric effective compression ratio is used and is defined as the ratio of cylinder volume at intake valve closing to the TDC volume. This is not the optimal definition to explain experimental results as it does not represent the actual in-cylinder compression process. As shown in Figure 6-2, the in-cylinder charge is partially compressed prior to IVC due to the high flow resistance across the intake valves. If a straight line is drawn on the compression stroke down to a line representing the average manifold air pressure (MAP), an effective volume can be defined at the intersection.

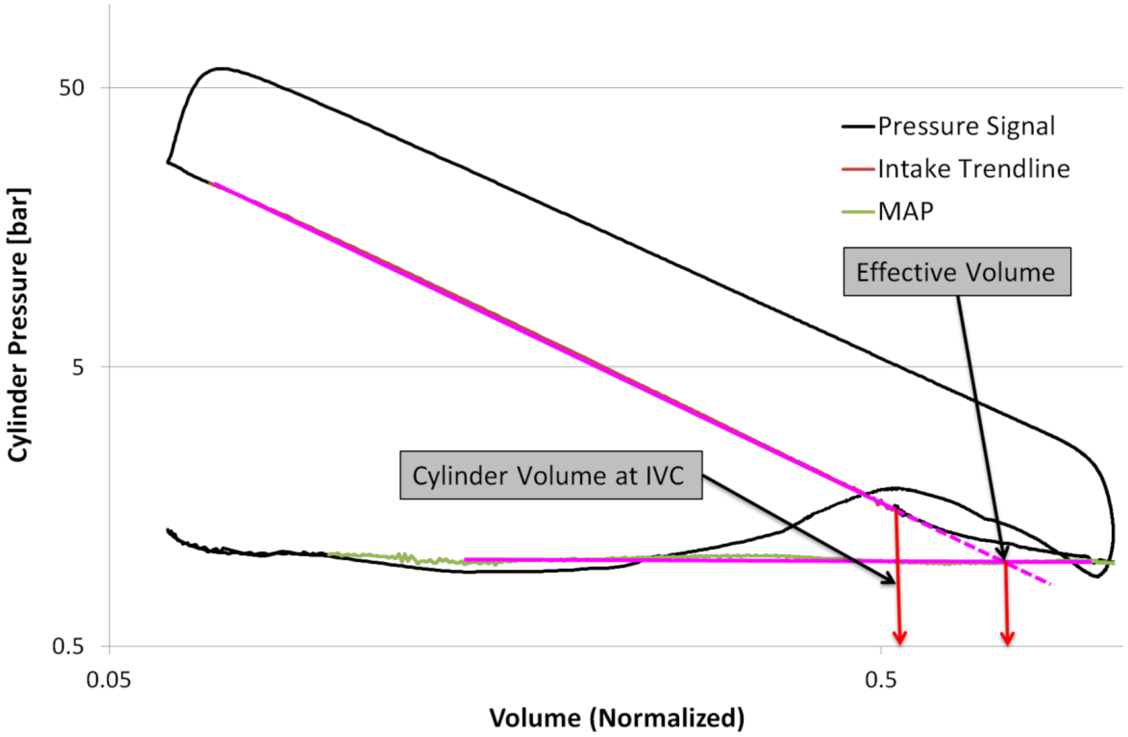

Figure 6-2: Illustration of the definition of pressure-based effective compression ratio

This can now be used to define the pressure-based effective compression ratio as the ratio of the effective volume to the TDC volume, thereby more accurately representing the compression conditions in-cylinder. The gap between geometric and pressure-based ECR is more pronounced the further LIVC is implemented, as shown in Table 6-1 and Figure 6-3. Pressure-based ECR will be used exclusively from this point onward.

Table 6-1: Intake cam duration with geometric and pressure-based effective compression ratios as a function of intake valve closure

Intake Valve Close	Intake Cam Duration	Geometric Effective CR	Pressure-Based Effective CR
deg ATDC	deg CA	-	-
-153	206	16.2	16.8
-140	218	15.2	16.7
-133	225	14.9	16.6
-124	235	14.1	16.4
-114	244	13.1	15.8
-105	254	12.1	15.1
-95	264	10.8	14.1
-85	274	9.4	13.2
-77	282	8.3	12.1

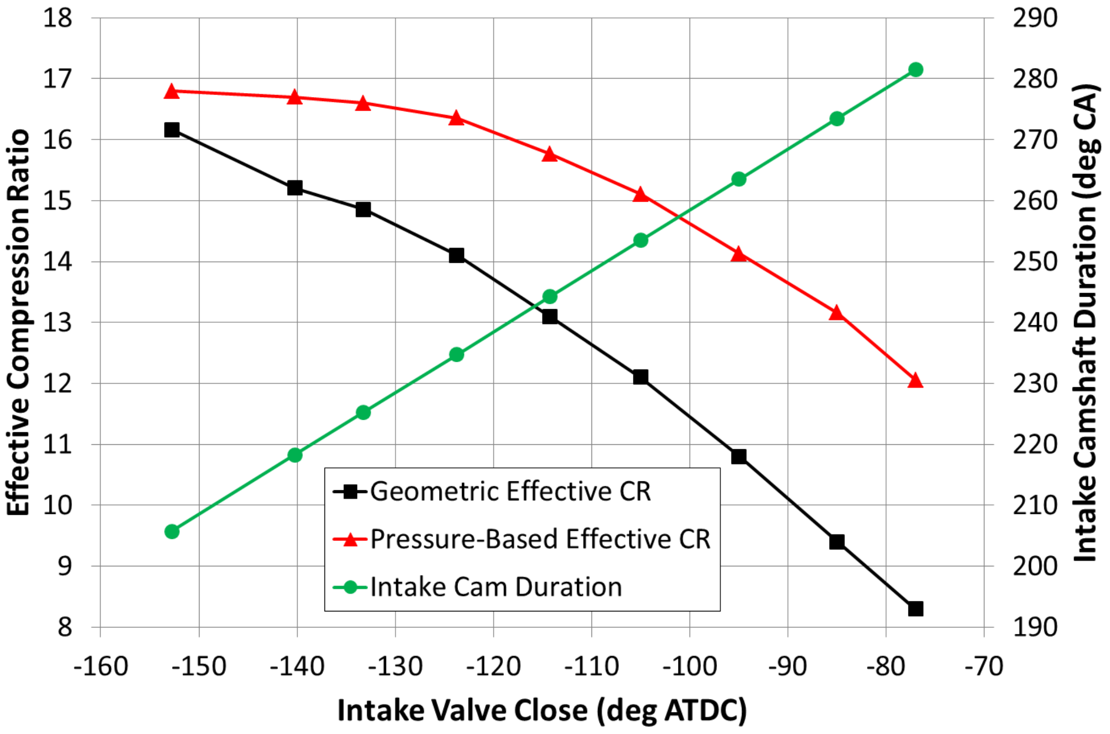

Figure 6-3: Graphical representation of effective compression ratio and intake cam duration

6.3.3 Miller Cycle and Throttling

The reduction of unburnt methane emissions was the primary goal of these particular throttling and Miller cycle strategies. The 0% and 21% cooled external EGR levels were tested to determine the limits of each strategy from a CH_4 reduction standpoint, as 0% would offer the best potential, but at the expense of increased NOx production. Relevant emissions and combustion parameters are presented followed by crank angle based cylinder pressure and heat release plots.

Displayed in Figure 6-4 are CH_4, CO, and NOx emissions as a function of in-cylinder λ. The red diamond and blue triangle lines represent cases that were ran without EGR, with the black square and purple circles depicting cases with EGR. Immediately it can be observed that the lowering of λ can reduce unburnt methane emissions as well as CO for all cases. The rate of the CH_4 and CO improvement diminishes as the in-cylinder λ approaches the peak laminar burning velocity for a methane-air mixture, which is approximately in the $\lambda = 0.95$ region [10,138,140,141]. In this scenario, laminar burning velocity is used as an indicator for the relative difference in global reaction rates and can be valuable in the analysis of fundamental processes such as ignition, heat release, and flame quenching. Arguably turbulent burning velocity should be considered with the diesel diffusion flame igniting a premixed natural gas charge, but optical evaluation would be needed to completely validate in-cylinder combustion processes [70]. However, turbulent flame models often prescribe the turbulent burning velocity as a function of laminar burning velocity [138] so consideration of laminar burning velocity is worthwhile. The CH_4 and CO improvement can vary depending on the specific composition of the cylinder charge, but the data also supports that the combustion chamber geometry can play a role in limiting the lowest achievable methane-out emissions level. This will be discussed further in the following graphs. Additionally, THC emissions follow the same trend as CH_4, as the majority of THC is comprised of CH_4.

The NOx emissions for the cases without EGR increase significantly with the lowering of λ. This can be attributed to the faster burning rate of the in-cylinder charge, resulting in higher, NOx-producing combustion temperatures. These emissions can be curbed with the addition of external EGR, as demonstrated by the 21% test lines, but results in an offset of increased CH_4 and CO emissions. This is to be expected, as EGR curbs the peak combustion temperature, thereby reducing NOx production. However, EGR simultaneously impedes flame propagation which results in the aforementioned increase of CH_4 and CO emissions. The throttling and Miller cycle strategies yield similar results for the emissions overall, particularly for CH_4. Lower CO accompanied by higher NOx production for Miller cycle experiments were due to the slightly more advanced combustion phasing of 8 deg ATDC compared to the 9 deg ATDC for the throttling cases.

ISSoot emissions are depicted in Figure 6-5 along with PMEP and net indicated efficiency. Overall, soot emissions were at a low level with the selected 700 bar rail pressure. Higher rail pressures would result in decreased soot, but predominantly at the expense of increased NOx production.

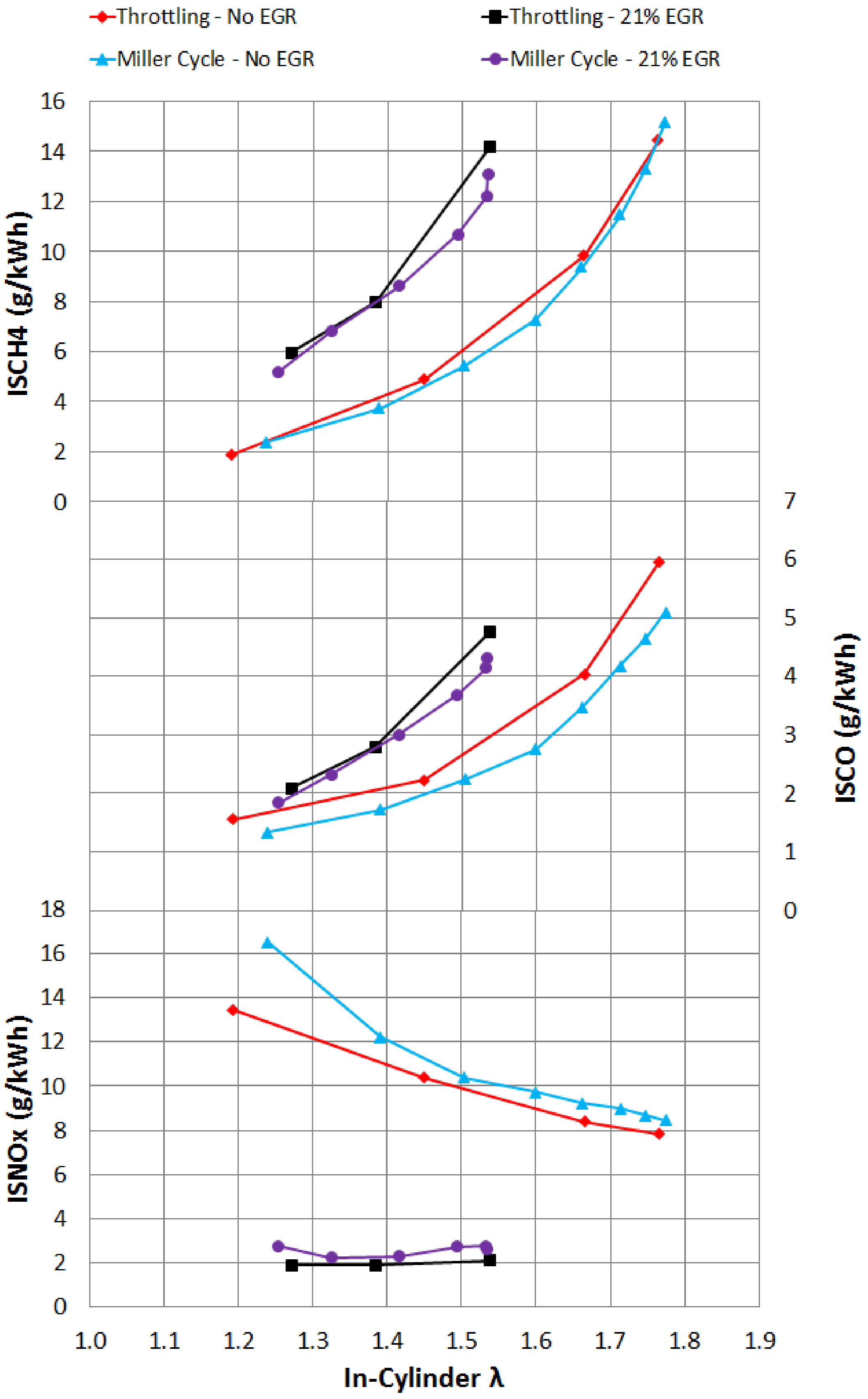

Figure 6-4: Engine-out ISCH4, ISCO, and ISNOx emissions vs in-cylinder λ

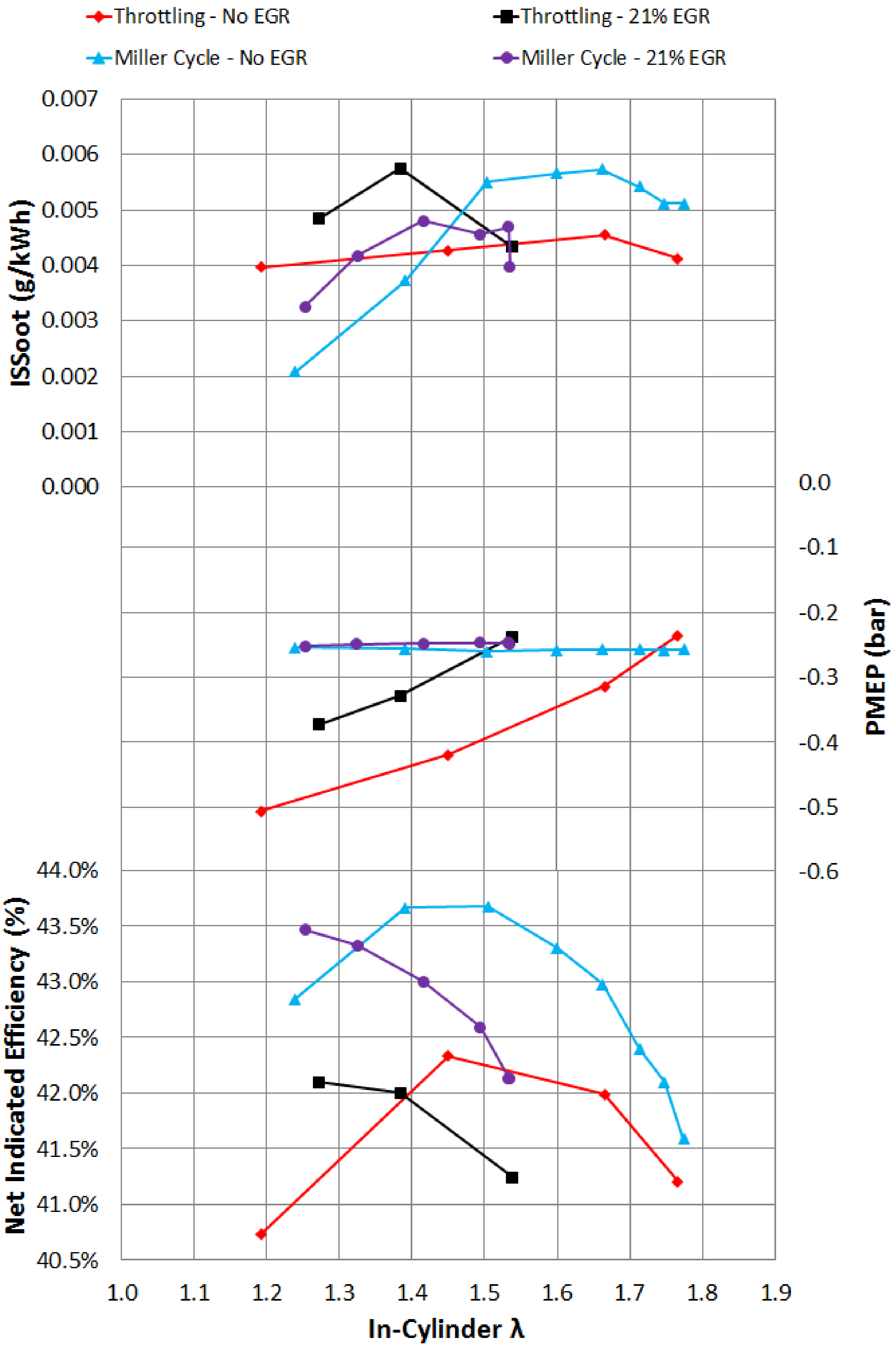

Figure 6-5: Engine-out ISSoot emissions, PMEP, and net indicated efficiency vs in-cylinder λ

PMEP was increased significantly for the throttling cases as λ was decreased. The substantial benefit of the Miller cycle strategy is demonstrated by this graph as the PMEP is held at a constant level with decreasing λ. This was due to the piston not working against the depression in the intake manifold caused by the throttle. EGR dampened the effect of throttling as it displaced fresh air entering the engine, thereby requiring less throttling for a given λ. This helped to explain the lowered pumping losses for the 21% EGR throttled case compared to the 0% throttled. It should also be mentioned that these experiments were hardware limited as the leakage of the throttle permitted no further restriction of fresh air entering the engine. As a result, the minimum λ achieved was about 1.18.

The net indicated efficiency reflects the difference between the throttling and Miller cycle strategies. The primary offset in efficiency between Miller cycle and throttling at the same λ could be attributed to the aforementioned combustion phasing difference. However, the divergence of efficiency with decreased λ was caused by the higher pumping losses of the throttled cases. The benefit of utilising the LIVC Miller cycle strategy was evident for both 0 and 21% EGR cases, asserting that controlling fresh air into the engine was more efficiently accomplished with the valvetrain rather than throttle. For both throttling and Miller cycle, the peak efficiency was in the λ = 1.4-1.5 region without EGR, and approximately in the λ = 1.2-1.3 region with EGR. The shift of the optimum to a lower λ for cases with EGR was caused by a decrease in combustion efficiency (additional diluent), the details of which will be discussed later. The efficiency lines with EGR would suggest that net indicated efficiency would continue to improve for both throttling and Miller cycle onward to approximately λ = 1.2. Beyond this point, it is highly likely that performance and emissions would degrade, as the combustion would be ignition/ECR limited, as significant SOI advanced was already required at λ = 1.25.

CA50, SOI, and combustion duration are displayed in Figure 6-6. As previously mentioned, the CA50 for throttling experiments were held in the 9-10 deg ATDC region while Miller cycle were in the 7-8 deg ATDC. The SOI was adjusted to maintain CA50, with approximately 2 deg CA of advance supplied to compensate for the addition of 21% EGR over 0%.

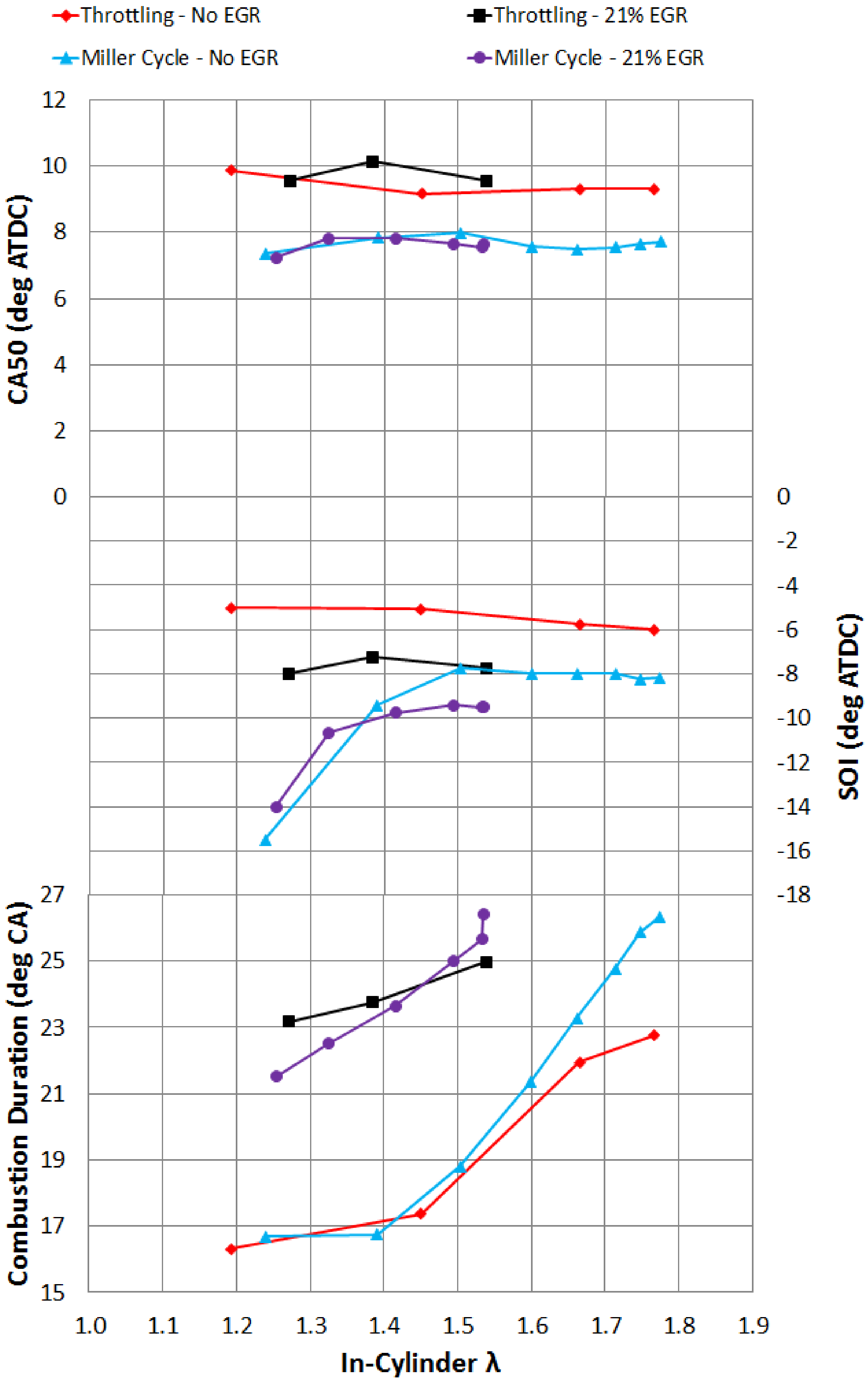

Figure 6-6: 50% mass fraction burned point, start of injection, and 10-90% combustion duration vs in-cylinder λ

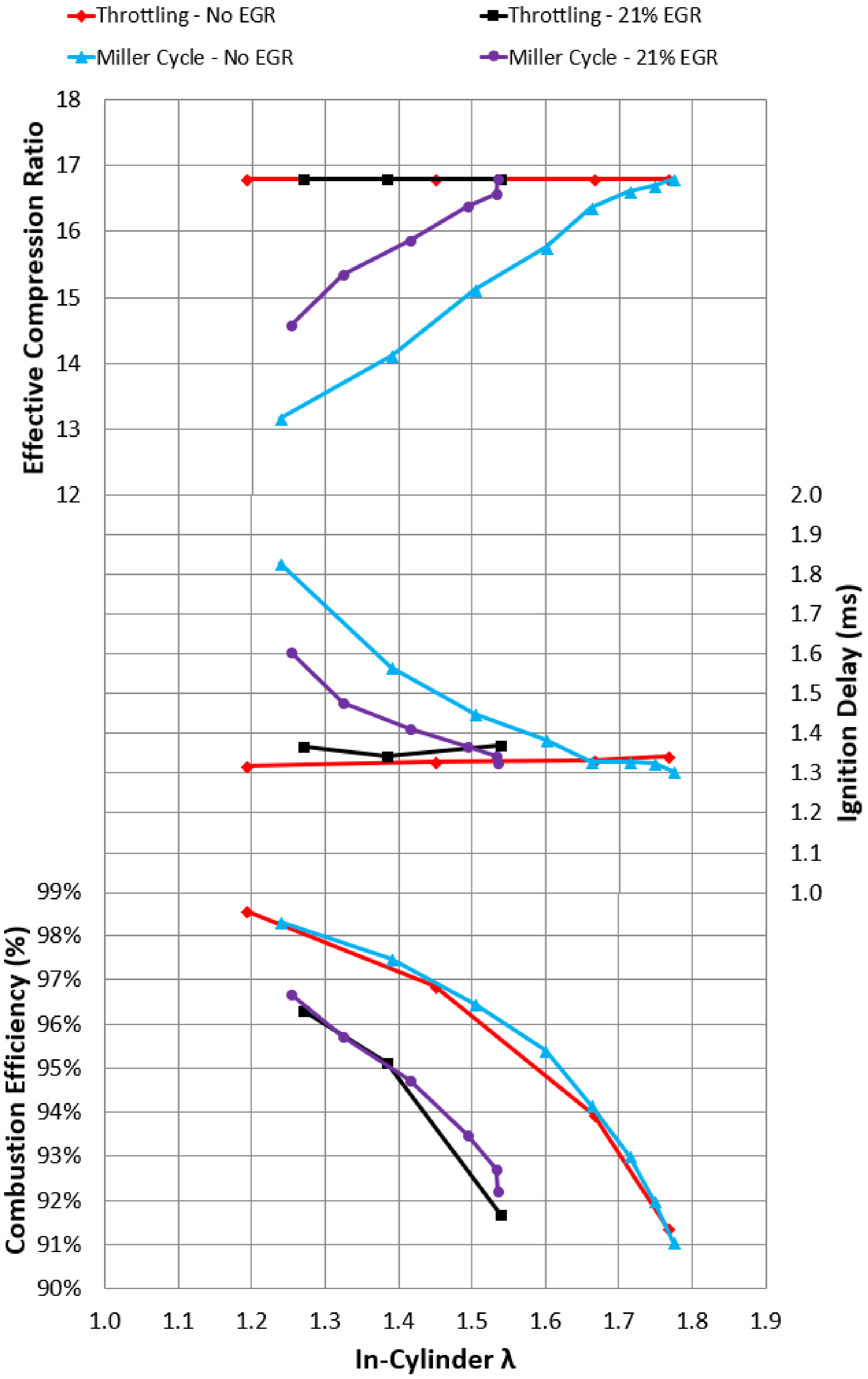

Figure 6-7: Pressure-based ECR, ignition delay, and combustion efficiency vs in-cylinder λ

The data presented in Figure 6-7 further illustrates the effect of the LIVC Miller cycle strategy on ECR and ignition delay. As ECR was dropped along with λ, the ignition delay increased as a result of the lowered compression temperatures. The SOI was adjusted to help maintain CA50 at a constant value, as to compensate for the delayed combustion phasing brought by lowered ECR. Throttling experiments required no adjustments to SOI, as the ignition delay, ECR, and CA50 did not change.

Lowered in-cylinder λ also resulted in decreased combustion duration as shown in Figure 6-6. The faster flame propagation of natural gas in a richer environment led to a shorter combustion duration. The combustion duration was further shortened if external EGR was removed, as removal of an inert mixture allowed for faster flame propagation. Additionally, both the increased flammability of natural gas and lack of EGR helped to shape a more ideal heat release nearer to TDC, which would result in higher indicated work and efficiency.

The data plotted in Figure 6-7 depicts increased combustion efficiency with lowered λ. This phenomenon tracks with the flammability of the in-cylinder charge, with richer conditions resulting in higher combustion efficiency. The presence of EGR dropped combustion efficiency by 1.5-3.5% depending on the λ. The EGR acted as a diluent which impeded flame propagation, resulting in higher amounts of unburnt methane. It should also be observed that the rate of combustion efficiency benefit decreased as λ was decreased. The experiments without EGR approached the theoretical limit for flame propagation type combustion, as the combustion chamber crevices account for approximately 1% or more of combustion efficiency loss.

PRR, PMax, and EGT are presented in Figure 6-8. A reduction of PRR and PMax were observed with lowered λ due to the decreased in-cylinder mass. Lower charge temperatures at the time of ignition likely affected the speed at which diesel combustion took place, which would result in lower PRR. The linearity of the PRR and PMax decline were affected by the changes to SOI necessary to maintain a constant CA50.

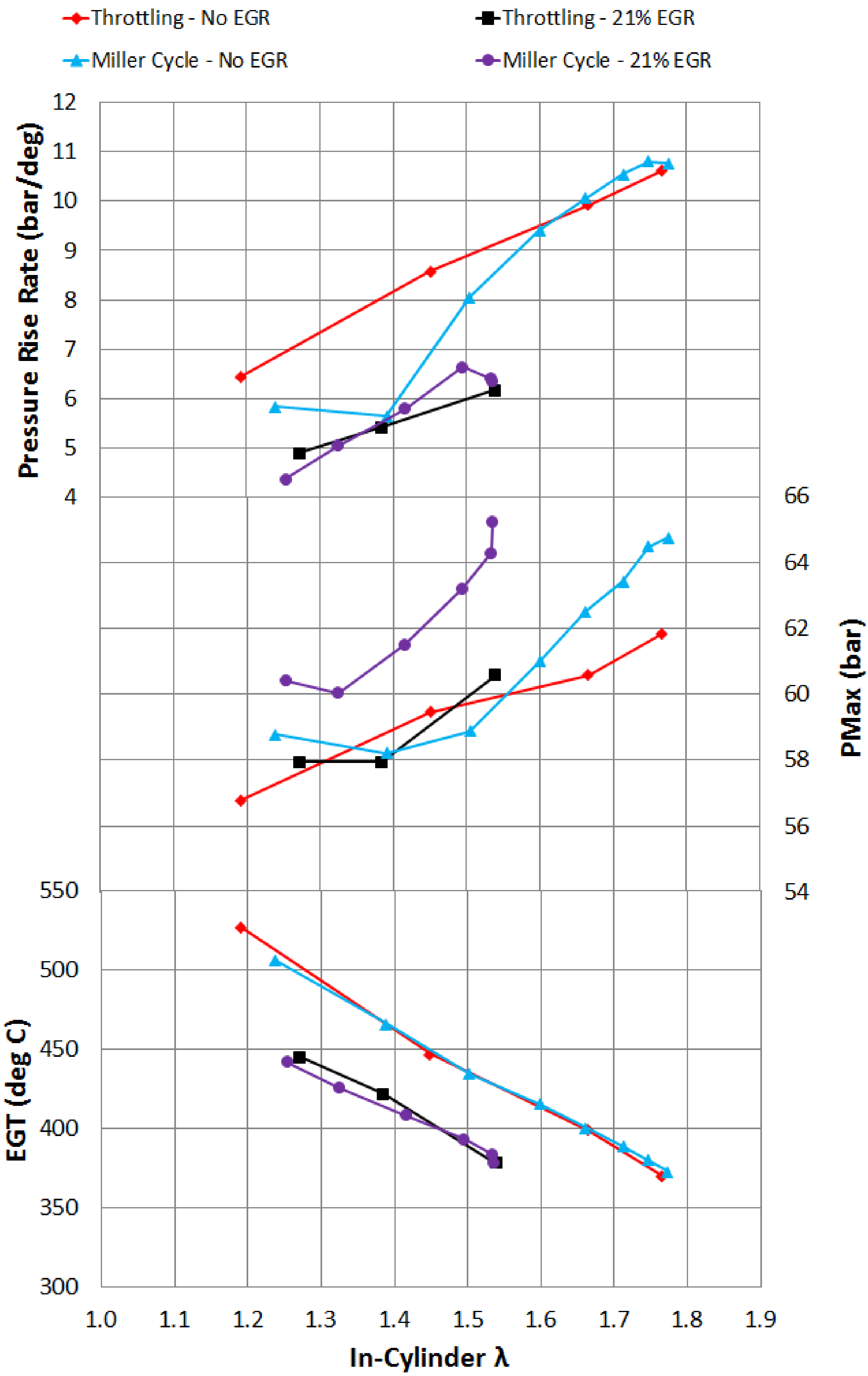

Figure 6-8: Pressure rise rate, maximum cylinder pressure, and exhaust gas temperature vs in-cylinder λ

The EGT increased linearly with decreasing λ, which could potentially benefit exhaust after-treatment conversion efficiencies via higher enthalpy. The increased combustion efficiency in addition to the reduced combustion duration helped raise EGT due to the additional fuel burned combined with a more efficient combustion process. Upon the addition of EGR, EGT was dropped due to the additional inert charge in-cylinder as well as the diluent impeding the rate of flame propagation. PRR was also reduced with EGR, as it slowed the speed of the diesel combustion, which generally tended to be the source of the highest PRR values.

Crank angle resolved cylinder pressure can be observed in Figure 6-9. ECR was lowered via the LIVC Miller cycle strategy and caused a drop in the motoring cylinder pressure due to the reduced in-cylinder mass. This resulted in lowered peak cylinder pressure and a smaller rate of pressure rise after the start of combustion. As ECR was dropped, the SOI was advanced in order to maintain a constant CA50 value.

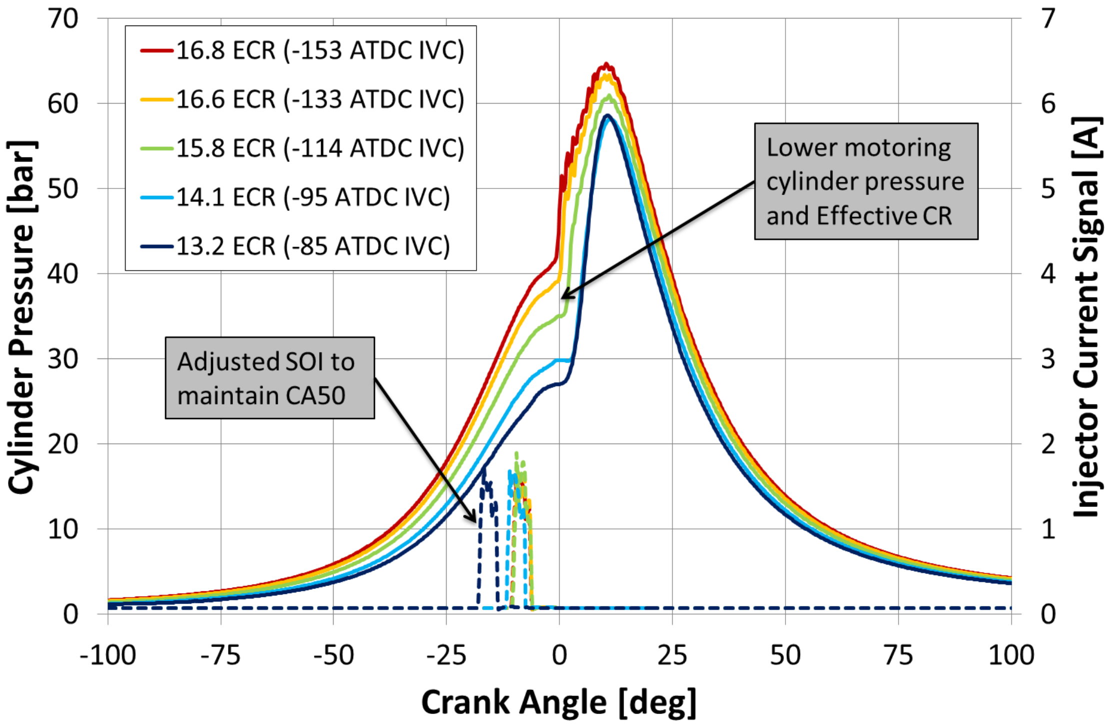

Figure 6-9: Cylinder pressure traces and injection signals vs crank angle for the LIVC Miller cycle strategy with 0% EGR

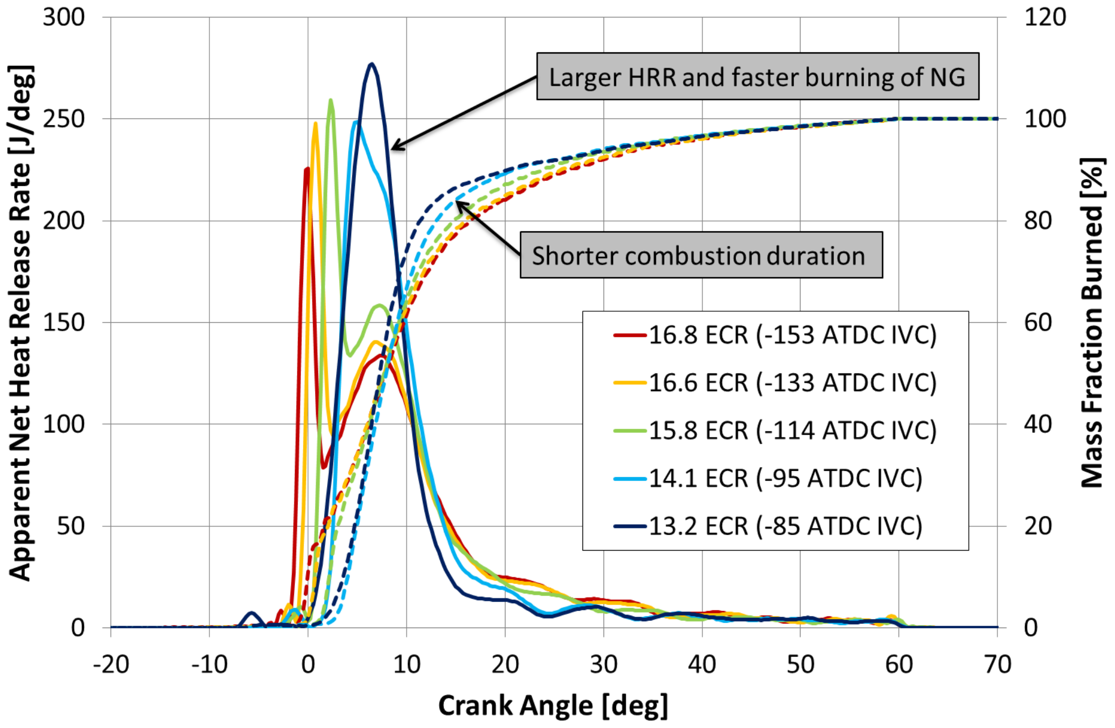

Figure 6-10: Apparent net heat release rate and mass fraction burned for the LIVC Miller cycle strategy with 0% EGR

The corresponding heat release and mass fraction burned data is presented in Figure 6-10. It can be observed that the shape of the HRR curve changes as ECR and in-cylinder λ was dropped. The characteristic double-hump HRR of conventional dual-fuel combustion was transformed into a single peak as λ was decreased. This suggests that the diffusion style diesel combustion and the resulting flame propagation of natural gas takes place more concurrently, rather than the two distinct peaks observed at higher ECR. The faster burning of natural gas is the probable explanation, which would be supported by the clear reduction in combustion duration as well as the higher peak HRR. This is further supported by the fact that the laminar burning velocity for methane-air mixtures also increases with lower global in-cylinder λ up until approximately λ = 0.95 [138,140,141]. Additionally, the reduced cylinder pressure of the lower λ cases would also cause the burning velocity to increase [138]. This is mainly due to the thermal diffusivity increasing via a reduction in charge density from the lower pressure [143]. However, a reduction of in-cylinder temperature is also experienced as a result of the lower cylinder pressures which would slow the chemical reaction rates and consequently lower the burning velocity [138], partially offsetting the increases from the other factors.

Overall, throttling and LIVC Miller cycle strategies were effective ways of reducing CO and unburnt methane emissions. For a given λ, both approaches had similar ability to reduce CH_4 emissions, as it was mainly a function of combustion efficiency, although altering λ via LIVC proved to be more efficient. It was possible to achieve the piston crevice limited combustion efficiency of ~98.6% with 0% EGR, but with excessive NOx production. The addition of EGR helped suppress NOx emissions, but at the expense of combustion efficiency and CH_4 emissions, so the ISNOx and $ISCH_4$ trade-off remains. The LIVC Miller cycle strategy helped to improve engine efficiency by reducing the pumping losses typically associated with throttling, but further benefits were limited by the ECR being too low to support stable diesel ignition.

6.3.4 Miller Cycle at a Constant In-Cylinder Lambda

The Miller cycle has traditionally been utilised in diesel engines as a pathway to reduce NOx emissions. Compression work being performed outside of the cylinder in conjunction with lower compression temperatures results in better mixing of the diesel spray before ignition, thereby curbing NOx formation. This approach could potentially be applied to the ISNOX/$ISCH_4$ trade-off in the previous section, with the goal of reducing NOx while maintaining CH_4 production.

To explore the effect of Miller cycle, the intake cam duration was increased by way of retarding IVC. Using this method, the ECR was varied from 16.8 to 12.1. The intake and exhaust pressures were controlled to maintain an in-cylinder λ = ~1.83. Holding a constant pressure differential across the cylinder helped to modulate the air mass flow rate into the cylinder, as graphically depicted in Figure 6-11. Intake and exhaust backpressure steadily increased with later IVC conditions, eventually breaking down for the latest IVC case due to poor combustion performance. However, up until that point, air mass flow into the cylinder was maintained at approximately 60 kg/h, which yielded the in-cylinder λ values depicted in Figure 6-12. Pumping work was increased slightly as exhaust blowdown conditions varied as a result of in-cylinder combustion changes. Intake air temperature was held at approximately 32 °C (lowest temperature possible on external boost rig), with gas substitution controlled to 80%. As a reminder, testing was performed at 1000 RPM, 6 bar IMEP$_{net}$ with no cooled external EGR.

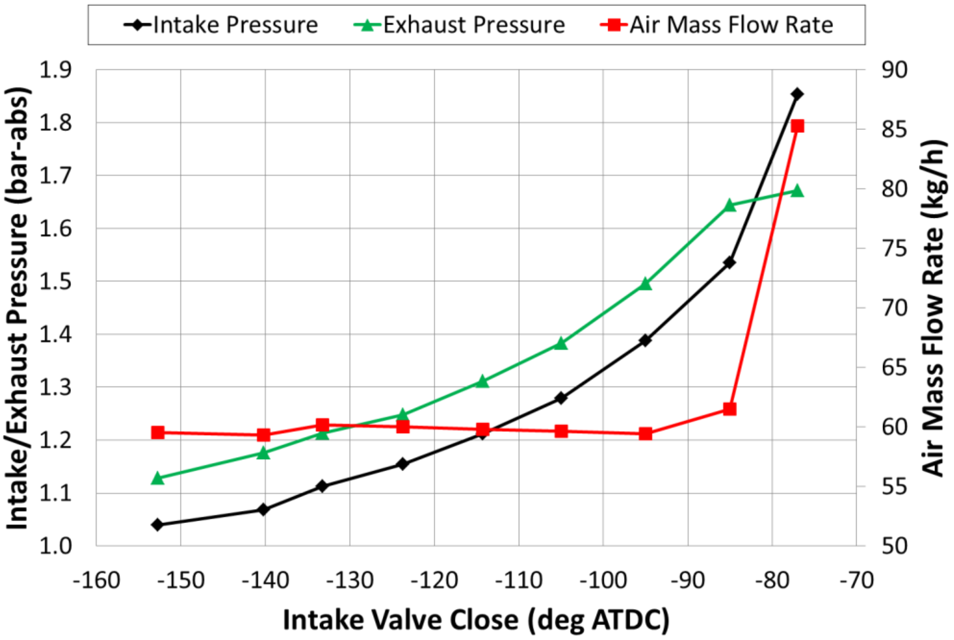

Figure 6-11: Intake and exhaust boundary conditions with air mass flow rate vs IVC

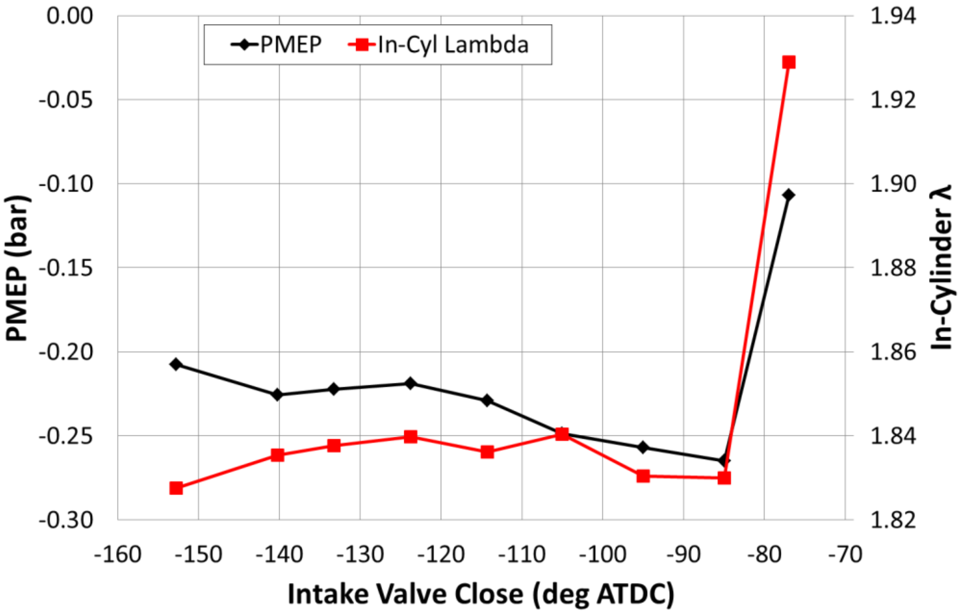

Figure 6-12: PMEP and in-cylinder λ vs IVC

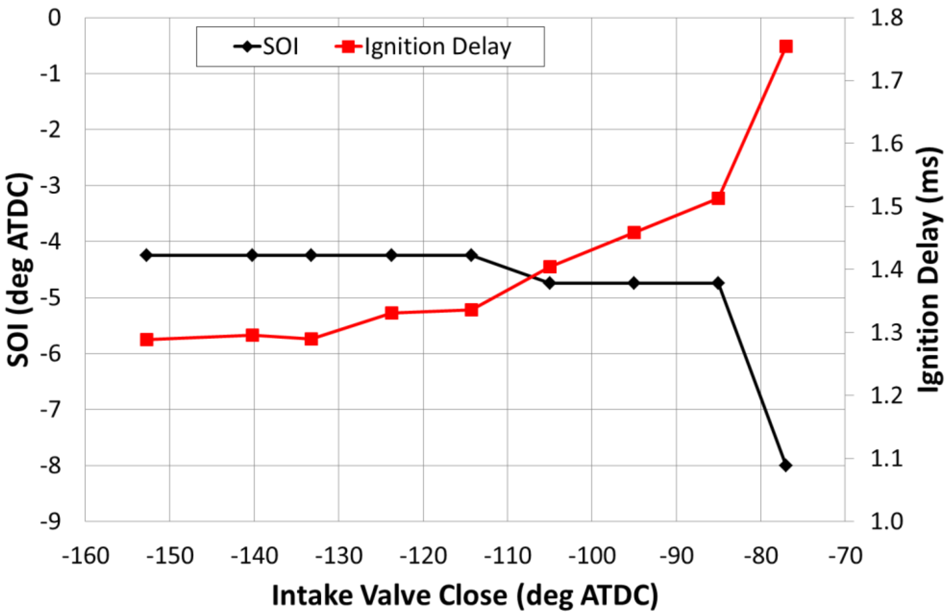

Figure 6-13: Start of injection and ignition delay vs IVC

Figure 6-13 includes the SOI and ignition delay as a function of IVC. The SOI was gradually advanced to maintain a CA50 of approximately 10 deg ATDC. Later IVCs resulted in lower ECRs, which caused an increase in ignition delay. Upon reaching the lowest ECR of 12.1 (-77 deg ATDC), significant advance of SOI was necessary due to the lack of sufficient compression temperature to ignite the diesel fuel. The resulting ignition delay was comparatively long, which ultimately caused a breakdown of the subsequent combustion process.

The engine-out emissions are presented in Figure 6-14 and Figure 6-15. ISNOx emissions were decreased with later IVC, with $ISCH_4$ and ISSoot remaining relatively constant. ISCO emissions were increased with decreased NOx, which supports that a NOx-CO trade-off exists. The aforementioned combustion degradation was observed for the lowest ECR in the form of poor CH_4, CO, and soot emissions, which suggests the diesel injection did not properly burn and initiate the ignition of the natural gas mixture. The NOx emissions were reduced by allowing the diesel fuel more time to better mix with the air before combustion begins. This was brought about by the lower compression temperatures of a lower ECR. However, the lower temperatures also contributed to CO formation as was expected in lower temperature, fuel-rich areas of combustion.

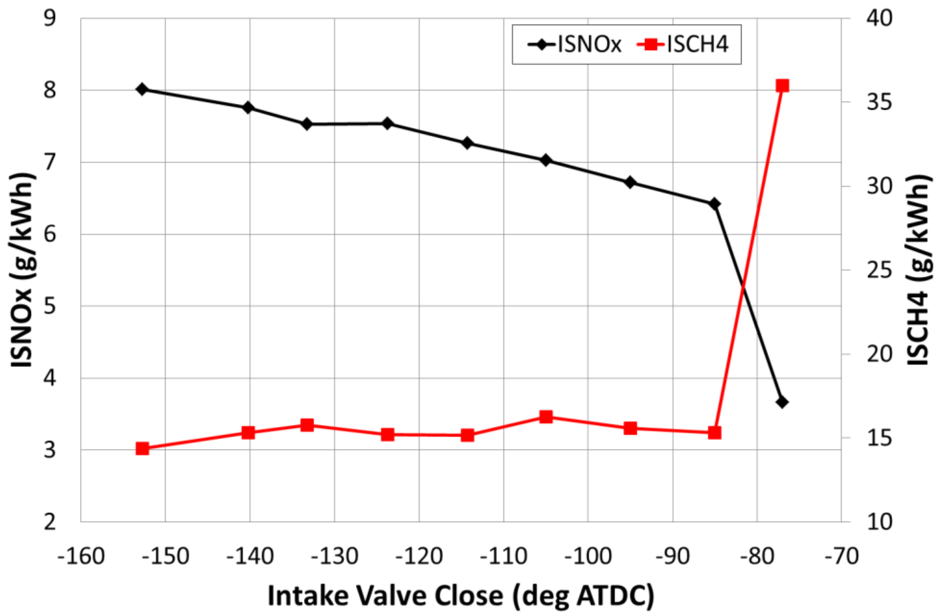

Figure 6-14: Engine-out ISNOx and $ISCH_4$ emissions vs IVC

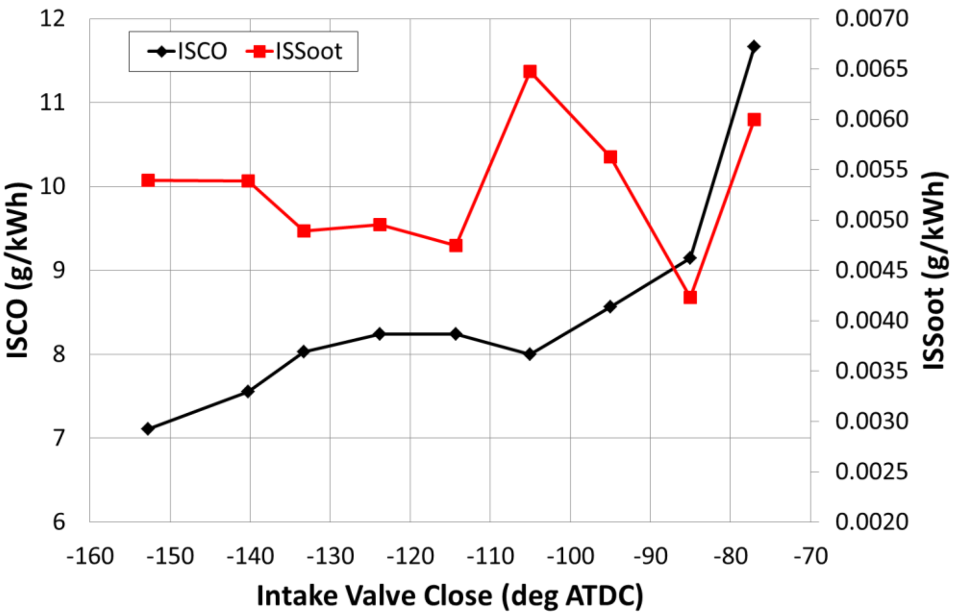

Figure 6-15: Engine-out ISCO and ISSoot emissions vs IVC

The data plotted in Figure 6-16 suggests that engine ISFC increased with lower ECR. The lowered efficiency was caused by the increased pumping work previously mentioned in Figure 6-12. It is also likely to degrade further outside of the dyno setting as most engine boosting devices have lowered efficiency under low-flow, high-pressure ratio operation (ie. Nearing surge limits on a turbocharger efficiency map). The use of an external boosting device for these experiments could mask these additional efficiency losses. The EGT was raised with later IVC due to slightly later heat release and shorter combustion duration. A significant drop in EGT was observed for the 12.1 ECR case as combustion efficiency was decreased. This was accompanied by a large increase in engine ISFC.

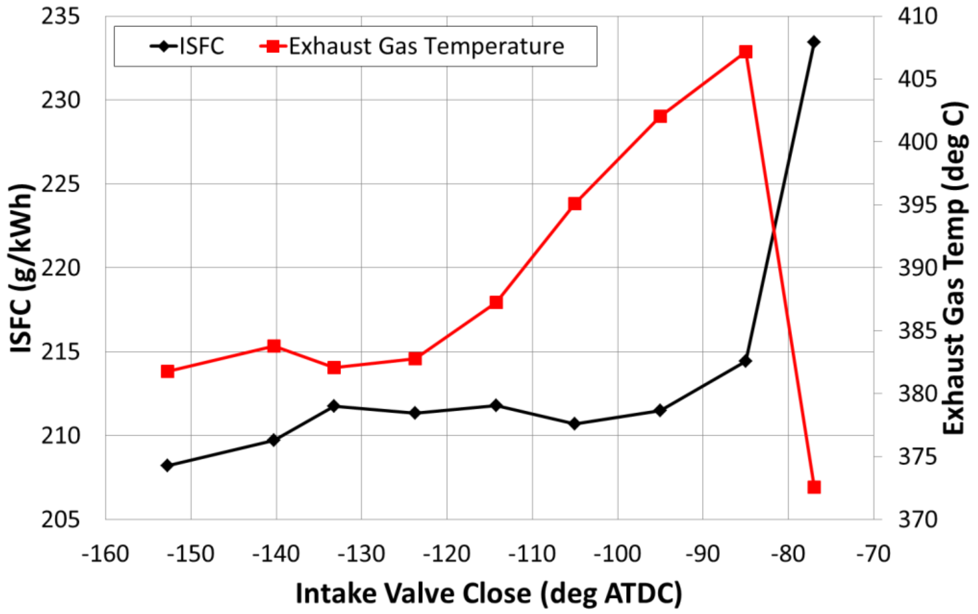

Figure 6-16: ISFC and EGT vs IVC

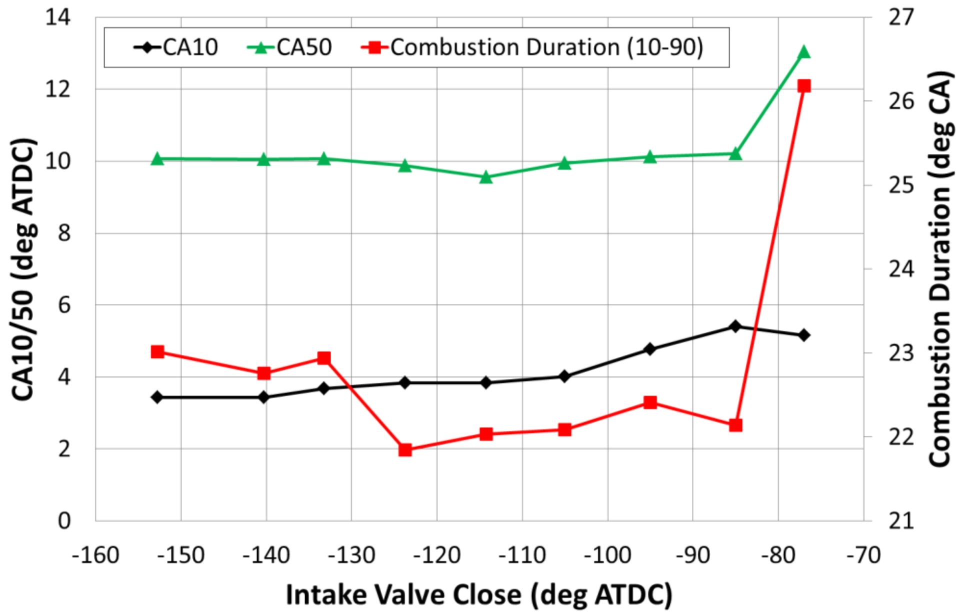

Figure 6-17: CA10 and CA50 with combustion duration vs IVC

The data plotted in Figure 6-17 confirms that CA50 was held at approximately 10 deg ATDC, while CA10 retarded slightly. The change in CA10 was reflected by the shortened combustion duration as the ECR was dropped. Combustion efficiency and COV of IMEP are presented in Figure 6-18 and show that both are maintained until the engine reached the ECR limit of 12.1. The significant drop off in combustion efficiency was due to incomplete combustion and resulted in a 6% COV of IMEP.

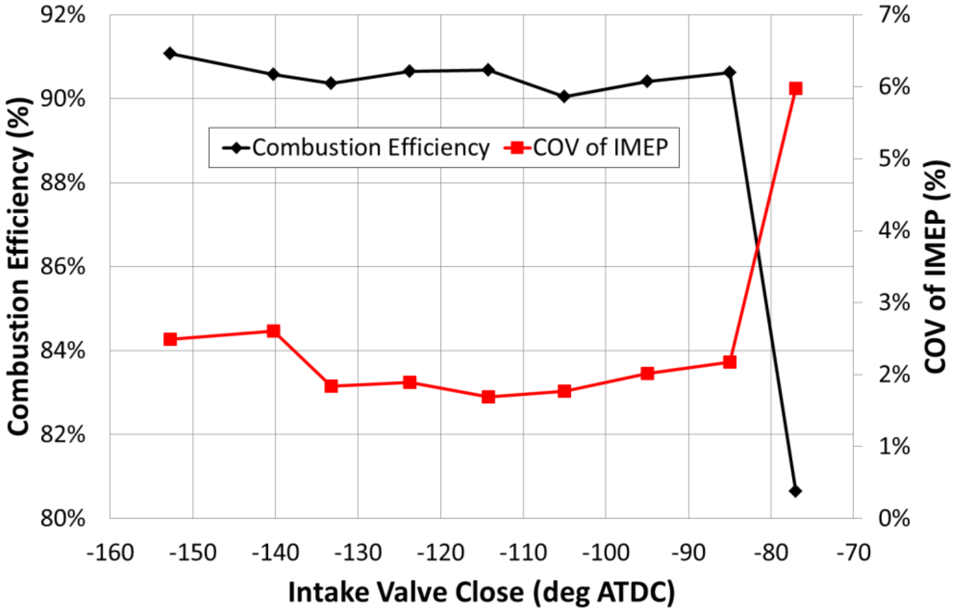

Figure 6-18: Combustion efficiency and COV of IMEP vs IVC

Finally, Figure 6-19 and Figure 6-20 are the crank angle resolved traces for cylinder pressure, HRR, and MFB. The selected cases of ECR detail the effects of Miller cycle and help to understand the mechanism for NOx reduction. Lower motoring cylinder pressure was observed for later IVC due to lower compression temperatures and higher charge density. The resulting temperature and pressure of the charge was reduced, which delayed the ignition of the diesel fuel. Despite advancing the SOI to maintain CA50, combustion of the diesel fuel was initiated later in the cycle and further away from TDC. The further proximity from TDC allowed the diesel spray more time to mix with air to help reduce NOx formation. The drawback of the Miller cycle strategy is that it requires high boost pressures in order to achieve the desired in-cylinder λ for a given load. This is a difficult task for most conventional boosting devices, particularly at low speed and light load.

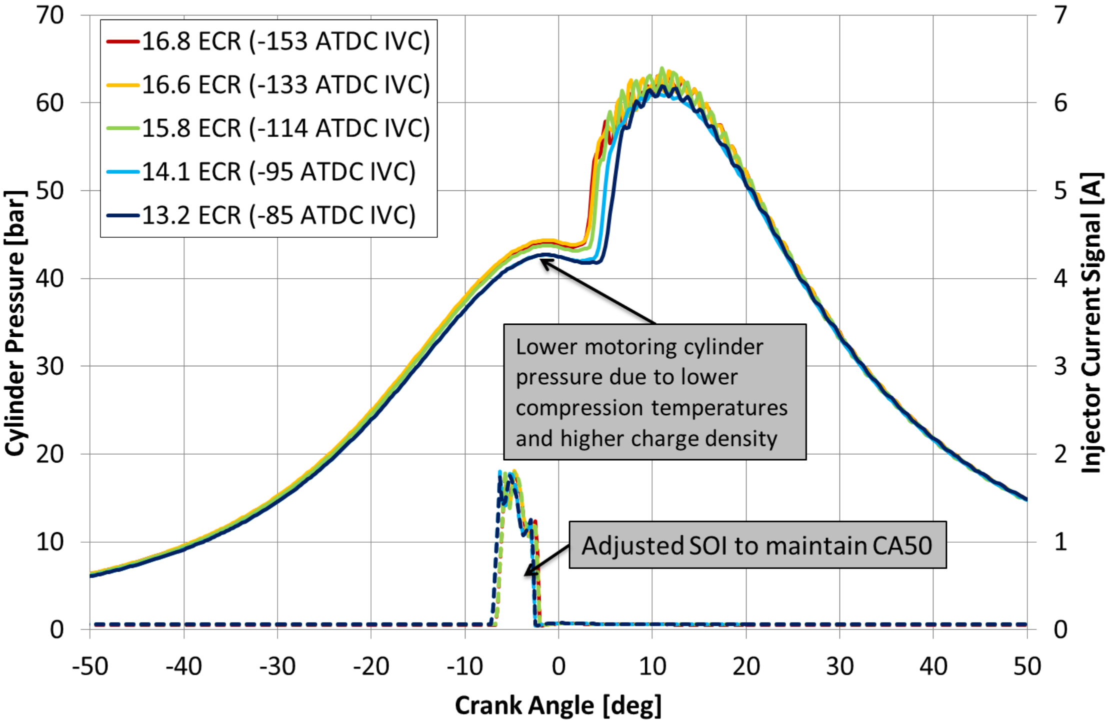

Figure 6-19: Cylinder pressure traces and injection signals vs crank angle for selected ECR/IVCs

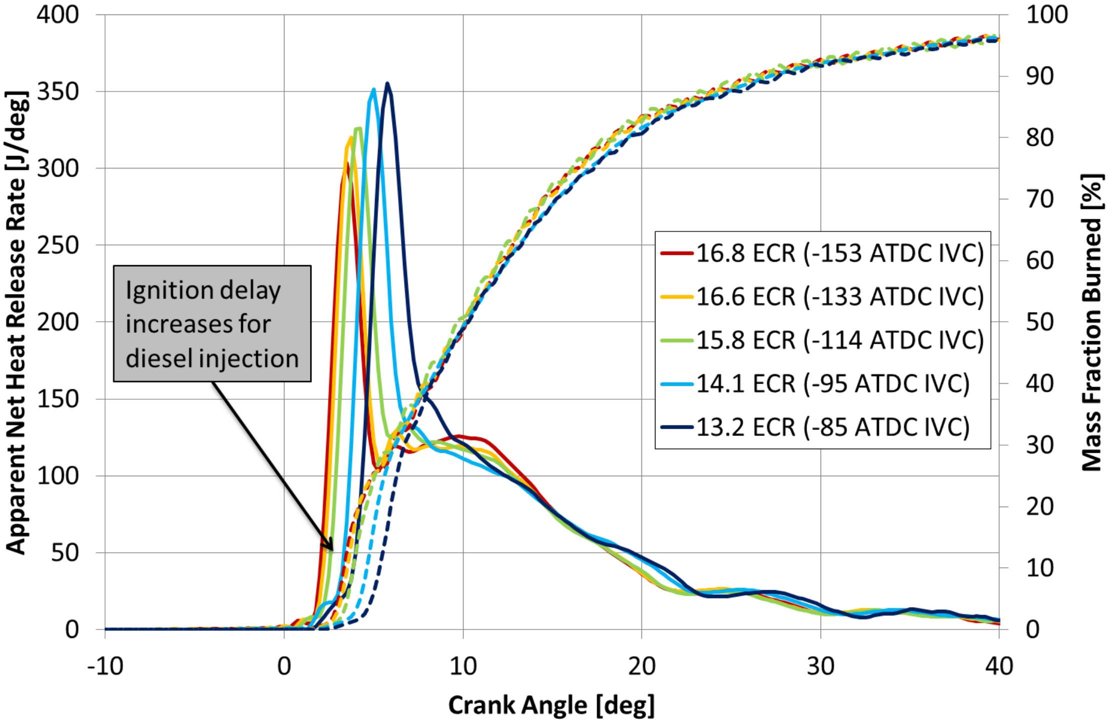

Figure 6-20: Apparent net heat release rate and mass fraction burned for selected ECR/IVCs

6.4 Internal Exhaust Gas Recirculation

Internal EGR (I-EGR) is one potential method for improving the operation of a lean-burn dual-fuel engine under light-load conditions. The additional temperature of internally recirculating residual can aid the auto-ignition of diesel, as well as potentially reduce the quenching of a natural gas flame front (albeit with a trade-off in slower reaction rate with increased EGR). This strategy will be evaluated against a cooled external EGR (E-EGR) baseline while considering key emissions and efficiency metrics. E-EGR has traditionally been used as a method to suppress NOx emissions, but the reduction of in-cylinder charge temperature can create conditions where it is challenging to burn natural gas, particularly in globally lean scenarios. Specifics of the experimental tests are outlined in Section 6.4.1 while the calculation of I-EGR percent via 1D simulation is presented in Section 6.4.2. Results from a baseline, I-EGR, and a combined (I-EGR+E-EGR) strategy are shown in Section 6.4.3.

6.4.1 Test Procedures

Conventional dual-fuel was run at a single speed and load of 1000 RPM and 6 bar IMEP_{net} under naturally aspirated conditions. Gas substitution was held at approximately 88% (~80% was targeted, but controls deviated to approximately 88%) with a single diesel injection igniting the natural gas mixture. Diesel rail pressure was 800 bar (per Z25 optimums in Table 5-5) with no pilot injection used ahead of the main diesel injection, which was timed at 12 deg BTDC.

Figure 6-21 includes the intake and exhaust valve lift curves compared to the maximum lift if there were to be no leak down from the hydraulic tappet. As leak down always occurs, the red and green dotted lines indicate the measured valve lift curves, where the methodology for introducing I-EGR is demonstrated. The red curve has a commanded opening of the intake valves from 175 to 225 degrees. The green curve is slightly longer in duration with the intake valves opening from 155 to 235 degrees during the exhaust stroke. This enables residual to be forced into the intake port to be re-ingested later during the following intake stroke. The green dotted curve is the valve lift profile used for all engine experiments except for the baseline case, which is denoted by the black dotted line. Exhaust backpressure was varied from 4 to 26 kPa gauge in order to help drive the desired amount of residual.

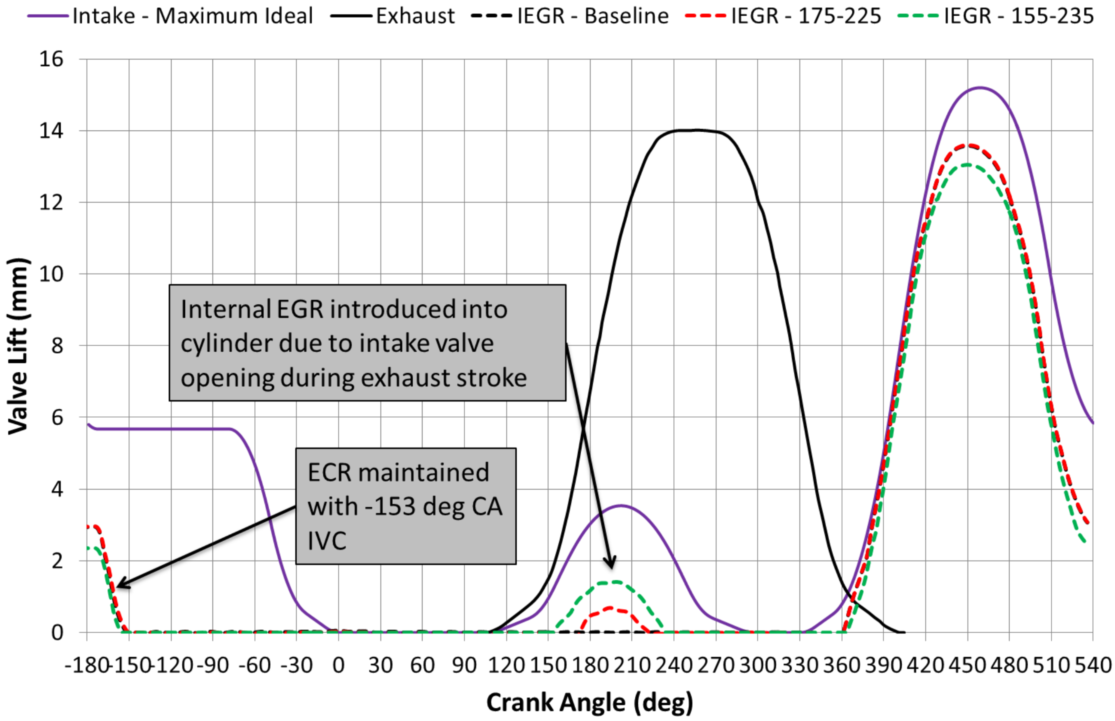

Figure 6-21: Engine valve lift curves depicting the intake valve reopening strategy used to increase I-EGR

The experimental tests began with a conventional dual-fuel baseline with 22% E-EGR and a trace 0.3% of I-EGR. This was followed with removal of E-EGR in favour of I-EGR, finally culminating with both I-EGR and E-EGR introduced simultaneously in different ratios. Calculation of I-EGR percentage was determined with 1D engine simulation, while the E-EGR was measured with the emissions analyser. Since the I-EGR percentage was calculated after the experiment and is a function of exhaust pressure, consistently spaced values were sometimes not achievable. E-EGR ranges of 18% to 23% were determined on observing emissions and fuel efficiency trends in real-time, specifically the ISNOx + ISCH4 trade-off as well as the ISFC vs exhaust backpressure trade-off.

6.4.2 Calculation of Residual Gas Fraction with Simulation

Due to the nature of its flow path backwards through the intake port, I-EGR could not be measured by the laboratory equipment available during testing. However, the need for accurate estimation of I-EGR percentage is important for drawing robust conclusions. It is possible to estimate the total in-cylinder residual gas fraction and I-EGR by way of a correlated 1D gas dynamics engine simulation model. The engine model was created with Ricardo Wave® 2015.1 simulation software, which uses the finite difference method to solve the unsteady compressible flow equations governing the conservation of mass, momentum, and energy. The simulation uses detailed thermodynamic gas properties, including equilibrium composition for the burnt gases, and enables the characterisation of the pulsating flows that occur in the engine. Through matching E-EGR and calculating the residual gas fraction, the I-EGR can be determined by subtracting the total residual in-cylinder from the known quantity of E-EGR. Shown in the left portion of Table 6-2 are the experimental test conditions that were matched by the 1D model. The right portion represents the key outputs from the Wave 1D simulation. E-EGR percentage was input into the model along with the engine boundary conditions of intake and exhaust pressure. The resulting residual gas fraction is calculated by the simulation and the final right-hand column reveals the I-EGR percentage.

Table 6-2: Residual gas fraction and I-EGR percentage calculated by 1D simulation

Experimental				**1D Simulation Model**		
I-EGR Valve Opening	**Intake Pressure**	**Exhaust Pressure**	**E-EGR**	**E-EGR**	**Residual Gas Fraction**	**I-EGR**
	bar-abs	**bar-abs**	**%**	**%**	**%**	**%**
Baseline	1.00	1.04	22	22	22.3	0.3
155-235	1.00	1.04	0	0	9	9
155-235	1.00	1.20	0	0	15	15
155-235	1.00	1.23	0	0	17	17
155-235	1.00	1.27	0	0	19	19
155-235	1.00	1.19	18	18	29	11
155-235	1.00	1.14	20	20	28	8
155-235	1.00	1.17	23	23	32	9

To ensure the accuracy of the values produced, the correlation of the Wave model was performed by matching cylinder pressure and heat release traces from the experimental tests. Experimental heat release data was input to a multi-

Wiebe combustion model to match the combustion profile. Recorded data from the fast response intake and exhaust pressure transducers were used to verify the wave dynamics in the intake and exhaust systems (shown in Appendix D – 1D Gas Dynamics Model Validation Graphs). Port flow discharge coefficients were tuned (referenced in Appendix E – 1D Gas Dynamics Model Flow Coefficients) to match total mass flow through the engine to within 2%. Additional convergence criteria also verified that the simulation reached steady-state before the cycles were terminated.

6.4.3 Results and Discussion

The key emissions and efficiency metrics are compared from a baseline, I-EGR, and a combined (I-EGR+E-EGR) strategy. The colour black denotes the baseline case, which characterises the engine running with 22% E-EGR and a nominal 0.3% I-EGR. The cases shaded with the colour green represent the removal of E-EGR, supplemented with the gradual addition of I-EGR from 9 to 19%. Finally, the red coloured cases illustrate a strategy with both I-EGR and E-EGR introduced simultaneously in different ratios.

The data plotted in Figure 6-22 helps to demonstrate how the exhaust pressure was used to achieve the desired amount of I-EGR. For the baseline case, exhaust pressure was run at 1.04 bar-abs which yielded a gas exchange efficiency of 96%. This efficiency was maintained as the I-EGR valve lift profile was activated. However, as larger amounts of I-EGR were required, the pressure differential across the cylinder needed to be increased in order to force a greater quantity of exhaust gas into the intake port. To achieve this, the exhaust pressure was raised until the desired amount of I-EGR was attained. Unfortunately, the drawback of this method was the lowered gas exchange efficiency resulting from the additional exhaust pumping work. This factor was something that needed to be taken into consideration when calculating the overall engine efficiency.

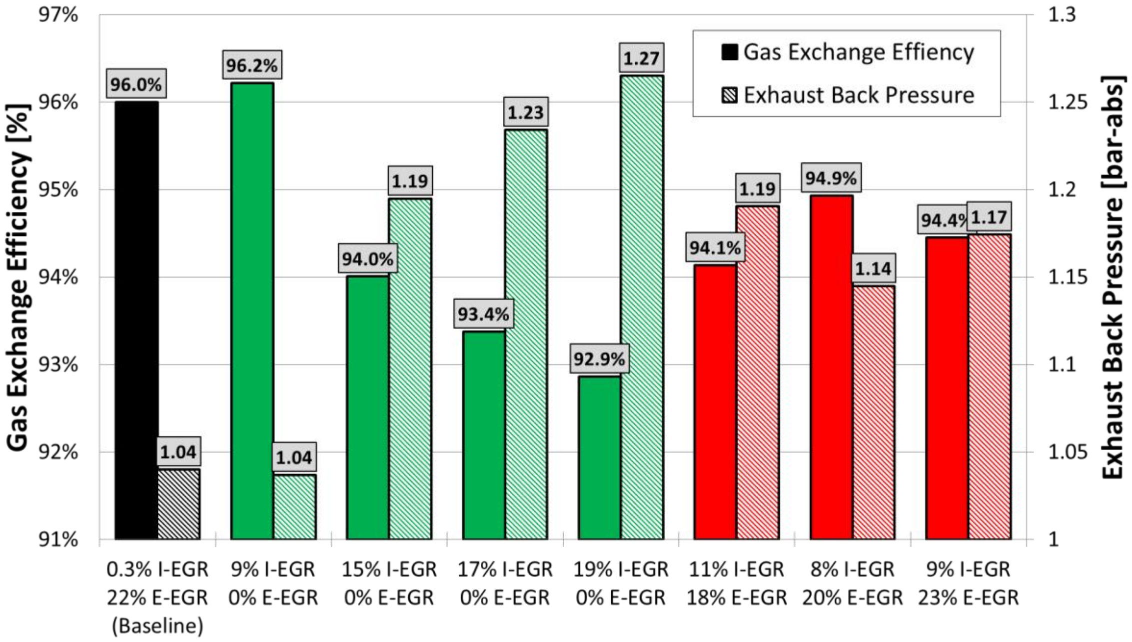

Figure 6-22: Gas exchange efficiency and exhaust pressure for various I-EGR and E-EGR combinations

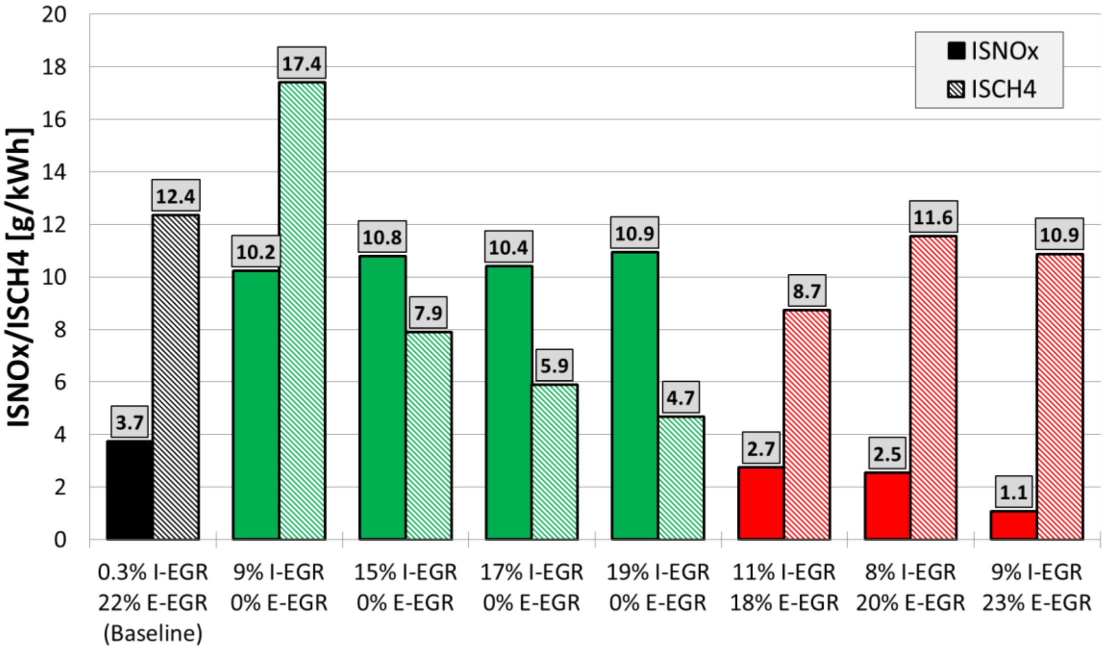

Figure 6-23: Engine-out $ISCH_4$ and ISNOx emissions for various I-EGR and E-EGR combinations

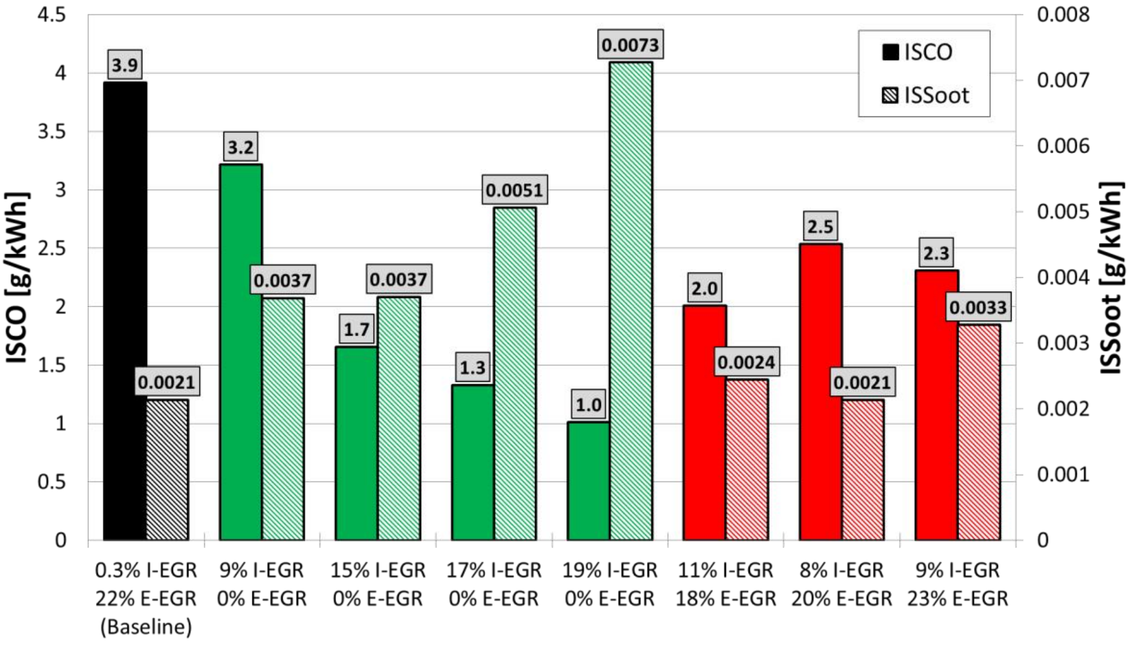

Figure 6-24: Engine-out ISCO and ISSoot emissions for various I-EGR and E-EGR combinations

Engine emissions results are presented in Figure 6-23 and Figure 6-24. As a reminder, the baseline conventional dual-fuel case is shown in black on the left of the bar charts. The removal of E-EGR from the baseline case resulted in an immediate increase in NOx emissions due to the higher temperature combustion process and the leaner local equivalence ratios. For the 9% I-EGR case, this was also accompanied by an increase in $ISCH_4$ emissions, due to the globally leaner in-cylinder conditions. As additional I-EGR was supplied to the cylinder to reduce the overall in-cylinder λ, NOx was maintained at the relatively high levels of 10-11 g/kWh, while the $ISCH_4$ emissions were significantly reduced. As E-EGR was re-introduced to quell the NOx emissions alongside I-EGR, the $ISCH_4$ emissions increased again. This behaviour suggests that an overall NOx and CH_4 trade-off exists with the I-EGR and E-EGR strategies. However, it should be noted that all combinations of the I-EGR/E-EGR (red) cases performed better than the baseline case when considering NOx and CH_4 emissions. This conclusion can also be extended to include ISCO, which performed similarly to $ISCH_4$ emissions. ISSoot emissions were maintained, but could be shown to increase with higher levels of I-EGR.

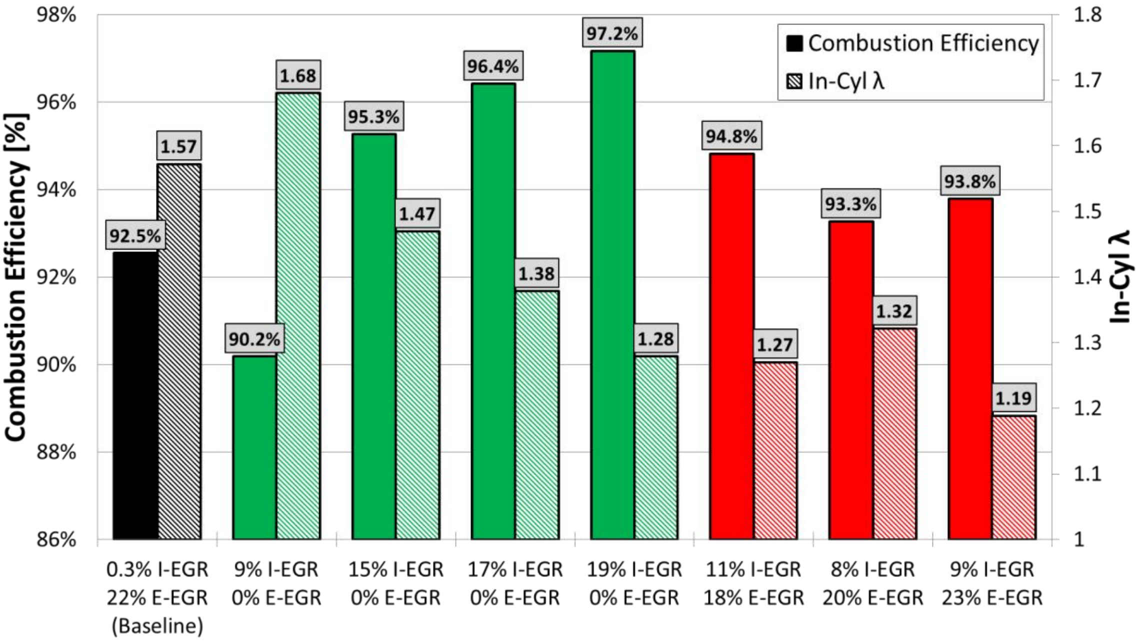

Figure 6-25: Combustion efficiency and in-cylinder λ for various I-EGR and E-EGR combinations

Shown in Figure 6-25 is a comparison between combustion efficiency and in-cylinder λ. The baseline case begins at a combustion efficiency of 92.5% at a global in-cylinder λ value of 1.57. These are fairly typical values for conventional dual-fuel combustion at this speed and load. As shown by the green cases, the removal of E-EGR initially caused a drop in combustion efficiency due to the higher in-cylinder λ. E-EGR normally would displace the fresh air entering the combustion chamber, but its absence created less favourable (leaner) burning conditions for natural gas. As the I-EGR quantity was increased, more fresh air was displaced, dropping λ. The combustion efficiency benefits from the richer burning conditions which yield faster burning velocities. However, an additional benefit is drawn from bulk auto-ignition of the end gas, which will be discussed later in the section. The re-introduction of E-EGR in the red cases reduced the combustion efficiency when compared against the I-EGR only cases (green), but was necessary in order to quell NOx emissions. Nevertheless, the combustion efficiency of both the green and red cases performed better than the black baseline case, which helps support the mechanism of the lowered $ISCH_4$ emissions found in Figure 6-23.

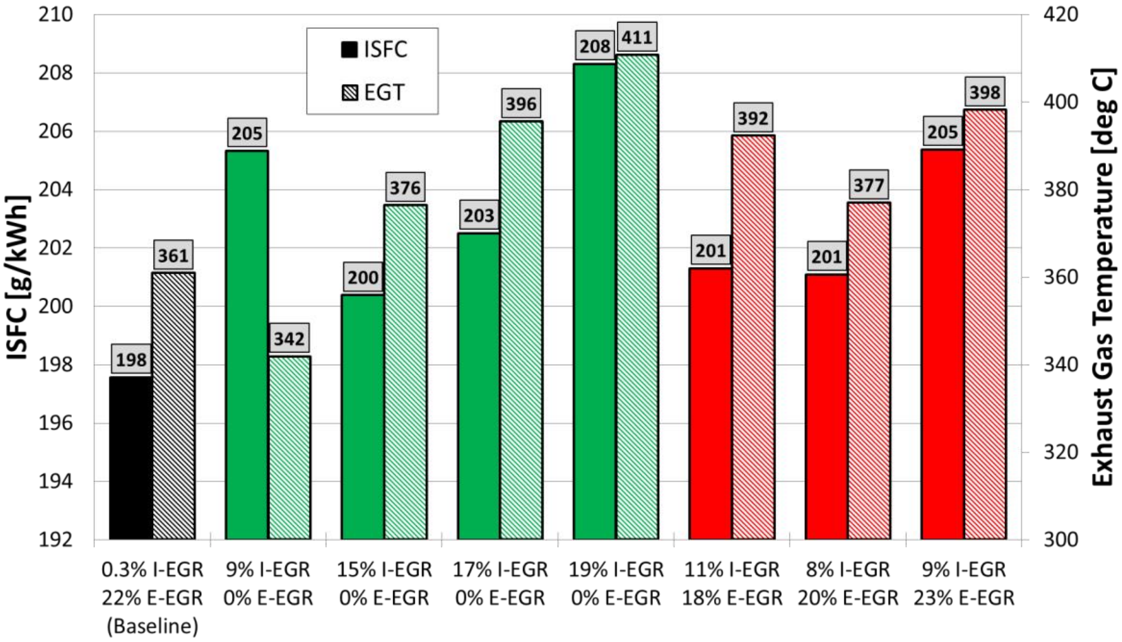

Figure 6-26: ISFC and EGT for various I-EGR and E-EGR combinations

The baseline case in Figure 6-26 attained an ISFC value of 198 g/kWh with an exhaust gas temperature of 361 °C. This was the lowest ISFC value when compared to the I-EGR only and combined E-EGR and I-EGR strategies, which were all at or above 200 g/kWh. The engine efficiency is primarily influenced by the combustion and gas exchange efficiencies, with combustion phasing and λ (γ) contributing on a secondary or resulting basis. The main trade-off is between the pumping losses associated with the higher exhaust pressure used to drive I-EGR and the greater percentage of fuel burned via the higher combustion efficiency. As E-EGR was initially removed, pumping losses were maintained while combustion efficiency decreased. The effects were observed as an increase in ISFC to 205 g/kWh and a decrease in EGT. As more I-EGR was introduced, the ISFC improved to 200 g/kWh due to a higher percentage of the fuel being consumed. The subsequent I-EGR only cases observed further improvements to combustion efficiency, but not at the rate necessary to offset the increased exhaust pumping losses. Similar trade-offs occurred with the combine E-EGR and I-EGR strategy, as ISFC improved as the exhaust pressure was decreased. Higher EGTs were achieved with I-EGR when compared to the baseline due to increased combustion efficiency, but also due to the reduction of in-cylinder λ. The secondary effects of increased EGT were not included in this specific study, but could possibly yield benefits towards exhaust after-treatment efficiency and tailpipe emissions.

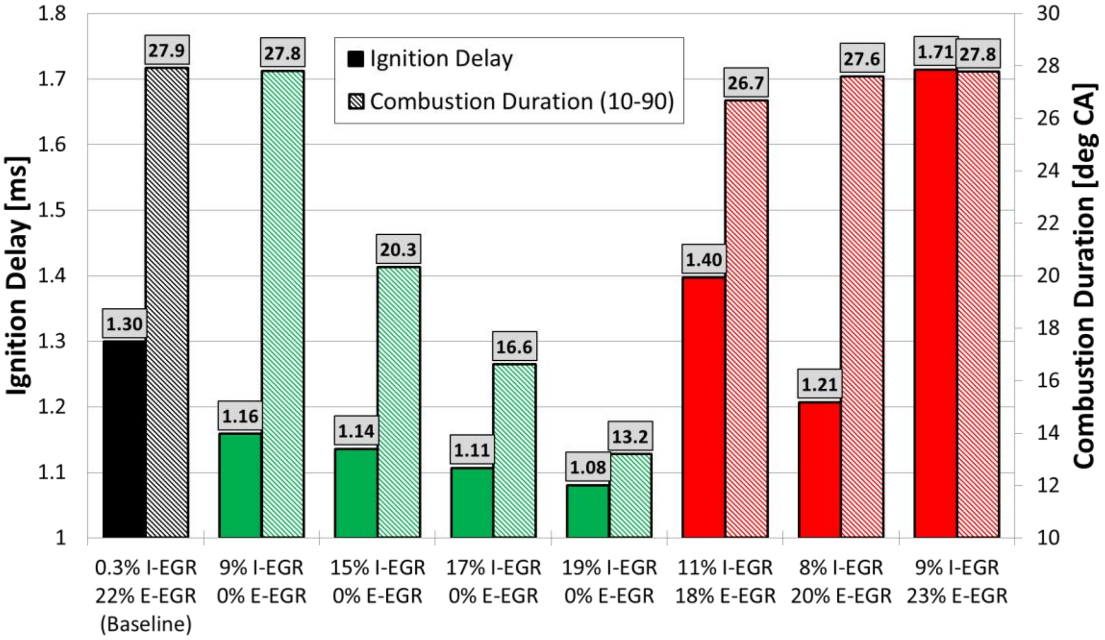

Figure 6-27: Ignition delay and (10-90%) combustion duration for various I-EGR and E-EGR combinations

The data plotted in Figure 6-27 shows that combustion duration was significantly reduced when E-EGR was removed and appropriate levels of I-EGR were added. Combustion duration was aided by the higher burning velocity brought about by the decreased λ, but also due to the bulk auto-ignition of the end gas. The auto-ignition was a result of the higher in-cylinder temperatures from hotter residual, which ultimately led to a rapid consumption of fuel during the later stages of combustion. The degree of bulk auto-ignition of the unburnt region can vary with λ and is arguably linked with flame propagation and burning velocity [70,138]. The higher chemical heat release rate with lower λ combustion combined with the increased temperature from internal residual can be beneficial for the completion of the combustion process via bulk auto-ignition close to TDC. Optical techniques can further enhance the understanding of how the aerodynamics and chemistry might interact to increase the burning velocity without the consequences of knock. Further, the ignition delay was steadily reduced during the I-EGR only cases, and suggests the hotter residual helped initiate the diesel fuel combustion sooner. It can also be observed that the ignition delay was particularly sensitive to E-EGR amounts, as larger delays were observed for the combined E-EGR/I-EGR strategy. This also highlights the temperamental and sporadic nature of this particular method of achieving auto-ignition, as relatively small differences in calibration can yield significant changes in combustion performance.

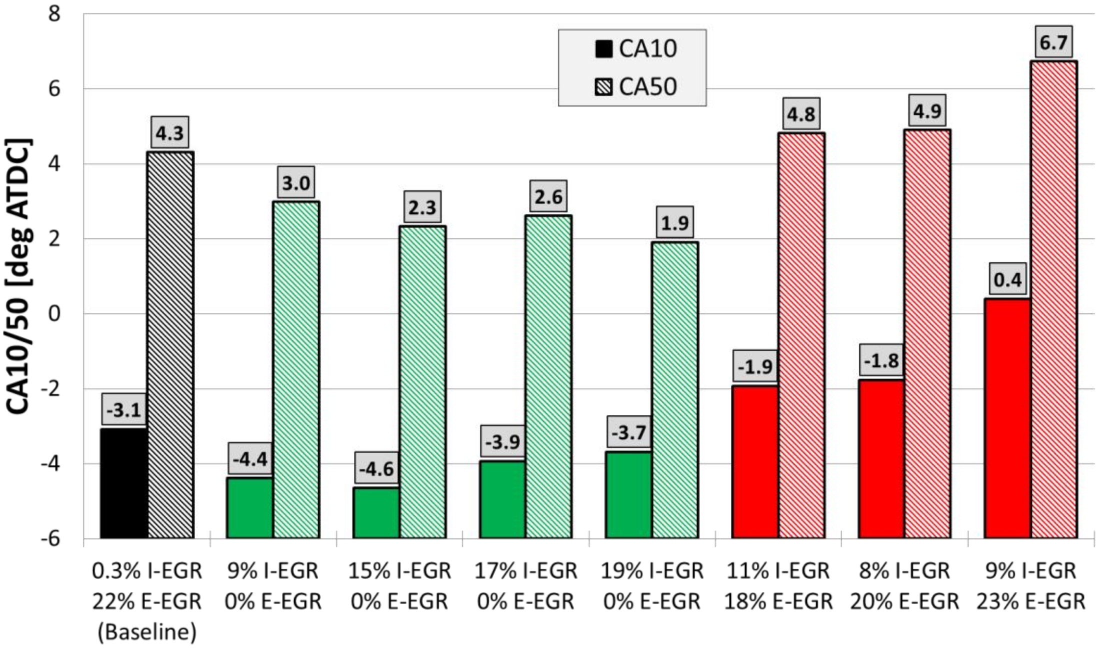

Figure 6-28: 10% and 50% mass fraction burned for various I-EGR and E-EGR combinations

Additional insight into the combustion process is provided by the data in Figure 6-28, which shows the CA10 and CA50. Both of these were advanced for the green cases due to the hotter in-cylinder residual from I-EGR. The CA50 values for the I-EGR only cases were slightly over advanced due to the injection timing being held constant. The over advancing of CA50 degraded ISFC due to the resulting work being performed on the piston while it was still on its way toward TDC.

The highest cylinder pressures were also achieved during the I-EGR only cases, as illustrated by Figure 6-29. As I-EGR percentage was increased, a larger degree of auto-ignition took place due to the hotter in-cylinder temperatures. The PRR was also increased when compared against the cases with E-EGR. It can also be observed that the maximum PRR can either be generated by the first diesel combustion bump or from the auto-ignition portion, which is why it did not track with cylinder pressure. PMax and PRR were decreased for the combined

E-EGR/I-EGR cases due to the overall higher residual gas fractions and delayed combustion.

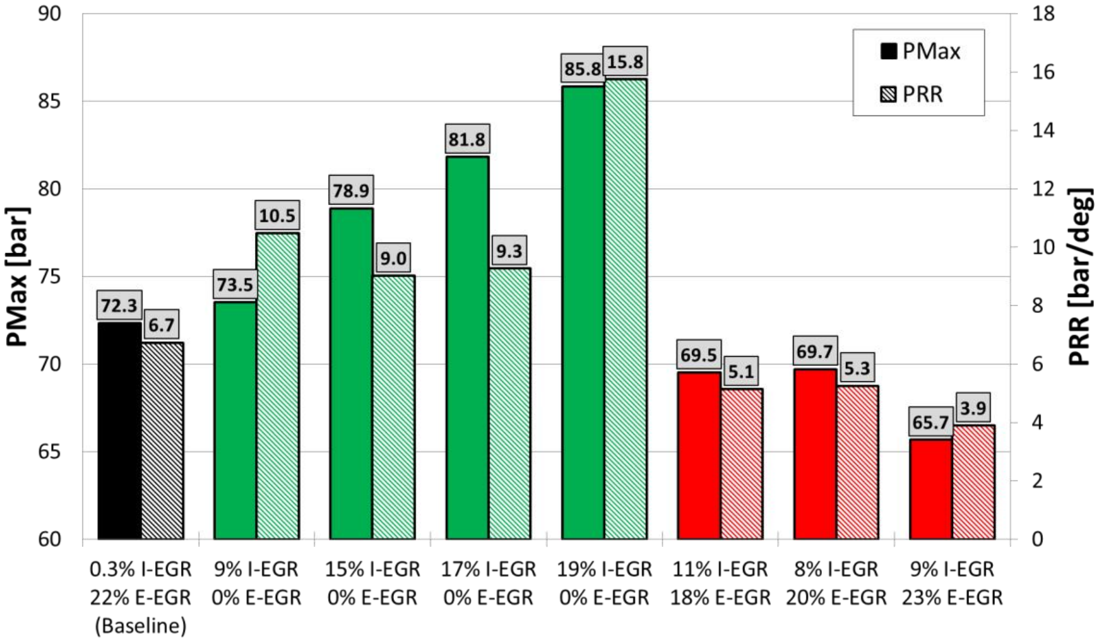

Figure 6-29: Maximum cylinder pressure and pressure rise rate for various I-EGR and E-EGR combinations

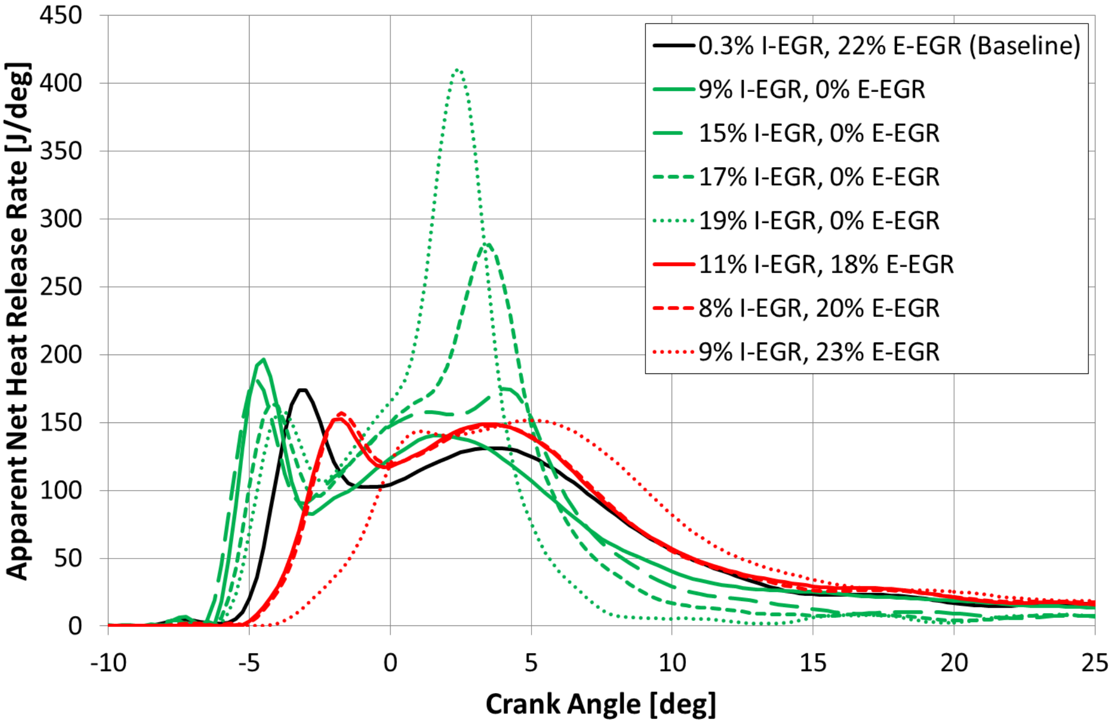

Figure 6-30: Apparent net heat release rate for various I-EGR and E-EGR combinations

The heat release profiles are shown in Figure 6-30, where the general colour scheme is carried over from the bar graphs. The black baseline case is shown with the typical double hump heat release shape associated with conventional dual-fuel combustion. The green I-EGR only cases retain this overall shape, though the first diesel combustion bump was shifted earlier due to the removal of E-EGR and the addition of higher temperature internal residual. This lowered the ignition delay of the diesel fuel, which created a higher and earlier first bump. The solid green 9% I-EGR profile has resemblance to the black baseline, as no auto-ignition was observed. However, as the I-EGR percentage was increased from 15% to 19%, a progressively larger auto-ignition bump was observed. The bulk auto-ignition of the end gas led to a faster and higher heat release, which helped to realise the efficiency and emissions benefits at this particular speed-load condition. As E-EGR was added back in to subdue NOx production, the auto-ignition characteristic disappeared, as observed by the combined E-EGR/I-EGR strategy in red.

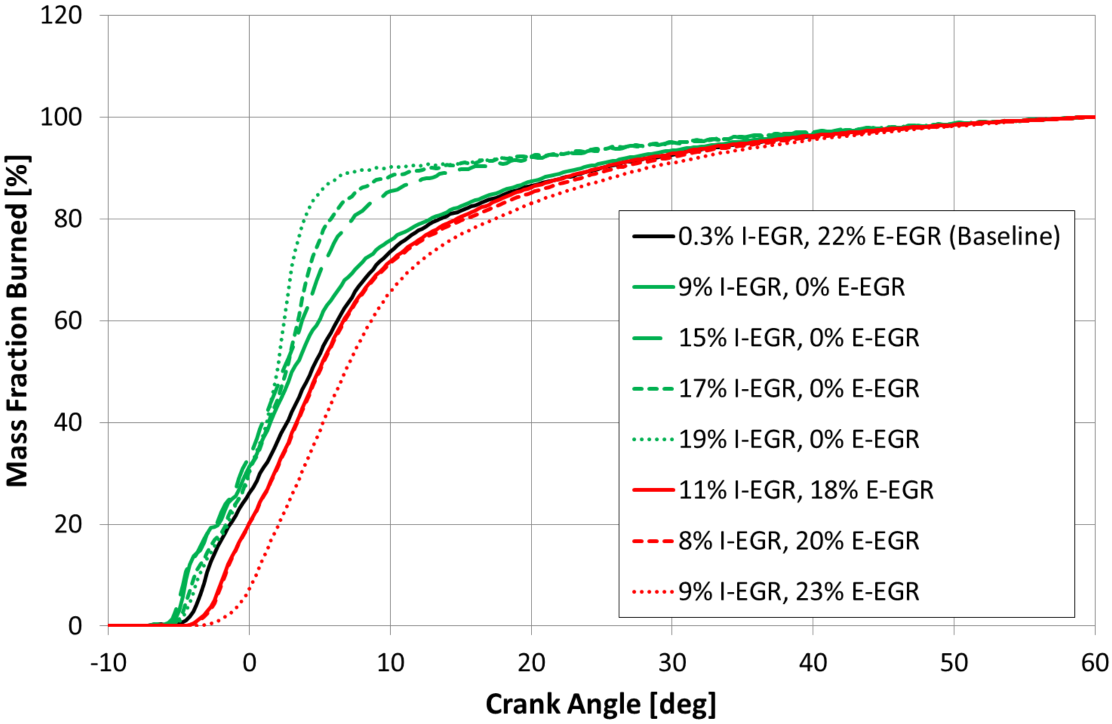

Figure 6-31: Mass fraction burned for various I-EGR and E-EGR combinations

The auto-ignition effect on mass fraction burned is further illustrated by the data in Figure 6-31, with the green lines of I-EGR burning significantly faster when compared to the other cases. The combustion duration was considerably shortened in a relatively narrow band of 9% to 19% I-EGR, which suggests that auto-ignition is sensitive to in-cylinder residual. This can pose challenges from an engine control and transient perspective, as balancing the ratio of E-EGR to I-EGR is critical to achieving auto-ignition with a reasonable level of NOx emissions. Furthermore, the upper limit of EGR is limited by combustion phasing control, as it can be difficult to provide consistent diesel ignition, particularly at high gas substitution percentages where the diesel injection quantity is small. Finally, there is the practical hurdle of introducing sufficient delta pressure across the cylinder in order to drive sufficient I-EGR in real-world applications. This would either require throttling or raising the exhaust pressure of the engine during operation, which would result in increased pumping losses and lowered efficiency.

6.5 Reactivity Controlled Compression Ignition

RCCI is an auto-ignition focused injection strategy which has the potential for improving the operation of a lean-burn dual-fuel engine under light-load conditions. The distribution of premixed diesel fuel at the correct timings and quantities before firing TDC can help to create favourable combustion conditions which yield low emissions and high efficiency. This section will be about determining the best ways to optimise the diesel injections with the specific focus to reduce engine-out methane emissions. The test plan for RCCI is outlined in Section 6.5.1, with the timing of the pilot and main diesel injections being determined in Section 6.5.2. Finally, explored in Section 6.5.3 is the sensitivity of the injected diesel quantities as well as the effects of double and single injection strategies.

6.5.1 Test Procedures

RCCI tests were run at a single speed and load of 1000 RPM and 6 bar $IMEP_{net}$ (25% of full load) under naturally aspirated conditions. Gas substitution was approximately 82% (80% targeted but deviated to 82% due to controls). A diesel rail pressure of 800 bar (per Z25 optimums in Table 5-5) was used for all experiments. Intake and exhaust pressure were maintained at 0.995 and 1.03 bar, respectively. Conventional valvetrain settings were used, which yielded a pressure-based effective compression ratio of 16.8. All experiments were run with 20% cooled E-EGR. Specific details of the diesel injections strategies will be outlined at the start of Sections 6.5.2 and 6.5.3.

6.5.2 Pilot and Main Injection Timing Optimisation

The diesel injections of an RCCI strategy are important in order to observe improvements to emissions and efficiency. In an effort to find an optimum, the pilot and main diesel injection timings were both varied while the other was held at a constant value as depicted in Table 6-3. A 50/50 and 60/40 quantity split of diesel fuel in the first (pilot) and second (main) injections were tested for each of the pilot and main injection timing sweeps. Quantity splits beyond 60/40 (i.e. 70/30) were not tested due to excessive pressure rise rates and/or issues with combustion control when executing the full range of the intended timing sweep (operating band narrows with larger pilot). Two different main injection timings of 17 and 27 deg BTDC were necessary for the pilot injection timing sweep as the diesel split changes the combustion timing and auto-ignition characteristics of the engine. “Round” injection timings of 20 and 30 deg BTDC were targeted from the ECU, but are slightly delayed to 17 and 27 deg BTDC respectively when considering injector delay. Typical injection quantities for this particular speed/load and substitution percentage were in the 6 to 8 mm^3 range.

Table 6-3: Test points for the pilot and main injection timing sweeps with a 50/50 and 60/40 quantity split of diesel injections

Pilot Injection Timing Sweep				**Main Injection Timing Sweep**		
Pilot	**Main (50/50)**	**Main (60/40)**		**Pilot**	**Main (50/50)**	**Main (60/40)**
deg BTDC	**deg BTDC**	**deg BTDC**		**deg BTDC**	**deg BTDC**	**deg BTDC**
69	17	27		49	37	32
59	17	27		49	32	22
49	17	27		49	27	17
39	17	27		49	22	
				49	17	
				49	7	

The data for engine-out emissions are displayed in Figure 6-32 and Figure 6-33, and were broken up into 4 individual cases. The black squares and red diamonds denote the pilot injection timing sweep, while the purple circles and blue triangles show the results of the main injection timing sweep. The dotted lines indicate the 50/50 diesel quantity split with the solid lines signifying 60/40. The emissions were plotted against the injection timing to determine the best trade-offs.

It can be observed that for a 50/50 diesel quantity split, the pilot injection timing was relatively insensitive to engine-out emissions, especially when compared to the main injection timing. Auto-ignition for the 50/50 split was subdued, as the amount of premixed diesel had not reached sufficient levels to initiate it. However, there was a slight improvement to emissions with introducing the quantity of premixed diesel fuel earlier in the cycle (i.e. 70 to 60 deg BTDC), possibly due to the increased amount of time the diesel had to evenly entrain with the cylinder contents. Shifting diesel quantities from 50/50 to 60/40 in favour of the first diesel injection created a higher sensitivity to injection timing, particularly with regard to ISNOx emissions, which increased significantly for the latest pilot case. The later that the premixed diesel fuel was introduced, the less benefit toward the burning of $ISCH_4$ it provided, as it was less evenly disbursed within the cylinder. A late diesel injection also allowed less time for the fuel to mix before ignition temperature was reached, which resulted in higher NOx emissions. Finally, an offset was observed in emissions for the 60/40 diesel quantity split due to the earlier main injection of 27 deg BTDC, rather than 17 deg BTDC. This shift in main injection timing was necessary in order to avoid high pressure rise rates caused by the shift to a 60/40 diesel quantity split.

The sensitivity of emissions to main injection timing was more direct, with the highest NOx and lowest CH_4 emissions occurring in the 35 to 20 degree BTDC injection window. The later diesel injections had lower NOx because they burned later relative to TDC resulting in a lower combustion temperature. The earlier diesel injections had lower NOx because they were better mixed, and relied on chemical kinetics led auto-ignition for the start of combustion. ISCO was also reduced during the 35 to 20 degree BTDC injection window, with soot remaining level. $ISCH_4$, ISCO, and ISSoot were increased for the latest injection case as combustion temperatures were significantly lowered and the diesel injection was later relative to TDC.

In addition to ISSoot emissions, the data presented in Figure 6-33 can be used to provide insight into the COV of IMEP and net indicated efficiency of the engine. The stability of the RCCI combustion mode was maintained below 2.5% COV for all of the test points, thereby demonstrating robust steady state performance. However, the application of RCCI in a multi-cylinder engine might result in a higher value of COV of IMEP, as auto-ignition is particularly susceptible to cylinder imbalances.

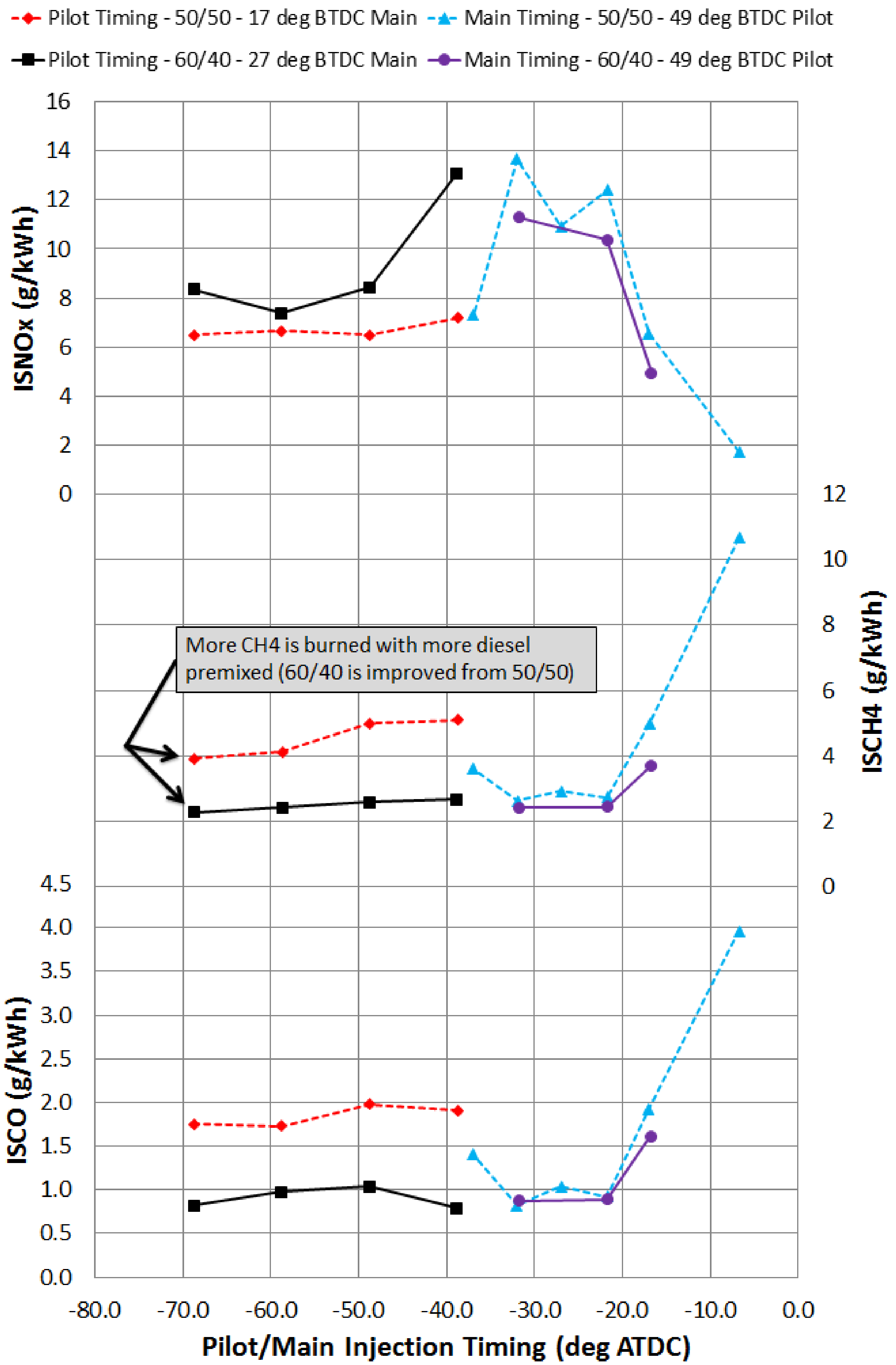

Figure 6-32: Engine-out ISNOx, ISCH₄, and ISCO emissions vs pilot and main injection timing for a 50/50 and 60/40 diesel quantity split

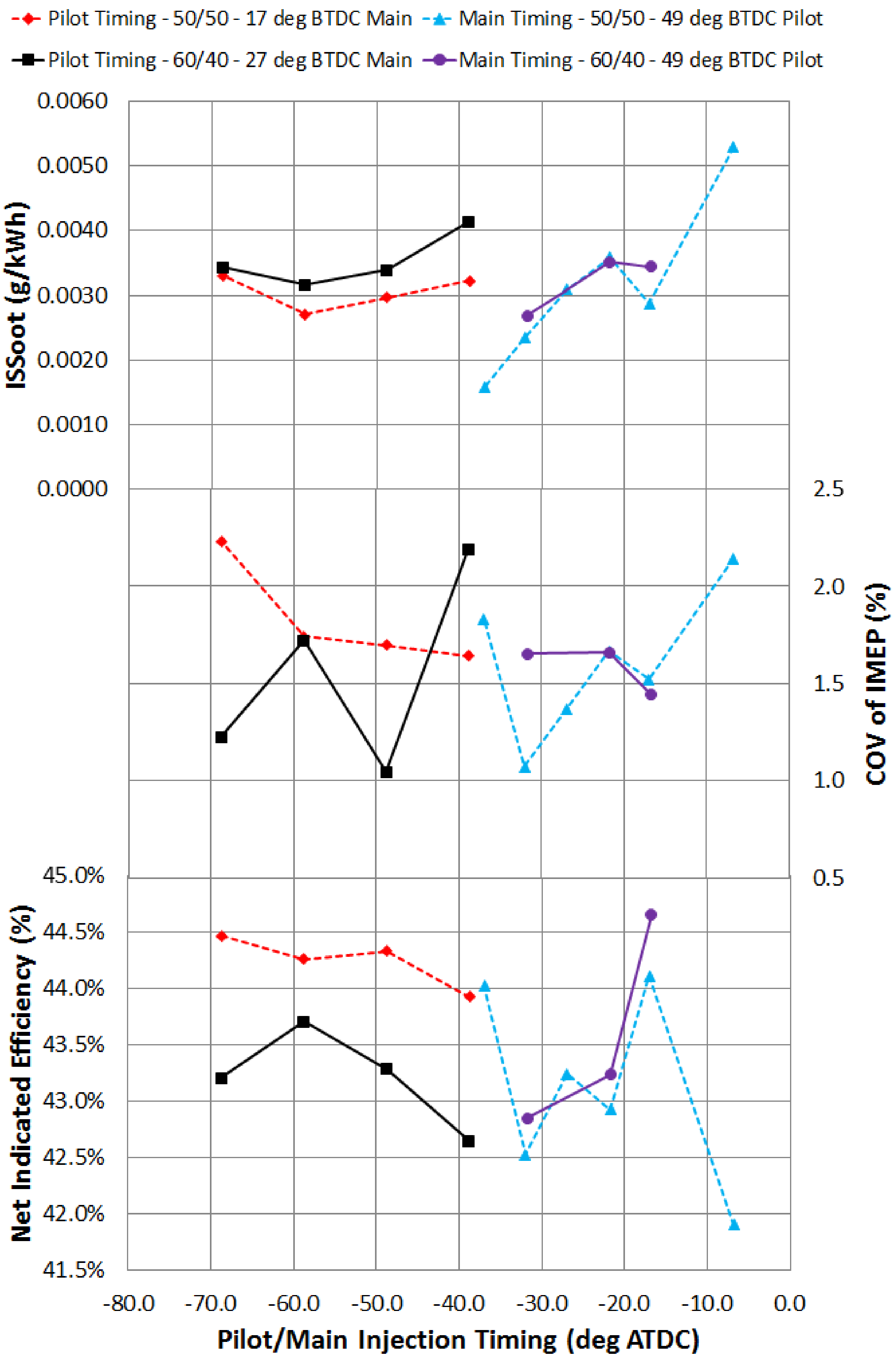

Figure 6-33: Engine-out ISSoot emissions, COV of IMEP, and net indicated efficiency vs pilot and main injection timing for a 50/50 and 60/40 diesel quantity split

The net indicated efficiency for the pilot timing sweep was observed to be higher for the 50/50 diesel quantity split when compared against the 60/40, despite the higher combustion efficiency experienced by the 60/40 case. The lower efficiency was due to the auto-ignition causing more of heat to be released while the piston was still on its way toward TDC, which resulted in a loss of useful work. It should be mentioned that net indicated efficiency is primarily affected by combustion efficiency and combustion phasing. Generally, with an earlier pilot injection, the resulting efficiency would improve, as the diesel would be more evenly distributed within the cylinder to aid the burning of natural gas. The combustion efficiency would increase and mean that a greater percentage of the fuel was converted into usable work. However, if auto-ignition was triggered such that a significant portion of the heat release occurred before TDC, then it would degrade the benefits gained by combustion efficiency. This can be demonstrated by the 50/50 and 60/40 diesel quantity splits not having a uniform increase in efficiency with pilot injection advance. Additionally, the net indicated efficiency for the main injection sweep was decreased in the 35 to 20 degree BTDC injection window, also due to a higher portion of the combustion taking place before TDC.

CA50 along with the combustion duration and efficiency are plotted in Figure 6-34. These data are used to provide further detail regarding the aforementioned combustion phasing and efficiency trade-off. The sensitivity of CA50 to pilot injection timing was dependent on how close the combustion was to auto-ignition. For the 50/50 diesel quantity split, the CA50 was relatively insensitive, whereas the 60/40 case was slightly more curved. There was a slight advancing of combustion for the latest pilot injection timing case for both the 50/50 and 60/40 cases, as the pilot began to extend into the main injection timing regime. An offset was observed between the 50/50 and 60/40 split cases, as the main injection timing of 27 deg BTDC helped to advance the combustion phasing for the 60/40 case. The CA50 for the main injection timing sweep was advanced in the 35 to 20 degree BTDC injection window, as that was where auto-ignition was the most prevalent. In this particular case, the combustion duration helped to signify the degree of auto-ignition as the shorter duration meant more of the cylinder contents were being consumed more rapidly.

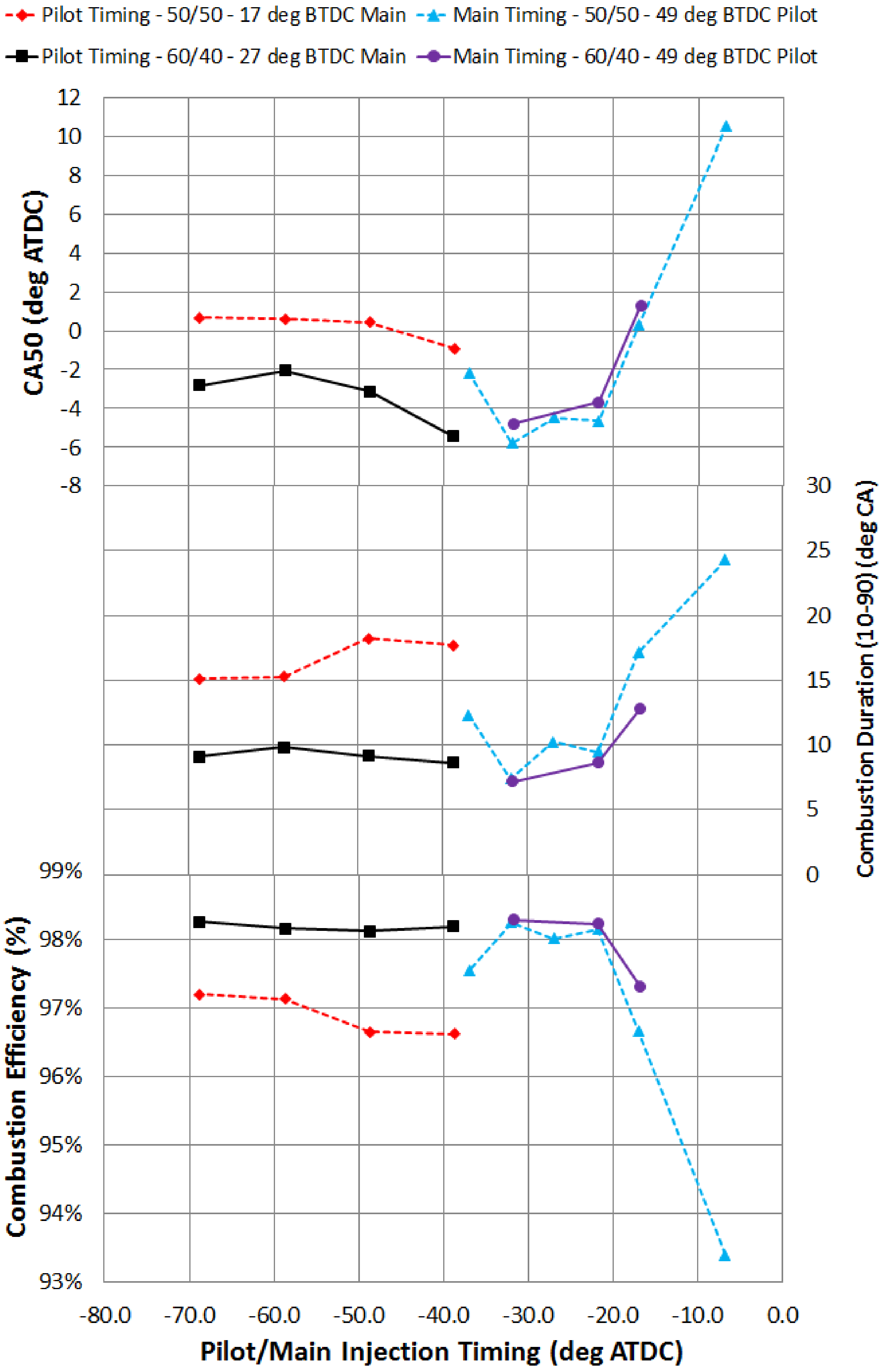

Figure 6-34: CA50, 10-90% combustion duration, and combustion efficiency vs pilot and main injection timing for a 50/50 and 60/40 diesel quantity split

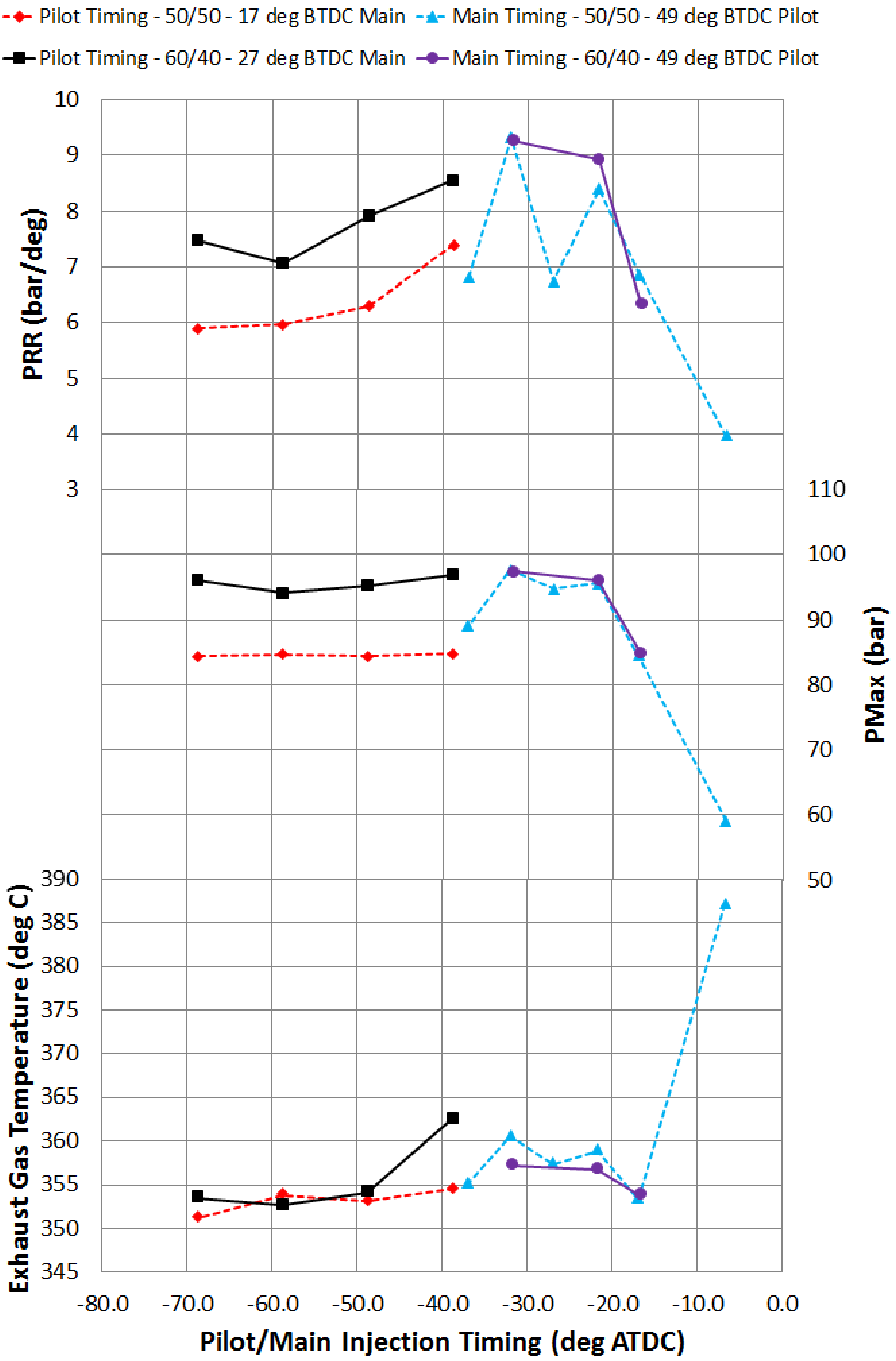

Figure 6-35: Maximum pressure rise rate, maximum cylinder pressure, and EGT vs pilot and main injection timing for a 50/50 and 60/40 diesel quantity split

This was accompanied by higher combustion efficiencies, which suggested the diesel fuel and natural gas were experiencing auto-ignition characteristics. The combustion efficiency was likely combustion chamber and crevice volume limited, as the cases with auto-ignition achieved a maximum value of approximately 98.3%.

The PRR and maximum cylinder pressure are included in Figure 6-35. As expected, these parameters were primarily a function of main injection timing, with the highest values occurring in the 35 to 20 deg BTDC injection window. This was due to the combustion event's proximity to TDC and the fact that auto-ignition was helping to shorten overall combustion duration. Again, an offset was observed for the 60/40 diesel quantity split case when compared to the 50/50 due to the advanced main injection timing. EGT was also included in Figure 6-35 and was fairly consistent with the majority of the test cases. The latest main injection timing case resulted in the highest EGT since it was relatively retarded combustion.

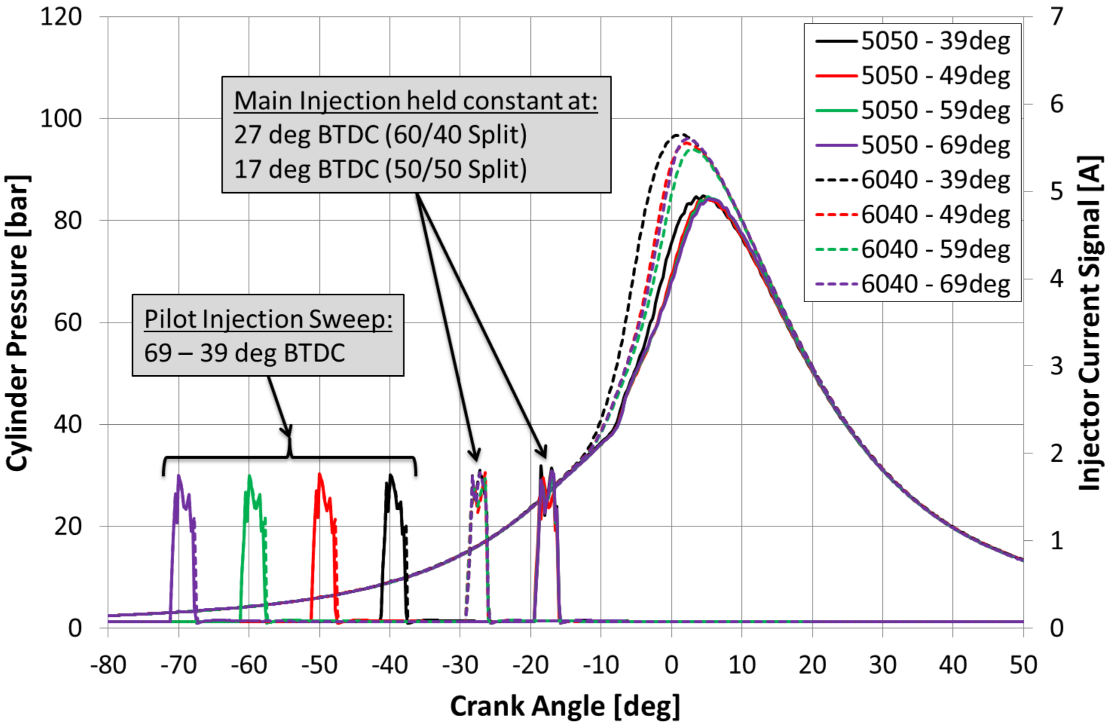

Figure 6-36: Cylinder pressure traces and injection signals vs crank angle for the pilot injection timing sweep

Figure 6-36 includes a crank angle based cylinder pressure comparison for the pilot injection timing sweep. The solid lines represent the 50/50 diesel quantity split cases, while the 60/40 cases are the dashed. The injection timings are also plotted on a secondary axis and help to visualise the difference between the 50/50 and 60/40 diesel quantity split. It can be observed that the latest pilot injection timing for both splits resulted in the highest cylinder pressure and the earliest start of combustion. This was likely due to the latest pilot injection introducing a larger local concentration of diesel fuel before combustion took place. This would lead to a stratified local λ and yield a highly reactive mixture. However, it should be noted that this injection timing resulted in the highest NOx and CH_4 emissions for the pilot timing sweep. The increased emissions were also attributed to the large concentration of diesel fuel droplets at the time of combustion, and that the diesel fuel was not well mixed enough in order to help the consumption of natural gas.

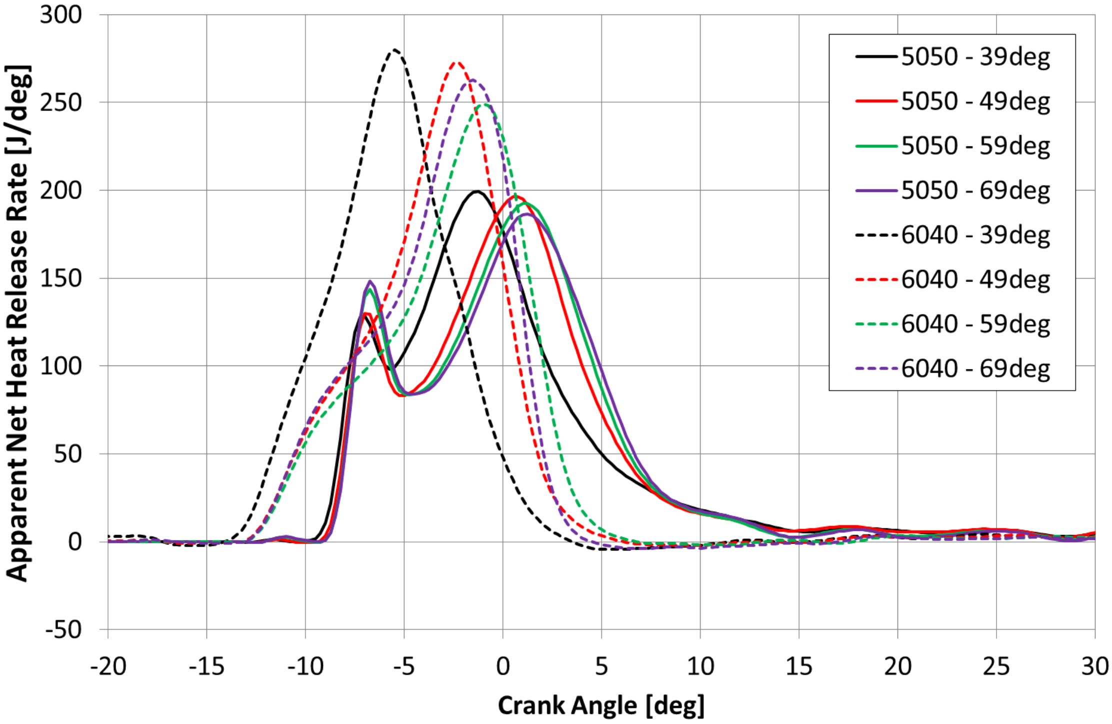

Figure 6-37: Apparent net heat release rate vs crank angle for the pilot injection timing sweep

The heat release plotted against crank angle is presented in Figure 6-37. Here it is shown that the later the pilot injection occurs, the earlier it shifts the HRR profile. The initial HRR bump, caused by the main diesel injection, was higher for the cases with the earlier premixed diesel injection. This could be caused by the entrained diesel helping to adjust the flammability of the mixture, yielding a slightly higher initial heat release. The 50/50 diesel quantity split exhibits a conventional double-hump shaped HRR, while the 60/40 is a single hump, more characteristic of auto-ignition. The majority of the heat release also takes place before TDC for the 60/40 case, which leads to decreased indicated efficiency. The corresponding mass fraction burned profiles are plotted in Figure 6-38, which supports that the combustion for the 60/40 cases were relatively over-advanced, but also that the combustion durations were short.

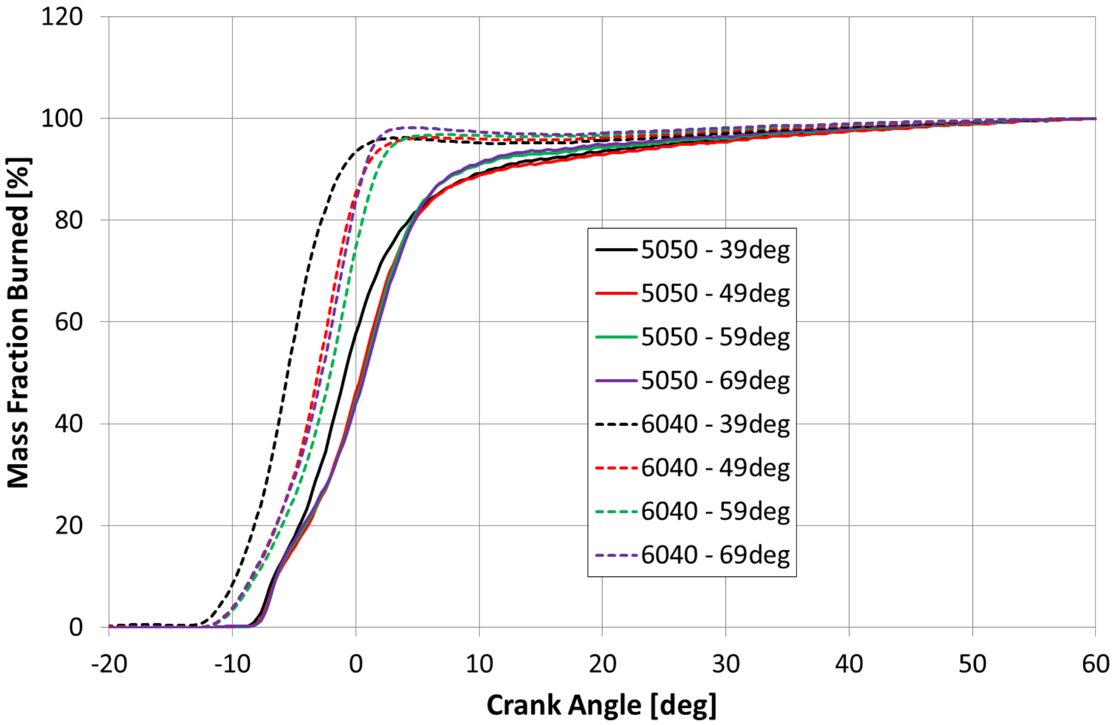

Figure 6-38: Mass fraction burned vs crank angle for the pilot injection timing sweep

The data plotted in Figure 6-39 and Figure 6-40 show the cylinder pressure and HRR profiles for the main injection timing sweep. The highest cylinder pressure resulted with a main injection timing of 32 deg BTDC. This corresponds to the highest and earliest HRR profile in Figure 6-40. The 37 deg HRR profile was later than the 32 deg due to the diesel being better mixed, which for a given quantity of diesel fuel, was less likely to trigger auto-ignition. It can also be observed that the HRR profiles evolve from a double hump to single hump shape as the main injection timing was advanced.

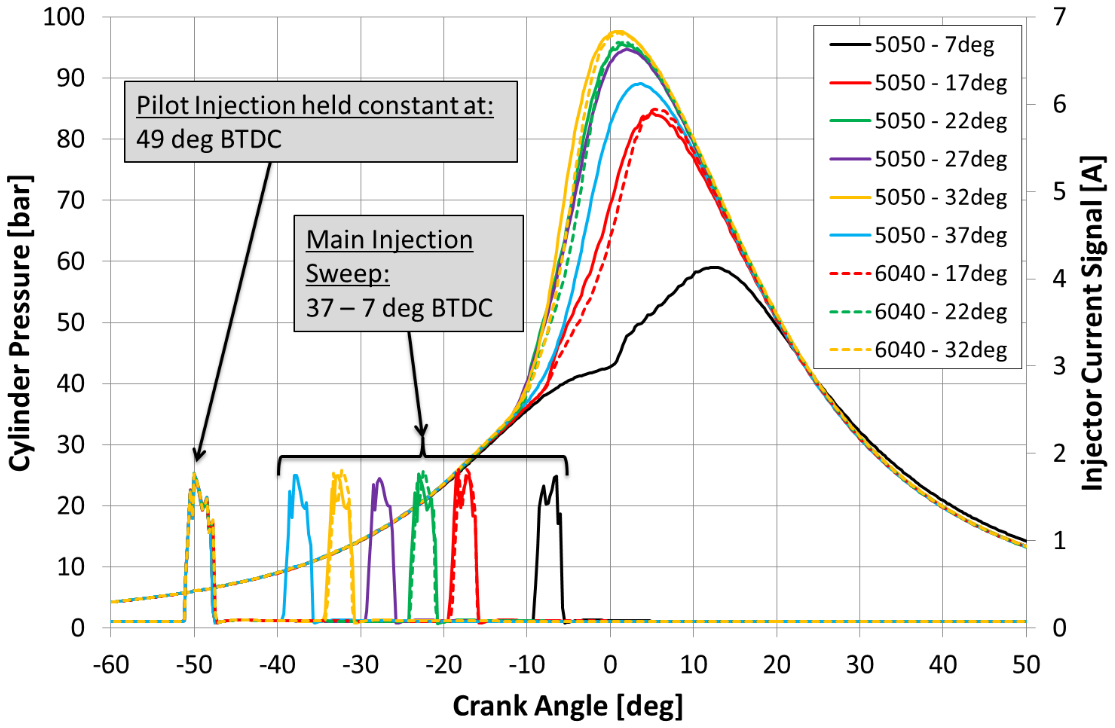

Figure 6-39: Cylinder pressure traces and injection signals vs crank angle for the main injection timing sweep

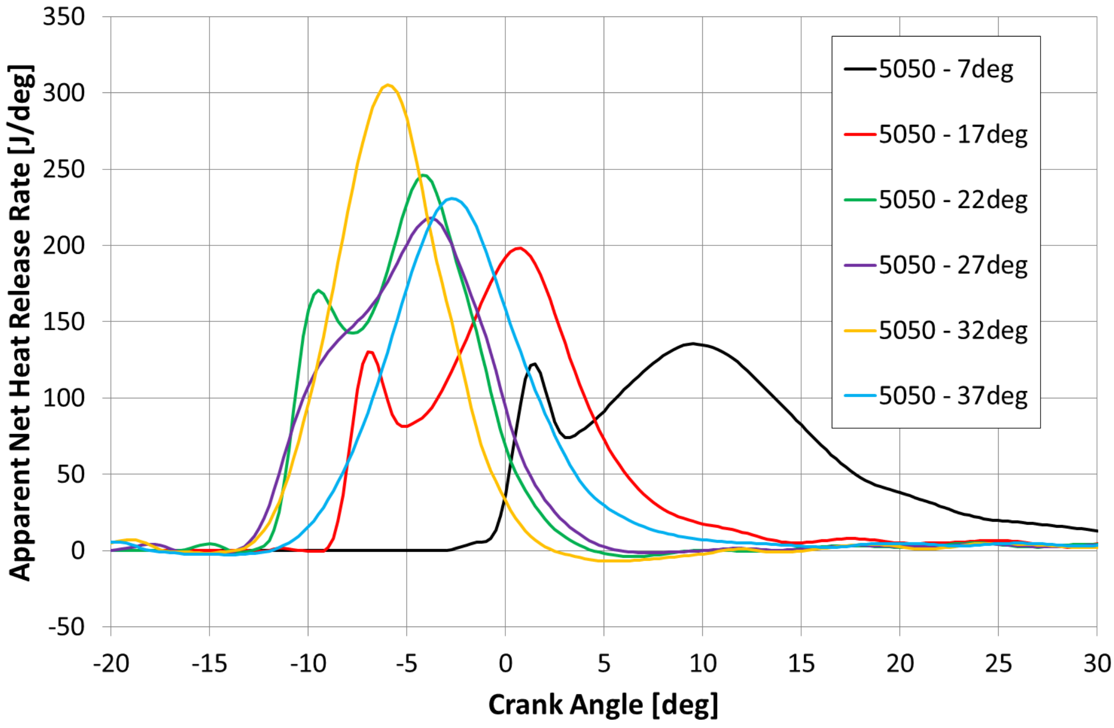

Figure 6-40: Apparent net heat release rate vs crank angle for the main injection timing sweep at a 50/50 diesel quantity split

The 50/50 and 60/40 diesel quantity splits are plotted at three equivalent main injection timings and presented in Figure 6-41. Here it can be shown that the 50/50 cases have a larger initial heat release when compared to the 60/40 cases. This was due to the larger quantity of diesel in the main injection for the 50/50 case, which equates to more ignition energy to initiate combustion. The 60/40 cases have a larger secondary hump than the equivalently timed 50/50 cases, due to a larger quantity of the diesel fuel being premixed.

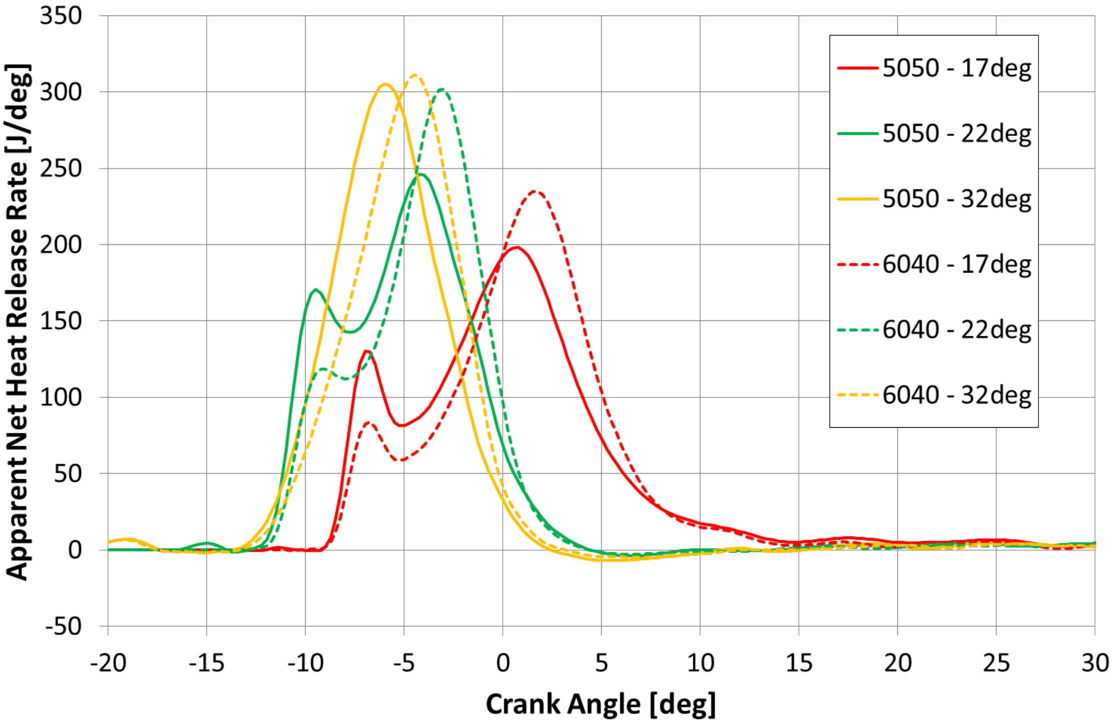

Figure 6-41: Apparent net heat release rate vs crank angle for a 50/50 and 60/40 diesel quantity split at common main injection timings

Finally, the mass fraction burned data for the main injection timing sweep are plotted in Figure 6-42. The main injection timing was very sensitive for determining the phasing and duration of the MFB profile. The 50/50 cases resulted in a faster initial burn than the 60/40 cases due to a higher quantity of diesel injected during the main. It can also be observed that the 32 to 22 deg BTDC cases were significantly advanced compared to the others, and yielded lower net indicated efficiencies.

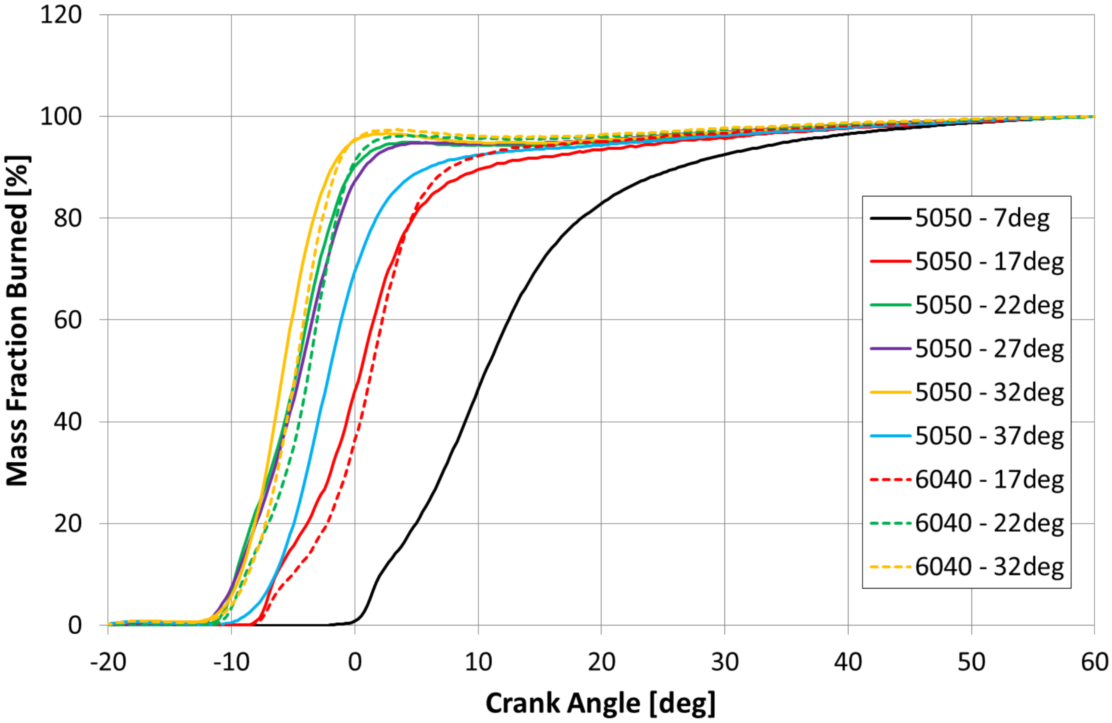

Figure 6-42: Mass fraction burned vs crank angle for the main injection timing sweep

6.5.3 Diesel Injection Split Sensitivity

The learnings of Section 6.5.2 are expanded upon in this section by testing a larger range of diesel quantity splits under RCCI operation. Additionally, a single diesel injection approach was compared alongside the double injection strategy. The same 1000 RPM, 6 bar load condition was maintained from the previous section, with key engine boundary conditions carried over as well. Natural gas substitution was held at approximately 82% (80% targeted but deviated due to controls), unless stated otherwise.

Four separate double injection strategies were tested, which ranged from a 40/60 to 70/30 diesel quantity split in 10% increments. A 40/60 case would mean that there was 40% of the total quantity of diesel fuel (by volume in mm^3) in the first injection, while the remaining 60% would be in the second injection. The impetus behind this experiment was to determine which split strategy would result in the best emissions and efficiency. In addition, three single injection strategies were also explored, where the total diesel fuel quantity was introduced in a single injection. Two different timings were tested with single injections, along with a change to a slightly higher gas substitution rate of 84% (special case to test robustness of combustion mode). The injection timings of both the single and double injection strategies are laid out in Table 6-4.

Table 6-4: Pilot and main injection timings for the injection strategy test points

	Pilot Injection Timing	**Main Injection Timing**
	deg BTDC	**deg BTDC**
Double - 40/60	59	27
Double - 50/50	59	27
Double - 60/40	59	27
Double - 70/30	59	27
Single - 57 deg BTDC	N/A	57
Single - 47 deg BTDC	N/A	47
Single - 47 deg BTDC, 84% Substitution	N/A	47

Typical injection quantities for this particular speed/load and substitution percentage were in the 6 to 10 mm^3 range. Fundamental emissions and efficiency metrics were compared in bar chart and crank angle based formats.

Plotted in Figure 6-43 are the ISNOx and $ISCH_4$ emissions for the injection strategies tested. The double injection strategies are plotted in black, while the single injection strategies are plotted in red. For the double injection strategy, increasing the quantity of diesel from the second to the first injection decreases the NOx and CH_4 emissions simultaneously. The degree of NOx reduction was significant, and suggests that the second diesel injection played a key role in NOx formation. As the second injection was closer to when combustion was taking place, the fuel would be more stratified, which was an enabler for NOx production. The 57 degree single injection strategy reduced NOx to very low levels, but resulted in slightly higher $ISCH_4$ emissions, due to delayed/retarded combustion. To advanced combustion phasing, the diesel injection timing was retarded to 47 deg BTDC, which enabled the $ISCH_4$ emissions to be reduced back to 2.0 g/kWh, but at the expense of increased NOx production to 2.4

g/kWh. This would still be favourable when compared to the double injection strategy, as the diesel fuel would be better mixed. However, this strategy was also reliant upon auto-ignition, which is sensitive to engine calibration changes. In order to test the robustness of this combustion mode, the gas substitution was raised by ~2% to 84%, as demonstrated by the last single injection case. The NOx reduced to 0.4 g/kWh, but the $ISCH_4$ emissions increased to very high levels of 5.0 g/kWh. The 47 deg BTDC single injection strategy is subjectively the optimum from a NOx and CH_4 trade-off standpoint, but is sensitive to engine calibration values such as injection timing or gas substitution. If exact auto-ignition conditions are not met, the CH_4 emissions will suffer. It should be noted that for both single and double injection strategies, a minimum value of ~2.0 g/kWh of $ISCH_4$ was achieved. This signifies a crevice volume limited level of emissions and translates to a value of ~98.3% combustion efficiency.

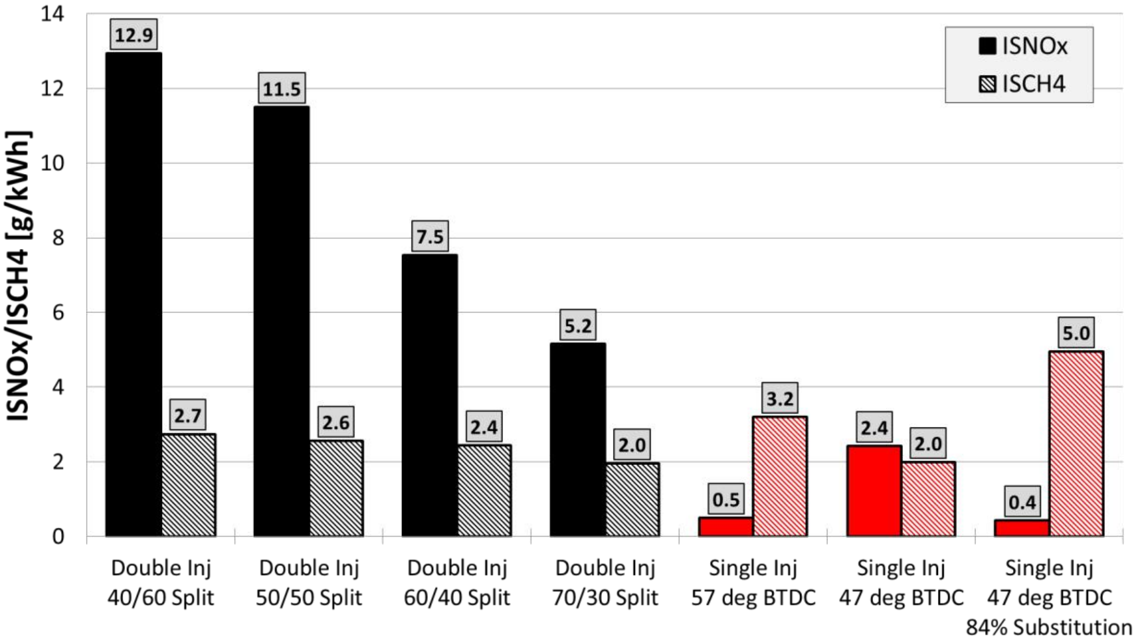

Figure 6-43: Engine-out $ISCH_4$ and ISNOx emissions for various injection strategies

ISCO and ISSoot emissions are presented in Figure 6-44. For the double injection strategy, varying the quantity of diesel between injections had very little impact on the ISCO and ISSoot emissions. The single injection strategies showed an increase in ISCO emissions when auto-ignition was not occurring, as exhibited in both the 57 deg BTDC and the 84% substitution cases. Combustion was retarded for these two cases, which would result in a lower value of combustion efficiency and increased ISCO emissions.

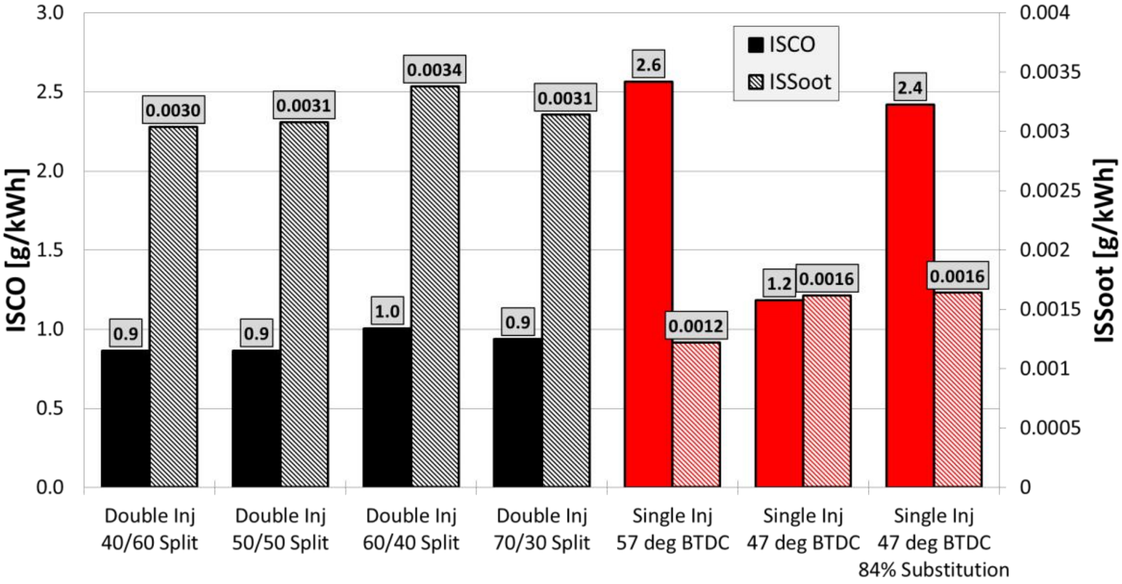

Figure 6-44: Engine-out ISCO and ISSoot emissions for various injection strategies

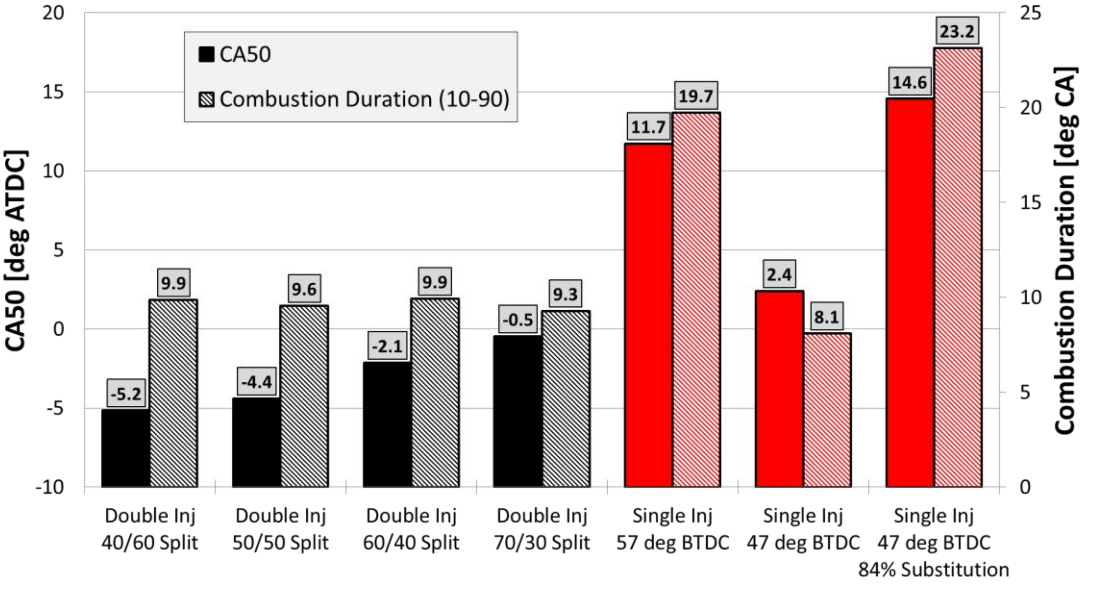

Figure 6-45: 50% mass fraction burned and 10-90% combustion duration for various injection strategies

CA50 and combustion duration are plotted in Figure 6-45. For the double injection strategy, increasing the quantity of diesel from the second to the first injection retards combustion phasing from -5.2 to -0.5 deg ATDC. Placing more of the given quantity of diesel in the earlier injection shifted the combustion from a diesel pilot ignited combustion event to an increasingly auto-ignition driven strategy. Combustion duration was slightly shortened when going to the 70/30 case, but was more or less maintained between 9 and 10 CA deg. The 47 deg BTDC single injection strategy results in the shortest combustion duration, but is very sensitive and dependent upon auto-ignition. This was demonstrated by the retarded CA50 and long combustion duration of the 57 deg BTDC and the 84% substitution cases.

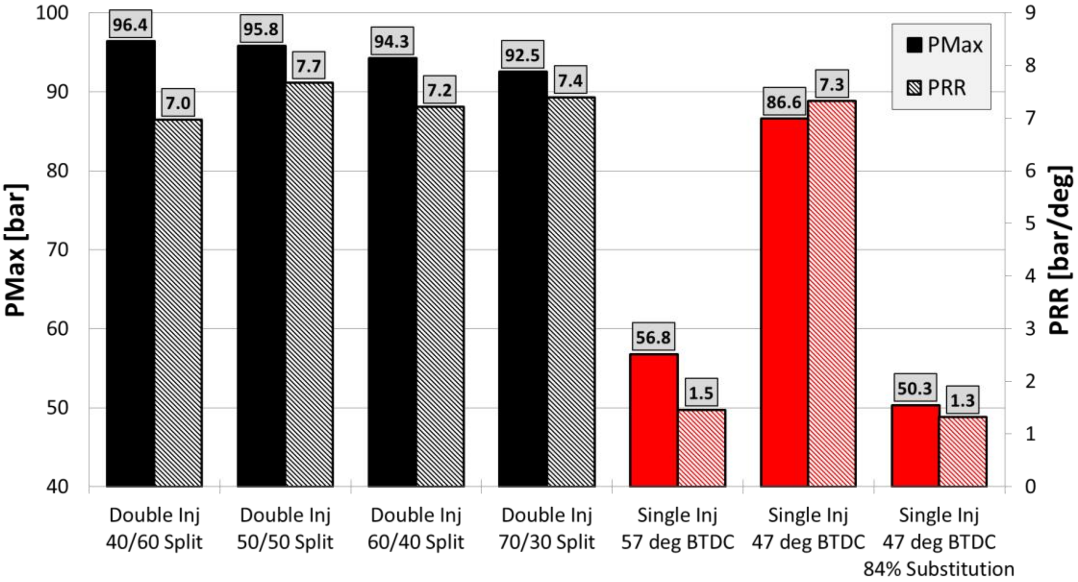

Figure 6-46: Maximum cylinder pressure and pressure rise rate for various injection strategies

The data plotted in Figure 6-46 reveals more about the combustion processes by showing maximum cylinder pressure and PRR. For the double injection cases, increasing the quantity of diesel in the first injection decreases the maximum cylinder pressure while maintaining the levels of PRR. The maximum cylinder pressure was reduced due to the retarding of combustion phasing, as shown in Figure 6-45. The 47 deg BTDC single injection strategy resulted in a lower cylinder pressure than the double injection strategy, due to later combustion phasing relative to TDC. Again, it is very sensitive and dependant on auto-ignition, as demonstrated by the low cylinder pressure and PRR exhibited by the other single injection strategies.

EGT and COV of IMEP are presented in Figure 6-47. For the double injection cases, increasing the quantity of diesel from the second to the first injection decreases EGT and increases the COV of IMEP. The action of shifting more diesel fuel to the first injection would suggest that there is an increasing degree of auto-ignition potential for the combustion process. EGT tends to decrease as the efficiency of the combustion process increases as more energy is extracted from the charge. Conversely, having a reliance upon auto-ignition to initiate the combustion process generally results in an increase in the COV of IMEP, especially when decreasing the amount of diesel in the second diesel injection. The single injection strategy of 47 deg BTDC resulted in a similar EGT to the 70/30 double injection case, but has relatively higher COV of IMEP of 2.5%. For the two other single injection cases, the retarding of combustion phasing results in higher EGT. The COV of IMEP values increased as well, as ideal auto-ignition conditions were not met.

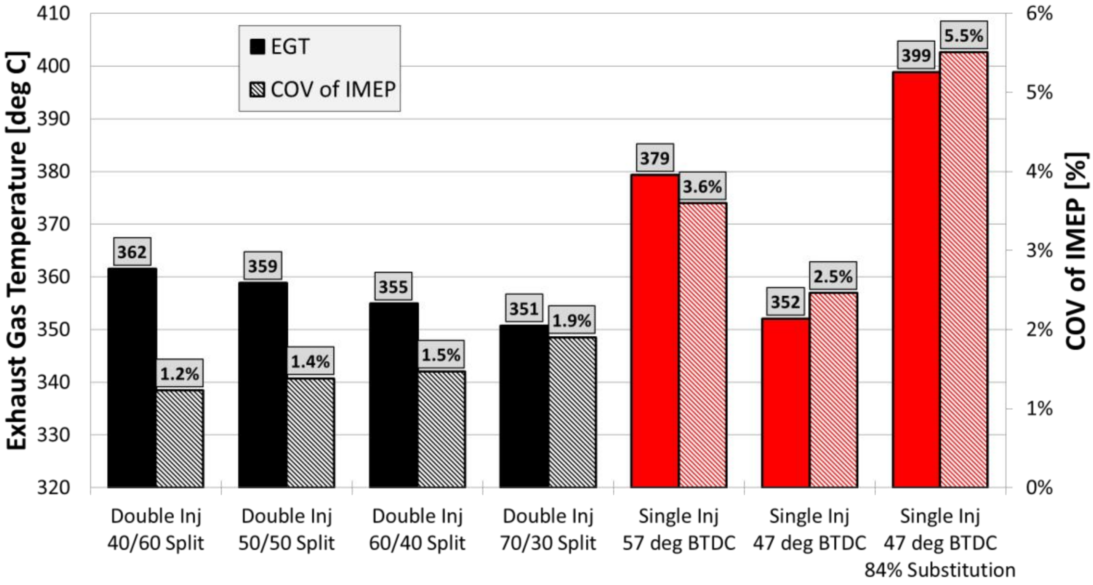

Figure 6-47: EGT and COV of IMEP for various injection strategies

The final bar chart of Figure 6-48 includes the combustion and net indicated efficiency. Increasing the amount of diesel in the first injection improves combustion and net indicated efficiency, as the entrained diesel fuel would help to burn the natural gas mixture. The combustion efficiency limit of ~98.3% was reached, and was likely the limit of the crevice volume of the conventional diesel combustion chamber. The single injection strategy of 47 deg BTDC resulted in the highest net indicated efficiency of any of the cases or strategies, accompanied with a value of 98.3% combustion efficiency. Once again, this injection strategy is very sensitive to diesel injection timing and gas substitution however, so the other two single injection cases result in degraded performance.

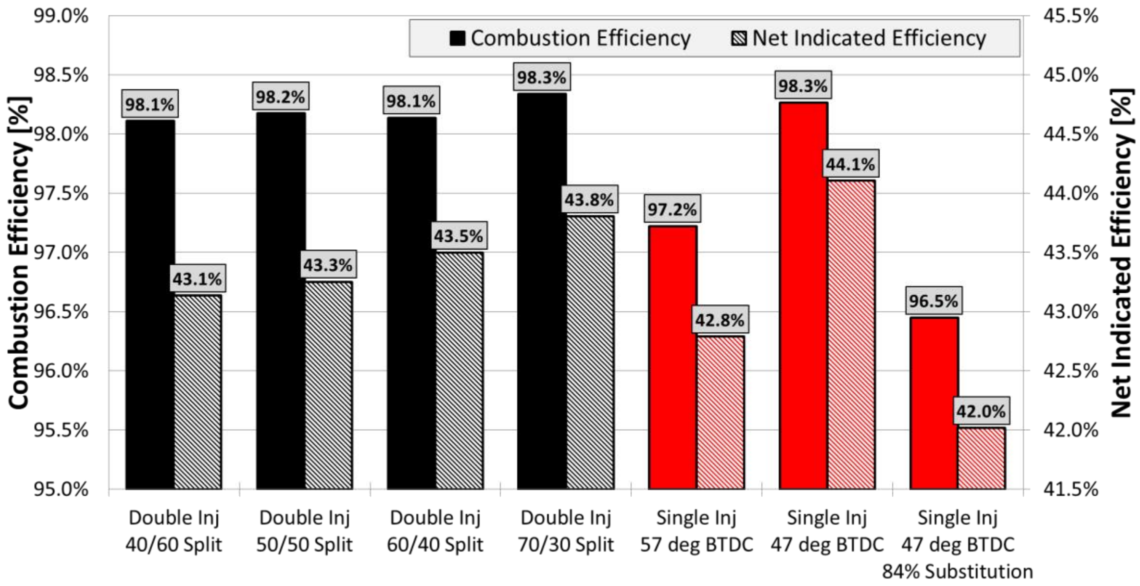

Figure 6-48: Combustion and net indicated efficiencies for various injection strategies

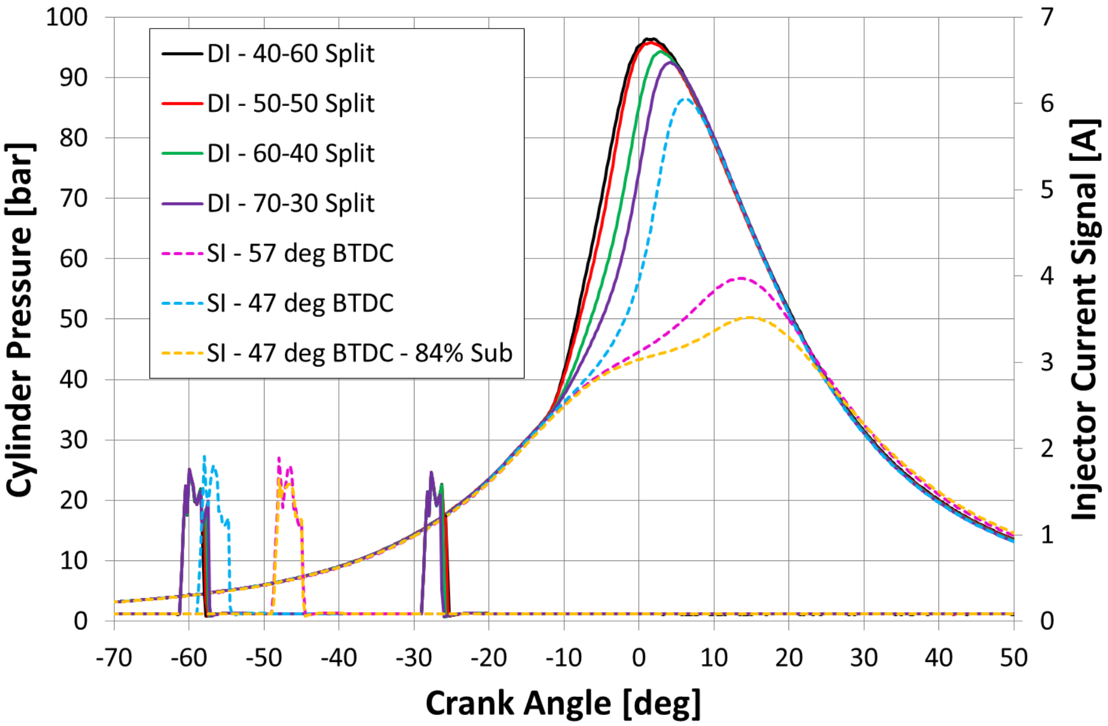

Figure 6-49: Cylinder pressure traces and injection signals vs crank angle for various injection strategies

Crank angle based cylinder pressure and injection profiles for both injection strategies are presented in Figure 6-49. The double injection cases are denoted by solid lines while the single injection cases are represented by dotted lines. For the double injection strategy, moving diesel from the second to the first injection retards combustion phasing and reduces the maximum cylinder pressure. For the single injection cases, a more retarded combustion phasing results in a lower cylinder pressure when compared to the double injection strategy. A 7.0 to 7.7 bar/deg span of PRRs were observed for all of the cases except for the two low cylinder pressure single injection cases.

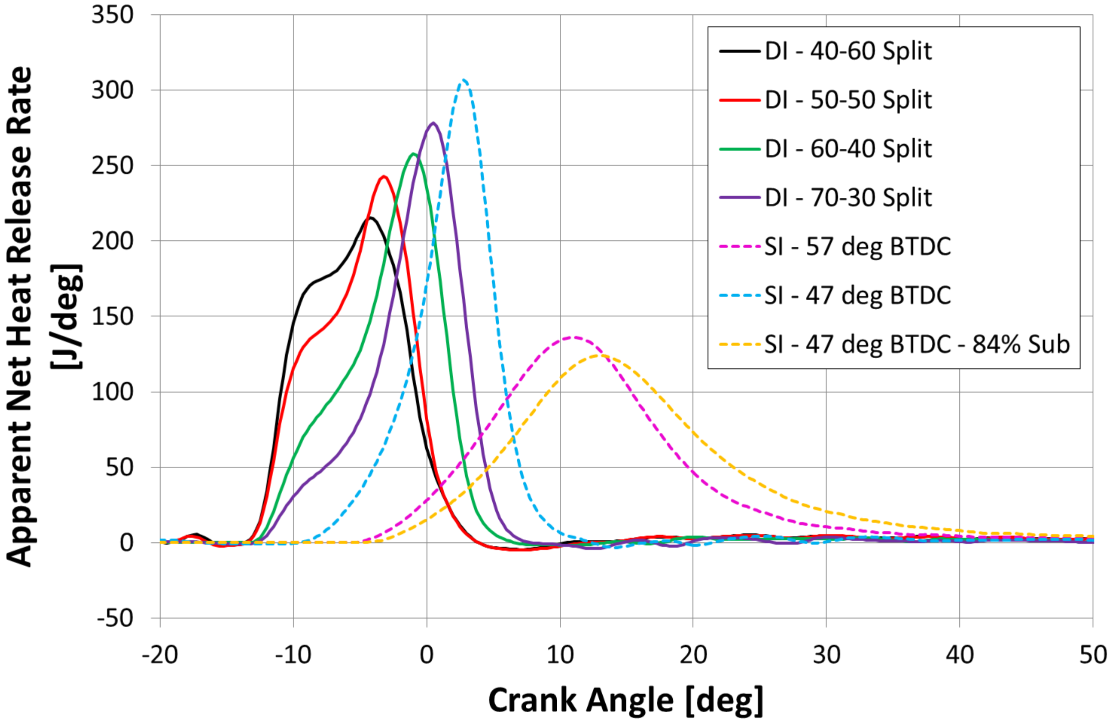

Figure 6-50: Apparent net heat release rate vs crank angle for various injection strategies

The shape of the double injection strategy in terms of HRR can be observed in Figure 6-50. Upon removing the diesel from the second injection to place it in the first injection, the shape of the HRR profile around 10 deg BTDC was reduced. As the split changes from a 40/60 split to a 70/30, the HRR peak becomes higher, and moves more toward a single hump shape. This was more favourable from an ideal heat release standpoint, as more of the energy was released closer to TDC. The 47 deg BTDC single injection case possesses a true single hump shape, with the highest HRR of all the profiles. The phasing of the HRR profile also results in higher efficiency than the double injection strategy since more of the HRR occurs after TDC when the piston is moving down in the cylinder. The lowest HRRs were for the two single injection cases that failed to meet ideal auto-ignition criteria. These cases resulted in single hump profiles, but are retarded in timing and have a relatively long and slow release of heat. This is best shown by Figure 6-51, where the mass fraction burned is displayed for all cases. The pink and yellow cases represent the slow burning single injection cases, while the shorter cases have more ideal shapes.

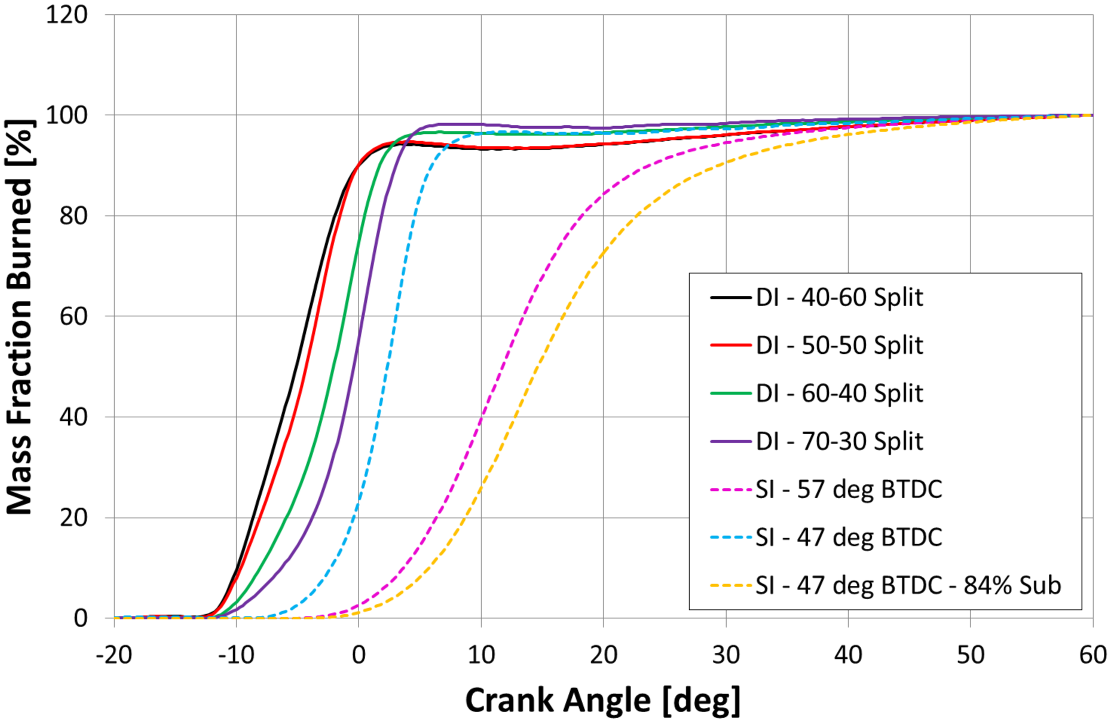

Figure 6-51: Mass fraction burned vs crank angle for various injection strategies

Overall, the single injection strategy possessed the greatest emissions and efficiency potential, but was particularly reliant upon ideal auto-ignition conditions. It was shown that small variations in injection timing and gas substitution could lead to a significant degradation of emissions performance and engine efficiency. The double injection strategy was more robust to variations and could be progressively tuned to achieve the desired amount of auto-ignition, but still should be considered as an auto-ignition focused strategy. Both the single and double injection cases were able to achieve the piston-crevice limited combustion efficiency of 98.3%, which yielded a ~2 g/kWh level of engine-out CH_4 emissions.

6.6 Light Load Dual-Fuel Combustion Strategy Comparison

A fundamental challenge for a lean-burn dual-fuel engine is operation under light-load conditions, as mixture flammability and low combustion temperature give rise to high CH_4 emissions. Increased engine-out NOx is often a trade-off of decreased CH_4 emissions, especially when using diesel injections as an ignition source. Ideally both NOx and CH_4 exhaust emissions would be decreased simultaneously, but each combustion strategy performs this function with varying degrees of success. The purpose of this section is to determine the advantages and drawbacks of each combustion strategy as to recommend which would be the most effective for use at light load.

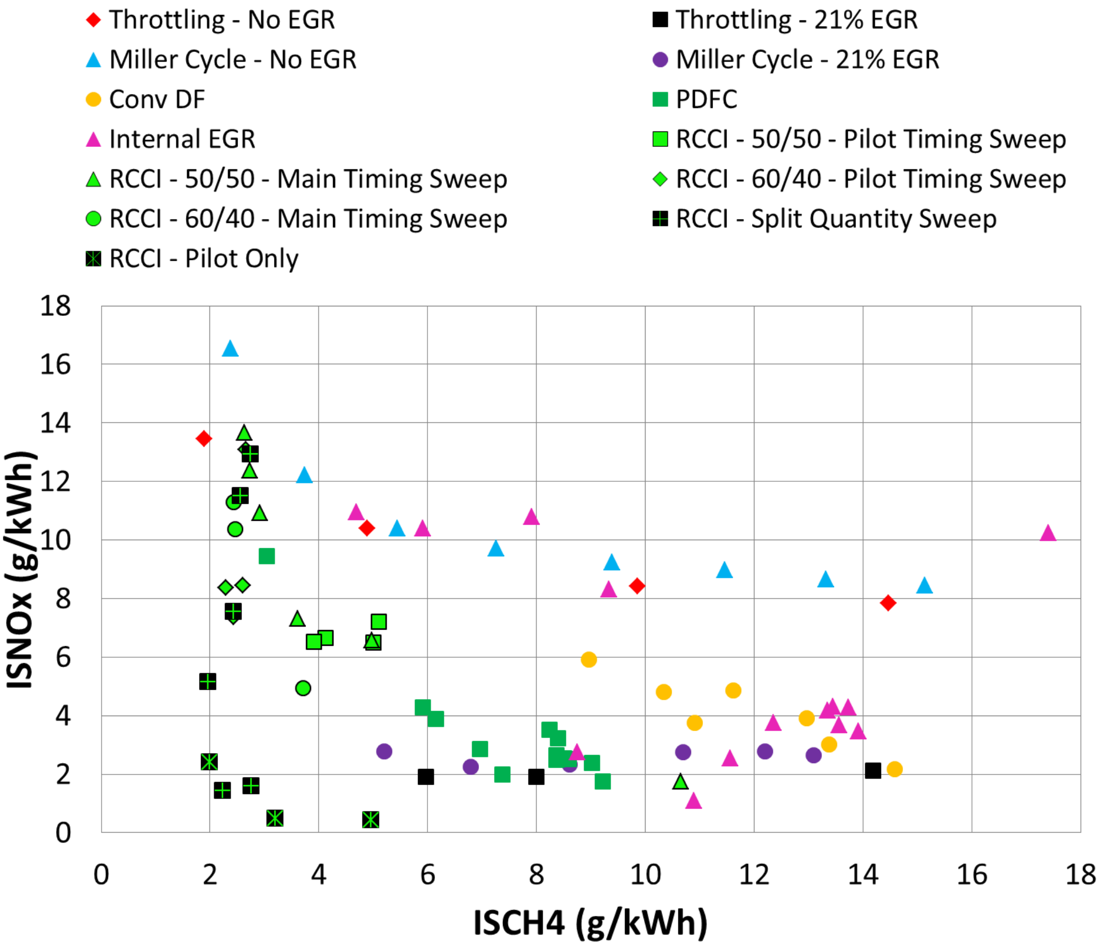

Figure 6-52: Engine-out $ISCH_4$ and ISNOx emissions for various dual-fuel combustion strategies at 1000 RPM 6 bar $IMEP_{net}$

A summary of combustion modes at 1000 RPM and 6 bar $IMEP_{net}$ are presented in Figure 6-52 with supplementary graphs included in Appendix F – Emissions Graphs for Dual-Fuel Combustion Strategies at 1000 RPM 6 bar IMEPnet. Engine-out $ISCH_4$ and ISNOx are the x and y axis respectively, where each data point represents an average of 300 combustion cycles. Ideal engine operation would be in the lower left-hand corner, where both emissions would be closest to zero.

Conventional dual-fuel serves as the baseline in this section and is represented by the yellow circles. Generally, it can be observed that CH_4 emissions were high with this strategy, ranging from ~9 to 15 g/kWh, while NOx was in the 2 to 6 g/kWh range. As previously outlined in Chapter Five, the drawback of conventional dual-fuel is that natural gas is difficult to burn in globally lean environments. Burning velocity slows with increasing λ and premature quenching of the flame front would lead to higher amounts of unburnt methane. NOx emissions remain, as a standard diesel injection is used to initiate combustion, resulting in local fuel-lean regions of high temperature combustion.

PDFC improves upon conventional dual-fuel, as shown by the green squares without borders. Premixed diesel injections were introduced with the purpose of increasing the mixture flammability and reducing unburnt methane. The benefits of the premixed injections are shown by the $ISCH_4$ dropping to 3 to 9 g/kWh with comparable levels of NOx emissions. An exception would be the aggressive PRR PDFC case at 3 g/kWh $ISCH_4$ and 9.5 g/kWh ISNOx, as NOx is more easily formed in times of high heat release and combustion temperature.

Engine throttling and Miller cycle without EGR are shown by the red diamonds and blue triangles. As in-cylinder λ was decreased, the $ISCH_4$ emissions were improved, but at the expense of higher ISNOx emissions. Both strategies without EGR were able to achieve relatively low values of unburnt methane, but at the highest levels of NOx production. In order to quell the NOx emissions, EGR was added to the throttling and Miller cycle cases, which are represented by the black squares and purple circles. These strategies achieved emissions performance comparable to that of conventional dual-fuel and PDFC, but at the expense of engine efficiency. This was mainly due to increased pumping losses as well as a lower ratio of specific heat resulting from decreased in-cylinder λ.

I-EGR cases are depicted by pink triangles and were run with varying percentages of E-EGR and I-EGR. The cases with low amounts of EGR were on par with the throttling and Miller cycle cases from a NOx production standpoint, but only achieved a minimum $ISCH_4$ value of 4.7 g/kWh. I-EGR cases with sufficient E-EGR achieved similar performance compared to that of conventional dual-fuel.

Finally, RCCI cases comprise the remainder of the data points under the two main strategies of double and single injection. The single injection strategy is denoted by the black square with a 6-point star in the middle, rather than the black square with cross representing the double injection split quantity sweep. The single injection strategy possesses the ability to achieve the lowest $ISCH_4$ emissions measurement with generating the lowest amount of ISNOx. The double injection strategy is very close in performance however, with the added benefit of being more robust from an engine calibration standpoint. Overall, it can be appreciated that RCCI has the ability to lower $ISCH_4$ emissions while lowering ISNOx when compared to the other combustion modes. However, the success of all RCCI strategies is largely based on ideal auto-ignition conditions, so should be approached with caution. This tumultuousness can be noted by the wide band of operation spanning the ISNOx and $ISCH_4$ axes. This is best demonstrated by the RCCI cases with the green square, triangle, diamond, and circle.

It is clear that a trade-off between emissions and efficiency benefits and auto-ignition is present for lot of these strategies. RCCI has the greatest potential from an efficiency and emissions standpoint but faces significant challenges for transient operation. Fast changes in load, EGR percentage, and cycle-to-cycle variability are just some of hurdles that must be overcome if this strategy is to be adopted. PDFC is one strategy that has potential to provide some promise, as the quantity of the premixed injection allows the engine to select the degree of auto-ignition it experiences. This results in the best trade-off between emissions and engine efficiency that is regularly attainable. Miller cycle and throttling are some viable alternatives to PDFC, but comes at the expense of engine efficiency.

6.7 Summary

Lean-burn dual-fuel engines experience poor emissions and efficiency during light load operation due to various factors surrounding mixture flammability and combustion temperature. Extension of the dual-fuel operating regime is desirable as it helps to improve the business case of natural gas as a fuel. However, the combustion of natural gas also needs to achieve a satisfactory level of emissions and efficiency to be commercially viable as an alternative to diesel. These shortcomings were addressed by investigating more sophisticated methods of light load combustion. Experimental engine testing of Miller cycle, throttling, I-EGR, and RCCI were carried out at 1000 RPM 6 bar $IMEP_{net}$.

Miller cycle and throttling were tested concurrently, as the engine valvetrain and throttle were both avenues by which to control the in-cylinder λ of the engine during light load operation. The premise is that the reduction of fresh air into the engine can help to increase the burning velocity of natural gas, thereby reducing quenching and decreasing the amount of unburnt methane. These λ control mechanisms were explored and it was determined that both were an effective means of CH_4 emissions reduction. However, each strategy also possesses individual drawbacks. Throttling limited the mass flow of fresh air into the engine via a butterfly valve which resulted in increased pumping losses and a loss of efficiency. The Miller cycle strategy utilised the engine valvetrain to control the mass air flow so had lower pumping losses and higher efficiency due to the piston not working against the depression caused by the throttle. Both Miller cycle and throttling were able to reach the combustion chamber limited level of CH_4 emissions with 0% E-EGR, but experienced excessive NOx production. Up to 21% E-EGR was added to suppress NOx emissions, but came at the expense of increased methane emissions due to reductions in combustion efficiency. For a given λ, throttling and Miller cycle performed similarly with respect to CH_4 emissions, as it was primarily a function of combustion efficiency and mixture flammability. As λ was decreased, NOx, EGT, and combustion efficiency increased, while CO, CH_4, and combustion duration decreased. The best observed efficiency without EGR was approximately λ = 1.4, while with EGR yielded λ = 1.2. Ultimately both strategies were ignition limited due to low effective compression ratio. The Miller cycle strategy was also run at a constant λ, with boost pressure used to supplement the late intake valve closing. It was found that NOx emissions slightly decreased due to compression work being performed outside of the cylinder, thereby reducing temperatures at SOI.

The I-EGR strategy was tested by utilising the engine valvetrain to open the intake valves during the exhaust stroke in order to recirculate exhaust gas directly into the intake port. The premise was that the increased temperature of the residual would help to increase the flammability of the in-cylinder contents, helping to burn CH_4. I-EGR was tested with and without E-EGR and compared back to a conventional dual-fuel baseline with E-EGR. It was determined that for a given level of NOx, the addition of I-EGR decreased CH_4 and CO emissions. The mechanism for the reduction was increased combustion efficiency, as higher in-cylinder temperatures gave rise to bulk auto-ignition of the end gas which helped to burn CH_4. The higher dilution also produced a lower in-cylinder λ, which increased burning velocity. The magnitude of CH_4 reduction was larger without E-EGR, but came at the expense of significantly increased NOx production. Efficiency for all I-EGR cases were lower compared to the conventional dual-fuel baseline. Lower gas exchange efficiency and higher pumping losses were a result from increased exhaust backpressure, which was essential in order to drive sufficient quantities of residual into the intake system.

The final strategy tested was RCCI, which utilised diesel injections to adjust the reactivity of the in-cylinder mixture in order to control auto-ignition. RCCI relies on the chemical kinetics of the fuel in order to initiate combustion. This is a departure from the aforementioned strategies where the diesel injections begin the combustion process directly. These premixed diesel injections were critical to emissions and efficiency so an optimisation of the diesel timing and quantity was performed. A double injection strategy using a 50/50 and 60/40 diesel quantity split was tested in order to determine optimum injection timings for both of the diesel injections. For the first injection of the 50/50 split, it was generally found that there was a slight improvement to emissions and efficiency when the timing was advanced, considering a window of 69 to 39 deg BTDC. The mechanism for this was theorised to be that the diesel fuel was better mixed with the cylinder contents before combustion occurred. This lowered the stratification of the local λ, which is typically associated with NOx and CO/soot production. As the diesel quantity split was changed to 60/40, more diesel fuel was placed in the first injection. This introduced the higher reactivity fuel earlier in the cycle, which created a higher sensitivity to injection timing with regard to emissions and efficiency. The sensitivity of emissions to second injection timing was more direct, with the highest NOx and lowest CH_4 emissions occurring in the 35 to 20 degree BTDC injection window. Finally, a diesel injection split sensitivity was performed where the emissions and efficiency for a double and single injection strategy were compared. It was found that the single injection strategy achieved the lowest $ISCH_4$ emissions measurement with generating the lowest amount of ISNOx. The double injection strategy was very close in performance however, with the added benefit of being more robust from an engine calibration and combustion stability standpoint. Overall, it can be stated that RCCI has the ability to lower $ISCH_4$ emissions while lowering ISNOx, but is reliant on ideal auto-ignition conditions. Caution must be taken, as transient operation, EGR percentage, fuel composition and cycle-to-cycle variability are just some of the major challenges that must be overcome in order for RCCI to gain widespread adoption. PDFC remains an attractive alternative, as the degree of auto-ignition can be controlled by the quantity of the premixed diesel injection, while the second (main) diesel injection anchors the start of combustion near TDC.

Chapter Seven

Conclusions and Future Work

7.1 Conclusions

The primary motivation of this work was to improve upon the efficiency and emissions of a lean-burn dual-fuel combustion system in an HD diesel/natural gas engine. These engines are problematic under light load operation, as the globally lean combustion environment creates flammability issues for natural gas. Addressing this matter, the overall project scope and context were defined in the first two chapters, while the subsequent two were about the experimental test rig and the measures that were taken to ensure high data quality.

Various steady-state operating points spanning different speeds and loads were tested in different combustion modes. The data produced led to the following conclusions for conventional and premixed dual-fuel combustion:

- The experimental test rig's combustion system during diesel operation was similar in efficiency and emissions performance when benchmarked against an EPA10 emissions compliant Volvo D13 multi-cylinder engine
- Typical NOx-CO and NOx-soot trade-offs were experienced during injection timing sweeps under diesel and conventional dual-fuel combustion, with the majority of operating points constrained by pressure rise rate (<10 bar/deg)
- The premixed diesel injections of PDFC demonstrated significant reductions in emissions for CH_4 (by up to 73%), THC (by up to 69%), CO (by up to 61%), and NOx (by up to 58%, but occasionally negative) for the majority of speed/load conditions when compared to conventional dual-fuel combustion
- Improvements in ISFC (by up to 7.4%) and thermal efficiency (by up to 3%) were observed by PDFC over conventional dual-fuel by increasing combustion efficiency (by up to 4.8% over baseline) and lowering combustion duration (by up to 55%)

- During high load operation, the benefits of PDFC are limited by the maximum cylinder pressure of the engine due to short duration combustion phased relatively close to TDC
- The maximum benefit of PDFC was extracted at mid load operation, while light load conditions suffered due to the flammability issues of natural gas in lean, low temperature and pressure conditions
- The CH_4 reduction mechanism was attributed to the premixed diesel injection introducing a non-uniform EQR/stratification into the combustion charge, thereby driving differences in the local chemical kinetic reaction rates, which in turn influences the ignition delay and resulting combustion duration
- In theory, the pockets of highly reactive fuel during PDFC also resulted in many different ignition sources once temperature and pressure were high enough for bulk ignition of the fuel mass to occur, but will need to be confirmed using optical diagnostic techniques

As outlined, lean-burn dual-fuel engines experience poor emissions and efficiency during light load operation due to issues surrounding mixture flammability and low temperature. In order to investigate ways to improve upon this light load drawback, experimental engine testing of Miller cycle, throttling, I-EGR, and RCCI were carried out at 1000 RPM / 6 bar $IMEP_{net}$ with the following conclusions made:

- Miller cycle and throttling were both effective strategies for reducing $ISCH_4$ emissions (~2 g/kWh with 0% EGR, 5-6 g/kWh with 21% EGR), yielding similar levels of reduction for a given λ
- Miller cycle had higher net indicated efficiency (~43.5%) compared to throttling (~42%) with lower pumping losses due to the piston not working against the depression caused by the throttle
- As λ was decreased with Miller cycle and throttling, NOx, EGT, and combustion efficiency increased, while CO, CH_4, and combustion duration decreased due to the higher burning velocity of natural gas
- Both Miller cycle and throttling were able to reach the combustion chamber limited level of CH_4 emissions ($ISCH_4$ = ~2 g/kWh) with 0% E-

EGR, but experienced excessive NOx production and were ultimately ignition limited due to low effective compression ratio

- For a given level of NOx, I-EGR decreased CH_4 and CO emissions at the expense of higher pumping losses and lowered efficiency compared to a conventional dual-fuel baseline
- I-EGR increased combustion efficiency through lowering in-cylinder λ and by creating higher in-cylinder temperatures, which gave rise to bulk auto-ignition of the end gas, helping to burn CH_4 ($ISCH_4$ as low as 4.7 g/kWh)
- RCCI possessed the greatest ability to simultaneously lower emissions of $ISCH_4$ (down to 2 g/kWh) and ISNOx (down to 2.4 g/kWh) when compared to all other low-load strategies, but is reliant upon ideal auto-ignition conditions

Overall, no operating condition tested throughout the entire engine map resulted in a brake engine-out methane emissions level of less than 0.5 g/kWh at gas substitutions greater than approximately 75%. This level of emissions would translate to combustion efficiency greater than 99.6%. The lowest engine-out brake methane emissions achieved during testing was approximately 1.4 g/kWh at A50, with 77% gas substitution and 98.8% combustion efficiency. This condition violated pressure rise rate limitations set forth, and would likely result in damage to the engine over long-term. This suggests that the limits of this particular lean-burn dual-fuel design were reached, and that it will likely require improvements to either the combustion system or the exhaust after-treatment if Euro VI levels are to be met. LTC has proven to be a useful method for reducing methane emissions and potential after-treatment costs, but caution must be taken as transient operation, EGR percentage, and cycle-to-cycle variability are just some of the major challenges that must be overcome in order for it to gain widespread adoption. Nonetheless, the benefits and drawbacks of various strategies have been demonstrated for possible extension of the dual-fuel operating regime to lighter load.

7.2 Recommendations for Future Work

Potential improvements to methane emissions and combustion efficiency can be obtained if the conventional diesel combustion chamber used in this work is modified, particularly with respect to the piston top land and ring pack volumes [103,104]. Furthermore, optical engine testing coupled with 3D-CFD simulation can aid in the understanding of how to better optimise combustion chambers for dual-fuel. It would also be useful to identify the areas in which end-gas knock occurs (inner bowl or periphery), such that this phenomenon can be alleviated or differentiated from auto-ignition.

Ensuring the robustness of auto-ignition to transient speed and load conditions needs to be explored, as emissions and efficiency can drastically degrade compared to steady-state operation. Engine controls and calibration work can be performed to best optimise the premixed diesel injections of PDFC or any other premixed LTC combustion mode. The addition of an electric motor or hybrid system to smooth and stabilise transient operation is also a possibility. This strategy would have potential benefits to LTC modes as metal temperatures along with EGR and airflow systems would have more time to adjust to the newly requested speed and load condition.

The dual-fuel operating envelope can be expanded with technologies such as cylinder deactivation [106] for light load and variable compression ratio [144] for both light to high load conditions. Cylinder deactivation can aid the burning of natural gas through favourable in-cylinder λ, while variable compression ratio can be used to adjust auto-ignition for LTC. A lower compression ratio can also be used at high load to avoid reaching the maximum cylinder pressure limit of the engine. It is also an option to redesign the engine to a higher maximum cylinder pressure limit and quantify the benefits to emissions and efficiency during LTC operation, which typically yields high cylinder pressures near TDC.

Finally, a system level approach can be taken for reaching Euro VI methane emissions compliance by utilising new exhaust gas after-treatment technology in conjunction with LTC. Electrically heated catalysts could be used to provide faster light-off times for oxidation catalysts [145] while thermal barrier coatings can be applied to pistons, exhaust valves, and exhaust manifolds to raise the temperature of the exhaust gases [38,39].

Appendix A – Maximum Motoring Cylinder Pressure Fluctuation with Engine Speed

Wave dynamics in the intake and exhaust systems cause fluctuations in the maximum motoring cylinder pressure as a function of engine speed. The effects are repeatable (4 test dates plotted below) enough where a bandwidth of about five engine cycles can be representative of the maximum motoring cylinder pressure of the engine at approximately 850 rpm. The selection of approximately 850 rpm results in a smaller spread of data as a local minimum occurs.

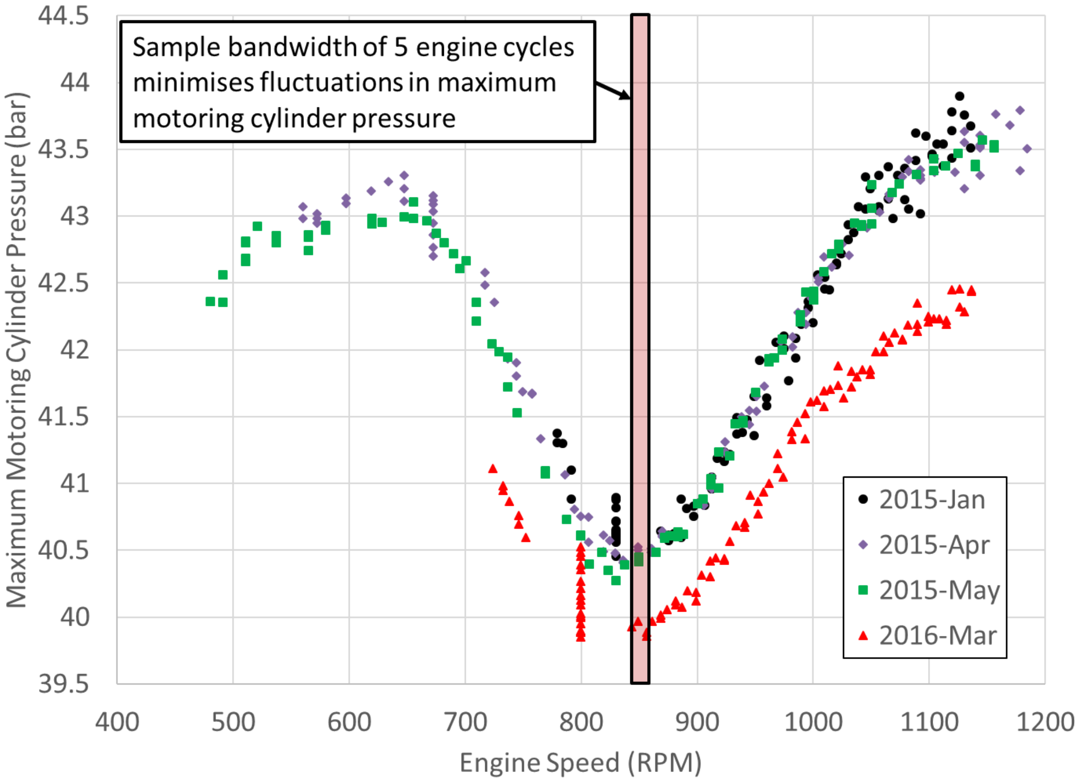

Appendix B – Firing Polytropic Coefficients of Compression and Expansion

Variability of the polytropic coefficients of compression (C) and expansion (E) with increasing number of engine cycles.

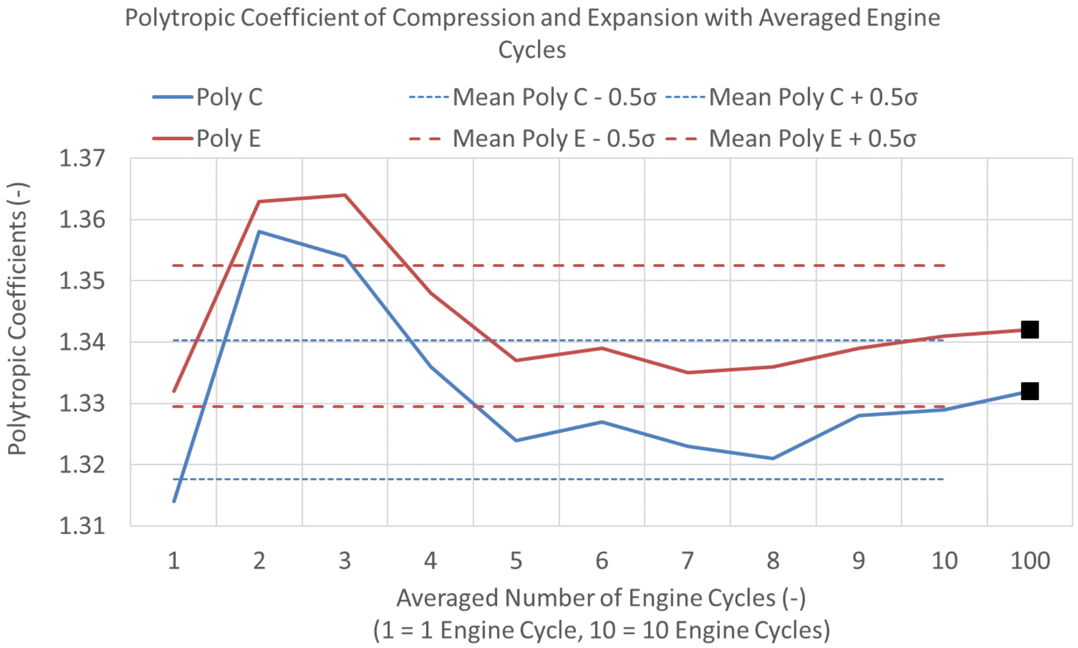

Appendix C – Miller Cycle with 800 bar Rail Pressure

Supplementary Miller cycle tests ran with 800 bar diesel rail pressure (RP).

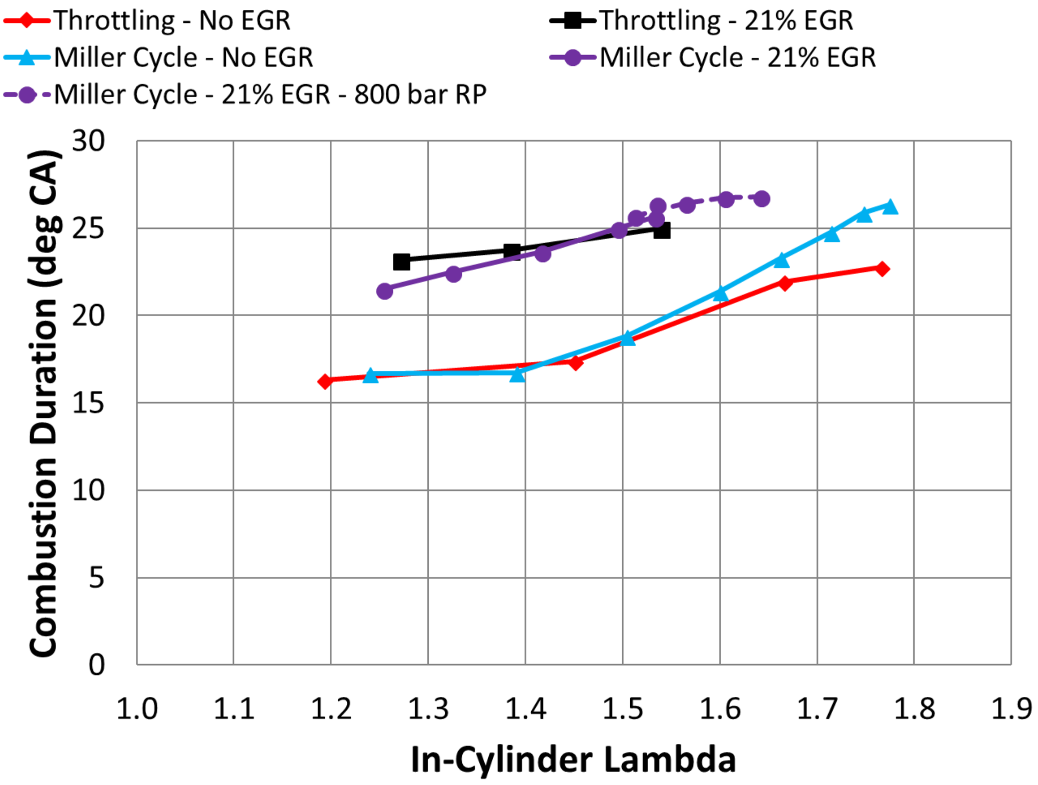

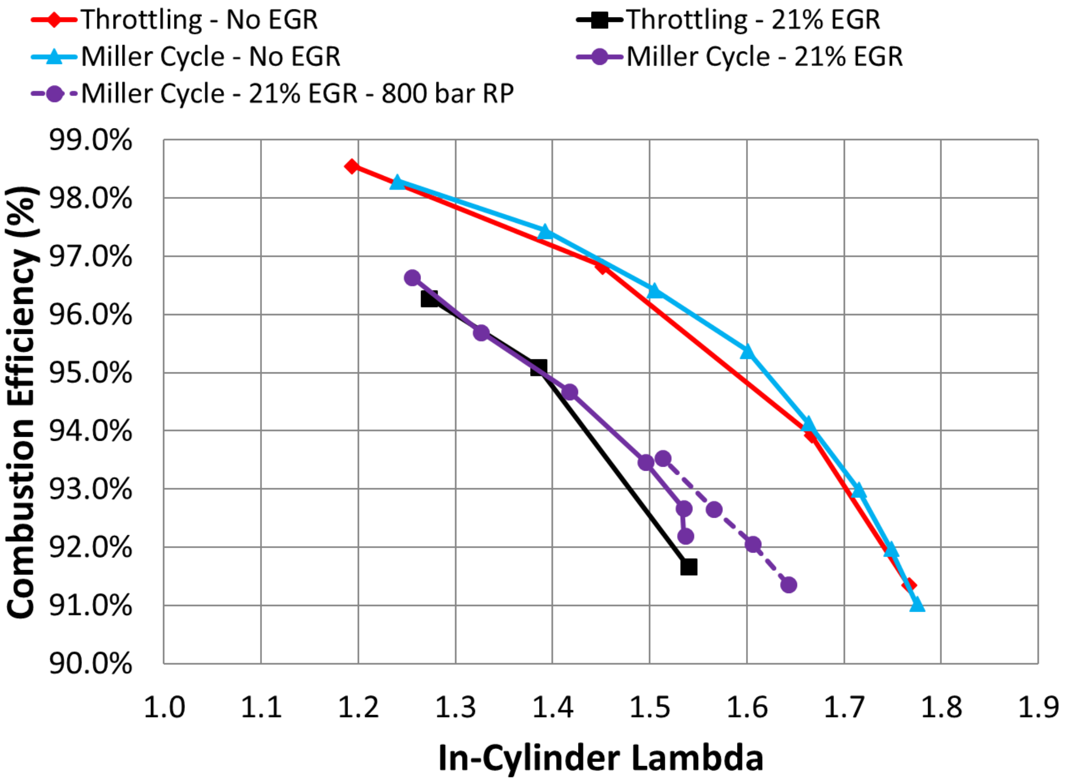

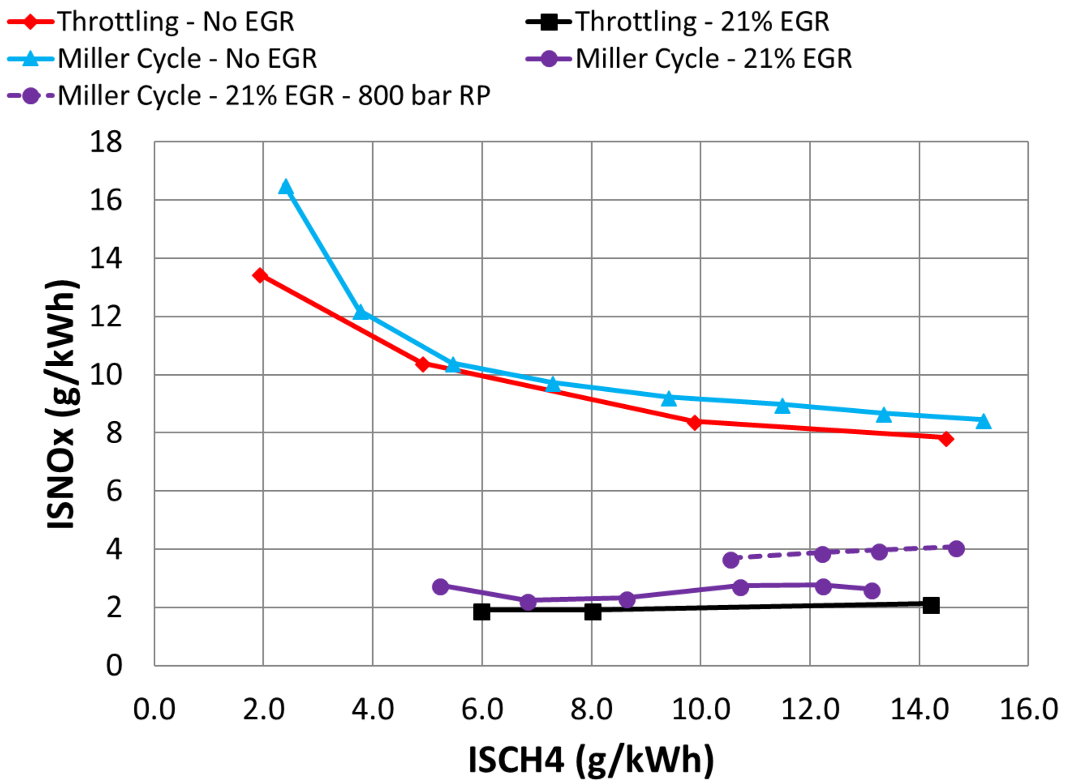
Throttling - No EGR
Throttling - 21% EGR
Miller Cycle - No EGR
Miller Cycle - 21% EGR
Miller Cycle - 21% EGR - 800 bar RP
18
16
14
12
10
8
6
4
2
0
ISNOx (g/kWh)
0.0
2.0
4.0
6.0
8.0
10.0
12.0
14.0
16.0
ISCH4 (g/kWh)

Appendix D – 1D Gas Dynamics Model Validation Graphs

Intake pressure, exhaust pressure, and in-cylinder pressure vs crank angle demonstrating model correlation to experimental data:

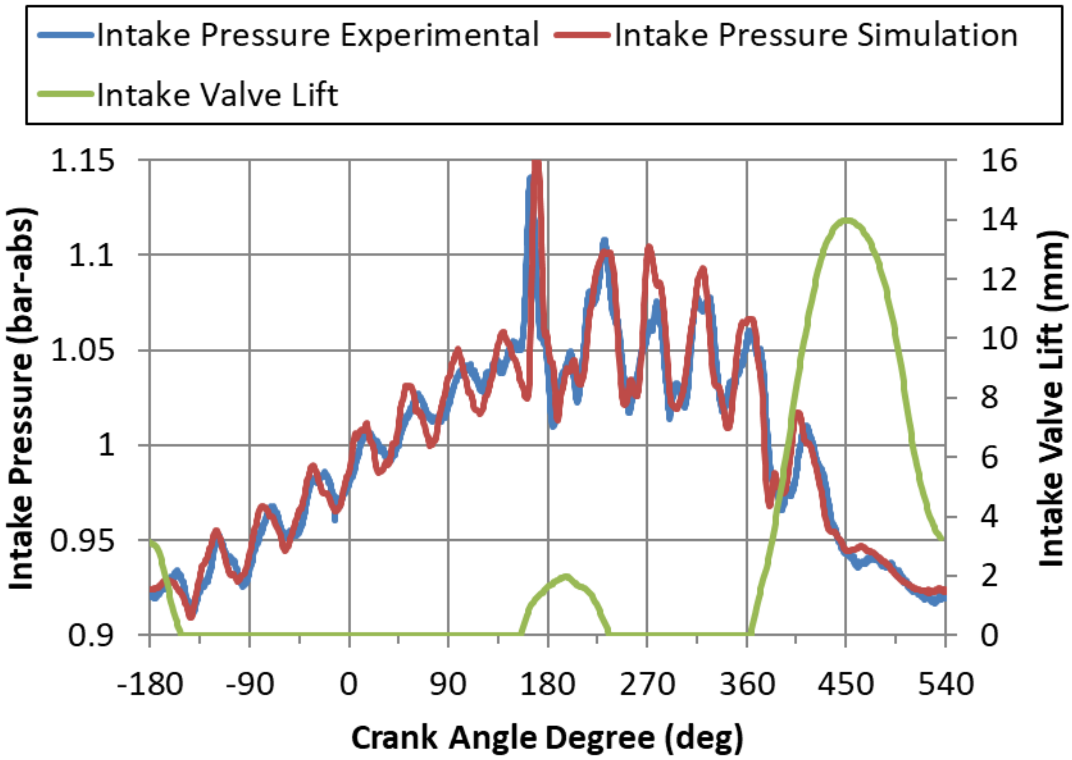

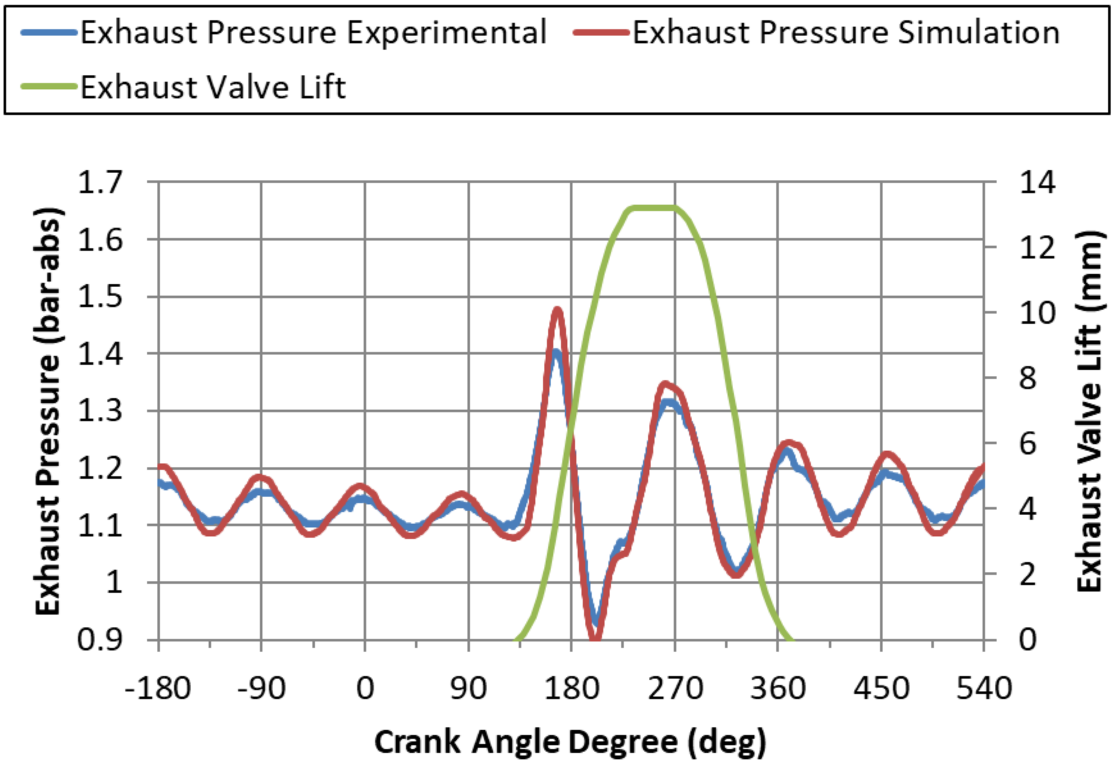
Exhaust Pressure Experimental
Exhaust Pressure Simulation
Exhaust Valve Lift
Exhaust Pressure (bar-abs)
Exhaust Valve Lift (mm)
Crank Angle Degree (deg)
1.7
1.6
1.5
1.4
1.3
1.2
1.1
1
0.9
14
12
10
8
6
4
2
0
-180
-90
0
90
180
270
360
450
540

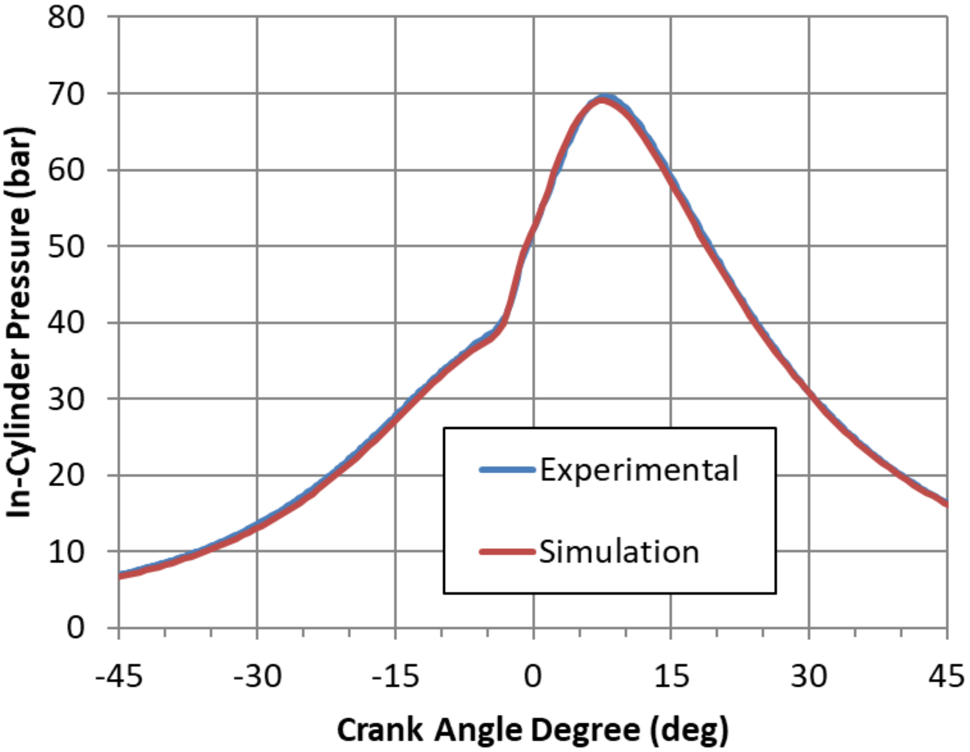
In-Cylinder Pressure (bar)
Crank Angle Degree (deg)
Experimental
Simulation
80
70
60
50
40
30
20
10
0
-45
-30
-15
0
15
30
45

Appendix E – 1D Gas Dynamics Model Flow Coefficients

Intake and exhaust port flow coefficients (valve curtain area) as a function of L (Lift) / D (Diameter) ratio. D was obtained from the inner valve seat diameter, which were 39.2 mm for the intake and 35.8 mm for the exhaust side.

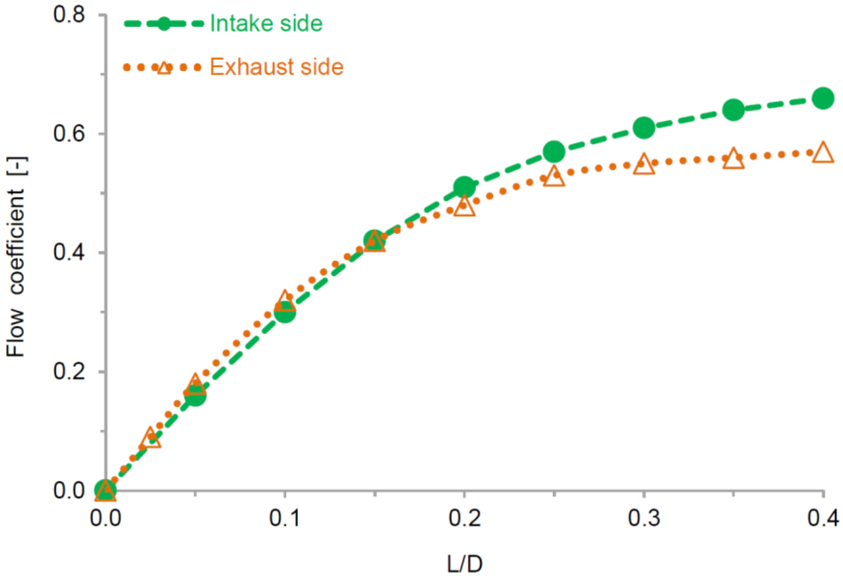

Appendix F – Emissions Graphs for Dual-Fuel Combustion Strategies at 1000 RPM 6 bar IMEPnet

Supplementary engine-out emissions graphs for ISCO vs ISCH4, ISSoot vs ISCH4, and ISNOx vs ISSoot for a variety of dual-fuel combustion modes at 1000 RPM and 6 bar IMEPnet. They are included for completeness.

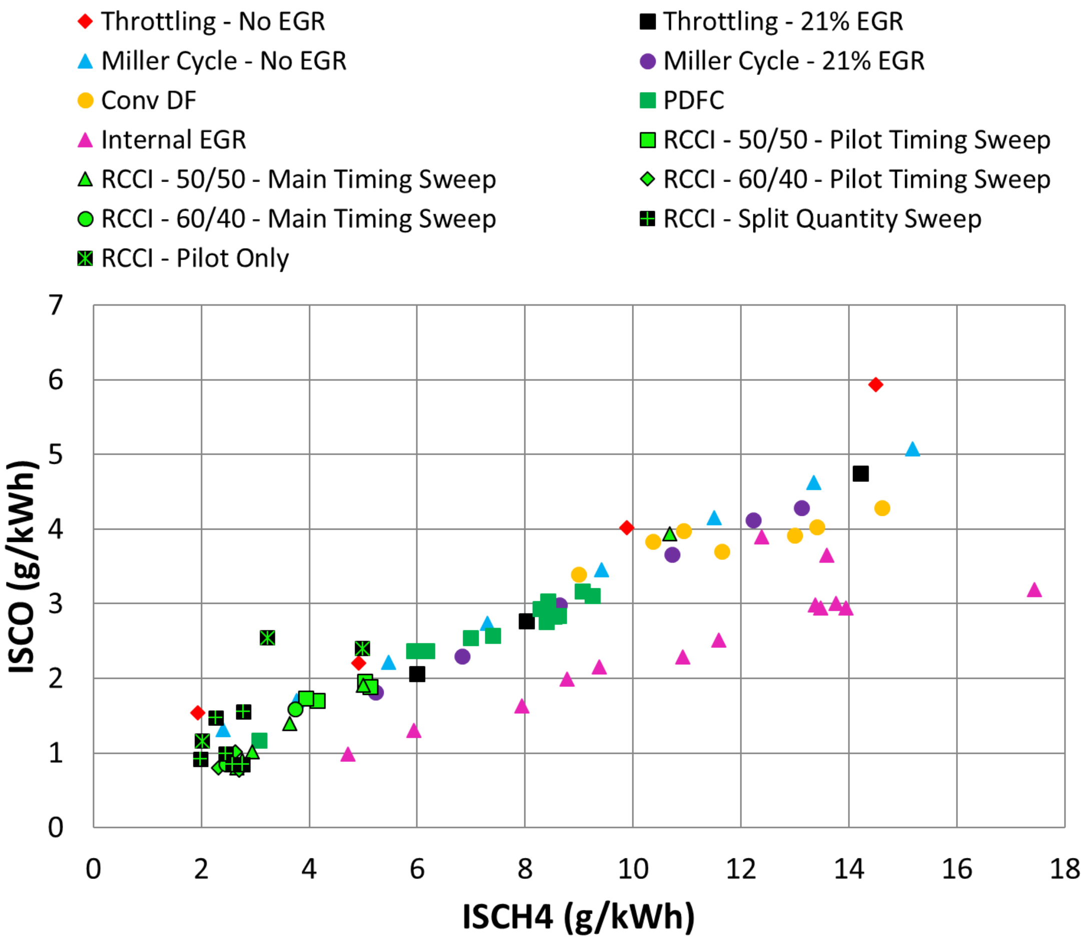

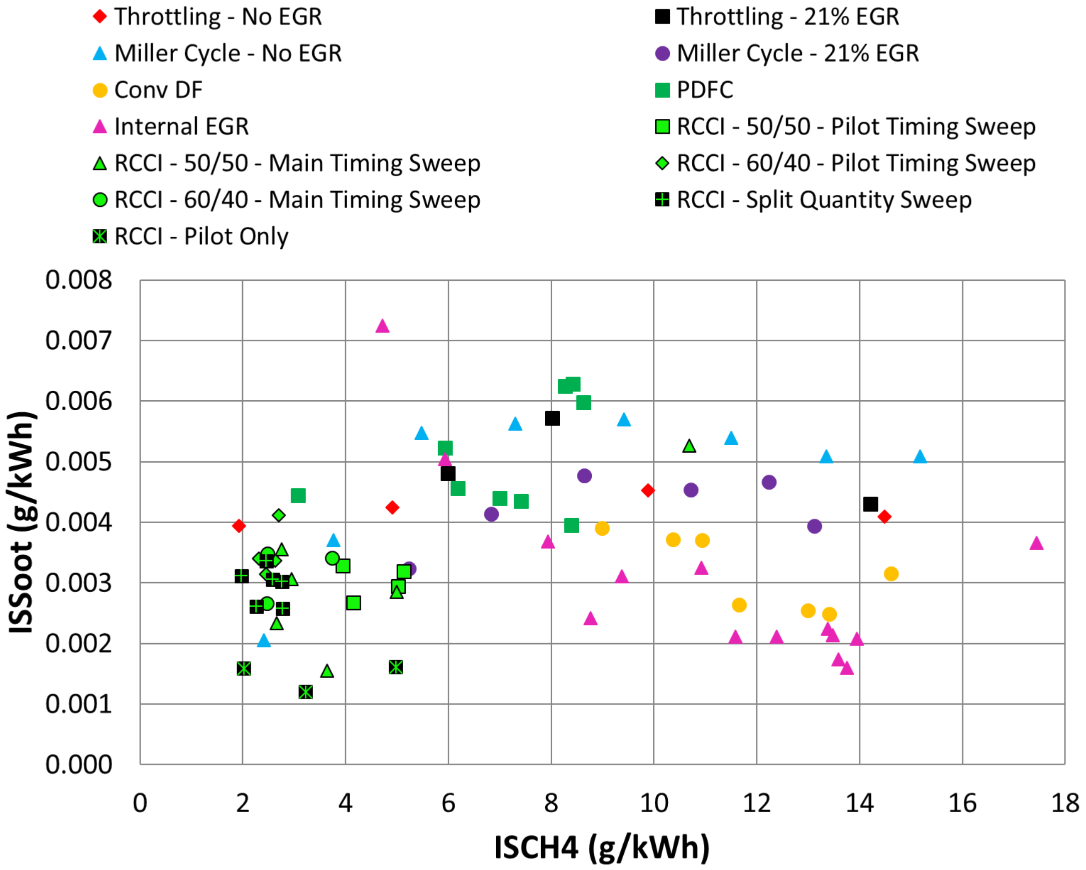
Throttling - No EGR
Throttling - 21% EGR
Miller Cycle - No EGR
Miller Cycle - 21% EGR
Conv DF
PDFC
Internal EGR
RCCI - 50/50 - Pilot Timing Sweep
RCCI - 50/50 - Main Timing Sweep
RCCI - 60/40 - Pilot Timing Sweep
RCCI - 60/40 - Main Timing Sweep
RCCI - Split Quantity Sweep
RCCI - Pilot Only
ISSoot (g/kWh)
0.008
0.007
0.006
0.005
0.004
0.003
0.002
0.001
0.000
0
2
4
6
8
10
12
14
16
18
ISCH4 (g/kWh)

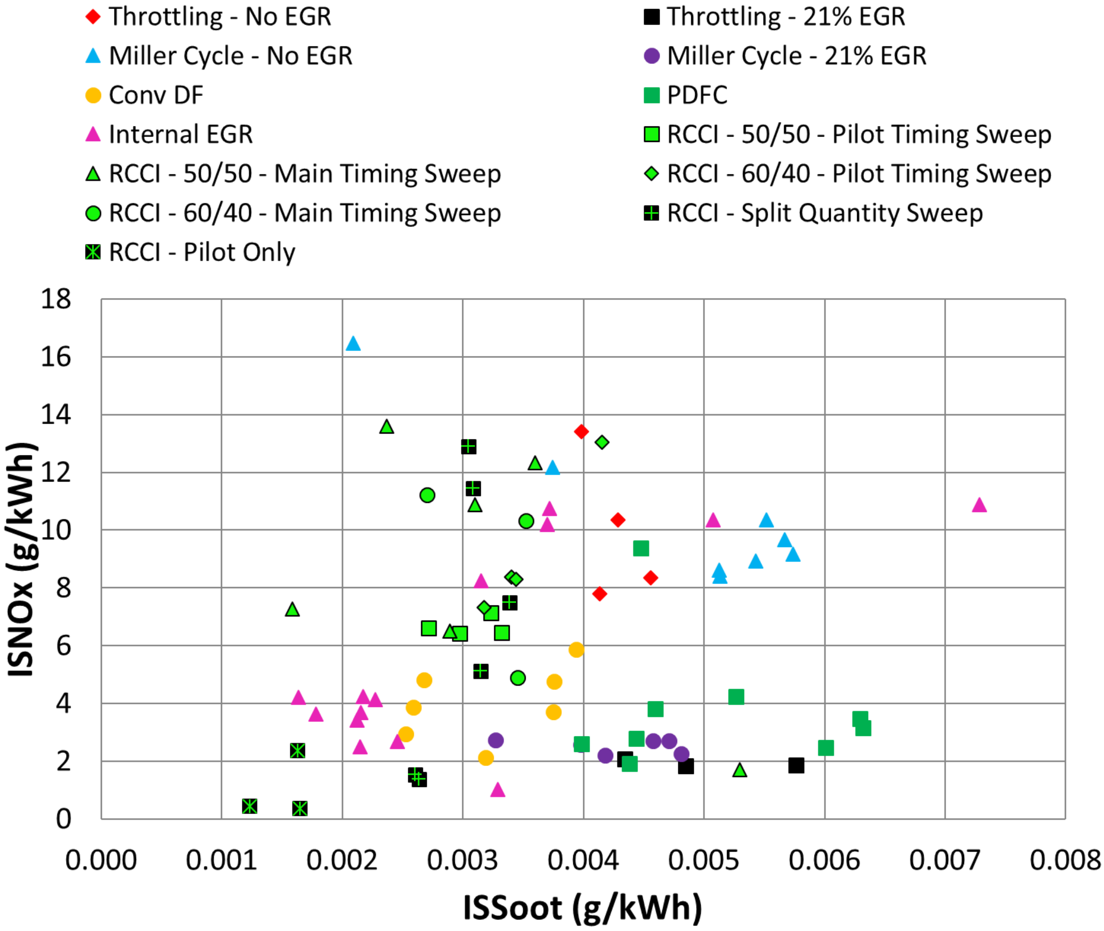
Throttling - No EGR
Throttling - 21% EGR
Miller Cycle - No EGR
Miller Cycle - 21% EGR
Conv DF
PDFC
Internal EGR
RCCI - 50/50 - Pilot Timing Sweep
RCCI - 50/50 - Main Timing Sweep
RCCI - 60/40 - Pilot Timing Sweep
RCCI - 60/40 - Main Timing Sweep
RCCI - Split Quantity Sweep
RCCI - Pilot Only
ISNOx (g/kWh)
18
16
14
12
10
8
6
4
2
0
0.000
0.001
0.002
0.003
0.004
0.005
0.006
0.007
0.008
ISSoot (g/kWh)

List of references

[1] IPCC. Climate Change 2013 - The Physical Science Basis. Cambridge: Cambridge University Press; 2014. doi:10.1017/CBO9781107415324.

[2] IPCC. Climate Change 2014: Synthesis Report. Contribution of Working Groups I, II and III to the Fifth Assessment Report of the Intergovernmental Panel on Climate Change. Cambridge: Cambridge University Press; 2014. doi:10.1017/CBO9781107415324.

[3] Davis SC, Williams SE, Boundy RG. Transportation Energy Data Book Edition 35. 2016.

[4] ExxonMobil. 2017 Outlook for Energy: A View to 2040. 2017.

[5] Gravel R. Freight Mobility and SuperTruck, 2016.

[6] Hicks B. Class 8 Electric Hybrids – Opportunities and Challenges. SAE Hybrid Veh. Technol. 2010 Symp., 2010.

[7] List H. Natural Gas and Renewable Methane for Powertrains. Cham: Springer International Publishing; 2016. doi:10.1007/978-3-319-23225-6.

[8] Torrey WF, Murray D. An Analysis of the Operational Costs of Trucking: 2015 Update. Am Transp Res Inst 2015.

[9] Office UGP. Title 40 : Protection of Environment; Part 98 - Mandatory Greenhouse Gas Reporting; Subpart A — General Provision. Electron CODE Fed Regul 2017. https://www.ecfr.gov/cgi-bin/text-idx?SID=ec77ff3b342de37b12ce98f62a6e1f9f&mc=true&node=ap40.23.98_19.1&rgn=div9 (accessed July 15, 2017).

[10] Heywood JB. Internal Combustion Engine Fundamentals. vol. 21. McGraw-Hill Book Co; 1988.

[11] Van Wylen GJ, Sonntag RE, Dybbs A. Fundamentals of classical thermodynamics. J Appl Mech 1975;42:522. doi:10.1115/1.3423632.

[12] UXL Encyclopedia of Science. Steam Engine. EncyclopediaCom 2017. http://www.encyclopedia.com (accessed June 8, 2017).

[13] Jaaskelainen H. Early History of the Diesel Engine. DieselNet 2013. https://www.dieselnet.com/tech/diesel_history.php (accessed June 8, 2017).

[14] Cummins CL. Early IC and Automotive Engines, SAE International; 1976. doi:10.4271/760604.

[15] William Robinson (M.E.). Gas & Petroleum Engines. 2nd ed. Spon; 1902.

[16] Stuart HA. United States Patent: Engine Operated by the Explosion of Mixtures of Gas or Hydrocarbon Vapor and Air 1893.

[17] Stone R. Introduction to Internal Combustion Engines. 4th ed. Palgrave Macmillan; 2012.

[18] Busch-Sulzer Bros.-Diesel Engine Company SL. The Diesel Engine. Busch-Sulzer Bros.-Diesel Engine Company; 1913.

[19] Woodyard D. Pounder's Marine Diesel Engines and Gas Turbines. 9th ed. Butterworth-Heinemann; 2009.

[20] Nunney MJ. Light and Heavy Vehicle Technology. Butterworth-Heinemann; 2007.

[21] AG D. Prosper L'Orange and the modern diesel engine n.d. http://media.daimler.com/marsMediaSite/en/instance/ko/Prosper-LOrange-and-the-modern-diesel-engine.xhtml?oid=9361309 (accessed June 16, 2017).

[22] AG D. Vorkammerkonstruktion des Prosper L'Orange n.d. https://mercedes-benz-publicarchive.com/marsClassic/en/instance/picture/Vorkammerkonstruktion-des-Prosper-LOrange.xhtml?oid=125239 (accessed June 16, 2017).

[23] Breton B. A Pioneer of the Internal Combustion Engine: Sir Harry Ricardo F.R.S. n.d. http://www-g.eng.cam.ac.uk/125/achievements/ricardo/ (accessed June 16, 2017).

[24] Jääskeläinen H, Khair MK. Diesel engines 2015. https://www.dieselnet.com/tech/diesel_engines.php (accessed June 8, 2017).

[25] Haagen-Smit AJ. Chemistry and Physiology of Los Angeles Smog. Ind Eng Chem 1952;44:1342–6. doi:10.1021/ie50510a045.

[26] Jääskeläinen H, Majewski WA. Engine Technology Evolution: Heavy-Duty Diesels. DieselNet Technol Guid 2014. https://www.dieselnet.com/tech/engine_heavy?duty.php (accessed June 12, 2017).

[27] Andreae M. Advanced engine technology. ICCT Work., 2013.

[28] EU. Directive 1999/96/EC. Off J Eur Communities 1999;16.2.2000. http://eur-lex.europa.eu/legal-

content/EN/TXT/PDF/?uri=CELEX:31999L0096&from=EN (accessed June 24, 2017).

[29] Henry M. Euro VI Product Experience. Emiss Solut J 2014;September.

[30] EU. Regulation (EC) No 595/2009. Off J Eur Union 2009;17.7.2009:L 188. http://eur-lex.europa.eu/legal-content/EN/TXT/PDF/?uri=CELEX:32009R0595&from=EN (accessed June 24, 2017).

[31] United States Environmental Protection Agency. Final Rule for Phase 1 Greenhouse Gas Emissions Standards and Fuel Efficiency Standards for Medium- and Heavy-Duty Engines and Vehicles 2016. https://www.epa.gov/regulations-emissions-vehicles-and-engines/final-rule-phase-1-greenhouse-gas-emissions-standards-and#rule-summary (accessed June 18, 2017).

[32] The Internation Council on Clean Transportation. United States Efficiency and Greenhouse Gas Emission Regulations for Model Year 2018-2027 Heavy-Duty Vehicles, Engines, and Trailers 2016.

[33] Yamaguchi T, Aoyagi Y, Uchida N, Fukunaga A, Kobayashi M, Adachi T, et al. Fundamental Study of Waste Heat Recovery in the High Boosted 6-cylinder Heavy Duty Diesel Engine. SAE Int J Mater Manuf 2015;8:2015-01–0326. doi:10.4271/2015-01-0326.

[34] Eichler K, Jeihouni Y, Ritterskamp C. Fuel Economy Benefits for Commercial Diesel Engines with Waste Heat Recovery. SAE Int J Commer Veh 2015;8:2015-01-2807. doi:10.4271/2015-01-2807.

[35] Stanton DW. Systematic Development of Highly Efficient and Clean Engines to Meet Future Commercial Vehicle Greenhouse Gas Regulations. SAE Int J Engines 2013;6:2013-01-2421. doi:10.4271/2013-01-2421.

[36] Nakamura Y, Tomizawa K, Onishi T, Hashimoto T, Sato M, Tatani T, et al. Development of Fuel Economy Engine Oil for Heavy Duty Diesel Engine, 2015. doi:10.4271/2015-01-2034.

[37] Campbell J, Watts W, Kittelson D. Reduction of Accessory Overdrive and Parasitic Loading on a Parallel Electric Hybrid City Bus. SAE World Congr., 2012, p. 1–7. doi:10.4271/2012-01-1005.

[38] Kosaka H, Wakisaka Y, Nomura Y, Hotta Y, Koike M, Nakakita K, et al.

Concept of “Temperature Swing Heat Insulation” in Combustion Chamber Walls, and Appropriate Thermo-Physical Properties for Heat Insulation Coat. SAE Int J Engines 2013;6:2013-01–0274. doi:10.4271/2013-01-0274.

[39] Kawaguchi A, Iguma H, Yamashita H, Takada N, Nishikawa N, Yamashita C, et al. Thermo-Swing Wall Insulation Technology; - A Novel Heat Loss Reduction Approach on Engine Combustion Chamber -. SAE Tech. Pap., 2016. doi:10.4271/2016-01-2333.

[40] Lyu MS, Doo BM, Ku YG. A Study of Vehicle Fuel Economy Improvement Potential by Optimization of the Cooling and Ancillary Systems of a Heavy Duty Engine. vol. 2007, 2007. doi:10.4271/2007-01-1772.

[41] Jääskeläinen H, Majewski WA. Heavy-Duty Diesel Engines with Aftertreatment. DieselNet Technol Guid 2015. https://www.dieselnet.com/tech/engine_heavy?duty_aftertreatment.php (accessed June 24, 2017).

[42] Gonzalez D MA, Di Nunno D. Internal Exhaust Gas Recirculation for Efficiency and Emissions in a 4-Cylinder Diesel Engine. SAE Tech. Pap., 2016. doi:10.4271/2016-01-2184.

[43] Schwoerer J a., Kumar K, Ruggiero B, Swanbon B. Lost-Motion VVA Systems for Enabling Next Generation Diesel Engine Efficiency and After-Treatment Optimization, 2010. doi:10.4271/2010-01-1189.

[44] Clark RH, Evans JD, Virrels IG, Global S, Us S. An Evaluation of Shell GTL Diesel – The Environmental Benefits. 8th Diesel Engine Emiss. Reduct. Work., 2002.

[45] Jaramillo P, Griffin WM, Matthews HS. Comparative Analysis of the Production Costs and Life-Cycle GHG Emissions of FT Liquid Fuels from Coal and Natural Gas. Environ Sci Technol 2008;42:7559–65. doi:10.1021/es8002074.

[46] Zhao H. Advanced Direct Injection Combustion Engine Technologies and Development: Diesel Engines. Elsevier Science; 2009.

[47] Jääskeläinen H, Khair MK. Combustion in Diesel Engines. DieselNet Technol Guid 2016. https://www.dieselnet.com/tech/diesel_combustion.php (accessed June 28, 2017).

[48] Flynn PF, Durrett RP, Hunter GL, zur Loye AO, Akinyemi OC, Dec JE, et al. Diesel Combustion: An Integrated View Combining Laser Diagnostics, Chemical Kinetics, And Empirical Validation. SAE Tech. Pap., 1999. doi:10.4271/1999-01-0509.

[49] Dec JE. A Conceptual Model of DI Diesel Combustion Based on Laser-Sheet Imaging*, 1997. doi:10.4271/970873.

[50] Akihama K, Takatori Y, Inagaki K, Sasaki S, Dean AM. Mechanism of the Smokeless Rich Diesel Combustion by Reducing Temperature. vol. 2001, 2001. doi:10.4271/2001-01-0655.

[51] Kitamura T, Ito T, Senda J, Fujimoto H. Mechanism of smokeless diesel combustion with oxygenated fuels based on the dependence of the equivalence ration and temperature on soot particle formation. Int J Engine Res 2002;3:223–48. doi:10.1243/146808702762230923.

[52] Adomeit, P. et al. Laser Optical Diagnostics and Numerical Analysis of HSDI Combustion Systems. Proc. Conf. thermo-and fluid Dyn. Process. diesel engines, Thiesel 2004, Valencia, Spain: 2004.

[53] Musculus MPB. Multiple Simultaneous Optical Diagnostic Imaging of Early-Injection Low-Temperature Combustion in a Heavy-Duty Diesel Engine. vol. 2006, 2006. doi:10.4271/2006-01-0079.

[54] Demirbas A. Methane Gas Hydrate. London: Springer London; 2010. doi:10.1007/978-1-84882-872-8.

[55] Energy USD of. Alternative Fuel Price Report. 2017.

[56] Ahlvik P. Natural Gas. DieselNet Technol Guid 2015. https://www.dieselnet.com/tech/fuel_cng.php (accessed June 15, 2017).

[57] Dahodwala M, Joshi S, Koehler EW, Franke M. Investigation of Diesel and CNG Combustion in a Dual Fuel Regime and as an Enabler to Achieve RCCI Combustion. SAE Tech. Pap., 2014. doi:10.4271/2014-01-1308.

[58] Majewski WA. Methane Oxidation Catalysts. DieselNet Technol Guid 2016. https://www.dieselnet.com/tech/cat_methane.php (accessed June 15, 2017).

[59] Howell J, Harger J. CNG and LNG : What's Best for Your Fleet? Westport and Clean Energy Webinar 2013.

[60] Mohamad TI, Yusoff A, Abdullah S, Jermy M, Harrison M, Geok HH. The Combustion and Performance of a Converted Direct Injection Compressed

Natural Gas Engine using Spark Plug Fuel Injector. SAE Tech. Pap., 2010. doi:10.4271/2010-32-0078.

[61] McTaggart-Cowan G, Mann K, Wu N, Munshi S. An Efficient Direct-Injection of Natural Gas Engine for Heavy Duty Vehicles. SAE Tech. Pap., 2014. doi:10.4271/2014-01-1332.

[62] Attard WP, Toulson E, Huisjen A, Chen X, Zhu G, Schock H. Spark Ignition and Pre-Chamber Turbulent Jet Ignition Combustion Visualization. SAE Tech. Pap., 2012. doi:10.4271/2012-01-0823.

[63] Toulson E, Watson HC, Attard WP. Gas Assisted Jet Ignition of Ultra-Lean LPG in a Spark Ignition Engine. SAE Tech. Pap., 2009. doi:10.4271/2009-01-0506.

[64] Königsson F, Stalhammar P, Angstrom H. Characterization and Potential of Dual Fuel Combustion in a Modern Diesel Engine. SAE Tech. Pap., 2011. doi:10.4271/2011-01-2223.

[65] Rimmer JE, Johnson SL, Clarke A. An experimental study into the effect of the pilot injection timing on the performance and emissions of a high-speed common-rail dual-fuel engine. Proc Inst Mech Eng Part D J Automob Eng 2014;228:929–42. doi:10.1177/0954407013506180.

[66] Karim GA. Dual-Fuel Diesel Engines. CRC Press; 2015.

[67] Cummins Westport Inc. Cummins ISL G n.d. http://www.cumminswestport.com/models/isl-g (accessed January 9, 2016).

[68] Gonzalez J. Spark Ignited Natural Gas Engine Technology. Clean Fleets Technol. Conf., 2014.

[69] Walser M. Natural Gas Why Now , and What are the Challenges, 2013.

[70] Dronniou N, Kashdan J, Lecointe B, Sauve K, Soleri D. Optical Investigation of Dual-fuel CNG/Diesel Combustion Strategies to Reduce CO 2 Emissions. SAE Int J Engines 2014;7:2014-01-1313. doi:10.4271/2014-01-1313.

[71] Doosje E, Willems F, Baert R. Experimental Demonstration of RCCI in Heavy-Duty Engines using Diesel and Natural Gas. SAE Tech Pap 2014;1. doi:10.4271/2014-01-1318.

[72] Tomita E, Fukatani N, Kawahara N, Maruyama K, Komoda T. Combustion Characteristics and Performance of Supercharged Pyrolysis Gas Engine

with Micro-Pilot Ignition. CIMAC 178, Vienna: 2007.

[73] Williams M, Minjares R. A technical summary of Euro 6/VI vehicle emission standards. 2016.

[74] DieselNet. World Harmonized Transient Cycle (WHTC) n.d. https://www.dieselnet.com/standards/cycles/whtc.php (accessed January 6, 2016).

[75] Davy MH. Whither Diesel ? An Overview of Combustion Concepts and Research Directions for Compression Ignition Engines JLR Centre of Excellence for Combustion in Compression Ignition Engines 2015.

[76] Kamimoto T, Bae M. High Combustion Temperature for the Reduction of Particulate in Diesel Engines. SAE Tech. Pap., 1988. doi:10.4271/880423.

[77] Kitamura T, Ito T, Kitamura Y, Ueda M, Senda J, Fujimoto H. Soot Kinetic Modeling and Empirical Validation on Smokeless Diesel Combustion with Oxygenated Fuels. SAE Tech. Pap., 2003. doi:10.4271/2003-01-1789.

[78] Kook S, Bae C, Miles PC, Choi D, Pickett LM. The Influence of Charge Dilution and Injection Timing on Low-Temperature Diesel Combustion and Emissions. SAE Tech. Pap., 2005. doi:10.4271/2005-01-3837.

[79] Sarangi AK, Garner CP, McTaggart-Cowan GP, Davy MH, Wahab E, Peckham M. Load transient between conventional diesel operation and low-temperature combustion. Proc Inst Mech Eng Part D J Automob Eng 2015;229:850–65. doi:10.1177/0954407014548737.

[80] Jääskeläinen H. Low Temperature Combustion. DieselNet Technol Guid 2010. https://www.dieselnet.com/tech/engine_ltc.php#intro (accessed June 15, 2017).

[81] Dec JE. Homogeneous Charge Compression Ignition (HCCI) Engines, Society of Automotive Engineers, Inc. Warrendale, PA; 2003.

[82] Kalghatgi GT, Risberg P, Ångström H. Advantages of Fuels with High Resistance to Auto-ignition in Late-injection, Low-temperature, Compression Ignition Combustion. SAE Tech. Pap., 2006. doi:10.4271/2006-01-3385.

[83] Kokjohn SL, Hanson RM, Splitter D a., Reitz RD. Experiments and Modeling of Dual-Fuel HCCI and PCCI Combustion Using In-Cylinder Fuel Blending. SAE Int J Engines 2009;2:2009-01-2647. doi:10.4271/2009-01-2647.

[84] Milovanovic N, Blundell D, Gedge S, Turner J. SI-HCCI-SI Mode Transition at Different Engine Operating Conditions. Library (Lond)., vol. 2005, 2005. doi:10.4271/2005-01-0156.

[85] Zhao H. HCCI and CAI Engines for the Automotive Industry. Elsevier Science; 2007.

[86] Keeler B, Shayler PJ. Constraints on Fuel Injection and EGR Strategies for Diesel PCCI-Type Combustion. vol. 2008, 2008, p. 776–90. doi:10.4271/2008-01-1327.

[87] Kook S, Bae C. Combustion Control Using Two-Stage Diesel Fuel Injection in a Single-Cylinder PCCI Engine. SAE Tech. Pap., vol. 2004, 2004. doi:10.4271/2004-01-0938.

[88] Neely GD, Sasaki S, Huang Y, Leet J a, Stewart DW. New Diesel Emission Control Strategy to Meet US Tier 2 Emissions Regulations. SAE Tech. Pap., vol. 2005, 2005. doi:10.4271/2005-01-1091.

[89] Opat R, Ra Y, Gonzalez D. MA, Krieger R, Reitz RD, Foster DE, et al. Investigation of Mixing and Temperature Effects on HC/CO Emissions for Highly Dilute Low Temperature Combustion in a Light Duty Diesel Engine. SAE Tech. Pap., vol. 2007, 2007, p. 776-0790. doi:10.4271/2007-01-0193.

[90] Musculus MPB, Miles PC, Pickett LM. Conceptual models for partially premixed low-temperature diesel combustion. Prog Energy Combust Sci 2013;39:246–83. doi:10.1016/j.pecs.2012.09.001.

[91] Kimura S, Aoki O, Kitahara Y, Aiyoshizawa E. Ultra-Clean Combustion Technology Combining a Low-Temperature and Premixed Combustion Concept for Meeting Future Emission Standards. SAE Tech. Pap., 2001. doi:10.4271/2001-01-0200.

[92] Sellnau MC, Sinnamon J, Hoyer K, Kim J, Cavotta M, Husted H. Part-Load Operation of Gasoline Direct-Injection Compression Ignition (GDCI) Engine. SAE Int. J. Engines, 2013. doi:10.4271/2013-01-0272.

[93] Sellnau M, Foster M, Hoyer K, Moore W, Sinnamon J, Husted H. Development of a Gasoline Direct Injection Compression Ignition (GDCI) Engine. SAE Int J Engines 2014;7:2014-01-1300. doi:10.4271/2014-01-1300.

[94] Kalghatgi GT, Risberg P, Angstrom H-E. Partially Pre-Mixed Auto-Ignition of Gasoline to Attain Low Smoke and Low NOx at High Load in a

Compression Ignition Engine and Comparison with a Diesel Fuel. SAE Tech. Pap., 2007, p. SAE 2007-01-0006. doi:10.4271/2007-01-0006.

[95] Dempsey A, Curran S, Storey J, Eibl M, Pihl J, Prikhodko V, et al. Particulate Matter Characterization of Reactivity Controlled Compression Ignition (RCCI) on a Light Duty Engine. sae te, 2014. doi:10.4271/2014-01-1596.

[96] Splitter D, Wissink M, Kokjohn S, Reitz R. Effect of Compression Ratio and Piston Geometry on RCCI Load Limits and Efficiency. SAE Tech Pap 2012-01-0383 2012. doi:10.4271/2012-01-0383.

[97] Kokjohn SL, Hanson RM, Splitter D a., Reitz RD. Fuel reactivity controlled compression ignition (RCCI): a pathway to controlled high-efficiency clean combustion. Int J Engine Res 2011;12:209–26. doi:10.1177/1468087411401548.

[98] Splitter D, Hanson R, Kokjohn S, Reitz RD. Reactivity Controlled Compression Ignition (RCCI) Heavy-Duty Engine Operation at Mid-and High-Loads with Conventional and Alternative Fuels. SAE Tech. Pap. Ser., vol. 1, 2011, p. 0363. doi:10.4271/2011-01-0363.

[99] Nieman DE, Dempsey AB, Reitz RD. Heavy-Duty RCCI Operation Using Natural Gas and Diesel. SAE Int J Engines 2012;5:2012-01–0379. doi:10.4271/2012-01-0379.

[100] Reitz RD, Duraisamy G. Review of high efficiency and clean reactivity controlled compression ignition (RCCI) combustion in internal combustion engines. Prog Energy Combust Sci 2015;46:12–71. doi:10.1016/j.pecs.2014.05.003.

[101] Johansson B. The path towards high efficiency ICE – Low temperature combustion and improved thermodynamics. JSAE/SAE Powertrains, Fuels Lubr. Int. Meet., 2015.

[102] Konigsson F, Stalhammar P, \aSngstr\arm H-E. Combustion Modes in a Diesel-CNG Dual Fuel Engine. SAE Tech. Pap., 2011, p. 2387–98. doi:10.4271/2011-01-1962.

[103] Königsson F, Kuyper J, Stalhammar P, Angstrom H-E. The Influence of Crevices on Hydrocarbon Emissions from a Diesel-Methane Dual Fuel Engine. SAE Int J Engines 2013;6:2013-01–0848. doi:10.4271/2013-01-0848.

[104] Lim JH, Reitz RD. Improving the Efficiency of Low Temperature Combustion Engines Using a Chamfered Ring-Land. Vol. 1 Large Bore Engines; Fuels; Adv. Combust. Emiss. Control Syst., ASME; 2014, p. V001T03A013. doi:10.1115/ICEF2014-5576.

[105] Cheng WK, Hamrin D, Heywood JB, Hochgreb S, Min K, Norris M. An Overview of Hydrocarbon Emissions Mechanisms in Spark-Ignition Engines. SAE Tech. Pap. 932708, 1993. doi:10.4271/932708.

[106] Zammit JP, McGhee MJ, Shayler PJ, Law T, Pegg I. The effects of early inlet valve closing and cylinder disablement on fuel economy and emissions of a direct injection diesel engine. Energy 2015;79:100–10. doi:10.1016/j.energy.2014.10.065.

[107] Ickes A, Hanson R, Wallner T. Impact of Effective Compression Ratio on Gasoline-Diesel Dual-Fuel Combustion in a Heavy-Duty Engine Using Variable Valve Actuation. SAE Tech. Pap., 2015. doi:10.4271/2015-01-1796.

[108] Patychuk B, Wu N, McTaggart-Cowan G, Hill P, Munshi S. Intake and Exhaust Valve Timing Control on a Heavy-Duty, Direct-Injection Natural Gas Engine, 2015. doi:10.4271/2015-01-0864.

[109] Bharath AN, Yang Y, Reitz RD, Rutland C. Comparison of Variable Valve Actuation, Cylinder Deactivation and Injection Strategies for Low-Load RCCI Operation of a Light Duty Engine, 2015. doi:10.4271/2015-01-0843.

[110] Atkinson J. Gas Engine. US Patent 336,505, 1886.

[111] Atkinson J. Gas Engine. US Patent 367,496, 1887.

[112] Miller R. High-pressure supercharging system. US Patent 2,670,595, 1954.

[113] Miller R. High expansion, spark ignited, gas burning, internal combustion engines. US Patent 2,773,490, 1956.

[114] Kawamoto N, Naiki K, Kawai T, Shikida T, Tomatsuri M. Development of New 1.8-Liter Engine for Hybrid Vehicles. SAE Tech. Pap., 2009. doi:10.4271/2009-01-1061.

[115] U.S. EPA. Draft Technical Assessment Report: Midterm Evaluation of Light-Duty Vehicle Greenhouse Gas Emission Standards and Corporate Average Fuel Economy Standards for Model Years 2022-2025 (EPA-420-D-16-900, July 2016). CARB, 2016.

[116] Goto T, Hatamura K, Takizawa S, Hayama N, Abe H, Kanesaka H.

Development of V6 Miller Cycle Gasoline Engine. SAE Tech. Pap., 1994. doi:10.4271/940198.

[117] Fukuzawa Y, Shimoda H, Kakuhama Y. Development of High Efficiency Miller cycle Gas Engine. Tech Rev 2001;38:146–50.

[118] Scania. Six new engines added to Scania's Euro 6 Range. Press Release 2017. https://www.scania.com/group/en/wp-content/uploads/sites/2/2017/06/p17067en-six-new-engines-added-to-scanias-euro-6-range.pdf.

[119] Hauser E. Proline t-mass 65F Manual n.d.

[120] ARB. Appendix D - Methane Number and Fuel Composition n.d. http://www.arb.ca.gov/regact/cng-lpg/appd.pdf (accessed January 1, 2016).

[121] Zhang Y. Experimental investigation of CAI combustion in a two-stroke poppet valve DI engine. PhD Thesis, Brunel University London, 2014.

[122] Zhao H, Ladommatos N. Engine Combustion Instrumentation and Diagnostics. Society of Automotive Engineers; 2001.

[123] Zoldak P, Sobiesiak A, Bergin M, Wickman DD. Computational Study of Reactivity Controlled Compression Ignition (RCCI) Combustion in a Heavy-Duty Diesel Engine Using Natural Gas, 2014. doi:10.4271/2014-01-1321.

[124] Economic Commission for Europe of the United Nations (UN/ECE). Regulation No 49 - Uniform provisions concerning the measures to be taken against the emission of gaseous and particulate pollutants from compression-ignition engines and positive ignition engines for use in vehicles 2013.

[125] de Melo TCC, de Brito MFM, Moreira MF, Machado GB, Fleischman R. Calculation of Uncertainty of Measurement for Diesel Engine ESC Test Emissions. SAE Tech. Pap., 2013. doi:10.4271/2013-36-0236.

[126] AVL. AVL Smoke Meter 415SE Manual 2002:333.

[127] Silvis WM. An Algorithm for Calculating the Air/Fuel Ratio from Exhaust Emissions. SAE Tech. Pap., 1997. doi:10.4271/970514.

[128] Koszalka G, Suchecki A. Durability Prediction of a Diesel Engine Piston-Rings-Cylinder Assembly on the Basis of Test Bench Results. SAE Tech. Pap., 2011. doi:10.4271/2011-24-0130.

[129] Kirsten M, Pirker G, Redtenbacher C, Wimmer A, Chmela F. Advanced

Knock Detection for Diesel/Natural Gas Engine Operation. SAE Int J Engines 2016;9:2016-01–0785. doi:10.4271/2016-01-0785.

[130] Brunt MFJ, Emtage AL. Evaluation of IMEP Routines and Analysis Errors. SAE Tech. Pap., 1996. doi:10.4271/960609.

[131] Königsson F, Risberg P, Angstrom H-E. Nozzle Coking in CNG-Diesel Dual Fuel Engines. SAE Tech. Pap., 2014. doi:10.4271/2014-01-2700.

[132] Winterbone DE, Clough E, Rao KK, Richards P, Williams D. The Effect of DI Nozzle Fouling on Fuel Spray Characteristics. SAE Tech. Pap., 1992. doi:10.4271/922232.

[133] Blanco JC. Effect of Diesel Fuel Quality and Additives on Engine Performance - An Update. Sae 911710, 1991. doi:10.4271/911710.

[134] Richards P, Walker RD, Williams D. Fouling of Two Stage Injectors - An Investigation into Some Causes and Effects. Sae 971619, 1997. doi:10.4271/971619.

[135] Volvo. Volvo D13 with SCR for EPA10 2010:2. http://www.volvotrucks.com/SiteCollectionDocuments/VTNA_Tree/ILF/Products/D13/D13_SCR_425-1550.pdf (accessed June 22, 2016).

[136] Arcoumanis C, Baniasad MS. Analysis of Consecutive Fuel Injection Rate Signals Obtained by the Zeuch and Bosch Methods. SAE Tech. Pap., 1993. doi:10.4271/930921.

[137] Ishikawa S, Ohmori Y, Fukushima S, Suzuki T, Takamura A, Kamimoto T. Measurement of Rate of Multiple-Injection in CDI Diesel Engines. SAE Tech. Pap., 2000, p. 1–6. doi:10.4271/2000-01-1257.

[138] El-Mahallawy, F., El-Din Habik S. Fundamentals and Technology of Combustion. 1st ed. Elsevier Science Ltd; 2002.

[139] Varea E, Modica V, Vandel A, Renou B. Measurement of laminar burning velocity and Markstein length relative to fresh gases using a new postprocessing procedure: Application to laminar spherical flames for methane, ethanol and isooctane/air mixtures. Combust Flame 2012;159:577–90. doi:10.1016/j.combustflame.2011.09.002.

[140] Gibbs GJ, Calcote HF. Effect of Molecular Structure on Burning Velocity. J Chem Eng Data 1959;4:226–37. doi:10.1021/je60003a011.

[141] Li S. NOx formation in two-stage methane–air flames. Combust Flame 1999;118:399–414. doi:10.1016/S0010-2180(99)00002-4.

[142] Eng JA. Characterization of Pressure Waves in HCCI Combustion. SAE Tech. Pap., 2002. doi:10.4271/2002-01-2859.

[143] Glassman I, Yetter R. Combustion. 4th ed. Elsevier Inc; 2008.

[144] Fujimoto Y. Introduction of Variable Compression Turbo Engine 2016.

[145] Kim CH, Paratore M, Gonze E, Solbrig C, Smith S. Electrically Heated Catalysts for Cold-Start Emissions in Diesel Aftertreatment. SAE Tech. Pap., 2012. doi:10.4271/2012-01-1092.